



**This electronic thesis or dissertation has been
downloaded from Explore Bristol Research,
<http://research-information.bristol.ac.uk>**

Author:

Aza, Chrysoula

Title:

Morphing Mechanisms Based on Nonlinear Helical Composite Elements

General rights

Access to the thesis is subject to the Creative Commons Attribution - NonCommercial-No Derivatives 4.0 International Public License. A copy of this may be found at <https://creativecommons.org/licenses/by-nc-nd/4.0/legalcode>. This license sets out your rights and the restrictions that apply to your access to the thesis so it is important you read this before proceeding.

Take down policy

Some pages of this thesis may have been removed for copyright restrictions prior to having it been deposited in Explore Bristol Research. However, if you have discovered material within the thesis that you consider to be unlawful e.g. breaches of copyright (either yours or that of a third party) or any other law, including but not limited to those relating to patent, trademark, confidentiality, data protection, obscenity, defamation, libel, then please contact collections-metadata@bristol.ac.uk and include the following information in your message:

- Your contact details
- Bibliographic details for the item, including a URL
- An outline nature of the complaint

Your claim will be investigated and, where appropriate, the item in question will be removed from public view as soon as possible.

Morphing Mechanisms Based on Nonlinear Helical Composite Elements

Chrysoula Aza

A dissertation submitted to the University of Bristol in accordance with the requirements for award of the degree of Doctor of Philosophy in the Faculty of Engineering.

School of Civil, Aerospace and Mechanical Engineering

November 2019

Word Count: 36604

Abstract

Tailoring structural nonlinearities offers the potential to design well-behaved nonlinear structures with increased functionality and enhance the performance of modern engineering structures. In light of this concept, this research focuses on the behaviour of structural assemblies of nonlinear morphing elements. A compliant, multistable, reconfigurable mechanism is introduced, which consists of nonlinear morphing structural elements assembled in a truss-like configuration.

Existing compliant mechanisms rely on flexible members and their elastic deformations to achieve multistability, but their range of motion is restricted by strength limitations. The compliant mechanism developed in this research uses morphing elements as the flexible members. These elements are composite structures of a double-helix architecture that can change shape and undergo large deformations while maintaining load-carrying capability and structural integrity. The variable geometry and customizable nonlinear stiffness characteristics of the double-helices enable the mechanism to be tailored and a variety of behaviours to be developed.

For the study of the mechanical characteristics and design space of this mechanism, a simple truss structure has been chosen; a modified von Mises truss, pin-jointed at the apex and base supports. Two different approaches have been employed for the structural analysis of the mechanism: (i) an energy approach to identify the stable configurations of the truss across its workspace, with energy minima and maxima corresponding to stable and unstable equilibria, respectively; (ii) a path-following method, the modified-Riks method, to explore the force-displacement space and obtain potential load paths between stable states under specific load cases.

Both the multistability and reconfigurability of this mechanism have been explored. The mechanism's multistable characteristics and response upon application of a load at the apex have been investigated parametrically by varying the lay-up of the composite strips, the geometry of the double-helix, and the initial truss geometry. Additionally, the reconfigurability of the mechanism has been explored. Based on the ability of the double-helical elements to switch twist direction when in fully extended state, the mechanism is able to change behaviour and operate in different modes, whilst maintaining its connectivity and mobility. Four reconfiguration modes can be obtained by combination of the two different helical deformation modes, resulting in significant variations in the mechanical response and stability characteristics of the mechanism between the different modes. The influence of the double-helices' design parameters, and the initial geometry of the truss itself is explored for this case as well.

Finally, a prototype is manufactured and tested for the validation of the results from the analytical model. A design of the test rig required for the setup and testing of the truss assembly has been developed. Overall, the experimental results have shown a good qualitative agreement with the predictions of the analytical model. Any discrepancies occurred can be well-justified by the experimental setup, limitations of the analytical model and an unexpected, nonuniform deformation of the double-helical elements along their lengths, noticed during testing.

Acknowledgement

I would like to express my sincere gratitude to my supervisors, Dr Alberto Pirrera and Dr Mark Schenk, for their continuous support and guidance throughout my PhD. I am also thankful for their availability to discussions. Their enthusiasm, suggestions and comments proved a catalyst for the fulfilment of this research.

Many thanks are extended to the Technicians and Apprentice of the Faculty of Engineering Workshop of the University of Bristol—Mr Rich Chaffey, Mr Rich Hooper, Mr Michael Williams, Mr Mike Bracey, Mr Rich Bragg and Mr Jack Marsh. Their work on the manufacture of the components of the test rig for my experiments is much appreciated, as their prompt response to my requests too. I would like also to acknowledge Ismaeel Zaman, a student at the University of Bristol, for his help with the preliminary CAD drawings of the test rig.

I would like to acknowledge the Engineering and Physical Sciences Research Council in the United Kingdom for funding this research through the EPSRC Centre for Doctoral Training in Advanced Composites for Innovation and Science under the grant number EP/L016028/1.

Finally, special thanks are due to my parents and my sister, for being always there urging me in their own way. To my sister and my dear friends for their understanding and support, mainly though for being that pleasant, much needed, distraction outside my research over these years—Thank you.

Declaration

I declare that the work in this dissertation was carried out in accordance with the requirements of the University's *Regulations and Code of Practice for Research Degree Programmes* and that it has not been submitted for any other academic award. Except where indicated by specific reference in the text, the work is the candidate's own work. Work done in collaboration with, or with the assistance of, others, is indicated as such. Any views expressed in the dissertation are those of the author.

SIGNED: DATE:

Publications

The following publications constitute an outcome of this research project. Published material of these papers has been reused in this thesis, composing either individual sections of Chapter 3, 4, 6 and 7 and/or the entire Chapter 5. Specifically, Chapter 5 comprise work published in (i) and (ii), and Chapter 6 contains some results from (iii). Section 3.4 contains results from (i) and (iii), Section 7.6 from (i). Section 3.2, Section 3.3, Section 4.1, Section 4.2 and Section 4.3 contain work included in all three publications.

Journal Publications

(i) Aza C., Pirrera A. and Schenk M., 2019, “Multistable morphing mechanisms of nonlinear springs,” *ASME J Mech Robot*, vol. 11, no. 5, p. 051014. DOI: 10.1115/1.4044210

Conference Papers

(ii) Aza C., Pirrera A. and Schenk M., 2018, “Multistable trusses of nonlinear morphing elements,” *2018 International Conference on Reconfigurable Mechanism and Robots (ReMAR)*, Delft, Netherlands, June 20-22, 2018, pp. 1-6. DOI: 10.119/REMAR.2018.8449846

(iii) Aza C., Pirrera A. and Schenk M., 2018, “Reconfigurable trusses of nonlinear morphing elements,” *ASME International Design Engineering Technical Conferences and Computers and Information in Engineering Conference (IDETC/CIE2018)*, Quebec City, Quebec, Canada, August 26-29, 2018, Paper No. DETC2018-85911. DOI: 10.1115/DETC2018-85911

Contents

Abstract	I
Acknowledgement	III
Declaration	V
Publications	VII
Contents	IX
List of tables	XIII
List of Figures	XV
Nomenclature	XXV
Chapter 1	
INTRODUCTION	1
1.1 Motivation	1
1.2 Objectives	4
1.3 Outline of the thesis	5
Chapter 2	
LITERATURE REVIEW	7
2.1 Introduction	7
2.2 Nonlinear Structures	7
2.3 Compliant Mechanisms	11
2.4 Reconfigurable Mechanisms	16
2.5 Summary	20
Chapter 3	
A DOUBLE-HELIX MORPHING COMPOSITE STRUCTURE	23
3.1 Introduction	23
3.2 Description of the double-helix morphing structure	24
3.3 Analytical model [26, 202]	25
3.4 Double-helix response	29
3.5 Summary	35
Chapter 4	
A COMPLIANT MECHANISM BASED ON DOUBLE-HELIX COMPOSITE STRUCTURES AND ITS ANALYSIS METHODS	37
4.1 Introduction	37
4.2 Structural Assemblies of Double-Helices	38
4.3 Analysis of the Structural Assemblies	41
4.3.1 Strain Energy Landscapes	41
4.3.2 Path-following Method	42
4.4 Summary	51

Chapter 5

MULTISTABILITY IN MECHANISMS OF NONLINEAR MORPHING ELEMENTS	53
5.1 Introduction.....	53
5.2 Initial results.....	54
5.3 Multistability.....	60
5.4 Constant stiffness	65
5.5 Summary	69

Chapter 6

RECONFIGURABILITY IN MECHANISMS OF NONLINEAR MORPHING ELEMENTS	71
6.1 Introduction.....	71
6.2 Reconfigurability	72
6.3 Effect of composite lay-up.....	79
6.3.1 Mode I.....	79
6.3.2 Mode II.....	82
6.3.3 Mode III	85
6.4 Effect of initial truss geometry, $\alpha_{0,i}$	88
6.5 Summary	94

Chapter 7

MANUFACTURE AND TEST OF A PROTOTYPE MECHANISM OF NONLINEAR MORPHING ELEMENTS	97
7.1 Introduction.....	97
7.2 Double-helix assembly mechanism test rig design	98
7.3 Adapted analytical model.....	101
7.4 Double-helix manufacture, experimental set-up and results	109
7.4.1 Double-helix manufacture.....	109
7.4.2 Experimental set-up	110
7.4.3 Results	111
7.5 Initial experimental set-up and results for assembly of double-helices.....	114
7.5.1 Initial experimental set-up	114
7.5.2 Results.....	115
7.6 Modified experimental set-up and results for assembly of double-helices	118
7.6.1 Modified experimental set-up.....	119
7.6.2 Results	119
7.7 Summary	123

Chapter 8

CONCLUSIONS AND FUTURE WORK	127
8.1 Conclusions.....	127
8.2 Future work.....	131
References	135
Appendix A.1 – Truss Prototype Test Rig	149

Appendix A.2 – Supplementary Rig for Drilling	165
Appendix A.3 – Helix Test Rig	167

List of tables

Table 3.1: Hexcel IM7/8552 unidirectional carbon fibre prepreg properties [25, 208]	30
--	----

List of Figures

Figure 1.1: Actuation system developed by Cappello et al. [27].	3
Figure 1.2: a) Simplified link-segment model for the lower human limb; b-c) potential configurations to simulate the gait motion.	4
Figure 2.1: Experimental images of four periodic porous structures of elastomeric material with differently arranged holes (50% initial porosity) loaded under uniaxial compression in the undeformed (top) and deformed (bottom) configuration with applied compressive engineering strain $\varepsilon = 0.21$ (scale bars: 20 mm) [83, 101].	9
Figure 2.2: a) Sequence of progressively deformed shapes of “Buckliball”, made of silicone-based rubber, pressurised by a motorised syringe pump (scale bar: 3 cm) [81]. b) Image of a vacuum-actuated muscle-inspired pneumatic structure made of Ecoflex lifting a small weight when actuated by applying a vacuum [42].	9
Figure 2.3: a) A tristable lattice structure assembled from four bistable nonsymmetric composite laminates in the plane (left), concave (middle) and convex (right) stable configurations [70]. b) Multistable lattice structures assembled from multiple tristable lattices in different arrangements [29]. c) A multistable composite twisting structure in a straight (left), twisted (middle) and coiled (right) configuration [25]. d) A bistable composite I-beam in a twisted configuration [74]. e) A multistable cylindrical lattice assembled from pre-stressed composite strips in an intermediate (top) and contracted (bottom) state [73].	10
Figure 2.4: a) Compliant aerofoil structure with a variable stiffness multistable composite element embedded [97]. b) A morphing composite air inlet demonstrator in a closed state (left), open state (middle), and bottom view in an open state (right) [66]. c) Twist morphing blade in the straight configuration without the skin (left), revealing the composite pre-stressed strips, and with the skin (right) [95].	11
Figure 2.5: a) Schematic of a corner-filletted flexure hinge [112]. b) Conceptual design of a compliant revolute (left) and translational (right) joint based on flexible beams [128]. c) Prototype of conjugated surfaces flexure hinge made from PVC in its neutral and deformed configurations [129]. d) Compliant tool tip prototype in a neutral (top) and fully bent (bottom) state [120]. e) Design of a compliant micro gripper with conjugated surfaces flexure hinges and its pseudo-rigid body model superimposed [124].	13
Figure 2.6: a) Prototype of a quadristable compliant mechanism in its four stable states [132]. b) Prototype of a rotational compliant mechanism from two serially connected bistable mechanisms in its four stable configurations [134]. c) Prototype of a tristable mechanism assembled from orthogonal compliant mechanisms in its three stable configurations [137]. d) Prototype of a compliant bistable release mechanism in its second stable (left) and its initial stable (right) configurations [118].	14
Figure 2.7: a) Statically balanced compliant mechanisms; two grippers and a multiplier prototypes (left to right) [141]. b) Prototype of a zero-stiffness compliant cross-axis flexural joint [142]. c) Prototype of the four-bar linkage compliant mechanism internally balanced with two pre-stressed leaf springs [147]. d) Prototype of a constant force mechanism over a certain displacement range at its two stable configurations [144]. e) Prototype of a constant force end effector combining linear springs with bistable beams [145]. f) A statically balanced compliant mechanism prototype assembled from individual constant force mechanisms [150]. g) A specially shaped polycarbonate double-clamped beam acting as a compliant gravity balancer mechanism [148].	16
Figure 2.8: a) An rT joint with an additional degree of rotation enabling axis 1 to rotate about axis 2 and can be fixed by bolting it to the groove [174]. b) Prototype of the reconfigurable canopy based on 4-bar mechanisms in two deployed configurations [181]. c) Prototype of a reconfigurable mechanism based on angulated elements in different configurations [160].	17

- Figure 2.9:** a) A variable geometry truss through its transformation from a completely folded to deployed configuration [182]. b) General structure of a variable geometry truss manipulator [184]. c) A zero stiffness tensegrity mechanism in different configurations [186]. 18
- Figure 2.10:** a) A polymer dome structure created using inks with different optical absorption under a blue LED (scale bar: 5 mm) [190]. b) Modification of the hexagonal twist pattern for a foldable structure using thickness variation for the hinges and a prototype of thick panels in its various configurations [162]. c) Prototype of a 2D and a 3D shape reconfigurable material using a bistable triangular unit hinge mechanism fabricated through laser cutting of Teflon sheets in various configurations [193]. 19
- Figure 3.1:** a) Initially curved (radius R_i) composite strips are flattened to introduce pre-stress; b) the strips are joined by rigid spokes to form a double-helix structure, which c) can deform from a straight (light grey) to twisted (dark) configurations. 25
- Figure 3.2:** Strain energy profiles as a function of the helix angle θ of double-helices with $L = 95$ mm, $R = 15$ mm, $R_i = 30$ mm, $W = 5$ mm for different strip lay-ups. Dots (●) represent unstable equilibria; crosses (+) stable equilibria; triangles (▲) boundary equilibria. 31
- Figure 3.3:** Load-displacement curves of double-helices with $L = 95$ mm, $R = 15$ mm, $R_i = 30$ mm, $W = 5$ mm for different strip lay-ups. a) $\theta \in [0^\circ, 90^\circ]$; b) $\theta \in [0^\circ, -90^\circ]$. The displacement Δl has been normalized to the length L of the strips, with $\Delta l/L = 0$ representing the fully-extended and $\Delta l/L = 1$ its fully coiled configurations. 31
- Figure 3.4:** Axial stiffness as a function of the displacement Δl of double-helices with $L = 95$ mm, $R = 15$ mm, $R_i = 30$ mm, $W = 5$ mm for different strip lay-ups. a) $\theta \in [0^\circ, 90^\circ]$; b) $\theta \in [0^\circ, -90^\circ]$. The displacement Δl is normalized to the length L of the strips, with $\Delta l/L = 0$ representing the fully-extended and $\Delta l/L = 1$ its fully coiled configurations. 32
- Figure 3.5:** Manufactured prototype of the double-helix structure of a symmetric $[90/45/0/45/90]$ strip lay-up, with dimensions $L = 292$ mm, $R = 30$ mm, $R_i = 60$ mm, $W = 10$ mm in a) straight configuration; b) stable, c) twisted, and d) fully coiled configurations for $\theta \in [0^\circ, 90^\circ]$; e) twisted, f) stable, and g) fully coiled configurations for $\theta \in [0^\circ, -90^\circ]$ 33
- Figure 3.6:** Load-displacement curves of double-helices of a $[45_2/0/45_2]$ strip lay-up: a) for different lengths L , $R = 15$ mm, $R_i = 30$ mm, $W = 5$ mm. b) for different widths W , $L = 95$ mm, $R = 15$ mm, $R_i = 30$ mm; c) for different radius R , $L = 95$ mm, $R_i = 30$ mm, $W = 5$ mm; d) for different initial curvatures of the strips R_i , $L = 95$ mm, $R = 15$ mm, $W = 5$ mm; e) for different dimensions L , R and R_i , keeping a constant ratio $R_i/R = 2$ and $L \approx 2\pi R$. The displacement Δl is normalized to the length L of the strips in each case for comparison purposes, with $\Delta l/L = 0$ representing the fully-extended and $\Delta l/L = 1$ its fully coiled configurations. 34
- Figure 4.1:** Schematic representation of the assembly of double-helices in a truss-like configuration with both supports pinned [207]. The initial configuration is determined by the equilibrium length $L_{0,i}$ of the double-helices and by the initial angle $\alpha_{0,i}$ of the truss configuration. 39
- Figure 4.2:** Schematic representation of a deformed configuration of the assembly of double-helices in a truss-like mechanism under an applied load at the apex. 39
- Figure 4.3:** Strain energy contour plot for a) a single linear spring with finite free length l_{s0} fixed at one end, and b) the assembled *von Mises* truss of two identical such linear spring elements pin-jointed. The attainable workspace is limited by the maximum elongation of the spring members; here this was set to 1.5 times of the spring's free length. The initial truss configuration is indicated with the black spring elements. Points labelled 1 and 2, corresponding to energy minima, denote stable equilibria, while point M identifies position of unstable equilibrium. 42
- Figure 4.4:** Free-body diagram of the assembly of double-helices in the truss-like configuration. 43

Figure 4.5: Load-displacement curve (purple) of the assembled *von Mises* truss of two identical linear spring elements under a vertical load P at the apex. Results are for initial truss angle $\alpha_{0,1} = 35^\circ$. Dashed line represents section of instability; points 1 and 2 are stable equilibrium points. Point M is an unstable equilibrium point. The load has been normalized with respect to the load value at the maximum peak (P_{crit}). The displacement has been normalized with respect to the initial height of the truss structure. The variation of the corresponding eigenvalues ω_j of the tangential stiffness matrix of the system are included (cyan lines). The eigenvalues have been normalised to a value 10^3 to fit the scale of the load-displacement curve. 49

Figure 5.1: Strain energy landscapes for a compliant mechanism of identical double-helices assembled in a truss-like configuration. Results are for initial truss angles $\alpha_{0,1} = 35^\circ$ and $\alpha_{0,1} = 70^\circ$, with composite strips of $[0_5]$, $[45_2/0/45_2]$ and $[45_2/0/-45_2]$ lay-ups. The initial truss configurations are indicated with black lines. Points labelled 1–5 denote stable equilibria, while points A–H, J, K and M identify positions of unstable equilibrium; points I–IV denote stable boundary equilibria. The positions of the truss apex under an applied vertical load ($P_h = 0$) and/or horizontal load ($P_v = 0$) are superimposed on the landscapes: red points indicate the equilibrium paths of the apex under the application of a vertical load; blue points indicate the equilibrium paths of the apex under the application of a horizontal load. 56

Figure 5.2: Load-displacement curves of the assembled structure of identical double-helices under the application of a vertical load at the apex. Results are for different initial truss angle a) $\alpha_{0,1} = 35^\circ$ and b) $\alpha_{0,1} = 70^\circ$ and of double-helices with varying lay-ups. Dashed line represents sections of instability; points 1–5 are stable equilibrium points. Points A–H, J, K and M are unstable equilibrium points. The load has been normalized with respect to the load value at the maximum peak (P_{crit}) in each case. The displacement has been normalized with respect to the initial height of the truss structure. 57

Figure 5.3: Load-displacement curves of the assembled structure of identical double-helices under the application of a horizontal load at the apex. Results are for different initial truss angle a) $\alpha_{0,1} = 35^\circ$ and b) $\alpha_{0,1} = 70^\circ$ and of double-helices with varying lay-ups. Dashed line represents sections of instability. Points 1 and 2 are stable equilibrium points; points A–H, J, K and M are unstable equilibrium points. The load has been normalized with respect to the load value at the maximum peak (P_{crit}) in each case. The displacement has been normalized with respect to the initial width of the truss structure. 57

Figure 5.4: Load-displacement curve (left) and deformation (right) of the assembled structure (with initial angle $\alpha_{0,1} = 35^\circ$) of two identical double-helices (with a $[45_2/0/45_2]$ lay-up) under combined loading ($P_h = P_v$) at the apex. Points 1 and 2 are stable equilibrium points; points J, K and M are unstable equilibrium positions. Dashed lines (left) represents areas of instability. The load has been normalized with respect to the load value at the maximum peak (P_{crit}). The displacement, v_p , of the apex in the direction of the applied load has been normalized with respect to the initial length L_0 . Black lines (right) indicate the initial truss configuration. ... 58

Figure 5.5: Load-displacement curves (left) and deformation (right) of the assembled structure of double-helices of different length under the application of a) a vertical load and b) a horizontal load at the apex. Points 1–4 are stable equilibrium points; points A–E are unstable equilibrium points. The truss has initial angle $\alpha_{0,1} = 35^\circ$ and double-helices of $[45_2/0/45_2]$ lay-up, and lengths $L_1 = 95$ mm, $L_2 = 71$ mm. Dashed lines (left) represent areas of instability. The load has been normalized with respect to the load value at the maximum peak (P_{crit}) for each case. The displacement has been normalized with respect to the initial height or width of the truss structure, respectively for vertical or horizontal loading. Black lines (right) indicate the initial truss configuration. 59

Figure 5.6: a) Load-displacement curve of a mechanism consisting of double-helices compared to one of linear springs under a vertical load at the apex. Initial truss angle $\alpha_{0,1} = 70^\circ$ is used for both assemblies. Points 1–4 are stable equilibrium points; points A–F, J, K and M are unstable equilibrium points. Dashed lines represent areas of instability. b) Deformation of the assembled structures. The initial truss configurations are indicated with black lines. c) Axial force with respect to displacement of a linear spring (left) and of a double-helix (right). 61

Figure 5.7: a) Load-displacement curves of a mechanism with different initial truss angles $\alpha_{0,1}$ consisting of double-helices of $[45_2/0/45_2]$ lay-up, under the application of a vertical load at the apex. Points 1–4 are stable equilibrium points. Points A–F, J, K and M are unstable equilibrium points. Dashed lines represent areas of instability. b) Axial forces of double-helices at selected equilibrium points for the different initial truss angles.62

Figure 5.8: Strain energy landscape for a compliant mechanism of identical double-helices with a $[45_2/0/45_2]$ composite strip lay-up, $L = 95$ mm, $R = 15$ mm, $R_i = 30$ mm, $W = 5$ mm, assembled in a truss-like configuration with initial base angle $\alpha_{0,1} = 45^\circ$. Points 1–4 denote stable equilibrium positions, while points C–F and M indicate positions of unstable equilibrium. The positions of the truss apex under an applied vertical load ($P_h = 0$) are superimposed as red points. The initial truss configuration is indicated with black lines.62

Figure 5.9: Load-displacement curves of the assembled structure into a steep truss with initial angle $\alpha_{0,1} = 70^\circ$ of identical double-helices for different symmetric lay-ups of the form of $[\beta_2/0/\beta_2]$ for a) $\beta = 0^\circ, 45^\circ, 90^\circ$ and b) $\beta = 30^\circ, 45^\circ, 60^\circ$ under the application of a vertical load at the apex. Points 1, 2 and 5 are stable equilibrium points on the main paths; points 3 and 4 on the bifurcation paths. Points A, M, B, G and H are unstable equilibrium points on the main paths; points C–F, J and K on the bifurcation paths. Dashed lines represent areas of instability. ...63

Figure 5.10: Load-displacement curves of the assembled structure into a steep truss with initial angle $\alpha_{0,1} = 70^\circ$ of identical double-helices under the application of a vertical load at the apex, with different a) widths W , lay-up $[45_2/0/45_2]$, $L = 95$ mm, $R = 15$ mm, $R_i = 30$ mm; b) radius R , lay-up $[45_2/0/45_2]$, $L = 95$ mm, $R_i = 30$ mm, $W = 5$ mm; c) initial curvatures of the strips R_i , lay-up $[45_2/0/45_2]$, $L = 95$ mm, $R = 15$ mm, $W = 5$ mm; d) dimensions L , R and R_i , keeping a constant ratio $R_i/R = 2$ and $L \approx 2\pi R$, lay-up $[45_2/0/45_2]$, $W = 5$ mm. Points 1 and 2 are stable equilibrium points on the main path; points 3 and 4 on the bifurcation path. Points A, M and B are unstable equilibrium points on the main path; points C–F on the bifurcation path. Dashed lines represent areas of instability.64

Figure 5.11: a) Load-displacement curve of a mechanism consisting of double-helices compared to one of linear springs under a horizontal load at the apex. Initial truss angle $\alpha_{0,1} = 70^\circ$ is used for both assemblies. Dashed lines represent areas of instability. b) Deformation of the assembled structures of linear springs (left) and of double-helices (right). The initial truss configurations are indicated with black lines. Points 1 and 2 are stable equilibrium positions; points J, K and M are unstable equilibrium positions.65

Figure 5.12: Load-displacement curves of a mechanism of different initial truss angles $\alpha_{0,1}$ consisting of double-helices of $[0_5]$ lay-up, under the application of a horizontal load at the apex. Points 1 and 2 are stable equilibrium points; points J, K and M are unstable equilibrium points. Dashed lines represent areas of instability.67

Figure 5.13: Load-displacement curves of the assembled structure into a steep truss with initial angle $\alpha_{0,1} = 70^\circ$ of identical double-helices for different symmetric lay-ups of the form of $[\beta_2/0/\beta_2]$ for a) $\beta = 0^\circ, 45^\circ, 90^\circ$ and b) $\beta = 30^\circ, 45^\circ, 60^\circ$ under the application of a horizontal load at the apex. Points 1–5 are stable equilibrium points; points A, C, F–H, J, K and M are unstable equilibrium positions. Dashed lines represent areas of instability.67

Figure 5.14: Load-displacement curves of the assembled structure into a steep truss with initial angle $\alpha_{0,1} = 70^\circ$ of identical double-helices under the application of a horizontal load at the apex with different d) widths W , lay-up $[0_5]$, $L = 95$ mm, $R = 15$ mm, $R_i = 30$ mm; b) radius R , lay-up $[0_5]$, $L = 95$ mm, $R_i = 30$ mm, $W = 5$ mm; c) initial curvatures of the strips R_i , lay-up $[0_5]$, $L = 95$ mm, $R = 15$ mm, $W = 5$ mm; d) dimensions L , R and R_i , keeping a constant ratio $R_i/R = 2$ and $L \approx 2\pi R$, lay-up $[0_5]$, $W = 5$ mm. Points 1 and 2 are stable equilibrium points; points J, K and M are unstable equilibrium points. Dashed lines represent areas of instability.68

Figure 6.1: Straight (light grey) and twisted (dark) configurations of the double-helix composite structure with (a) $\theta \in [0^\circ, 90^\circ]$ and (b) $\theta \in [0^\circ, -90^\circ]$73

Figure 6.2: Strain energy landscapes for a compliant mechanism of double-helices of a $[45_2/0/45_2]$ composite strip lay-up, $L = 95$ mm, $R = 15$ mm, $R_i = 30$ mm, $W = 5$ mm assembled in a truss-like configuration with an initial angle $\alpha_{0,1} = 70^\circ$ for different reconfiguration modes. a) Mode I: $\theta_i \in [0^\circ, 90^\circ]$; b) Mode II: $\theta_i \in [0^\circ, -90^\circ]$; c) Mode III: $\theta_i \in [0^\circ, 90^\circ]$, $\theta_2 \in [0^\circ, -90^\circ]$. Points labelled 1–4 denote stable equilibria, while points A–H identify positions of unstable equilibrium. Points I–IV denote stable boundary equilibria. Black lines represent the double-helices at the initial truss configuration. 74

Figure 6.3: End effector positions upon application of a load P on the apex superimposed on the corresponding strain energy landscapes for different reconfiguration modes of the truss with an initial angle $\alpha_{0,1} = 70^\circ$ consisting of double helices of $[45_2/0/45_2]$ layup, $L = 95$ mm, $R = 15$ mm, $R_i = 30$ mm, $W = 5$ mm. a) Mode I; b) Mode II; c) Mode III. Red points indicate the equilibrium paths of the apex under the application of a vertical load ($P_h = 0$). Blue points indicate the equilibrium paths of the apex under the application of a horizontal load ($P_v = 0$). Green points indicate the equilibrium paths of the apex under the application of a combined load ($P_h = P_v$). Points 1–4 are stable equilibrium points. Points A–H are unstable equilibrium points. Points I–IV denote stable boundary equilibria. 75

Figure 6.4: Load-displacement curves of the truss with an initial angle $\alpha_{0,1} = 70^\circ$ consisting of double helices of $[45_2/0/45_2]$ layup, $L = 95$ mm, $R = 15$ mm, $R_i = 30$ mm, $W = 5$ mm under the application of a vertical load at the apex ($P_h = 0$) for different reconfiguration modes: a) Mode I; b) Mode II; c) Mode III. Points 1–4 are stable equilibrium points. Points A–H are unstable equilibrium points. Dashed line represents the areas of instability. The load is normalized with respect to the load value at the maximum peak (P_{crit}) in each case. 76

Figure 6.5: Load-displacement curves of the truss with an initial angle $\alpha_{0,1} = 70^\circ$ consisting of double helices of $[45_2/0/45_2]$ layup, $L = 95$ mm, $R = 15$ mm, $R_i = 30$ mm, $W = 5$ mm under the application of a horizontal load at the apex ($P_v = 0$) for different reconfiguration modes: a) Mode I; b) Mode II; c) Mode III. Points 1–4 are stable equilibrium points. Points A–H are unstable equilibrium points. Dashed line represents the areas of instability. The load is normalized with respect to the load value at the maximum peak (P_{crit}) in each case. 77

Figure 6.6: Load-displacement curves of the truss with an initial angle $\alpha_{0,1} = 70^\circ$ consisting of double helices of $[45_2/0/45_2]$ layup, $L = 95$ mm, $R = 15$ mm, $R_i = 30$ mm, $W = 5$ mm under the application of a combined load at the apex ($P_h = P_v$) for different reconfiguration modes: a) Mode I; b) Mode II; c) Mode III. Points 1–4 are stable equilibrium points. Points A–H are unstable equilibrium points. Dashed line represents the areas of instability. The load is normalized with respect to the load value at the maximum peak (P_{crit}) in each case. 79

Figure 6.7: Strain energy landscapes for a compliant mechanism of double-helices of $L = 95$ mm, $R = 15$ mm, $R_i = 30$ mm, $W = 5$ mm assembled in a truss-like configuration with an initial angle $\alpha_{0,1} = 70^\circ$ for composite strips of $[\beta_2/0/\beta_2]$ lay-up for the reconfiguration Mode I. a) $[30_2/0/30_2]$; b) $[60_2/0/60_2]$. Points labelled 1–4 denote stable equilibria, while points A–G identify positions of unstable equilibrium. Black lines represent the double-helices at the initial truss configuration. 80

Figure 6.8: End effector positions upon application of a load P on the apex superimposed on the corresponding strain energy landscapes for reconfiguration Mode I of the truss with an initial angle $\alpha_{0,1} = 70^\circ$ consisting of double helices of $L = 95$ mm, $R = 15$ mm, $R_i = 30$ mm, $W = 5$ mm and lay-ups: a) $[30_2/0/30_2]$; b) $[60_2/0/60_2]$. Red points indicate the equilibrium paths of the apex under the application of a vertical load ($P_h = 0$). Blue points indicate the equilibrium paths of the apex under the application of a horizontal load ($P_v = 0$). Green points indicate the equilibrium paths of the apex under the application of a combined load ($P_h = P_v$). Points 1–4 are stable equilibrium points. Points A–G are unstable equilibrium points. 80

Figure 6.9: Load-displacement curves of the truss with an initial angle $\alpha_{0,1} = 70^\circ$ for different lay-ups, $[30_2/0/30_2]$ and $[60_2/0/60_2]$, for the reconfiguration Mode I under the application of a-b) a vertical ($P_h = 0$), c-d) a horizontal ($P_v = 0$) and e-f) a combined ($P_h = P_v$) load at the apex. Points 1–4 are stable equilibrium points. Points A–G are unstable equilibrium points. Dashed line represents the areas of instability. The load is normalized with respect to the load value at the maximum peak (P_{crit}) in each case. 81

Figure 6.10: Strain energy landscapes for a compliant mechanism of double-helices of $L = 95$ mm, $R = 15$ mm, $R_i = 30$ mm, $W = 5$ mm assembled in a truss-like configuration with an initial angle $\alpha_{0,1} = 70^\circ$ for composite strips of $[\beta_2/0/\beta_2]$ lay-up for the reconfiguration Mode II. a) $[30_2/0/30_2]$; b) $[60_2/0/60_2]$. Points labelled 1 and 2 denote stable equilibria, while points A–H and K identify positions of unstable equilibrium. Points I–IV denote stable boundary equilibria. Black lines represent the double-helices at the initial truss configuration.83

Figure 6.11: End effector positions upon application of a load P on the apex superimposed on the corresponding strain energy landscapes for reconfiguration Mode II of the truss with an initial angle $\alpha_{0,1} = 70^\circ$ consisting of double helices of $L = 95$ mm, $R = 15$ mm, $R_i = 30$ mm, $W = 5$ mm and lay-ups: a) $[30_2/0/30_2]$; b) $[60_2/0/60_2]$. Red points indicate the equilibrium paths of the apex under the application of a vertical load ($P_h = 0$). Blue points indicate the equilibrium paths of the apex under the application of a horizontal load ($P_v = 0$). Green points indicate the equilibrium paths of the apex under the application of a combined load ($P_h = P_v$). Points 1 and 2 are stable equilibrium points. Point A–H and K are unstable equilibrium points. Points I–IV denote stable boundary equilibria.83

Figure 6.12: Load-displacement curves of the truss with an initial angle $\alpha_{0,1} = 70^\circ$ for different lay-ups, $[30_2/0/30_2]$ and $[60_2/0/60_2]$, for the reconfiguration Mode II under the application of a-b) a vertical ($P_h = 0$), c-d) a horizontal ($P_v = 0$) and e-f) a combined ($P_h = P_v$) load at the apex. Points 1 and 2 are stable equilibrium points. Points A–H and K are unstable equilibrium points. Dashed line represents the areas of instability. The load is normalized with respect to the load value at the maximum peak (P_{crit}) in each case.84

Figure 6.13: Strain energy landscapes for a compliant mechanism of double-helices of $L = 95$ mm, $R = 15$ mm, $R_i = 30$ mm, $W = 5$ mm assembled in a truss-like configuration with an initial angle $\alpha_{0,1} = 70^\circ$ for composite strips of $[\beta_2/0/\beta_2]$ lay-up for reconfiguration Mode III. a) $[30_2/0/30_2]$; b) $[60_2/0/60_2]$. Points labelled 1–3 denote stable equilibria, while points A–H and K identify positions of unstable equilibrium. Points I–III denote stable boundary equilibria. Black lines represent the double-helices at the initial truss configuration.86

Figure 6.14: End effector positions upon application of a load P on the apex superimposed on the corresponding strain energy landscapes for reconfiguration Mode III of the truss with an initial angle $\alpha_{0,1} = 70^\circ$ consisting of double helices of $L = 95$ mm, $R = 15$ mm, $R_i = 30$ mm, $W = 5$ mm and lay-ups: a) $[30_2/0/30_2]$; b) $[60_2/0/60_2]$. Red points indicate the equilibrium paths of the apex under the application of a vertical load ($P_h = 0$). Blue points indicate the equilibrium paths of the apex under the application of a horizontal load ($P_v = 0$). Green points indicate the equilibrium paths of the apex under the application of a combined load ($P_h = P_v$). Points 1–3 are stable equilibrium points. Points A–H and K are unstable equilibrium points. Points I–IV denote stable boundary equilibria.86

Figure 6.15: Load-displacement curves of the truss with an initial angle $\alpha_{0,1} = 70^\circ$ for different lay-ups, $[30_2/0/30_2]$ and $[60_2/0/60_2]$, for the reconfiguration Mode III under the application of a-b) a vertical ($P_h = 0$), c-d) a horizontal ($P_v = 0$) and e-f) a combined ($P_h = P_v$) load at the apex. Points 1–3 are stable equilibrium points. Points A–H and K are unstable equilibrium points. Dashed line represents the areas of instability. The load is normalized with respect to the load value at the maximum peak (P_{crit}) in each case.87

Figure 6.16: Strain energy landscapes for a compliant mechanism of double-helices of a $[45_2/0/45_2]$ composite strip lay-up, $L = 95$ mm, $R = 15$ mm, $R_i = 30$ mm, $W = 5$ mm assembled in a truss-like configuration with an initial angle $\alpha_{0,1} = 35^\circ$ for different reconfiguration modes. a) Mode I: $\theta_i \in [0^\circ, 90^\circ]$; b) Mode II: $\theta_i \in [0^\circ, -90^\circ]$; c) Mode III: $\theta_1 \in [0^\circ, 90^\circ]$, $\theta_2 \in [0^\circ, -90^\circ]$. Points labelled 1 and 2 denote stable equilibria, while points A–C identify positions of unstable equilibrium. Points I–III denote stable boundary equilibria. Black lines represent the double-helices at the initial truss configuration.89

- Figure 6.17:** End effector positions upon application of a load P on the apex superimposed on the corresponding strain energy landscapes for different reconfiguration modes of the truss with an initial angle $\alpha_{0,1} = 35^\circ$ consisting of double helices of $[45_2/0/45_2]$ layup, $L = 95$ mm, $R = 15$ mm, $R_i = 30$ mm, $W = 5$ mm. a) Mode I; b) Mode II; c) Mode III. Red points indicate the equilibrium paths of the apex under the application of a vertical load ($P_h = 0$). Blue points indicate the equilibrium paths of the apex under the application of a horizontal load ($P_v = 0$). Green points indicate the equilibrium paths of the apex under the application of a combined load ($P_h = P_v$). Points 1 and 2 denote stable equilibria, while points A–C identify positions of unstable equilibrium. Points I–III denote stable boundary equilibria. 90
- Figure 6.18:** Load-displacement curves of the truss with an initial angle $\alpha_{0,1} = 35^\circ$ consisting of double helices of $[45_2/0/45_2]$ layup, $L = 95$ mm, $R = 15$ mm, $R_i = 30$ mm, $W = 5$ mm under the application of a vertical load at the apex ($P_h = 0$) for different reconfiguration modes: a) Mode I; b) Mode II; c) Mode III. Points 1 and 2 are stable equilibrium points. Points A–C are unstable equilibrium points. Dashed line represents the areas of instability. The load is normalized with respect to the load value at the maximum peak (P_{crit}) in each case. 91
- Figure 6.19:** Load-displacement curves of the truss with an initial angle $\alpha_{0,1} = 35^\circ$ consisting of double helices of $[45_2/0/45_2]$ layup, $L = 95$ mm, $R = 15$ mm, $R_i = 30$ mm, $W = 5$ mm under the application of a horizontal load at the apex ($P_v = 0$) for different reconfiguration modes: a) Mode I; b) Mode II; c) Mode III. Points 1 and 2 are stable equilibrium points. Points A–C are unstable equilibrium points. Dashed line represents the areas of instability. The load is normalized with respect to the load value at the maximum peak (P_{crit}) in each case. 92
- Figure 6.20:** Load-displacement curves of the truss with an initial angle $\alpha_{0,1} = 35^\circ$ consisting of double helices of $[45_2/0/45_2]$ layup, $L = 95$ mm, $R = 15$ mm, $R_i = 30$ mm, $W = 5$ mm under the application of a combined load at the apex ($P_h = P_v$) for different reconfiguration modes: a) Mode I; b) Mode II; c) Mode III. Points 1 and 2 are stable equilibrium points. Points A–C are unstable equilibrium points. Dashed line represents the areas of instability. The load is normalized with respect to the load value at the maximum peak (P_{crit}) in each case. 93
- Figure 7.1:** CAD design of the fixture for the assembly of the double-helices in a truss-like configuration. The two helices of the mechanism connect to a single rod along the apex of the truss. The apex is attached to a test machine to measure force and displacement, and is allowed to move vertically in a U-shaped frame (green profiles). The supports of the helices are attached to a base frame (blue profiles) that can move horizontally with respect to the fixed lower base frame (red profiles). This configuration effectively enables the lateral movement of the apex under a purely vertical applied load. 98
- Figure 7.2:** Test rig for the experimental testing of the mechanism of double-helices. 98
- Figure 7.3:** Double-helix configuration a) with a pin between the two end spokes to ensure deformation of the helix along the longitudinal X -axis of the helix; b) without a pin resulting in out of plane deformation. 101
- Figure 7.4:** Schematic specifying the lengths for the constituent parts of the truss member in the mechanism. 102
- Figure 7.5:** Schematic representation of the new geometry of the assembly of double-helices in a truss-like configuration. The initial configuration is determined by the equilibrium length $L_{0,i}$ of the double-helices, the lengths for the end fittings at the base support and apex, $l_{end_b,i}$ and $l_{end_a,i}$ respectively, and by the initial angle $\alpha_{0,i}$ of the truss configuration. 102

Figure 7.6: Strain energy landscapes for a compliant mechanism of double-helices of a $[45_2/0/45_2]$ composite strip lay-up, $L = 95$ mm, $R = 15$ mm, $R_i = 30$ mm, $W = 5$ mm assembled in a truss-like configuration with an initial angle $\alpha_{0,1} = 70^\circ$, $l_{end,a,i} = 25$ mm and $l_{end,b,i} = 0$ mm for different reconfiguration modes. a) Mode I: $\theta_i \in [0^\circ, 90^\circ]$; b) Mode II: $\theta_i \in [0^\circ, -90^\circ]$; c) Mode III: $\theta_1 \in [0^\circ, 90^\circ]$, $\theta_2 \in [0^\circ, -90^\circ]$. Points labelled 1–5 denote stable equilibria, while points A–H identify positions of unstable equilibrium. Points I–IV denote stable boundary equilibria. Black lines represent the double-helices at the initial truss configuration. Red points indicate the equilibrium paths of the apex under the application of a vertical load ($P_h = 0$). Shaded ring areas represent the limitation from the stowed length of the helix. 104

Figure 7.7: Axial forces of double-helices of a $[45_2/0/45_2]$ composite strip lay-up, $L = 95$ mm, $R = 15$ mm, $R_i = 30$ mm, $W = 5$ mm at selected equilibrium points of the mechanism for the reconfiguration Mode I. 105

Figure 7.8: Strain energy landscapes for a compliant mechanism of double-helices of a $[45_2/0/45_2]$ composite strip lay-up, $L = 300$ mm, $R = 30$ mm, $R_i = 60$ mm, $W = 10$ mm assembled in a truss-like configuration with an initial angle $\alpha_{0,1} = 70^\circ$, $l_{end,a,i} = 25$ mm and $l_{end,b,i} = 0$ mm for different reconfiguration modes. a) Mode I: $\theta_i \in [0^\circ, 90^\circ]$; b) Mode II: $\theta_i \in [0^\circ, -90^\circ]$; c) Mode III: $\theta_1 \in [0^\circ, 90^\circ]$, $\theta_2 \in [0^\circ, -90^\circ]$. Points labelled 1–5 denote stable equilibria, while points A–G identify positions of unstable equilibrium. Points I–IV denote stable boundary equilibria. Black lines represent the double-helices at the initial truss configuration. Red points indicate the equilibrium paths of the apex under the application of a vertical load ($P_h = 0$). Shaded ring areas represent the limitation from the stowed length of the helix. 107

Figure 7.9: Strain energy landscapes for a compliant mechanism of double-helices of a $[90/45/0/45/90]$ composite strip lay-up, $L = 300$ mm, $R = 30$ mm, $R_i = 60$ mm, $W = 10$ mm assembled in a truss-like configuration with an initial angle $\alpha_{0,1} = 70^\circ$, $l_{end,a,i} = 25$ mm and $l_{end,b,i} = 0$ mm for different reconfiguration modes. a) Mode I: $\theta_i \in [0^\circ, 90^\circ]$; b) Mode II: $\theta_i \in [0^\circ, -90^\circ]$; c) Mode III: $\theta_1 \in [0^\circ, 90^\circ]$, $\theta_2 \in [0^\circ, -90^\circ]$. Points labelled 1–5 denote stable equilibria, while points A–H identify positions of unstable equilibrium. Points I–IV denote stable boundary equilibria. Black lines represent the double-helices at the initial truss configuration. Red points indicate the equilibrium paths of the apex under the application of a vertical load ($P_h = 0$). Shaded ring areas represent the limitation from the stowed length of the helix. 108

Figure 7.10: Manufacture stages of the helix strips: a) lay-up of the strips flat, including local reinforcement at the interface with the spokes; b) place of the strips on an aluminium cylindrical tool; c) vacuum bag of the laminate. 109

Figure 7.11: Experimental set-up at different configurations: a) slightly twisted, b) twisted and c) coiled. 110

Figure 7.12: Load-displacement curves of double-helices for helix deformations with $\theta \in [0^\circ, 90^\circ]$ under a) a compression test and b) a tensile test. Results are for double-helices of a $[90/45/0/45/90]$ lay-up, with dimensions $L = 292$ mm, $R = 30$ mm, $R_i = 60$ mm, $W = 10$ mm. The displacement Δl is normalized to the length L of the strips, with $\Delta l/L = 0$ representing the fully-extended and $\Delta l/L = 1$ its fully coiled configuration. 111

Figure 7.13: Load-displacement curves of double-helices for helix deformations with $\theta \in [0^\circ, -90^\circ]$ under a) a compression test and b) a tensile test. Results are for double-helices of a $[90/45/0/45/90]$ lay-up, with dimensions $L = 292$ mm, $R = 30$ mm, $R_i = 60$ mm, $W = 10$ mm. The displacement Δl is normalized to the length L of the strips, with $\Delta l/L = 0$ representing the fully-extended and $\Delta l/L = 1$ its fully coiled configuration. 112

Figure 7.14: Misalignment of the spokes with respect to the centre-line of the strip. Dashed line represents the axis that passes through the middle of the width of the strip along its length. 112

Figure 7.15: a) Shear buckling of the helix; b) nonuniform deformation of the helix; c) contact between adjacent spokes. 113

- Figure 7.16:** Experimental set-up of the truss assembly of double helices in different configurations during testing: a) configuration with both helices fully-extended; b-c) configurations along the main equilibrium path between points 1 and B for Mode I with both helices twisted equally; d-e) configurations along the main equilibrium path between points 1 and A for Mode II with both helices twisted equally. 115
- Figure 7.17:** Load-displacement curves under the application of a vertical load at the apex of the truss of double-helices for reconfiguration Mode I, $\theta \in [0^\circ, 90^\circ]$, for a) a compression test and b) a tensile test. Dashed lines represent areas of instability for the analytical data. Results are for initial truss angle $\alpha_{0,1} = 70^\circ$ and double-helices of a [90/45/0/45/90] lay-up, with dimensions $L = 292$ mm, $R = 30$ mm, $R_i = 60$ mm, $W = 10$ mm. Points 1–4 are stable equilibrium points. Points A–G are unstable equilibrium points. The displacement has been normalized with respect to the initial height of the truss structure. 116
- Figure 7.18:** a-b) Localised buckling of the helix strips; c-d) nonuniform deformation of the helix along its length; e-f) contact between adjacent spokes during coiling/uncoiling. 117
- Figure 7.19:** Load-displacement curves under the application of a vertical load at the apex of the truss of double-helices for reconfiguration Mode II, $\theta \in [0^\circ, -90^\circ]$, for a) a compression test and b) a tensile test. Dashed lines represent areas of instability for the analytical data. Results are for initial truss angle $\alpha_{0,1} = 70^\circ$ and double-helices of a [90/45/0/45/90] lay-up, with dimensions $L = 292$ mm, $R = 30$ mm, $R_i = 60$ mm, $W = 10$ mm. Point 1 denote a stable equilibrium. Points A–H are unstable equilibrium points. The displacement has been normalized with respect to the initial height of the truss structure. 118
- Figure 7.20:** a) Modified experimental set-up, comprising rollers, of the truss assembly of double-helices. b-e) Different configurations of a prototype during testing: b) a configuration along the main equilibrium path between points 1 and A for Mode I with both helices twisted equally; c) a configuration close to point B for Mode I, with the helices collinear and twisted equally; d) a configuration on the bifurcation path between points 1 and D for Mode I, with the helices twisted to different extent; e) a configuration close to point 3 for Mode I, with the helices collinear but one in a slightly twisted and the other in a coiled configuration. 119
- Figure 7.21:** Load-displacement curves (left) under the application of a vertical load at the apex of the truss of double-helices for reconfiguration Mode I. Dashed lines represent areas of instability for the analytical data. The truss has initial angle $\alpha_{0,1} = 70^\circ$ and double-helices of [90/45/0/45/90] lay-up, with dimensions $L = 292$ mm, $R = 30$ mm, $R_i = 60$ mm, $W = 10$ mm. The positions of the truss apex under an applied vertical load ($P_h = 0$) at the end effector are superimposed on the corresponding strain energy landscape (right); red markers are used for the analytical and green markers for the experimental data. Black lines represent the double-helices at the initial truss configuration. Points 1–4 are stable equilibrium points. Points A–G are unstable equilibrium points. Shaded ring areas represent the limitation from the stowed length of the helix. 120
- Figure 7.22:** Load-displacement curves (left) under the application of a vertical load at the apex of the truss of double-helices for reconfiguration Mode II. Dashed lines represent areas of instability for the analytical data. The truss has initial angle $\alpha_{0,1} = 70^\circ$ and double-helices of [90/45/0/45/90] lay-up, with dimensions $L = 292$ mm, $R = 30$ mm, $R_i = 60$ mm, $W = 10$ mm. The positions of the truss apex under an applied vertical load ($P_h = 0$) at the end effector are superimposed on the corresponding strain energy landscape (right); red markers are used for the analytical and green markers for the experimental data. Black lines represent the double-helices at the initial truss configuration. Point 1 denote a stable equilibrium. Points A–H are unstable equilibrium points. Points I–IV denote stable boundary equilibria. Shaded ring areas represent the limitation from the stowed length of the helix. 121

Figure 7.23: Load-displacement curves (left) under the application of a vertical load at the apex of the truss of double-helices for reconfiguration Mode III. Dashed lines represent areas of instability for the analytical data. The truss has initial angle $\alpha_{0,1} = 70^\circ$ and double-helices of [90/45/0/45/90] lay-up, with dimensions $L = 292$ mm, $R = 30$ mm, $R_i = 60$ mm, $W = 10$ mm. The positions of the truss apex under an applied vertical load ($P_h = 0$) at the end effector are superimposed on the corresponding strain energy landscape (right); red markers are used for the analytical and green markers for the experimental data. Black lines represent the double-helices at the initial truss configuration. Points 1 and 2 are stable equilibrium points. Points A–G are unstable equilibrium points. Points I–III denote stable boundary equilibria. Shaded ring areas represent the limitation from the stowed length of the helix..... 122

Figure 8.1: Schematic representation of potential different initial configurations for the truss-like mechanism of double-helices: a) two-element truss with one support (right) a roller; b) three-element truss with one support (right) a roller..... 133

Figure 8.2: Schematic representation of potential initial configuration for a mechanism assembled of double-helices in a pyramid configuration in the 3D space..... 133

Nomenclature

2D	Two-Dimensional
3D	Three-Dimensional
$[90/45/0]_s$	symmetric composite lay-up with an odd number of plies; the centre ply is noted with the underscore, the numbers indicate the fibre orientation in each ply
$[\beta_2/0/\beta_2]$	symmetric composite lay-up with a centre ply with fibre orientation at 0° , the subscript indicates the number of plies with fibre orientation at an angle β
$[\beta_2/0/-\beta_2]$	antisymmetric composite lay-up with a centre ply with fibre orientation at 0° , the subscript indicates the number of plies with fibre orientation at an angle β
A	in-plane stiffness matrix of the Classical Laminate Theory
B	bending-extension coupling stiffness matrix of the Classical Laminate Theory
CAD	Computer-Aided Design
CFRP	carbon fibre reinforced polymer
c_x	initial manufactured x -curvature of the composite strip
c_{xy}	initial manufactured xy -curvature of the composite strip
c_y	initial manufactured y -curvature of the composite strip
D	bending stiffness matrix of the Classical Laminate Theory
D*	reduced bending stiffness matrix
F	double-helix axial force
H	distance between the strips of the double-helix
H_0	initial truss height
I_0	number of actual iterations performed in the previous step
I_d	number of desired iterations
K_T	tangential stiffness matrix of the truss mechanism system
k	axial stiffness of the double-helix
L	double-helix length in the fully extended configuration
$L_{0,i}$	length of the longest self-equilibrated configuration of the helix
$l_{\text{bar},i}$	total length of a truss member
$l_{\text{end_a},i}$	length for the helix end fitting at the truss apex
$l_{\text{end_b},i}$	length for the helix end fitting at the base support of the truss
l_i	projected helix length along the longitudinal axis of the cylinder
l_{s0}	finite free length of a linear spring
M_y	moment across the width of the composite strip

N_x	axial force arising during deformation of the composite structure
n	number of composite strips in the helix
P	applied load at the truss apex
P_{crit}	load value at the maximum peak of the load-displacement curve
\mathbf{P}_{ext}	external load vector
$\bar{\mathbf{P}}_{\text{ext}}$	a constant external load vector
P_h	horizontal component of the applied load at the truss apex
\bar{P}_h	constant horizontal external load applied
\mathbf{P}_{int}	internal load vector
P_v	vertical component of the applied load at the truss apex
\bar{P}_v	constant vertical external load applied
q_1, q_2, q_3	coefficients used in the modified-Riks method
\mathbf{R}	the residual vector of the truss mechanism system
R	radius of an underlying cylinder in the double-helix geometry
R_h	horizontal component of the residual
R_i	radius of the cylindrical model for the manufacture of the helix composite strips
R_v	vertical component of the residual
SE	standard error of the best fit curve
tol	tolerance number used for the convergence check in the modified-Riks method
U	strain energy of the double-helix
U_{tot}	total strain energy of the truss mechanism
u_h	horizontal displacement of the truss apex
u_p	displacement of the apex at the direction of the applied load at the truss apex
u_v	vertical displacement of the truss apex
V_0	initial truss width
W	width of the composite strip of the helix
X -axis	global longitudinal axis of the helix
x -axis	local longitudinal axis of the composite strips
$\boldsymbol{\alpha}$	in-plane compliance matrix of the Classical Laminated Theory
$\alpha_{0,i}$	initial truss base angle
β	fibre orientation in a composite ply
ΔL_i	displacement of the truss members from the initial truss configuration

Δl	axial displacement of the double-helix
Δs	the arc-length of the path-following method
$\Delta \boldsymbol{\kappa}$	tensor of the change in curvature of the composite strip
$\Delta \mathbf{v}_n^{(r)}$	correction to the solution in the modified-Riks method
$\delta \lambda_n^{(r)}$	incremental load parameter at the r th iteration
$\delta \mathbf{v}_n^{(r)}$	incremental displacement solution
$\boldsymbol{\varepsilon}^0$	tensor of the mid-plane strains of the composite strip
θ	helix angle
κ_x	x -curvature of the deformed composite strip
κ_{xy}	xy -curvature of the deformed composite strip
κ_y	y -curvature of the deformed composite strip
λ	a scalar load parameter in the modified-Riks method
ζ_j	scaling factor used in the computation of the branching path
τ_j	imperfection factor
\mathbf{v}	nodal displacement vector of the truss system
$\boldsymbol{\varphi}$	eigenvector of a specific eigenvalue problem
ω_j	eigenvalues of the tangential stiffness matrix

Chapter 1

Introduction

1.1 Motivation

In the field of robotics, there is a growing interest in the development of wearable devices—exosuits or exoskeletons—that assist or enhance human mobility. Over the past few years, a variety of such devices has been designed [1]; however, there are still challenges to be overcome, especially regarding the actuation technologies used to provide the motion. Current actuation systems are unable to offer agility and dexterity similar to that of biological muscles; the use of conventional mechatronics still limits their performance. Current systems are primarily based on electric motors, hydraulics or pneumatics that combine components like motors, cylinders, pumps and valves, resulting in heavy, rigid and quite bulky actuators [2]. Functional wearable devices also involve human-robot interaction, an interaction in a dynamic and uncontrolled environment, and thus require an actuation system that provides compliance. An actuation system that can simultaneously provide force control authority and power efficiency, whilst exhibiting back drivability, modularity and being lightweight and portable, remains a challenge for the design of functional wearable devices [3–5].

Recent advances in the field of actuation for wearable robotics have focused on the design and implementation of actuators with variable stiffness or adaptable compliance [5–9]. This type of actuator has the ability to provide control of the interaction force as well as to store and release energy due to the presence of elastic elements [10–12], allowing safer human-robot interaction, shock absorption, and greater power efficiency compared to stiff actuators [13, 14]. This is of particular interest in applications

where direct human-robot interaction is involved and safety is a critical concern, including prosthetics, wearable robotic devices, and rehabilitation robots [6, 15].

Over the past few years a variety of innovative compliant actuators have been designed, including electric compliant actuators [13] and pneumatic actuators [16]. The most widely developed have been the series elastic actuators (SEAs) [17–21]. To provide compliance and the potential to store energy, SEAs consist of an elastic component connected in series with a stiff actuator. Essentially a spring, either a linear or a torsion spring, depending on the application [21, 22], is introduced between the electro-mechanical actuator and the load [23]. The compliance of these actuators is defined by the spring constant, thus setting limitations to the performance of the system depending on the selected spring stiffness [24]. On the other hand, designs of varying compliance are more complex [13], requiring more components, *e.g.* two motors to control the stiffness and the equilibrium position or an additional damper device to efficiently store and retrieve energy. Based on a different design approach, pneumatic actuators usually follow an antagonistic setup, *i.e.* a parallel elasticity setup, to achieve bidirectional actuation similar to that of biological muscles and create nonlinear elastic behaviour [16]. This approach can be advantageous. However, disadvantages such as slow dynamics, hysteresis and the need for pressurized air set limitations to their successful application [7, 13].

This research draws upon the work on a composite morphing structure of a double-helix architecture by Lachenal *et al.* [25, 26]. The helical structure exhibits multiple stable states and nonlinear stiffness characteristics that could be exploited in robotic applications where force control, position accuracy and power efficiency, in addition to compliance, are key requirements, *e.g.* assistive support devices, exoskeletons [12, 23]. Indeed, following Lachenal's work, Cappello *et al.* [12, 23, 27] employed the helix as the component of a transmission in the actuation system of a robotic exoskeleton device assisting human mobility.

The actuation system developed by Cappello *et al.* [27] is based on the concept of series elastic actuators and combines current mechatronic technology with composite structures. It attempts to overcome current limitations of SEAs, by introducing the double-helix as the transmission connected in series with an electrical motor at one end and a reconfiguration actuator (ReAct) at the other. The torque generated by the motor evokes a twist of the double-helix which is then transformed into an axial force and a translation. Bowden cables are used to transfer the motion to the joint following an antagonistic setup (Figure 1.1).

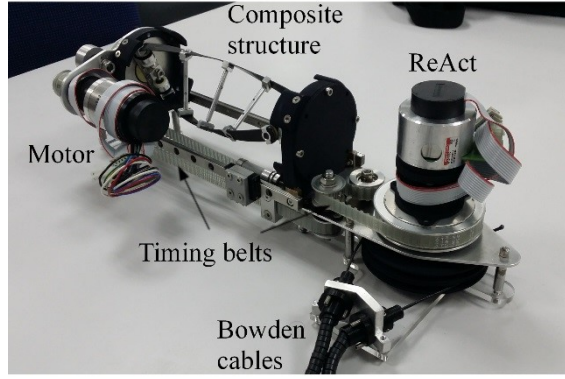


Figure 1.1: Actuation system developed by Cappello et al. [27].

The actuation system was aimed at an application to assist elbow motion while being carried as a backpack. Introducing a multistable composite structure in the compliant actuator instead of the conventional springs presents many advantages. The safety of the system is increased through fine force and position control; energy can be saved since power is only needed to move the structure from one stable configuration to another, not to hold it [28, 29]; and, finally, the low weight of the composites can reduce the weight of the system, which is important when it comes to wearable devices. Nevertheless, weaknesses in the developed actuation system urge a design optimization or a redesign [27]. These include: system complexity; control issues arising by the backlash introduced by a non-backdrivable mechanism incorporated to avoid back drivability of the ReAct; the relatively bulky design; and the low resulting passive stiffness at the joint. Additionally, the potential of the composite helical structure remains underexploited in the proposed configuration.

Thus, moving on from this concept and building upon the idea to exploit the nonlinear stiffness characteristics of the helical structure for the generation of movement in robotic applications, we directed towards the development of a variable stiffness compliant mechanism [30–32]. The concept is inspired by the biological mechanism of the muscles’ operation and the spring-like property of tendons [33–35], in conjunction with the approaches of exoskeletons and of soft robots that, respectively, combine springs in parallel with a muscle-tendon to assist its motion [8, 36–39] and use elastomeric materials to mimic the properties of muscles [40–42]. The helical structure is proposed as a nonlinear elastic element to develop a compliant mechanism which approaches a movement similar to that of human limbs.

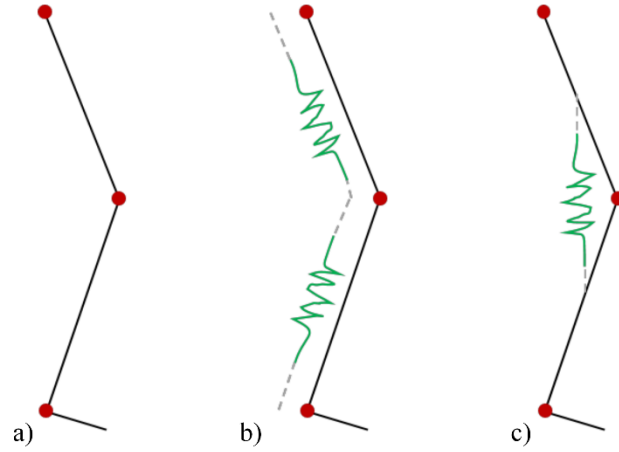


Figure 1.2: a) Simplified link-segment model for the lower human limb; b-c) potential configurations to simulate the gait motion.

A link-segment structure with pin joints (Figure 1.2a) is frequently used to model human limbs and various ways to simulate its motion exist [43–54]. Some simple configurations are shown in Figure 1.2b, c where the double-helices could be employed to provide the motion and compliance.

Nonetheless, it was considered paramount to first explore further the mechanics of the double-helix and of potential structural assemblies of double-helices, separately out of the scope of the human limb. Our knowledge of their implementation, interaction and performance for such applications is still limited. Therefore, this work focuses on a more fundamental work and the study of assemblies of double-helices in truss-like mechanisms. Their stability characteristics and potential mechanical properties are of primary interest in the general endeavour to master and expand the use of nonlinear elastic mechanisms in future applications, *e.g.* robotic applications, deployable structures *etc.*

1.2 Objectives

This work involves the development of a mechanism composed of morphing composite elements of a double-helix architecture. We exploit the morphing structures' variable geometry and nonlinear stiffness characteristics to expand the design space of current compliant mechanisms by extending their range of motion and stability characteristics.

Previous work by Lachenal *et al.* [25] has shown that the nonlinear mechanical characteristics of the helical composite morphing structure are highly tailorable. Our primary goal is to demonstrate the wide range of mechanical responses attainable with a mechanism that combines multiple double-helices. The design space of assemblies of nonlinear helical structures in a truss-like mechanism is explored and an attempt is

made to introduce the mechanism's potential to the wider research community. To achieve this goal, the thesis focuses on the analysis of a mechanism of two double-helices assembled in a simple truss-like configuration. The stability characteristics of the mechanism are investigated by employing an energy approach, and potential load paths between stable states are predicted implementing a path-following method. The effect of key design parameters on the mechanism's behaviour is explored. Parameters include: composite lay-up, geometrical features (sizing) and initial truss geometry. The purpose of this investigation is twofold: to reveal the high tailorability of the proposed mechanism's characteristics, and to unveil the variety of potential mechanical responses.

The reconfigurability of the proposed mechanism is studied alongside its multistability. The aim is to show the various available operation modes of the mechanism and the effect of these reconfiguration modes on the mechanism's stability characteristics and mechanical response. Moreover, the effect of the composite lay-up of the helix and the initial truss geometry on the reconfiguration modes is explored. The result is a multistable, reconfigurable compliant mechanism that can be customized by tuning the properties of its constituent members and/or its geometry.

A final objective of this study is to put into practice the proposed concept of a mechanism assembled of nonlinear morphing elements. A prototype of the mechanism is designed and manufactured to prove its feasibility, and experimentally assess the predictions of the analytical model. In conjunction with these, the purpose of the design and testing of a prototype is also to recognise any challenges to be addressed in future refined designs of this mechanism to make it suitable for future applications.

1.3 Outline of the thesis

This thesis introduces a novel compliant, reconfigurable mechanism consisting of nonlinear morphing elements assembled in truss-like configurations. Chapter 2 details a review of existing compliant and reconfigurable mechanisms, and provides an initiation of the reader to nonlinear structures, in particular to morphing structures. Chapter 3 focuses on the morphing structure of a double-helix architecture developed by Lachenal *et al.* [25], its analytical model and mechanical characteristics. These helical structures, capable of large axial deformations and with tailorable nonlinear stiffness characteristics, are further explored and combined in structural assemblies forming a truss-like mechanism. The synthesis of the structural assembly along with the methods employed for its analysis are presented in Chapter 4. The design space and the range of potential mechanical behaviour, stability characteristics and

reconfigurability, of the mechanism composed of these helical nonlinear morphing elements are explored in Chapter 5 and Chapter 6. A design, manufacture and testing of a prototype of such a truss-like mechanism is presented in Chapter 7. Finally, conclusions, final remarks and thoughts for future work are given in Chapter 8.

Chapter 2

Literature Review

2.1 Introduction

The subject of this research lies between two engineering fields; from one aspect, we exploit composite morphing structures and their nonlinearities, exploring further their unique mechanical behaviour and rich design space; on the other, we attempt to introduce these structures to the field of mechanisms and robotics for potential future applications. Thus, we review these fields individually and introduce the wide research background of this work. First, the nonlinear behaviour of structures is presented and the exploitation of such phenomena for a wide range of applications in the engineering field is discussed. Next, a brief review on compliant mechanisms is performed, concentrating on mechanisms with characteristics of interest, including multistable and large displacement mechanisms. Finally, a concise overview of reconfigurable mechanisms is provided before concluding the chapter with a summary.

2.2 Nonlinear Structures

Conventionally, nonlinear behaviours, *e.g.* large displacements or strains, elastoplastic characteristics and variation in stiffness during loading, encountered in structures [55] were considered mechanisms of failure. These were often associated with collapse of the structure or an undesired response, *e.g.* the buckling of a slender beam or a thin shell or a cylinder under a compressive load. Engineers would try to avoid such behaviours during the design process, often resulting in overly conservative designs. In recent years, however, there has been an increasing interest to exploit nonlinear structural phenomena and the induced elastic instabilities—*e.g.* multistability and snap-through—to achieve new functionalities and improve the

performance of engineering structures [56–59]. Advances in analysis techniques and models to predict these features reliably [60, 61] also contribute towards this goal.

Recent contributions in modern engineering designs that take into consideration structural nonlinearities for the development of well-behaved nonlinear structures reveal a variety of structural forms for diverse applications. These include structures that operate in the post-buckling regime [62, 63], where large motions and deformations are likely to occur; morphing structures that use multistability and snap-through behaviour to switch between different configurations [25, 29, 64–78]; and programmable materials that rely on elastic instabilities for their functionality [42, 79–87]. The field of applications of these structures is very broad. The sudden energy released when a structure buckles and the large deformation involved are advantageous features for adaptive and smart applications [58], applications that are energy related, such as actuators [42, 88, 89], MEMS [90], energy harvesters [91, 92], dampers [93, 94], or motion-related applications, such as morphing structures [64, 71, 95–97], deployable structures [81, 98–100].

Mechanical instabilities in polymeric materials are appealing for the development of smart structures. Patterned in periodic two- or three-dimensional porous structures and taking advantage of the underlying beam buckling, elastomers can be used to develop collapsible structures [42, 79, 80, 82–84, 87]. Shim *et al.* [83] have investigated diverse arrangements of holes in 2D elastomer plates and developed material structures with novel properties, *i.e.* metamaterials (Figure 2.1), with the potential to apply similar patterns onto curved surfaces or 3D structures [81, 82]. The “Buckliball” developed by Shim *et al.* [81] uses such arrays of voids on a spherical shell to enable folding and self-encapsulation (Figure 2.2a). More recently, Yang *et al.* [42] have used such elastomeric materials with a pattern of voids that resembles the pattern of mortar in a brick wall to achieve muscle-like motion in a pneumatic actuator (Figure 2.2b). Despite the high flexibility elastomeric materials offer and the reversibility and repeatability in their foldable behaviour, their load-carrying capability is still restricted, limiting their implementation primarily to soft structures applications.

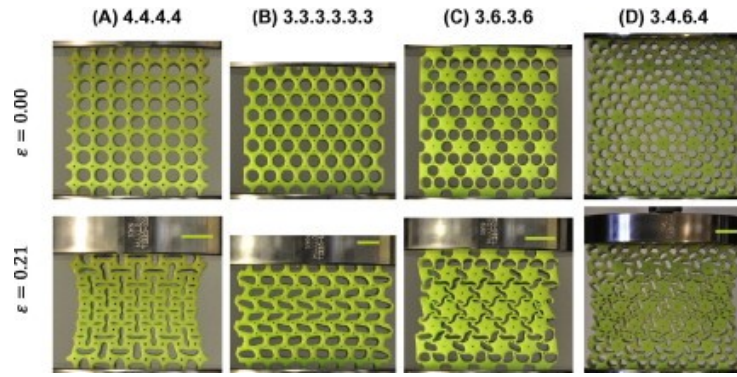


Figure 2.1: Experimental images of four periodic porous structures of elastomeric material with differently arranged holes (50% initial porosity) loaded under uniaxial compression in the undeformed (top) and deformed (bottom) configuration with applied compressive engineering strain $\varepsilon = 0.21$ (scale bars: 20 mm) [83, 101].

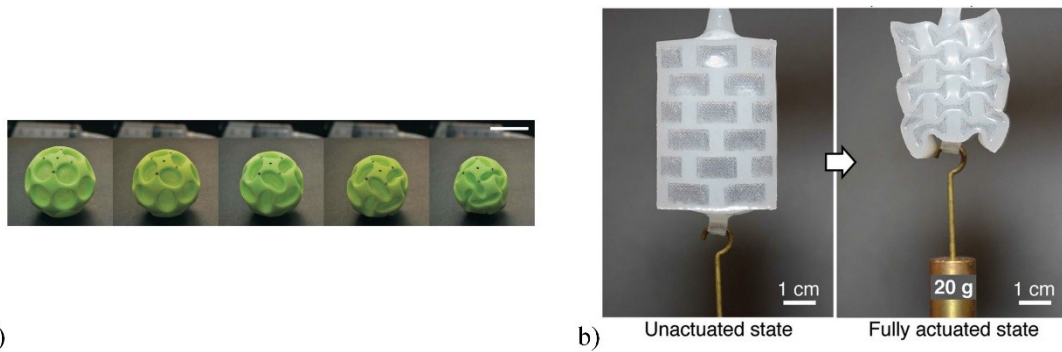


Figure 2.2: a) Sequence of progressively deformed shapes of “Buckliball”, made of silicone-based rubber, pressurised by a motorised syringe pump (scale bar: 3 cm) [81]. b) Image of a vacuum-actuated muscle-inspired pneumatic structure made of Ecoflex lifting a small weight when actuated by applying a vacuum [42].

In contrast, fibre-reinforced polymer composites are widely used in load-bearing applications, such as in aerospace, automotive and marine industry. The ability to control the stacking sequence, the fibre orientation and material properties in each ply facilitates stiffness variability and tailorability, and the resulting anisotropy enables the development of multiple stable states. These features are attractive to smart applications. Multistability and buckling phenomena in composite laminates have been extensively studied [65, 67, 68, 72, 102–110]. The composites’ multistable behaviour is attributed to an induced stress field that can be achieved by diverse phenomena, including nonsymmetric lamination and residual stresses occurring from the cure cycle [102, 103, 109], Gaussian curvature [67, 72, 105, 108], tailored lamination [106] or fibre pre-stress [107]. Building upon the bistable behaviour encountered in nonsymmetric laminates, Dai *et al.* [70] introduced a grid structure formed from four identical nonsymmetric composite laminate shells that exhibits tristability (Figure 2.3a). Later, they expanded this work and developed multistable composite lattice structures using multiple tristable lattices in different arrangements (Figure 2.3b) [29]. Lachenal *et al.* [25, 26] took advantage of the presence of initial curvature

in composite strips to introduce a pre-stress and developed a bistable twisting structure assembled of two pre-stressed composite strips joined by spokes (Figure 2.3c). Developing this concept further, Lachenel *et al.* [74] designed a bistable twisting I-beam capable of large deformations (Figure 2.3d), whereas Pirrera *et al.* [73] introduced a multistable helical lattice structure by combining initially curved composite strips on a cylindrical geometry (Figure 2.3e). The large displacements and nonlinear deformations that characterise these multistable structures, owing to the snap-through behaviour between stable states, while retaining their load-carrying capability make them suitable candidates for use in morphing structures to enhance their shape adaptability and functionality.

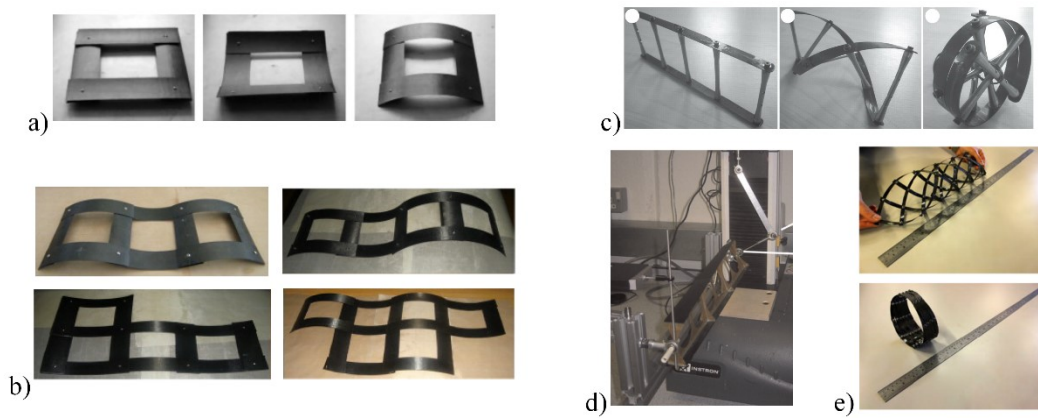


Figure 2.3: a) A tristable lattice structure assembled from four bistable nonsymmetric composite laminates in the plane (left), concave (middle) and convex (right) stable configurations [70]. b) Multistable lattice structures assembled from multiple tristable lattices in different arrangements [29]. c) A multistable composite twisting structure in a straight (left), twisted (middle) and coiled (right) configuration [25]. d) A bistable composite I-beam in a twisted configuration [74]. e) A multistable cylindrical lattice assembled from pre-stressed composite strips in an intermediate (top) and contracted (bottom) state [73].

Morphing structures are structures that change shape and undergo large deformations between the different states, thus requiring high compliance in the shape adaptation direction, while maintaining their structural integrity and load-carrying capability along the load direction [26, 64, 76]. Several studies in the past years have explored the ability to use morphing structures in aircraft or wind turbine designs to enhance their performance [64, 66, 68, 71, 77, 95, 97]. These morphing structures rely on multistable composite structures to develop the ability to adapt their shape and structural response to changes in the surrounding conditions. Diaconu *et al.* [64] presented three different concepts to induce morphing in an aerofoil section by introducing bistable composite structures in different parts within the aerofoil section, *e.g.* a flap-like structure with bistable shapes in the trailing edge or a bistable composite plate either parallel to the chord or along the main spar. Similar to these concepts, Arrieta *et al.* [97] used a multistable composite plate with variable stiffness [76], embedded diagonally along the rib in the aerofoil section, to achieve structural

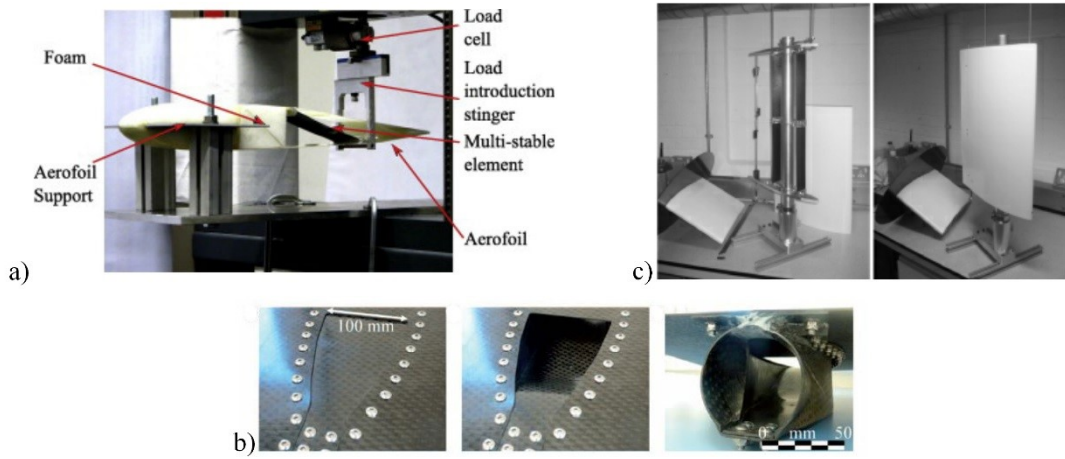


Figure 2.4: a) Compliant aerofoil structure with a variable stiffness multistable composite element embedded [97]. b) A morphing composite air inlet demonstrator in a closed state (left), open state (middle), and bottom view in an open state (right) [66]. c) Twist morphing blade in the straight configuration without the skin (left), revealing the composite pre-stressed strips, and with the skin (right) [95].

adaptability with passive means (Figure 2.4a). A bistable morphing composite structure has been developed by Daynes *et al.* [66] to serve as an air inlet in an aircraft, capable of operating opened or closed without any holding force (Figure 2.4b). Lachenal *et al.* [95] employed their previously developed bistable twisting composite structure with its customizable stiffness characteristics in a wind turbine blade to improve the aerodynamic performance of the blade (Figure 2.4c).

These implementations of nonlinear phenomena in the design of structures with advanced properties, like the composite morphing structures, can be regarded beneficial for the aerospace sector as well as other engineering applications, *e.g.* civil engineering applications, robotics *etc.* By integrating such structures and phenomena, new functional mechanisms can be developed for use in mechanical devices, deployable structures or actuation systems in robotics. The shape adaptability and geometrically nonlinear behaviour, combined with the variable stiffness of the composite morphing structures in particular, may also enable the ability to tune the desired behaviour in such mechanisms and/or structures.

2.3 Compliant Mechanisms

Compliant mechanisms are mechanisms that derive their mobility entirely or partially from elastically deformable components. Conversely to traditional rigid-body mechanisms that consist of rigid links and kinematic joints, compliant mechanisms transfer or transform motion, force, or energy using flexible or compliant members and their elastic deformations [111–114]. The flexibility of the mechanism can be increased either by changing the material composition or/and the geometry of its component or by

replacing the corresponding kinematic joint with flexure hinges [111, 112]. Technological advances with new materials becoming available and the development of the analysis techniques and tools have facilitated the design of compliant mechanisms [113–115]; the advantages offered by compliant mechanisms have significantly increased the scientific interest in this area and their consideration for a variety of applications [116, 117]. Compliant mechanisms can be beneficial in aerospace applications [116, 118], precision engineering [119–121], rehabilitation robotics [30, 122], MEMS devices [119, 123, 124], actuators [88], switches or valves [125] or for vibration isolation [126, 127].

By definition, compliant mechanisms rely, for their performance, on the elastic deflection of their members which results in large deformations and the ability of energy being stored in these elements and released at a later stage in addition to the development of nonlinear characteristics. Moreover, compliant mechanisms essentially have reduced number of kinematic joints, some are even monolithic, thus they are characterized by reduced friction, wear and backlash, which results in increased precision. In addition, the reduced number of parts may facilitate the assembly of the mechanism, reduce the weight and promote ease of scalability under certain conditions, *i.e.* material strains permitting, in a compliant mechanism. Taking advantage of these potentials, numerous studies on the development of compliant mechanisms exist in the literature.

Inspired by spring elements, notably nonlinear leaf springs, Lobontiu [112] studied flexible hinges designed to undergo large deformations by introducing thin elements that bend or buckle between two rigid parts to provide the necessary flexibility and mobility, *e.g.* Figure 2.5a. Recognising limitations and challenges in the earlier flexures designs, *i.e.* limited range of motion, poor off-axis stiffness and high stress concentrations, Trease *et al.* [128] developed new designs for large-displacement compliant joints using multiple thin flexible beams (Figure 2.5b). In more recent years, Verotti *et al.* [129] introduced a flexure hinge built from a flexible curved beam connecting a pair of conjugate surfaces (Figure 2.5c), and Hanke *et al.* [130] used flexible beam elements with distributed stiffness made from fibre reinforced composite material to substitute traditional kinematic joints to develop compliant mechanisms and facilitate their design by exploiting the predefined beam deflection of the composite elements. The grasper tool tip (Figure 2.5d) developed by Chandrasekaran and Thondiyath [120] for surgical operations is based on such compliant joints, *i.e.* a corner-filletted flexure hinge (Figure 2.5a) [112], of polymer resin flexible beams arranged perpendicularly in succession, while the silicon micro gripper introduced by Verotti *et*

al. [124] relies for its mobility on the flexure hinges with the conjugated surfaces and the flexible curved beam (Figure 2.5e) [129].

Considerable work has been done on the development of multistable compliant mechanisms; a desirable feature for many applications. Various approaches and concepts have been introduced for the design of multistable compliant mechanisms exploiting diverse principles; the majority relies on buckling beams and their snap-through behaviour [88, 118, 131–138], while Wilcox and Howell [123] and Chen *et al.* [139] used tensile flexural pivots to design fully compliant bi- and tristable mechanisms, suitable for performance under tension and bending loads. Ohsaki and Nishiwaki [131] introduced an approach to design pin-jointed multistable compliant mechanisms taking advantage of the local snap-through behaviour of the mechanism's individual elements. Han *et al.* [132] developed a planar quadristable compliant mechanism relying on the bistability of fully fixed curved beams; a monolithic compliant mechanism consisting of two nested frames, each incorporating a pair of curved beams, was manufactured and exhibited two stable states in each direction (Figure 2.6a). Oh and Cota [134, 135] presented a method to synthesize multistable mechanisms through a series combination of multiple bistable mechanisms of different load thresholds; by

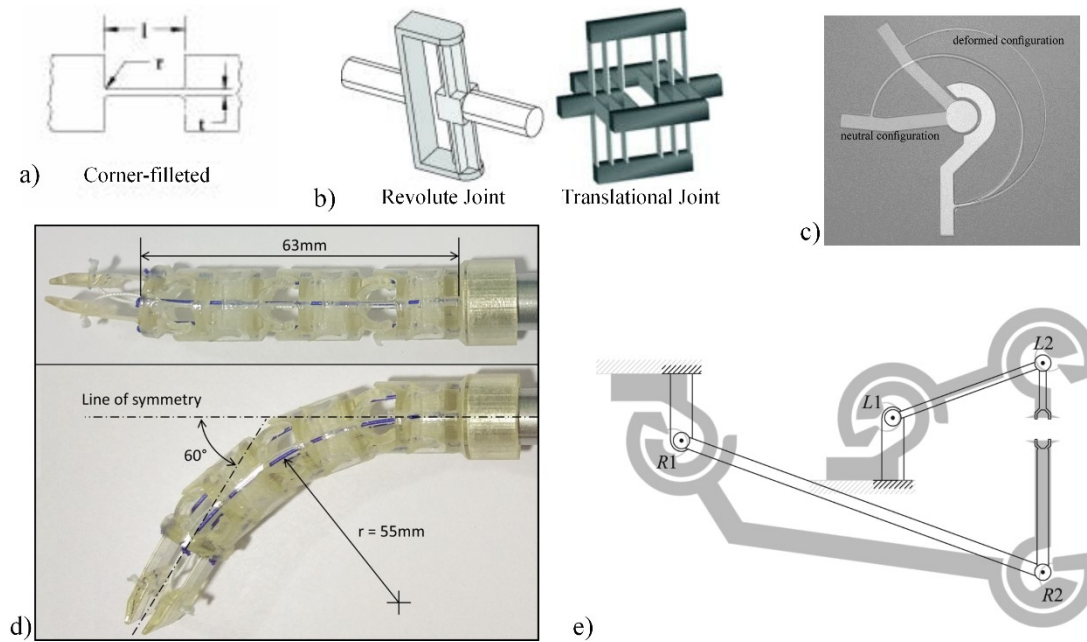


Figure 2.5: a) Schematic of a corner-filleted flexure hinge [112]. b) Conceptual design of a compliant revolute (left) and translational (right) joint based on flexible beams [128]. c) Prototype of conjugated surfaces flexure hinge made from PVC in its neutral and deformed configurations [129]. d) Compliant tool tip prototype in a neutral (top) and fully bent (bottom) state [120]. e) Design of a compliant micro gripper with conjugated surfaces flexure hinges and its pseudo-rigid body model superimposed [124].

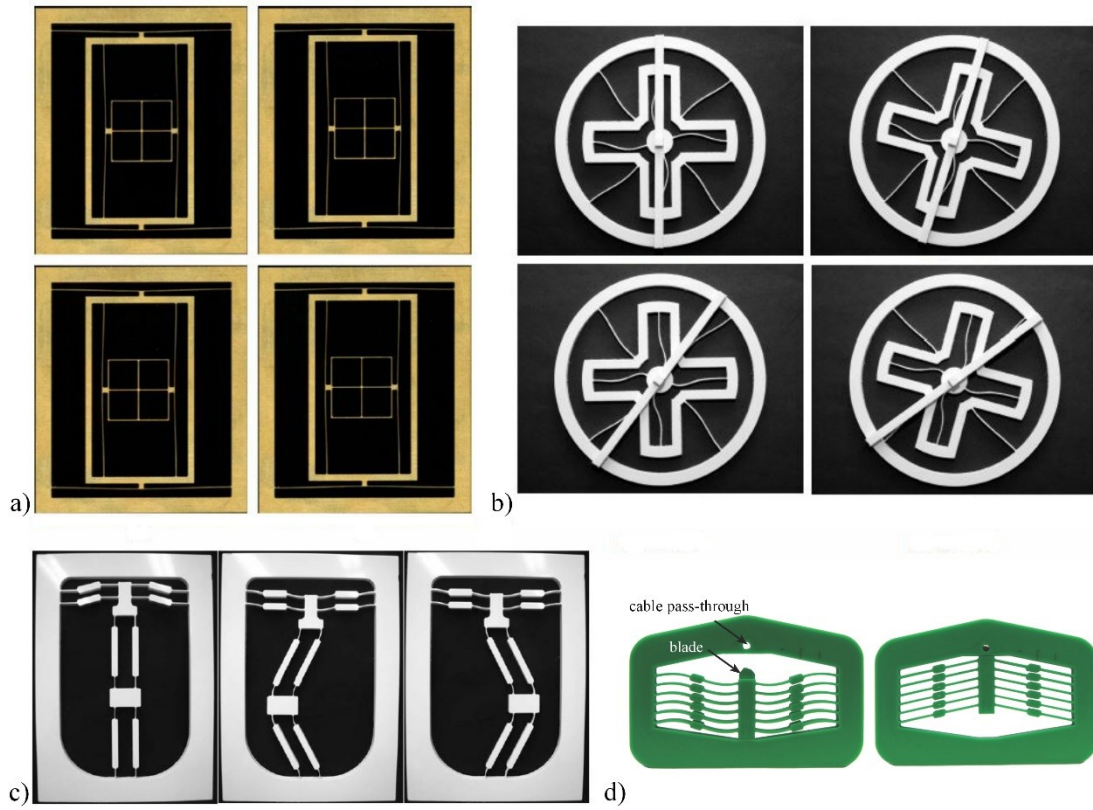


Figure 2.6: a) Prototype of a quadristable compliant mechanism in its four stable states [132]. b) Prototype of a rotational compliant mechanism from two serially connected bistable mechanisms in its four stable configurations [134]. c) Prototype of a tristable mechanism assembled from orthogonal compliant mechanisms in its three stable configurations [137]. d) Prototype of a compliant bistable release mechanism in its second stable (left) and its initial stable (right) configurations [118].

serially connecting two bistable mechanisms a mechanism with up to four stable configurations can be developed (Figure 2.6b). Following a similar concept, Gerson *et al.* [88] developed a multistable micro actuator capable of large displacements. A tristable compliant mechanism was introduced by Chen *et al.* [137] by combining two bistable mechanisms in a perpendicular configuration. The bistability of the individual mechanisms was achieved by a parallel combination of flexible beams with thicker midsections (Figure 2.6c). Zirbel *et al.* [118] used such variable thickness flexible beams to construct a compliant bistable mechanism as a non-explosive release mechanism (Figure 2.6d).

Another promising field of compliant mechanisms is the development of statically balanced compliant mechanisms [121, 140–151]. Statically balanced mechanisms, unlike multistable mechanisms that exhibit static equilibrium in limited distinct positions, are characterized by static equilibrium throughout their range of motion [140]. This translates into a constant potential energy system, a system that deforms under a constant force, thus possessing zero or nearly zero stiffness [152]. In contrast to multistable compliant mechanisms that take advantage of the elastic response of their constituent elements for functionality, for

this type of mechanisms stiffness is considered unfavourable and thus needs to be minimised or eliminated. Different approaches can be adopted to achieve a statically balanced mechanism, mainly orientated towards means to balance the positive stiffness that compliant mechanisms usually exhibit over their elastic deformation with a negative stiffness mechanism either by introducing pre-stressed elements or relying on bistability and buckling phenomena in beams. Hoetmer *et al.* [141] used a compressed plate spring with preloaded displacement as the negative stiffness element and developed three statically balanced mechanisms exhibiting nearly zero stiffness, two grippers and a multiplier (Figure 2.7a). A generic zero-stiffness compliant joint was designed by Morsch and Herder [142]. The joint is essentially a flexural pivot made of leaf springs arranged crosswise in two different parallel planes combined with two pairs of pre-stressed compliant leaf springs (Figure 2.7b). Berntsen *et al.* [147] developed a compliant four-bar linkage mechanism balanced internally using opposing pre-stressed leaf springs to compensate for the energy from the curved leaf springs constituting the joints of the four-bar mechanism during its deformation (Figure 2.7c). Elsewhere, Chen and Zhang [143] presented two concepts to achieve fully compliant statically balanced mechanisms from multistable mechanisms, relying on the performance of buckling beams instead of pre-stressed elements. Thus, they introduced a weight compensator developed from a constant force bistable mechanism, while by combining different multistable mechanisms the ability to develop a mechanism with zero stiffness over a prescribed range of motion was demonstrated. Similarly, Pham and Wang [144] developed a bistable mechanism for force regulation and overload protection consisting of multiple curved buckling beams exhibiting constant force over a specified displacement range (Figure 2.7d), and Chen and Lan [145] introduced a constant force end effector by combining the positive stiffness of a linear spring with the negative stiffness of a bistable mechanism composed of buckling beams (Figure 2.7e). Moreover, they showed that by pre-stressing the linear spring, the balanced mechanism can be adjusted to operate in different environments. Tolman *et al.* [150] combined constant force mechanisms with a sliding joint and a fixed link consisting of initially angled beams in parallel to develop a statically balanced system (Figure 2.7f), while by combining two straight positive-stiffness beams and two inclined negative-stiffness beams Liu [121] developed a constant force micro gripper. Radaelli and Herder [148] proposed a gravity balancer by designing a specially shaped beam clamped at both ends capable of balancing a defined weight over a large range displacement (Figure 2.7g).

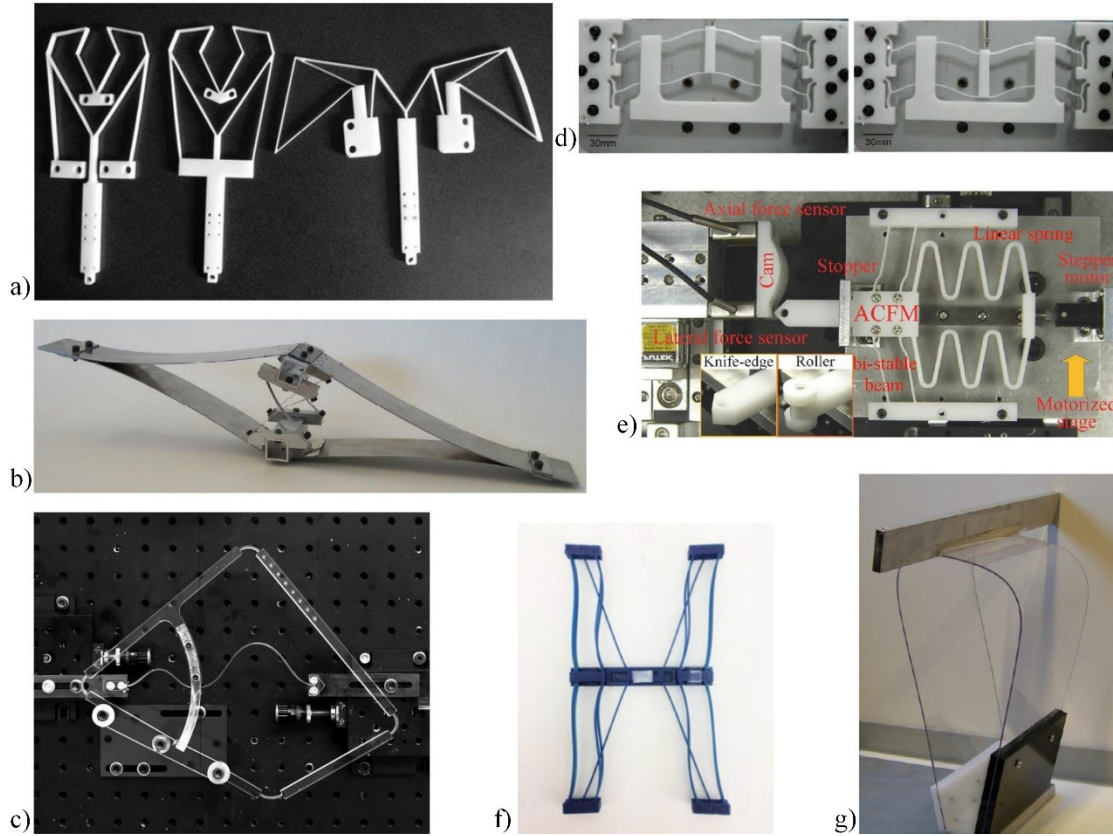


Figure 2.7: a) Statically balanced compliant mechanisms; two grippers and a multiplier prototypes (left to right) [141]. b) Prototype of a zero-stiffness compliant cross-axis flexural joint [142]. c) Prototype of the four-bar linkage compliant mechanism internally balanced with two pre-stressed leaf springs [147]. d) Prototype of a constant force mechanism over a certain displacement range at its two stable configurations [144]. e) Prototype of a constant force end effector combining linear springs with bistable beams [145]. f) A statically balanced compliant mechanism prototype assembled from individual constant force mechanisms [150]. g) A specially shaped polycarbonate double-clamped beam acting as a compliant gravity balancer mechanism [148].

Besides the numerous advantages associated with compliant mechanisms, there are still several challenges to overcome for their systematic use in the various applications. Compliant mechanisms rely for their operation on the elastic deformation and the nonlinear behaviour of their flexible components. Even though this might provide the ability to achieve large displacements and multistability, in many instances, limitations may arise to the designs from the development of high stresses, thus restricting the full exploitation of the mechanism's capabilities. Moreover, another issue that compliant mechanisms may face is fatigue depending the application [114].

2.4 Reconfigurable Mechanisms

New perspectives in the design of mechanisms, robotic devices and/or structures have been opened by incorporating nonlinear structural responses and compliance in mechanisms. Nevertheless, the ever-increasing functional demands in these fields have drawn researchers' interest towards another feature: the

reconfigurability of the mechanisms or structures. Reconfigurability provides flexibility and enables a mechanism or structure to adapt to different environments and to perform multiple tasks [153–155]. In recent years, the field of reconfigurable mechanisms has shown rapid growth. Several mechanisms have been developed that can exhibit reconfiguration and operate in different modes for use in a variety of applications, *e.g.* antennas [156, 157], packaging manipulation [158], foldable or deployable structures [159–162], robotics [163–166] and adaptive building architecture [167, 168].

This ability of a mechanism to change its configuration and perform multiple tasks is strongly related to changes in the connectivity and mobility of the mechanism's components. Various ways to attain reconfigurability have been explored in the literature; the majority concentrates on the development of reconfigurable mechanisms through alterations in the kinematic joints, the degrees of freedom, the orientation of the joint axes or links and the number of links, and taking advantage of any singularities or variations in the constraints that would change the mechanism's mobility [155, 159–161, 164, 169–180]. Gan *et al.* [174] modified a traditional Hooke's joint to an rT joint (Figure 2.8a), by inserting an additional rotational degree of freedom to enable reconfiguration. Plitea *et al.* [176] introduced a reconfigurable robot design using a modular structure and interchanging its active to passive joints between reconfiguration modes, whereas Matheou *et al.* [168] used a 4-bar mechanism combined with struts and cables to construct an adaptable spatial structure achieving reconfiguration by selectively locking joints. Using parallelogram 4-bar mechanisms, a reconfigurable deployable canopy was developed by Jovichikj *et al.* [181] which attains reconfigurability by relative alignment of its links (Figure 2.8b). Meanwhile, Galletti and Fanghella [170] presented the design of reconfigurable closed loop mechanisms based on serial kinematic

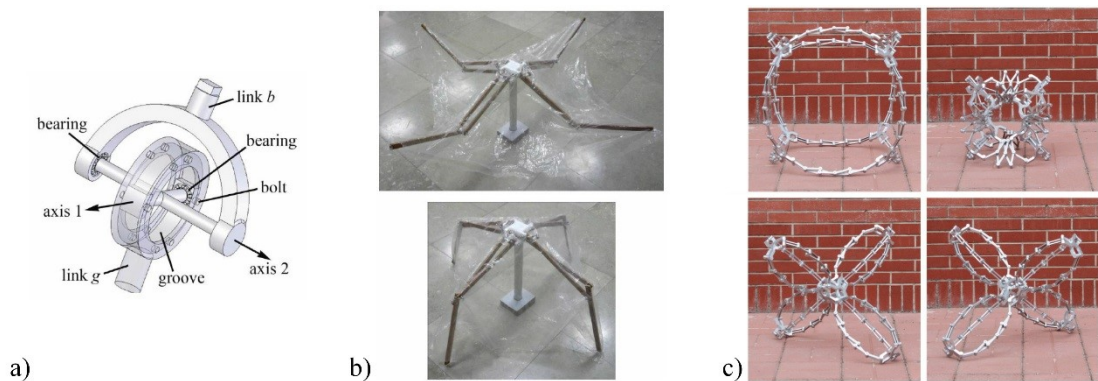


Figure 2.8: a) An rT joint with an additional degree of rotation enabling axis 1 to rotate about axis 2 and can be fixed by bolting it to the groove [174]. b) Prototype of the reconfigurable canopy based on 4-bar mechanisms in two deployed configurations [181]. c) Prototype of a reconfigurable mechanism based on angulated elements in different configurations [160].

chains by modifying their constraints, and Li *et al.* [160, 161, 180] explored the use of angulated elements to design reconfigurable deployable mechanisms exploiting the singularity in the angulated elements at certain transition configurations (Figure 2.8c).

Another approach to attaining reconfigurability, mostly in structures for foldable and deployable applications, has been the use of variable geometry trusses. Miura *et al.* [182] introduced a tessellation of octahedral trusses forming a variable geometry truss structure; the structure combined extendable and fixed length members connected with hinges to change the geometric configuration of the assembly (Figure 2.9a). They explored its application to trusses with arbitrary curvature and their use as manipulator arms, as other researchers did later as well [183, 184] (Figure 2.9b). Finistauri and Xi [185] employed the variable geometry truss concept to develop a mechanism for a morphing aircraft wing. A successor of these trusses can be considered the tensegrity truss structures which incorporate cables instead of struts to create reconfigurable structures or mechanisms (Figure 2.9c) [186–188].

Reconfigurability can also be achieved by various other means, including the use of shape memory alloys or polymers [189, 190], architected materials [191–194] and/or origami principles [158, 162, 189, 193, 195–198]. Liu *et al.* [190] used pre-strained polymer sheets to create foldable 3D shapes with the aid of

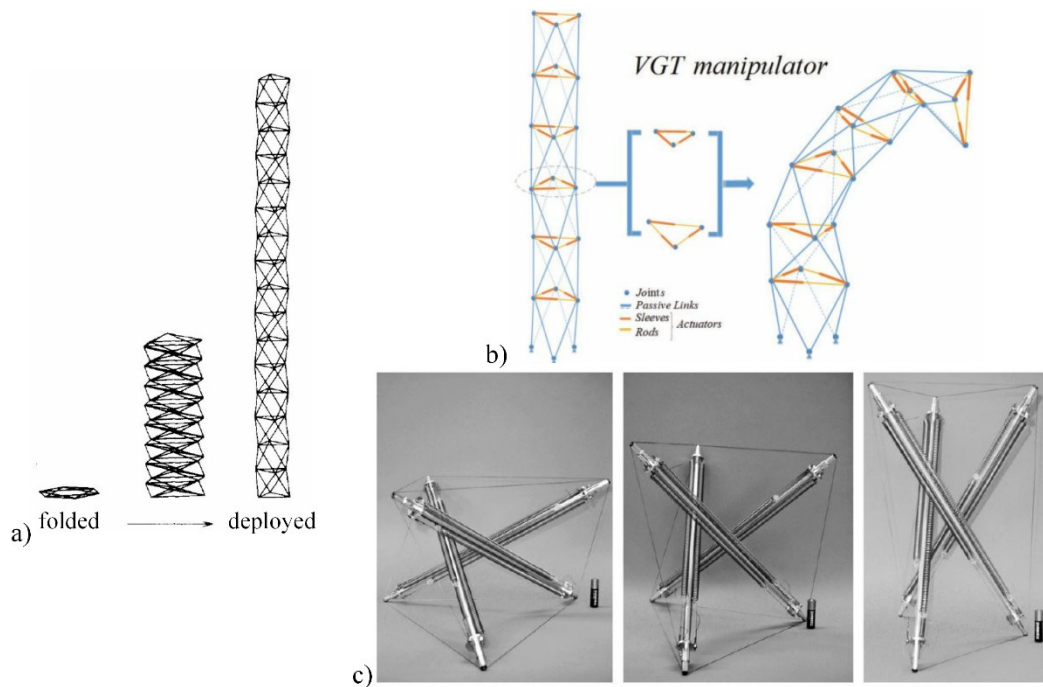


Figure 2.9: a) A variable geometry truss through its transformation from a completely folded to deployed configuration [182]. b) General structure of a variable geometry truss manipulator [184]. c) A zero stiffness tensegrity mechanism in different configurations [186].

light-absorbing inks as hinges, relying on the different absorption coefficients and various ink patterns to achieve controllability (Figure 2.10a). Self-folding structures were also generated by Hernandez *et al.* [189] based on foldable, shape memory alloy sheets and origami patterns. A deployable, reconfigurable structure developed by Pehrson *et al.* [198] used a monolithic thick sheet incorporating folds as in origami, introducing compliance along the folds by accommodating the thickness of the material. In further extension of this latter concept, De Figueiredo *et al.* [162] developed a design method to synthesize thick rigid origami-based structures for applications that require foldability and stiffness (Figure 2.10b). By exploiting architected materials with underlying nonlinearities and mechanical instabilities, in situ changes of their spatial architecture may be achieved, enabling switching between different configurations [193, 194, 197]. For example, the shape reconfigurable architected materials by Haghapanah *et al.* [193] rely on bistable structural elements for the development of 2D or 3D lattice materials with high multi-axial deformation and shape change that could be used for energy absorption applications (Figure 2.10c). In a similar aspect, 3D reconfigurable architected materials were developed by Overvelde *et al.* [192] by exploiting tessellations of assemblies of rigid plates with elastic hinges, exhibiting a broad range of responses and mobility.

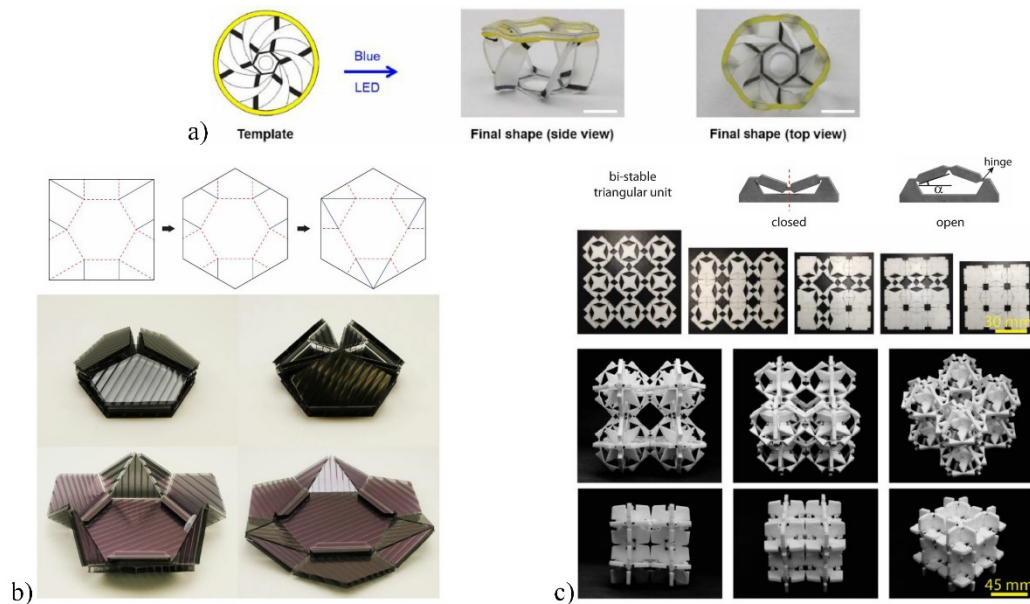


Figure 2.10: a) A polymer dome structure created using inks with different optical absorption under a blue LED (scale bar: 5 mm) [190]. b) Modification of the hexagonal twist pattern for a foldable structure using thickness variation for the hinges and a prototype of thick panels in its various configurations [162]. c) Prototype of a 2D and a 3D shape reconfigurable material using a bistable triangular unit hinge mechanism fabricated through laser cutting of Teflon sheets in various configurations [193].

2.5 Summary

Researchers' and engineers' attitude towards nonlinear phenomena in structures has changed over the past decades. Large displacements or strains and buckling phenomena that were associated with failure, compromising the integrity and stability of the structure, are now being exploited for efficiency and functionality. Increasing number of studies explore these nonlinear phenomena and their potential, in an attempt to provide a better understanding and the ability to harness these nonlinearities in the design of engineering structures. New routes in the design of mechanisms and/or structures are also opened up, new architected materials are emerging, enabling to enhance their functionality and performance. Nonlinearities are already being explored in new technologies, *e.g.* the development of smart structures, shape adaptable structures or compliant mechanisms. Compliant mechanisms have been developed that use nonlinear responses to increase flexibility and advance their stability characteristics, as well as reconfigurable architected materials that base their ability to transform on nonlinear phenomena, *e.g.* buckling. Thus, it becomes evident that the integration of these fields and technologies is inevitable and it seems promising for the development of mechanisms for diverse applications.

In this work a compliant mechanism is introduced that exploits the nonlinear characteristics of a composite helical morphing structure that can undergo large deformations while maintaining its load-carrying capability. For the first time, these helical elements are combined into structural assemblies introducing a compliant, multistable and reconfigurable mechanism. The structural assemblies are studied both analytically, using energy landscapes and conventional path-following methodologies, and experimentally, using a custom designed test rig. It is the first time that the manufacture of such assemblies is attempted and presented herein. The mechanism is essentially a hybrid compliant mechanism; it still comprises of traditional joints for the assembly of its constituent elements and the mechanism's geometry itself, yet it relies on the compliance of its composite morphing components and their elastic response for functionality. The use of these morphing elements as the flexible components of the mechanism is originally exploited in this work and the additional benefits these assemblies may offer are investigated. The underlying incentive in using these morphing elements is to enable large deformations to be achieved and stability characteristics of interest to be developed. Additionally, the nonlinear characteristics of the composite morphing elements can be highly tailorable; thus, the ensuing mechanism can be tuned to feature a variety of responses. Besides the featured multistability, the mechanism's reconfigurability can be considered, *i.e.*

its ability to change its configuration and behaviour in multiple operation modes. All these potentials are considered for the mechanism proposed in the scope of this work.

The following chapters explore the aforementioned concept: the development of a compliant mechanism assembled of morphing structures that exhibits multistability as well as reconfigurability. Specifically, the following chapter (Chapter 3) introduces the geometrical and mechanical characteristics of the morphing structure selected for this purpose. Next, the assembly of a mechanism consisting of these morphing elements is introduced; its kinematics and the methods employed for its analysis are presented too. The mechanism's stability characteristics and its sensitivity to key design parameters are explored in Chapter 5. Chapter 6 investigates the mechanism's reconfigurability and the effect of the different reconfiguration modes on the mechanism's stability and mechanical response. The design, manufacture and test of a prototype are presented in Chapter 7, and final remarks and thoughts for potential future directions of this work are included in the final chapter (Chapter 8).

Chapter 3

A Double-Helix Morphing Composite Structure

3.1 Introduction

Unlike conventional structures where nonlinearities and large deformations are considered undesirable and associated with failure phenomena, like buckling, [42, 199–201] morphing structures are able to undergo large deformations and change their shape while maintaining their structural integrity and load carrying capability [26]. Such structures and their nonlinear characteristics can be exploited for potential use in various applications such as mechanisms, deployable structures and robotics. Lachenal *et al.* [25] introduced a morphing structure made of two carbon fibre reinforced polymer (CFRP) strips arranged in a double-helix architecture. This helical element is capable of large axial deformation and, beyond its variable geometry, exhibits highly tailorable nonlinear stiffness characteristics. The analytical model of the structure has been developed by Lachenal [202], and its mechanical behaviour has been extensively analysed. Lachenal *et al.* [95, 202] exploited the variable stiffness of the helical structure and manufactured a prototype of a twist morphing tip for wind turbine applications, while Masia *et al.* [12] and Cappello *et al.* [27] taking advantage of the multistability of the helical structure introduced a compliant actuator for wearable exoskeletons assisting elbow motion. In this work, building upon these previous researches, we take a step further and combine these helical elements into structural assemblies introducing a compliant, multistable mechanism. Thus, we first introduce this helical morphing element itself.

In this chapter, a description of this helical morphing structure is detailed in §3.2 and the above-mentioned analytical model is presented in §3.3, based upon which the synthesis and analysis of a truss-like

mechanism composed of these helical elements combined in structural assemblies are developed in this thesis. The behaviour of the composite morphing structure and its sensitivity to various design parameters are discussed in §3.4.

3.2 Description of the double-helix morphing structure

The morphing structure consists of two carbon fibre reinforced plastic strips of dimensions $L \times W$, connected by rigid spokes placed at equal distances (Figure 3.1). The spokes maintain the strips at a constant distance $H = 2R$, where R is the radius of an underlying cylinder, upon which the deformed strips can be assumed to lie [23, 25]. A pre-stress, in particular a distributed bending moment, is introduced in the strips by manufacturing them on a cylindrical mould of radius R_i and subsequently flattening them to form the double-helix. The double-helix is able to twist under the application of an axial force at its ends, which results in large axial displacement, Δl . The structure can deform from a straight to a completely coiled configuration, defined by the helix angle $\theta \in [-90^\circ, 90^\circ]$ between the local x -axis and the global X -axis of the helix [26]. The angle θ is defined to be positive for anti-clockwise rotations starting from the straight configuration. The displacement Δl of one end of the structure from the straight configuration is given by [25]:

$$\Delta l = L - l = L(1 - \cos \theta), \quad (3.1)$$

where l is the projected length of the strip along the axis of the cylinder.

In each helix the number of spokes varies depending on the length L of the strips with their actual in-between distance defined in an intuitive-like way to address the following. On one side, the selected distance should ensure that the strips will deform along the surface of an underlying cylinder, with the helix maintaining a circular cross section when twisted, and avoid buckling of the strip section between two consecutive spokes, which would result in an ellipsoidal cross section when the helix moves towards the coiled configuration. On the other side, the distance between the spokes should be sufficient enough to allow the seamless twist of the helix from an extended to a fully coiled configuration. This is to avoid: i) increasing the stiffness structure due to the limited available free length of the strip between the spokes and maintain the helix compliance, and ii) the spokes colliding early enough during the helix deformation limiting its range of motion.

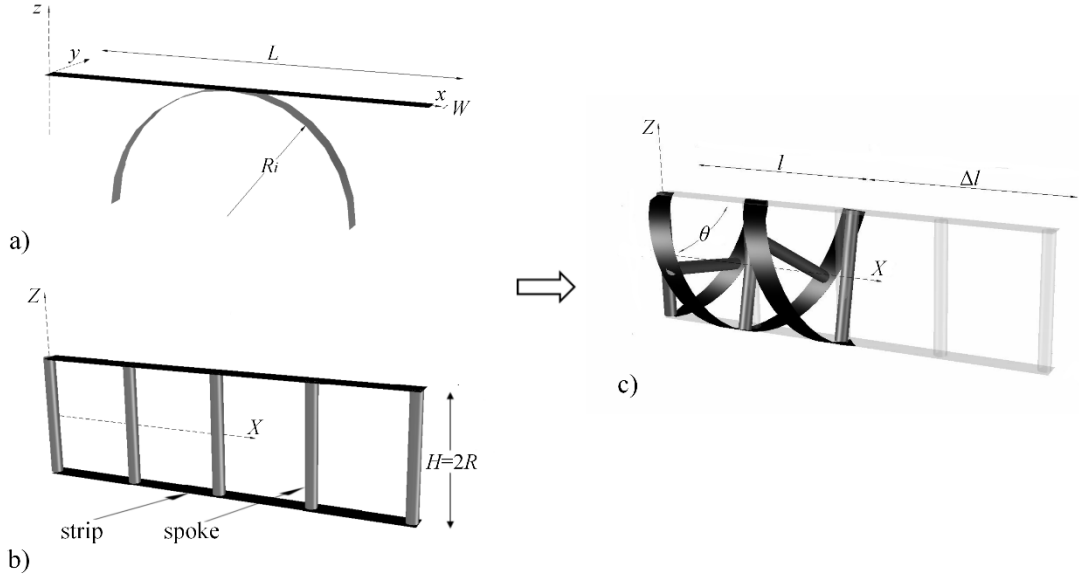


Figure 3.1: a) Initially curved (radius R_i) composite strips are flattened to introduce pre-stress; b) the strips are joined by rigid spokes to form a double-helix structure, which c) can deform from a straight (light grey) to twisted (dark) configurations.

3.3 Analytical model [26, 202]

A two-dimensional analytical model of the strain energy of the helix was developed by Lachenal [202]. His work drew from an earlier, inextensional model on cylindrical shells of Guest and Pellegrino [108], extended to account for extensional deformations and membrane strains based on the work of Giomi and Mahadevan [203]. The main assumptions and expressions of this model are given below.

In this model, double-helices each consisting of composite strips with the same lay-up are assumed. The composite strips of the double-helix are considered as two-dimensional elements of dimensions $L \times W$ with both bending and membrane deformations occurring in them, thus the total strain energy of a double-helix can be calculated by [204]:

$$U = \frac{n}{2} \int_0^L \int_{-W/2}^{W/2} \begin{bmatrix} \boldsymbol{\epsilon}^0 \\ \Delta \boldsymbol{\kappa} \end{bmatrix}^T \begin{bmatrix} \mathbf{A} & \mathbf{B} \\ \mathbf{B} & \mathbf{D} \end{bmatrix} \begin{bmatrix} \boldsymbol{\epsilon}^0 \\ \Delta \boldsymbol{\kappa} \end{bmatrix} dx dy, \quad (3.2)$$

where n is the number of composite strips, $\boldsymbol{\epsilon}^0$ is the tensor of the mid-plane strains and $\Delta \boldsymbol{\kappa}$ is the tensor of the change in curvature, both referring to the local coordinate system of the strips. \mathbf{A} , \mathbf{B} and \mathbf{D} are the in-plane, bending-extension coupling and bending stiffness matrices of the Classical Laminate Theory, respectively [205]. Equation (3.2) expands to:

$$U = \frac{n}{2} \int_0^L \int_{-W/2}^{W/2} \boldsymbol{\varepsilon}^{0T} \mathbf{A} \boldsymbol{\varepsilon}^0 dx dy + n \int_0^L \int_{-W/2}^{W/2} \boldsymbol{\varepsilon}^{0T} \mathbf{B} \Delta \boldsymbol{\kappa} dx dy + \frac{n}{2} \int_0^L \int_{-W/2}^{W/2} \Delta \boldsymbol{\kappa}^T \mathbf{D} \Delta \boldsymbol{\kappa} dx dy, \quad (3.3)$$

with the three terms on the right-hand side capturing the energy contribution due to the stretching, bending-extension coupling and bending deformations, respectively [202]. It is worth noting that the major contribution to the total strain energy of the double-helix is made by bending deformations. The assumption by Giomi and Mahadevan [203], that only x -axis strains result from the deformation of the helix, is also taken into consideration in this model. Therefore, the membrane strain energy and the bending-extension elastic energy contributions are reduced to expressions that include only the terms A_{11} and B_{11} . It is also worth noting that the bending-extension contribution can be neglected due to the near-zero B_{11} for the selected composite lay-ups in this work (as described in Section 3.4).

Following Giomi and Mahadevan [203] that only x -axis strains are developed during the deformation of the structure, the mid-plane strain tensor is calculated as:

$$\boldsymbol{\varepsilon}^0 = \begin{bmatrix} \varepsilon_x^0 \\ \varepsilon_y^0 \\ \gamma_{xy}^0 \end{bmatrix} = \begin{bmatrix} \alpha_{11} N_x \\ 0 \\ 0 \end{bmatrix}, \quad (3.4)$$

where α_{11} refers to the term of the in-plane compliance matrix of the composite ($\boldsymbol{\alpha} = \mathbf{A}^{-1}$) and N_x is the axial force that arises during the deformation of the structure, given by [203]:

$$N_x = D_{22}^* C_2' \cosh(k_1 y) \cos(k_2 y) - D_{22}^* C_1' \sinh(k_1 y) \sin(k_2 y), \quad (3.5)$$

where $\mathbf{D}^* = \mathbf{B} \mathbf{A}^{-1} \mathbf{B}$ is the reduced bending stiffness matrix, and the following terms are defined [203]:

$$C_1' = \frac{(\alpha_{11} D_{22}^*)^{1/2} C_1 + H_{21} C_2}{\alpha_{11} D_{22}^* + H_{21}^2} \quad (3.6)$$

$$C_2' = \frac{(\alpha_{11} D_{22}^*)^{1/2} C_2 - H_{21} C_1}{\alpha_{11} D_{22}^* + H_{21}^2} \quad (3.7)$$

$$C_1 = (\Delta \kappa_y^c - \kappa_y^G) \frac{k_1 \cosh\left(\frac{W}{2} k_1\right) \sin\left(\frac{W}{2} k_2\right) + k_2 \sinh\left(\frac{W}{2} k_1\right) \cos\left(\frac{W}{2} k_2\right)}{k_1 \sin\left(\frac{W}{2} k_2\right) \cos\left(\frac{W}{2} k_2\right) + k_2 \sinh\left(\frac{W}{2} k_1\right) \cosh\left(\frac{W}{2} k_1\right)} \quad (3.8)$$

$$C_2 = (\Delta\kappa_y^c - \kappa_y^G) \frac{k_2 \cosh\left(\frac{W}{2}k_1\right) \sin\left(\frac{W}{2}k_2\right) - k_1 \sinh\left(\frac{W}{2}k_1\right) \cos\left(\frac{W}{2}k_2\right)}{k_1 \sin\left(\frac{W}{2}k_2\right) \cos\left(\frac{W}{2}k_2\right) + k_2 \sinh\left(\frac{W}{2}k_1\right) \cosh\left(\frac{W}{2}k_1\right)} \quad (3.9)$$

$$\Delta\kappa_y^c = -\frac{D_{12}^* \Delta\kappa_x + D_{26}^* \Delta\kappa_{xy}}{D_{22}^*} \quad (3.10)$$

$$\kappa_y^G = \frac{\kappa_{xy}^2}{4\kappa_x} \quad (3.11)$$

$$k_1 = \left(\frac{\sqrt{s_2} + s_1}{2}\right)^{1/2} \quad (3.12)$$

$$k_2 = \left(\frac{\sqrt{s_2} - s_1}{2}\right)^{1/2} \quad (3.13)$$

$$s_1 = -\frac{H_{21}\kappa_x}{\alpha_{11}D_{22}^* + H_{21}^2} \quad (3.14)$$

$$s_2 = -\frac{\kappa_x^2}{\alpha_{11}D_{22}^* + H_{21}^2} \quad (3.15)$$

where $\mathbf{H} = -\mathbf{A}^{-1}\mathbf{B}$, $\Delta\kappa_y^c$ is the transverse curvature developed from constitutive behaviour (thus the superscript c), and κ_y^G is the transverse curvature developed to eliminate Gaussian curvature (thus the superscript G).

With the spokes keeping the strips at a constant distance throughout the transformation of the helix, the strips are assumed to deform tangent to the surface of a cylinder of constant radius R , while uniform deformation of the mid-surface of the strips is also assumed. Thus, only $\Delta\kappa_x$ and $\Delta\kappa_{xy}$ changes of curvature can occur with regards to the manufactured shape. Whereas deformations in the y -direction are the result of boundary conditions and material properties. According to Giomi and Mahadevan [203], the transverse change of curvature of the strip is found by solving the fourth order differential equation:

$$\begin{aligned} & (\alpha_{11}D_{22}^* + H_{21}^2) \frac{\partial^4 M_y}{\partial y^4} + 2H_{21}\kappa_x \frac{\partial^2 M_y}{\partial y^2} + \kappa_x^2 M_y \\ & = \kappa_x \{D_{22}^*(c_x c_y - c_{xy}^2 + \kappa_{xy}^2) + \kappa_x [D_{12}^*(\kappa_x - c_x) + D_{26}^*(\kappa_{xy} - c_{xy}) - D_{22}^* c_y]\}, \end{aligned} \quad (3.16)$$

where M_y is the moment across the width of the strip (assumed constant along the length L), $c_x = 1/R_i$, $c_y = c_{xy} = 0$ are the initial manufactured curvatures, and κ_x, κ_{xy} are the curvatures of the deformed strip expressed as [26]:

$$\kappa_x = \frac{1}{2R}(1 - \cos(2\theta)) \quad (3.17)$$

$$\kappa_{xy} = \frac{1}{R}\sin(2\theta) \quad (3.18)$$

Given no forces or torques are applied on the longitudinal edges of the strip, the boundary conditions are:

$$\frac{\partial M_y}{\partial y} = M_y = 0, \quad y = \pm W/2 \quad (3.19)$$

and the general solution of Eq. (3.16) is developed as below:

$$\Delta \kappa_y^i = \kappa_y^G + (C_1 + H_{21}C_2') \cosh(k_1 y) \cos(k_2 y) + (C_2 - H_{21}C_1') \sinh(k_1 y) \sin(k_2 y) \quad (3.20)$$

Therefore, the tensor of the change in curvature $\Delta \mathbf{\kappa}$ is calculated as:

$$\Delta \mathbf{\kappa} = \begin{bmatrix} \Delta \kappa_x \\ \Delta \kappa_y \\ \Delta \kappa_{xy} \end{bmatrix} = \frac{1}{2R} \begin{bmatrix} 1 - \cos(2\theta) - \frac{2R}{R_i} \\ 2R\Delta \kappa_y^i \\ 2\sin(2\theta) \end{bmatrix} \quad (3.21)$$

The total strain energy of the helical structure can be used to explore its stability. Equilibrium configurations can be found by setting the first derivative of the total strain energy U with respect to the helix angle θ equal to zero, with the stable ones defined by a strictly positive second derivative of the total strain energy U with respect to the helix angle θ in addition [26].

$$\frac{\partial U}{\partial \theta} = 0, \quad \frac{\partial^2 U}{\partial \theta^2} > 0 \quad (3.22)$$

The axial force F necessary to extend or contract the composite structure is also derived from the strain energy U by applying Castigliano's theorem [25]:

$$F = \frac{\partial U}{\partial \Delta l}, \quad (3.23)$$

where Δl is the deformation of the structure from the straight configuration and the axial stiffness k is subsequently given by [25]:

$$k = \frac{\partial^2 U}{\partial \Delta l^2} \quad (3.24)$$

3.4 Double-helix response

Based on the analytical model above, the helical structure can be tailored to provide customizable stiffness characteristics and strain energy profiles through appropriate selection of various design parameters, such as the lay-up of the strips, the pre-stress and the geometry of the structure [25]. In this work, we focus on lay-ups of five plies of the form $[\beta_2/0/\beta_2]$ and $[\beta_2/0/-\beta_2]$, where $\beta \in [0^\circ, 90^\circ]$ is the fibre angle, measured with respect to the longitudinal, local x -axis of the composite strip. The angle β is defined to be positive towards the y -axis and the plies are stacked in the positive z -direction. Five plies are considered sufficient to provide significant strain energy variation during the helix deformation, with additionally the 0° ply in the middle ensuring a minimum strength and preventing delamination issues [25]. Conceptually, a symmetric lay-up, *i.e.* the $[\beta_2/0/\beta_2]$ herein, exhibits no coupling between bending and extensional responses, while a balanced and antisymmetric lay-up, *i.e.* the $[\beta_2/0/-\beta_2]$ lay-ups, exhibits no extension-shear or bend-twist coupling.

For the results herein, helices with dimensions $L = 95$ mm, $R = 15$ mm, $R_i = 30$ mm and $W = 5$ mm have been used; these dimensions followed from an optimization of the helical structure performed to meet specific design requirements in earlier work by the author done as part of the Extended Project of the CDT program [206]. In that work, as the helical structure was aimed to be used as part of an actuator of a wearable robotic device assisting the motion of the arm and carried as a backpack, space and weight limitations applied, in addition to requirements regarding the performance of the helix and the safe interaction between the human and the device. Thus, the helical structure was optimised with regards to its dimensions, while a point of stable equilibrium was required ideally at a helix angle θ of 45° , transitioning from the extended to the complete coiled configuration. Moreover, a limitation of 50 N to the maximum axial force of the helix was applied to minimise peak force outputs whilst maintaining the ability to sustain the weight of the arm given the current exoskeleton. The material properties used for the helical strips are given in Table 3.1.

Table 3.1: Hexcel IM7/8552 unidirectional carbon fibre prepreg properties [25, 208]

Material	E_{11} (GPa)	E_{22} (GPa)	G_{12} (GPa)	ν_{12} (–)	thickness (mm)
IM7/8552	163.7	11.5	5	0.3	0.105

Figure 3.2 shows the evolution of the strain energy of the helix over its entire workspace as a function of the helix angle θ and for double helices of different laminates of symmetric and antisymmetric stacking sequence: respectively, $[\beta_2/0/\beta_2]$ and $[\beta_2/0/-\beta_2]$. The corresponding axial blocking force is shown in Figure 3.3 as a function of Δl . For strips where $\beta = 0^\circ$, $\beta = 90^\circ$ or antisymmetric ones, the strain energy is periodic and symmetric with respect to $\theta = 0^\circ$ (Figure 3.2), meaning that, in these cases, helices will exhibit identical behaviours in $\theta \in [0^\circ, 90^\circ]$ and $\theta \in [0^\circ, -90^\circ]$, and therefore, the same force-displacement response (identical responses between Figure 3.3a, b for these lay-ups). This is in contrast to the behaviour of symmetric angle-ply lay-ups. For instance, the strain energy for the $[45_2/0/45_2]$ lay-up in Figure 3.2 retains the periodicity but breaks the symmetry around $\theta = 0^\circ$, meaning that the force-displacement response will differ in $\theta \in [0^\circ, 90^\circ]$ and $\theta \in [0^\circ, -90^\circ]$ (diverse responses between Figure 3.3a, b for such lay-ups). This difference provides the basis for the reconfigurability of the helix [207].

In addition, the double-helix features bistability, meaning that two self-equilibrated shapes may exist. The stability of the structure can be found by inspection of its strain energy evolution (Figure 3.2), with stable (marked as crosses in Figure 3.2) and unstable (marked as dots in Figure 3.2) configurations corresponding to minima and maxima of the strain energy, respectively. For laminates where $\beta = 0^\circ$, the straight and the fully coiled configurations correspond to energy maxima, thus these configurations are unstable, while the stable equilibria can be found at $\theta = \pm 45^\circ$. In contrast, for strips where $\beta = 90^\circ$ or antisymmetric lay-ups, the structure exhibits energy maxima at $\theta = \pm 45^\circ$, *i.e.* unstable equilibria, whereas its stable equilibria are positioned at $\theta = 0^\circ$ —the straight configuration—and at $\theta = \pm 90^\circ$ —the fully coiled ones. For symmetric angle-ply lay-ups, the position of the equilibria, both stable and unstable, can take any value of $\theta \in [-90^\circ, 90^\circ]$. It is observed, however, that for deformation of the helix with $\theta \in [0^\circ, -90^\circ]$, the stability point will lie closer to the fully coiled configuration, as opposed to the deformation mode with $\theta \in [0^\circ, 90^\circ]$, where the stable position takes a helix angle value closer to the straight configuration and additionally a stable boundary equilibria is achieved at $\theta = 90^\circ$ (marked with triangles in Figure 3.2).

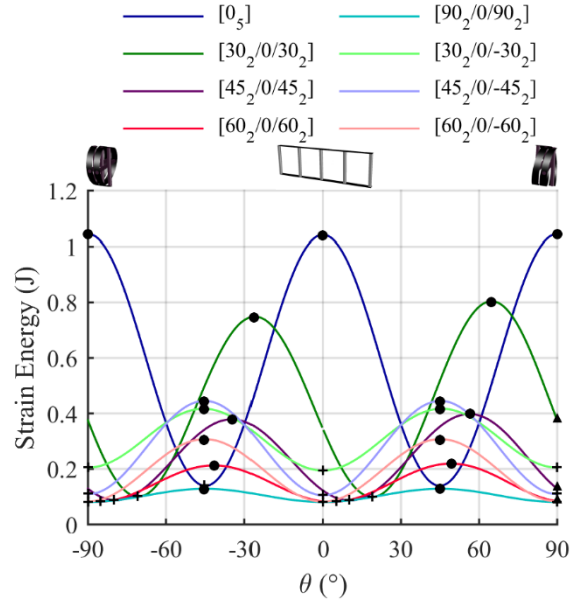


Figure 3.2: Strain energy profiles as a function of the helix angle θ of double-helices with $L = 95$ mm, $R = 15$ mm, $R_i = 30$ mm, $W = 5$ mm for different strip lay-ups. Dots (•) represent unstable equilibria; crosses (+) stable equilibria; triangles (▲) boundary equilibria.

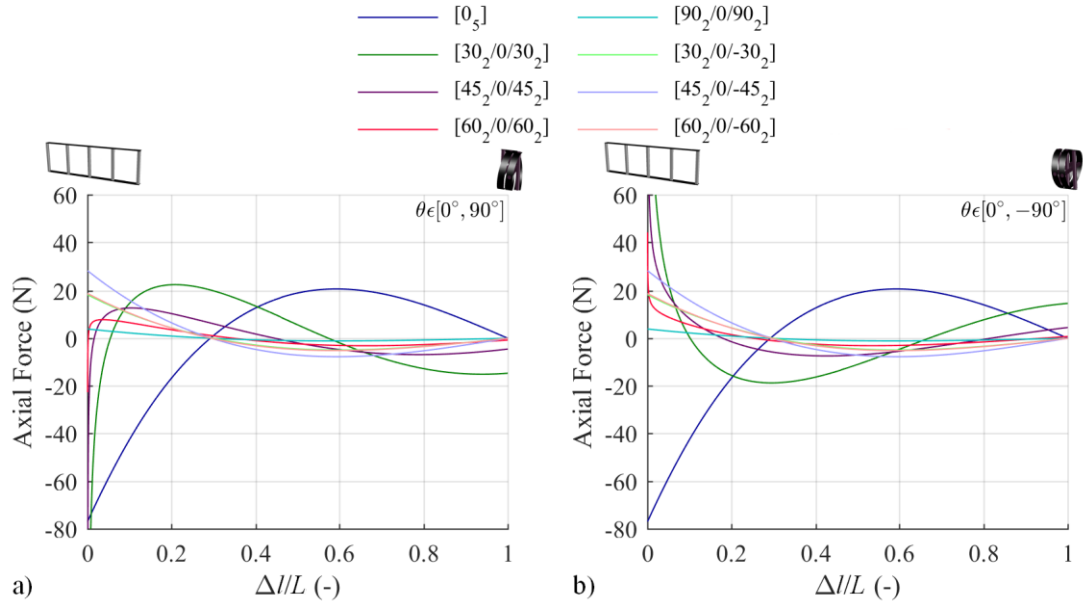


Figure 3.3: Load-displacement curves of double-helices with $L = 95$ mm, $R = 15$ mm, $R_i = 30$ mm, $W = 5$ mm for different strip lay-ups. a) $\theta \in [0^\circ, 90^\circ]$; b) $\theta \in [0^\circ, -90^\circ]$. The displacement Δ has been normalized to the length L of the strips, with $\Delta/L = 0$ representing the fully-extended and $\Delta/L = 1$ its fully coiled configurations.

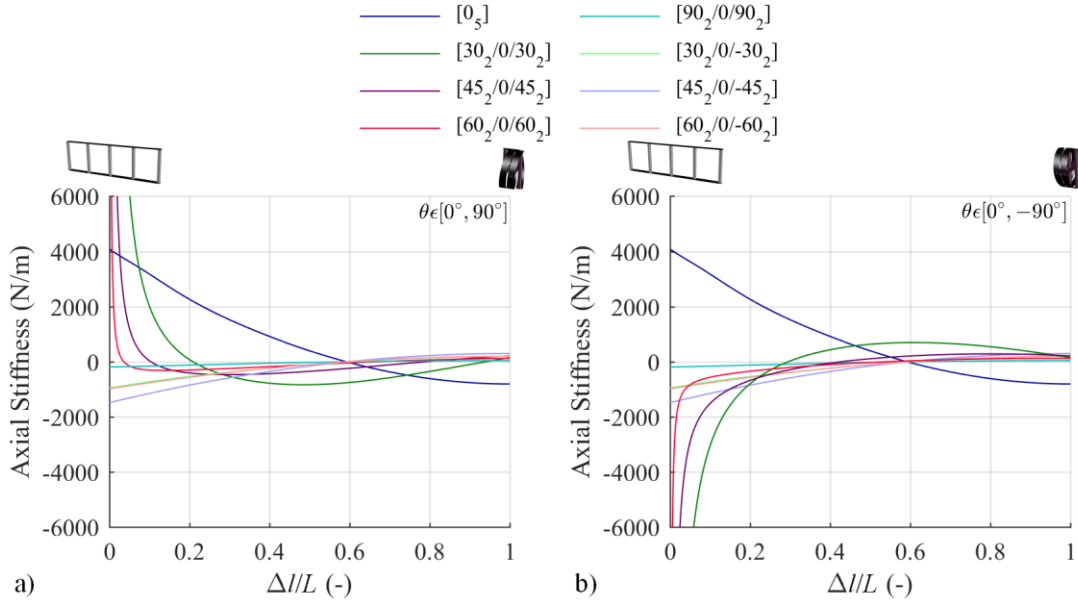


Figure 3.4: Axial stiffness as a function of the displacement Δl of double-helices with $L = 95$ mm, $R = 15$ mm, $R_i = 30$ mm, $W = 5$ mm for different strip lay-ups. a) $\theta \in [0^\circ, 90^\circ]$; b) $\theta \in [0^\circ, -90^\circ]$. The displacement Δl is normalized to the length L of the strips, with $\Delta l/L = 0$ representing the fully-extended and $\Delta l/L = 1$ its fully coiled configurations.

Another interesting feature in the behaviour of the double-helix is its highly tailorable nonlinear characteristics. Focusing on the load-displacement response of the helix in Figure 3.3, it is observed that the load-displacement curve is nonlinear, with the axial force altering signs as the helix deforms from a straight to a fully coiled configuration. Thus, the helix exhibits nonlinear stiffness characteristics as well, with its stiffness interchanging between areas of either positive or negative stiffness over its workspace (Figure 3.4). The negative stiffness of the helix can be exploited for vibration isolation and energy harvesting applications [91, 209].

A manufactured prototype of a double-helix of a symmetric angle-ply strip lay-up is presented in Figure 3.5 in different configurations for helix angles both $\theta \in [0^\circ, 90^\circ]$ and $\theta \in [0^\circ, -90^\circ]$. An external force is required to keep such double-helix in its extended configuration, thus the hands holding it in that configuration (Figure 3.5a). For deformations in $\theta \in [0^\circ, 90^\circ]$, the helix is stable at a slightly twisted configuration (Figure 3.5b)—it stays at that configuration by itself—while for further coiled configurations an external force is required (Figure 3.5c) until it reaches its fully coiled position that in this case is a stable boundary equilibrium (Figure 3.5d). On the other hand, for deformations in $\theta \in [0^\circ, -90^\circ]$, an external force is required to hold the helix in a slightly twisted configuration (Figure 3.5e), while the helix is stable at a further coiled configuration (Figure 3.5f)—no hands holding the helix at this position—and again an external force is required at its fully coiled configuration (Figure 3.5g).

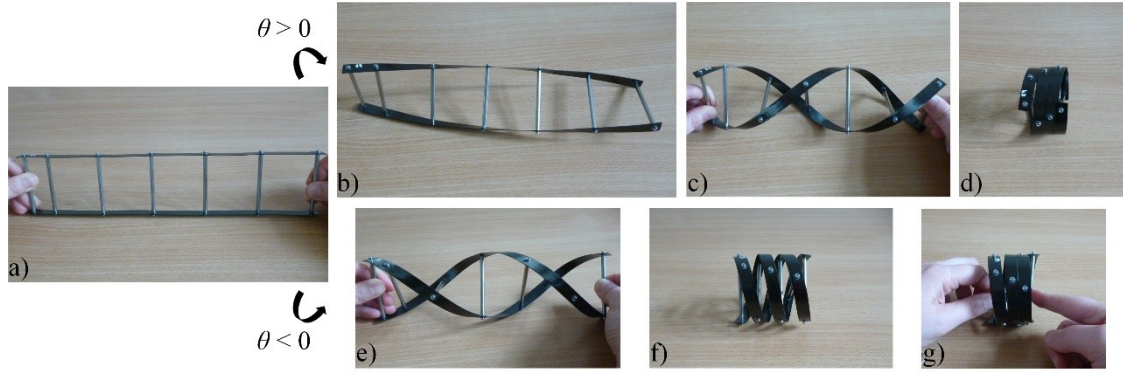


Figure 3.5: Manufactured prototype of the double-helix structure of a symmetric $[90/45/0/45/90]$ strip lay-up, with dimensions $L = 292$ mm, $R = 30$ mm, $R_i = 60$ mm, $W = 10$ mm in a) straight configuration; b) stable, c) twisted, and d) fully coiled configurations for $\theta \in [0^\circ, 90^\circ]$; e) twisted, f) stable, and g) fully coiled configurations for $\theta \in [0^\circ, -90^\circ]$.

It was found that the lay-up of the composite strips has the most significant effect in the load-displacement curves of the double-helices; the sensitivity to varying geometric parameters has also been explored. The results shown in Figure 3.6 are for helices of a symmetric angle-ply strip lay-up with $\beta = 45^\circ$ of different geometric characteristics. For Figure 3.6a-d a single geometric feature of the double-helix is altered each time keeping everything else constant, while for Figure 3.6e the dimensions of the helix are changed keeping a constant ratio $R_i/R = 2$ and $L \approx 2\pi R$ for a constant strip width value. As mentioned, the effect of the geometric characteristics in the load-displacement curves of the helices is not as significant as that of varying the composite strip lay-up. Specifically, it is observed that the helix response remains the same for helices of different strip length L (coinciding lines in Figure 3.6a); similar responses occur for helices of different strip width W (Figure 3.6b), radius R (Figure 3.6c), or different pre-stress, as captured by the radius R_i (Figure 3.6d), with slight differences in the absolute values of the axial force and stiffness of the helix. To add to this, even a proportional change of the double-helix geometric features maintains a similar load-displacement response (Figure 3.6e).

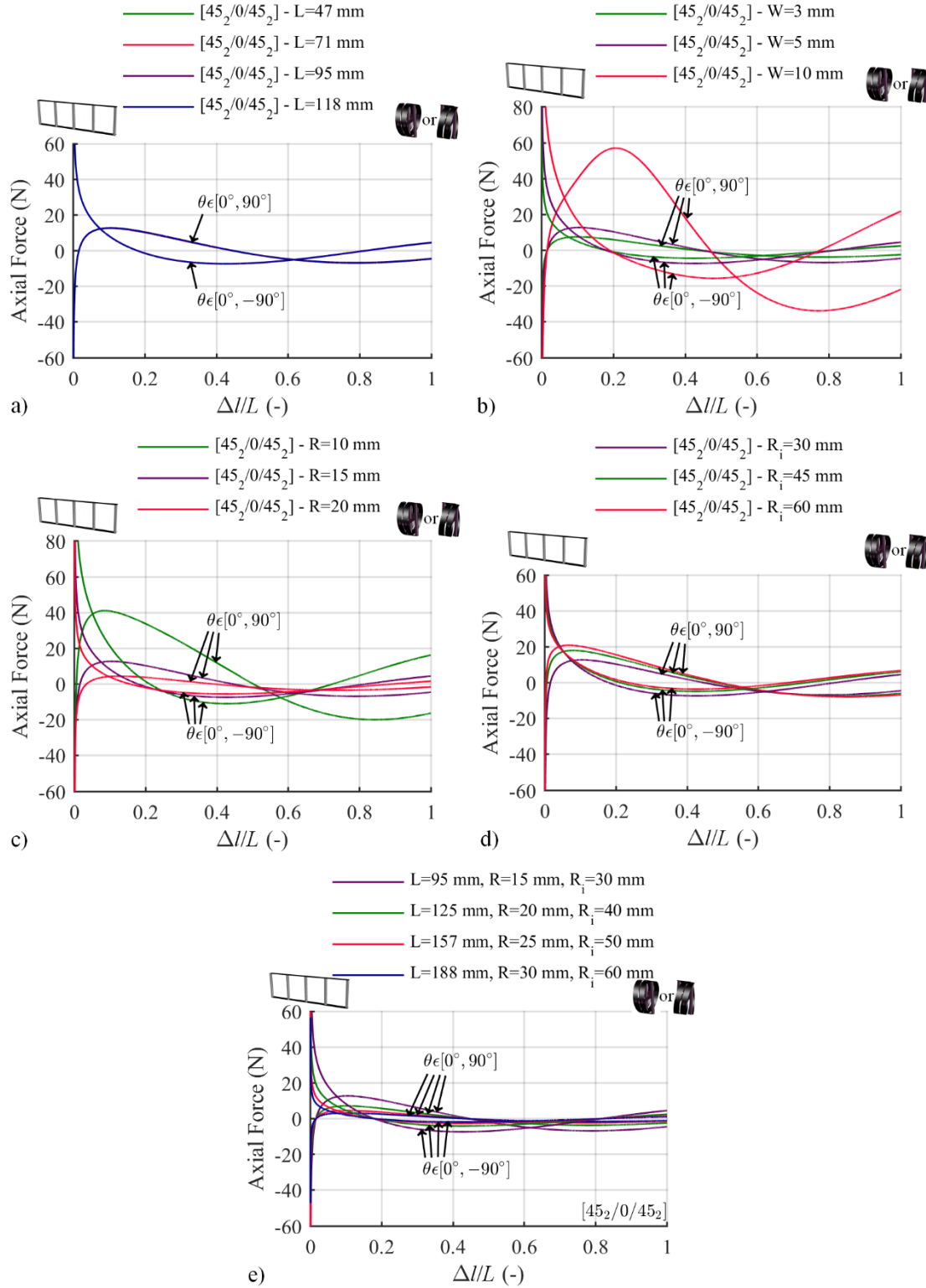


Figure 3.6: Load-displacement curves of double-helices of a $[45_2/0/45_2]$ strip lay-up: a) for different lengths L , $R = 15$ mm, $R_i = 30$ mm, $W = 5$ mm. b) for different widths W , $L = 95$ mm, $R = 15$ mm, $R_i = 30$ mm; c) for different radius R , $L = 95$ mm, $R_i = 30$ mm, $W = 5$ mm; d) for different initial curvatures of the strips R_i , $L = 95$ mm, $R = 15$ mm, $W = 5$ mm; e) for different dimensions L , R and R_i , keeping a constant ratio $R_i/R = 2$ and $L \approx 2\pi R$. The displacement Δ/L is normalized to the length L of the strips in each case for comparison purposes, with $\Delta/L = 0$ representing the fully-extended and $\Delta/L = 1$ its fully coiled configurations.

3.5 Summary

The morphing structure consisting of two pre-stressed, composite strips joined by rigid spokes, initially introduced by Lachenal [202] and presented in the sections above, exhibits a remarkable behaviour as a structure. This helical structure is able to undergo large deformations and maintain its structural integrity; can deform from an extended to a fully coiled configuration, similar to a spring element, while exhibiting nonlinear stiffness characteristics. These characteristics are highly tailorable and along with the different stability behaviours that can be achieved, can be exploited in a variety of applications [12, 91, 95]. With Lachenal [202] having already explored the design space of this helical structure as individual elements, what triggered our interest is the potential these structures might present if multiple are combined together. Our curiosity on the behaviour of assemblies composed of such elements and exploring their design space have been the primary subject of this research.

In this thesis, drawing upon this helical structure a mechanism is introduced that uses these morphing structures as its flexible members. In the next chapter, the assembly of such helical structures in a mechanism of a truss-like configuration is presented along with the methods employed for the structural analysis and investigation of the stability response of this mechanism. The results of the analysis and the sensitivity of the mechanism to various design parameters, followed by the manufacture and experimental testing of a prototype are included in the chapters further below.

Chapter 4

A Compliant Mechanism Based on Double-Helix Composite Structures and its Analysis Methods

4.1 Introduction

Compliant devices have been of great interest among researchers in the fields of mechanisms, robotics and morphing structures. This interest stems from their capabilities and the variety of promising applications both in micro and macro scale devices [117]. Mechanisms are parts of machines and other devices used to transfer motion, force or energy. Conventional mechanisms consist of rigid links and base their mobility on movable joints. Unlike rigid-link mechanisms, compliant mechanisms utilize the flexibility of their members to transmit or transform motion and forces [210]. The field of application for compliant mechanisms is broad [117].

Compliant mechanisms can be considered as variable stiffness structures. To modulate their stiffness characteristics or to achieve desired nonlinear behaviour, combinations of cam and beam structures [211] or cam rollers with floating springs have been used, leading to complex and relatively bulky designs [212]. State-of-the-art compliant mechanisms take advantage of the flexibility of their constituent materials to obtain designs that are lightweight, easily scalable and with reduced friction and no need for lubricants. However, these compliant mechanisms often rely on flexures, whose range of motion is limited by stresses developed upon elastic deformation [128]. To achieve higher effective strains and extend the range of motion currently available, this work proposes the use of morphing composite structures as the flexible elements in a compliant mechanism.

The compliant mechanism developed in this research uses morphing elements as the flexible members, that can change shape and undergo large deformations while maintaining their load-carrying capability and structural integrity. The composite morphing double-helical structures presented in the previous chapter (Chapter 3) are able to extend and coil like springs, yet, with nonlinear stiffness characteristics. With this helical structure as the deformable component for compliance, a mechanism consisting of such structures, assembled in a simple truss configuration, is introduced and its design space and mechanical behaviours are explored. The result is a rich mechanical response stemming from the interaction of geometric and elastic nonlinearity, as well as the inherent nonlinearity of the morphing components.

The proposed illustrative mechanism could be used as the structural building block to design more complex assemblies for bespoke mechanical properties and kinematics, *e.g.* [213, 214]. For instance, lattice structures have already been shown to provide unique combinations of properties and behaviours [193, 213]. In this respect, by tailoring its architecture and properties, the proposed mechanism may be used as the unit cell to create 2D and 3D structures with reconfigurable behaviour, for dynamic applications, energy efficiency, to control structural deployability or isolate vibrations [193, 215].

In this chapter, the proposed compliant mechanism is introduced. Section 4.2 presents the synthesis of a compliant mechanism in a truss-like configuration consisting of nonlinear double-helical elements and its design parameters, followed by a description of the analysis methods employed for the investigation of the mechanical characteristics and behaviour of these mechanisms in §4.3.

4.2 Structural Assemblies of Double-Helices

The composite double-helical structure developed by Lachenal *et al.* [25, 26] can deform from an extended to a completely coiled configuration, and functions as a nonlinear spring. The present work further explores these elements and their nonlinearities, combining them in structural assemblies. For simplicity and the sake of illustration, to present the family of possible new mechanisms conceptually arising from the ideas put forward in this work, we focus on a simple structure resembling a *von Mises* truss [216, 217]. This structure serves as a well-known reference for the study of nonlinear, compliant mechanisms and their stability [218].

The proposed assembly of two double-helices forms a truss-like structure, as shown in Figure 4.1. The assembly is a 2-degree-of-freedom, modified *von Mises* truss with two double-helices forming the truss

members, connected by pin joints at the apex and base. Consequently, the truss members are only loaded axially. As such, their transverse and bending stiffness characteristics are not considered here. In its initial configuration, the structure has height H_0 and a base angle $\alpha_{0,i}$ with respect to the horizontal; its members have length $L_{0,i}$ corresponding to the length of their longest self-equilibrated configuration, and an axial stiffness k_i that varies upon deformation. An external load P is applied at the apex, which is free to move horizontally and vertically by v_h and v_v , respectively. Henceforth, we shall refer to v_p as to the displacement of the apex in the direction of the applied load. Figure 4.2 shows the geometry of the assembly of double-helices in a deformed configuration under an applied load at the apex.

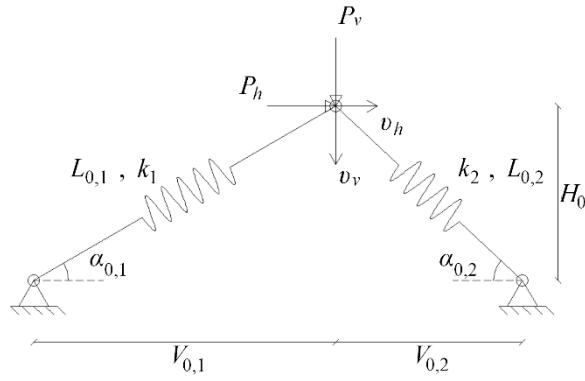


Figure 4.1: Schematic representation of the assembly of double-helices in a truss-like configuration with both supports pinned [207]. The initial configuration is determined by the equilibrium length $L_{0,i}$ of the double-helices and by the initial angle $\alpha_{0,i}$ of the truss configuration.

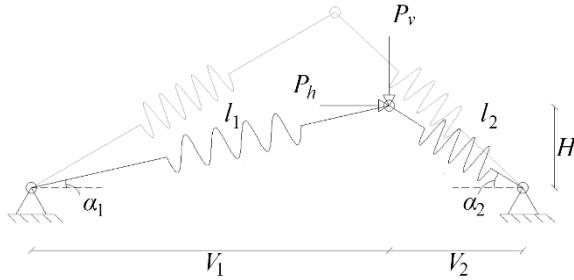


Figure 4.2: Schematic representation of a deformed configuration of the assembly of double-helices in a truss-like mechanism under an applied load at the apex.

The following geometrical relations, with notation presented in Figure 4.1 and Figure 4.2, describe the initial and deformed configurations, with the deformed configuration's characteristics expressed as a function of the horizontal and/or vertical displacement of the apex:

$$V_{0,1} = L_{0,1} \cos \alpha_{0,1}, \quad (4.1)$$

$$H_0 = L_{0,1} \sin \alpha_{0,1}, \quad (4.2)$$

$$\alpha_{0,2} = \arcsin\left(\frac{H_0}{L_{0,2}}\right), \quad (4.3)$$

$$V_{0,2} = L_{0,2} \cos \alpha_{0,2}, \quad (4.4)$$

$$l_1 = L_{0,1} \sqrt{1 - 2 \frac{v_v}{L_{0,1}} \sin \alpha_{0,1} + \left(\frac{v_v}{L_{0,1}}\right)^2 + 2 \frac{v_h}{L_{0,1}} \cos \alpha_{0,1} + \left(\frac{v_h}{L_{0,1}}\right)^2}, \quad (4.5)$$

$$\sin \alpha_1 = \frac{H_0 - v_v}{l_1} = \frac{\sin \alpha_{0,1} - v_v/L_{0,1}}{\sqrt{1 - 2 \frac{v_v}{L_{0,1}} \sin \alpha_{0,1} + \left(\frac{v_v}{L_{0,1}}\right)^2 + 2 \frac{v_h}{L_{0,1}} \cos \alpha_{0,1} + \left(\frac{v_h}{L_{0,1}}\right)^2}}, \quad (4.6)$$

$$\cos \alpha_1 = \frac{V_{0,1} + v_h}{l_1} = \frac{\cos \alpha_{0,1} + v_h/L_{0,1}}{\sqrt{1 - 2 \frac{v_v}{L_{0,1}} \sin \alpha_{0,1} + \left(\frac{v_v}{L_{0,1}}\right)^2 + 2 \frac{v_h}{L_{0,1}} \cos \alpha_{0,1} + \left(\frac{v_h}{L_{0,1}}\right)^2}}, \quad (4.7)$$

$$l_2 = L_{0,2} \sqrt{1 - 2 \frac{v_v}{L_{0,2}} \sin \alpha_{0,2} + \left(\frac{v_v}{L_{0,2}}\right)^2 - 2 \frac{v_h}{L_{0,2}} \cos \alpha_{0,2} + \left(\frac{v_h}{L_{0,2}}\right)^2}, \quad (4.8)$$

$$\sin \alpha_2 = \frac{H_0 - v_v}{l_2} = \frac{\sin \alpha_{0,2} - v_v/L_{0,2}}{\sqrt{1 - 2 \frac{v_v}{L_{0,2}} \sin \alpha_{0,2} + \left(\frac{v_v}{L_{0,2}}\right)^2 - 2 \frac{v_h}{L_{0,2}} \cos \alpha_{0,2} + \left(\frac{v_h}{L_{0,2}}\right)^2}}, \quad (4.9)$$

$$\cos \alpha_2 = \frac{V_{0,2} - v_h}{l_2} = \frac{\cos \alpha_{0,2} - v_h/L_{0,2}}{\sqrt{1 - 2 \frac{v_v}{L_{0,2}} \sin \alpha_{0,2} + \left(\frac{v_v}{L_{0,2}}\right)^2 - 2 \frac{v_h}{L_{0,2}} \cos \alpha_{0,2} + \left(\frac{v_h}{L_{0,2}}\right)^2}}. \quad (4.10)$$

The elongation ΔL_i of the truss members from the initial configuration of the assembly is:

$$\Delta L_1 = L_{0,1} - l_1 = L_{0,1} \left(1 - \sqrt{1 - 2 \frac{v_v}{L_{0,1}} \sin \alpha_{0,1} + \left(\frac{v_v}{L_{0,1}}\right)^2 + 2 \frac{v_h}{L_{0,1}} \cos \alpha_{0,1} + \left(\frac{v_h}{L_{0,1}}\right)^2} \right), \quad (4.11)$$

$$\Delta L_2 = L_{0,2} - l_2 = L_{0,2} \left(1 - \sqrt{1 - 2 \frac{v_v}{L_{0,2}} \sin \alpha_{0,2} + \left(\frac{v_v}{L_{0,2}}\right)^2 - 2 \frac{v_h}{L_{0,2}} \cos \alpha_{0,2} + \left(\frac{v_h}{L_{0,2}}\right)^2} \right). \quad (4.12)$$

4.3 Analysis of the Structural Assemblies

Two approaches are employed for the analysis of the structural assemblies. First, energy landscapes are used to represent and characterize the behaviour of the compliant mechanism over its workspace. Next, a path following method is applied to investigate the mechanism's response under specific load cases and to obtain potential load paths between stable positions.

4.3.1 Strain Energy Landscapes

Strain energy landscapes are an effective way to identify stable configurations of the structure at either global or local minima of the strain energy across the mechanism's workspace. Herder [140] and Radaelli *et al.* [219, 220] have used potential (strain) energy landscapes to design statically-balanced structures, while Kala and Kadina [221] used the potential energy to study the stability of steep *von Mises* trusses.

With the potential energy defined as the energy stored in a body when it is being deformed, the energy of a system can be described as a function of the possible positions of an endpoint [220]. The corresponding strain energy landscape can be determined by mapping the values of the strain energy corresponding to this endpoint at its range of positions [140, 220]. For a more complex system, *i.e.* a mechanism or structure consisting of multiple parts connected at an end effector, the total strain energy can be calculated from the individual components' strain energy at that point, similar to a building block approach [219]. Thus, the strain energy landscape can be derived from the sum of the strain energy of the constituents at each potential position of the selected point; this presumes that the strain energy function of the constituents is single-valued at each position of the end effector. As mentioned in [220], this technique can be applied irrespectively of the type and shape of the constituents members.

Herein, stable and unstable equilibria of the truss are identified by inspection of the strain energy landscape. For this particular configuration of the assembly of double-helices (Figure 4.1), where their free ends are connected to a single moving point (the apex), the total strain energy is uniquely determined by the position of the end effector (the apex), and is the sum of the strain energy of the constituent helical members. In this thesis, the strain energy, U_i , of each helix given by Eq. (3.2) is used to calculate the total potential energy, U_{tot} , of the truss mechanism (Eq. (4.13)) and the corresponding contour plots are produced. Stable and unstable equilibria are pinpointed, respectively, as minima and maxima of the strain energy functional.

The strain energy landscapes provide a means to qualitatively compare the structural response of the truss structures with different design parameters.

$$U_{\text{tot}} = \sum U_i. \quad (4.13)$$

Indicatively, we present here in Figure 4.3 the case of a simple *von Mises* truss consisting of two identical members pin-jointed at the apex and base supports with a vertical load at the apex. For simplicity, we have considered linear springs as the constituent elements of the truss. The corresponding contour plots of the strain energy for a single linear spring and for the assembled *von Mises* truss are shown in Figure 4.3. It is observed that the stability points are effectively captured in these plots: the shallow configuration of a *von Mises* truss is stable at the initial configuration and its reverse state (points 1 and 2 in Figure 4.3b), while it exhibits a single unstable equilibrium position when the constituent members are collinear (point M in Figure 4.3b) [222].

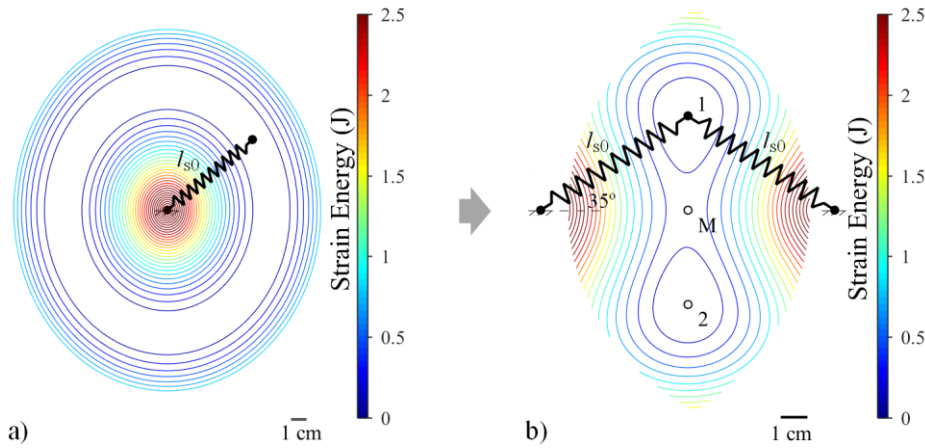


Figure 4.3: Strain energy contour plot for a) a single linear spring with finite free length l_{s0} fixed at one end, and b) the assembled *von Mises* truss of two identical such linear spring elements pin-jointed. The attainable workspace is limited by the maximum elongation of the spring members; here this was set to 1.5 times of the spring's free length. The initial truss configuration is indicated with the black spring elements. Points labelled 1 and 2, corresponding to energy minima, denote stable equilibria, while point M identifies position of unstable equilibrium.

4.3.2 Path-following Method

Figure 4.4 shows the free-body diagram for the apex, displaced at an arbitrary position. The following equilibrium equations occur:

$$P_h = -(F_1 \cos \alpha_1 - F_2 \cos \alpha_2), \quad (4.14)$$

$$P_v = -(F_1 \sin \alpha_1 + F_2 \sin \alpha_2), \quad (4.15)$$

where F_1, F_2 correspond to the helix axial forces obtained by Eq. (3.23), and α_1, α_2 are the deformed truss angles of each truss member with respect to the horizontal (Figure 4.4) with their trigonometric functions of sine and cosine defined in Eqs. (4.6), (4.7), (4.9) and (4.10).

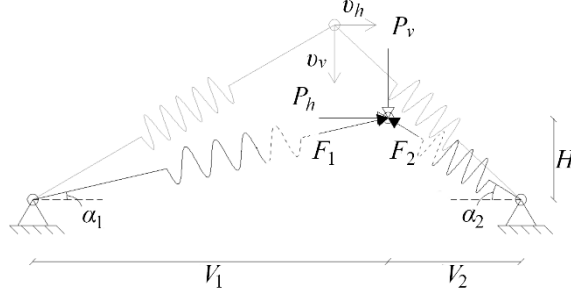


Figure 4.4: Free-body diagram of the assembly of double-helices in the truss-like configuration.

These equations are nonlinear and it is difficult to find the roots to define positions of possible equilibrium and to check their stability, let alone to determine complete equilibrium paths [223]. Thus, a numerical procedure is required to solve this system of Eqs. (4.14), (4.15).

Previous studies on the behaviour of the *von Mises* truss suggest that the structure undergoes a snap-through when loaded beyond a critical value with a vertical force at the apex [222, 224, 225]. By modifying the original system of the *von Mises* truss, introducing geometrical and/or structural imperfections, *e.g.* increasing the height to base width ratio [223] or adding springs [226, 227], further instabilities are introduced. This may lead to a variety of different post-critical structural responses, including snap-through and snap-back, primary and secondary branches both with multiple critical points [228–230]. To solve these nonlinear problems, iterative algorithms are employed.

As the double-helices are expected to introduce further nonlinearities, an iterative path-following algorithm is required to determine the load-displacement response of the structural assemblies. The arc-length method is an efficient method to solve nonlinear systems and capture behaviours like snap-through and snap-back including the areas of instability [135, 231–234]. Specifically, in this work we use the modified-Riks method developed by Crisfield [231] as presented in [235].

The system of governing equilibrium equations of the assembly is obtained by balancing the forces acting on the mechanism (both internal and external), thus, in its general form, the system of nonlinear equations we are interested to solve is written:

$$\mathbf{R}(\mathbf{v}) = 0, \quad (4.16)$$

where \mathbf{v} is the nodal displacement vector, in our case of the apex so $\mathbf{v} = [v_h \ v_v]^T$, and \mathbf{R} is the residual:

$$\mathbf{R}(\mathbf{v}) = \mathbf{P}_{\text{int}}(\mathbf{v}) - \mathbf{P}_{\text{ext}} = \mathbf{P}_{\text{int}}(\mathbf{v}) - \lambda \bar{\mathbf{P}}_{\text{ext}}, \quad (4.17)$$

where \mathbf{P}_{ext} is the external load vector, in our case $\mathbf{P}_{\text{ext}} = [P_h \ P_v]^T$, λ is a scalar load parameter and $\bar{\mathbf{P}}_{\text{ext}}$ is a constant external load vector, and \mathbf{P}_{int} is the internal load vector, here expressed as:

$$\mathbf{P}_{\text{int}}(\mathbf{v}) = \begin{bmatrix} F_1 \cos \alpha_1 - F_2 \cos \alpha_2 \\ F_1 \sin \alpha_1 + F_2 \sin \alpha_2 \end{bmatrix}. \quad (4.18)$$

Therefore, the residual vector \mathbf{R} is considered as a function of both \mathbf{v} and λ .

Hence, for the assembly of double-helices in the truss configuration of Figure 4.1, the problem becomes:

$$\begin{bmatrix} R_h \\ R_v \end{bmatrix} = \begin{bmatrix} F_1 \cos \alpha_1 - F_2 \cos \alpha_2 \\ F_1 \sin \alpha_1 + F_2 \sin \alpha_2 \end{bmatrix} - \lambda \begin{bmatrix} \bar{P}_h \\ \bar{P}_v \end{bmatrix}, \quad (4.19)$$

where R_h, R_v refer, respectively, to the horizontal and vertical components of the residual, and \bar{P}_h, \bar{P}_v are the constant horizontal and vertical external loads applied, respectively.

Based on the modified-Riks method by Crisfield [231] in [235], the solution at the r th iteration of the n th load step, given the solution $(\mathbf{v}_n^{(r-1)}, \lambda_n^{(r-1)})$ at the $(r-1)$ st iteration of the same load step, is determined as follows:

$$\mathbf{R}_n^{(r-1)} - \delta \lambda_n^{(r)} \bar{\mathbf{P}}_{\text{ext}} + \mathbf{K}_T \delta \mathbf{v}_n^{(r)} = 0, \quad (4.20)$$

where $\mathbf{R}_n^{(r-1)}$ is the unbalanced load vector at the $(r-1)$ st iteration, $\delta \lambda_n^{(r)}$ and $\delta \mathbf{v}_n^{(r)}$ are the load and displacement incremental solutions, respectively, and \mathbf{K}_T is the tangential stiffness matrix defined as:

$$\mathbf{K}_T = \frac{\partial \mathbf{R}}{\partial \mathbf{v}}, \quad (4.21)$$

calculated at the converged solution of the previous load step, \mathbf{v}_{n-1} . For the assembly of the double-helices, the tangential stiffness matrix is given by:

$$\mathbf{K}_T = \begin{bmatrix} \frac{\partial R_h}{\partial v_h} & \frac{\partial R_h}{\partial v_v} \\ \frac{\partial R_v}{\partial v_h} & \frac{\partial R_v}{\partial v_v} \end{bmatrix}, \quad (4.22)$$

where

$$\begin{aligned} \frac{\partial R_h}{\partial v_h} &= \frac{\partial(F_1 \cos \alpha_1 - F_2 \cos \alpha_2 - \lambda \bar{P}_h)}{\partial v_h} = \frac{\partial(F_1 \cos \alpha_1 - F_2 \cos \alpha_2)}{\partial v_h} \\ &= \cos \alpha_1 \frac{\partial F_1}{\partial v_h} + F_1 \frac{\partial \cos \alpha_1}{\partial v_h} - \cos \alpha_2 \frac{\partial F_2}{\partial v_h} - F_2 \frac{\partial \cos \alpha_2}{\partial v_h}, \end{aligned} \quad (4.23)$$

$$\begin{aligned} \frac{\partial R_h}{\partial v_v} &= \frac{\partial(F_1 \cos \alpha_1 - F_2 \cos \alpha_2 - \lambda \bar{P}_h)}{\partial v_v} = \frac{\partial(F_1 \cos \alpha_1 - F_2 \cos \alpha_2)}{\partial v_v} \\ &= \cos \alpha_1 \frac{\partial F_1}{\partial v_v} + F_1 \frac{\partial \cos \alpha_1}{\partial v_v} - \cos \alpha_2 \frac{\partial F_2}{\partial v_v} - F_2 \frac{\partial \cos \alpha_2}{\partial v_v}, \end{aligned} \quad (4.24)$$

$$\begin{aligned} \frac{\partial R_v}{\partial v_h} &= \frac{\partial(F_1 \sin \alpha_1 + F_2 \sin \alpha_2 - \lambda \bar{P}_v)}{\partial v_h} = \frac{\partial(F_1 \sin \alpha_1 + F_2 \sin \alpha_2)}{\partial v_h} \\ &= \sin \alpha_1 \frac{\partial F_1}{\partial v_h} + F_1 \frac{\partial \sin \alpha_1}{\partial v_h} + \sin \alpha_2 \frac{\partial F_2}{\partial v_h} + F_2 \frac{\partial \sin \alpha_2}{\partial v_h}, \end{aligned} \quad (4.25)$$

$$\begin{aligned} \frac{\partial R_v}{\partial v_v} &= \frac{\partial(F_1 \sin \alpha_1 + F_2 \sin \alpha_2 - \lambda \bar{P}_v)}{\partial v_v} = \frac{\partial(F_1 \sin \alpha_1 + F_2 \sin \alpha_2)}{\partial v_v} \\ &= \sin \alpha_1 \frac{\partial F_1}{\partial v_v} + F_1 \frac{\partial \sin \alpha_1}{\partial v_v} + \sin \alpha_2 \frac{\partial F_2}{\partial v_v} + F_2 \frac{\partial \sin \alpha_2}{\partial v_v}, \end{aligned} \quad (4.26)$$

$$\frac{\partial F_1}{\partial v_h} = \frac{\partial F_1}{\partial \Delta l_1} \frac{\partial \Delta l_1}{\partial v_h}, \quad (4.27)$$

$$\frac{\partial F_1}{\partial v_v} = \frac{\partial F_1}{\partial \Delta l_1} \frac{\partial \Delta l_1}{\partial v_v}, \quad (4.28)$$

$$\frac{\partial F_2}{\partial v_h} = \frac{\partial F_2}{\partial \Delta l_2} \frac{\partial \Delta l_2}{\partial v_h}, \quad (4.29)$$

$$\frac{\partial F_2}{\partial v_v} = \frac{\partial F_2}{\partial \Delta l_2} \frac{\partial \Delta l_2}{\partial v_v}, \quad (4.30)$$

$$\Delta l_1 = L_1 - l_1 = \Delta L_1 + L_1 - L_{0,1}, \quad (4.31)$$

$$\Delta l_2 = L_2 - l_2 = \Delta L_2 + L_2 - L_{0,2}, \quad (4.32)$$

with L_i being the length of the helix in its fully extended configuration, l_i the projected length of the helix along the axis of its underlying cylinder and ΔL_i the elongation of the truss members from the initial configuration of the assembly. It is worth mentioning that in these calculations the axial helix forces have been estimated from the helix strain energy U numerically using central finite differences.

Equation (4.20) can be rewritten as:

$$\delta \mathbf{v}_n^{(r)} = -(\mathbf{K}_T)^{-1} \mathbf{R}_n^{(r-1)} + \delta \lambda_n^{(r)} (\mathbf{K}_T)^{-1} \bar{\mathbf{P}}_{\text{ext}}, \quad (4.33)$$

$$\delta \mathbf{v}_n^{(r)} \equiv \delta \bar{\mathbf{v}}_n^{(r)} + \delta \lambda_n^{(r)} \delta \hat{\mathbf{v}}_n, \quad (4.34)$$

$$\delta \bar{\mathbf{v}}_n^{(r)} = -(\mathbf{K}_T)^{-1} \mathbf{R}_n^{(r-1)}, \quad (4.35)$$

$$\delta \hat{\mathbf{v}}_n = (\mathbf{K}_T)^{-1} \bar{\mathbf{P}}_{\text{ext}}, \quad (4.36)$$

with $\delta \hat{\mathbf{v}}_n$ calculated at the beginning of each load step.

The incremental load parameter $\delta \lambda_n^{(r)}$ is obtained from the solution of the following equation:

$$q_1 (\delta \lambda_n^{(r)})^2 - 2q_2 \delta \lambda_n^{(r)} + q_3 = 0, \quad (4.37)$$

where the coefficients q_1 , q_2 and q_3 are given by:

$$q_1 = \delta \hat{\mathbf{v}}_n^T \delta \hat{\mathbf{v}}_n, \quad (4.38)$$

$$q_2 = (\delta \bar{\mathbf{v}}_n^{(r)} + \Delta \mathbf{v}_n^{(r-1)})^T \delta \hat{\mathbf{v}}_n, \quad (4.39)$$

$$q_3 = (\delta \bar{\mathbf{v}}_n^{(r)} + \Delta \mathbf{v}_n^{(r-1)})^T (\delta \bar{\mathbf{v}}_n^{(r)} + \Delta \mathbf{v}_n^{(r-1)}) - (\Delta s_n)^2. \quad (4.40)$$

From the two solutions of this quadratic equation (Eq. (4.37)), we choose the one that gives a correction closer to the previous converged correction so that the solution evolves forward. This can be defined by the product of the $\Delta \mathbf{v}_n^{(r-1)}$ and $\Delta \mathbf{v}_n^{(r)}$, selecting the root with the positive one. In case of both roots giving a positive value for this product, $\delta \lambda_n^{(r)} = -q_3/(2q_2)$.

The initial incremental load parameter in each load step is given by [233]:

$$\delta\lambda_n^{(0)} = \left(\text{sign of } (\Delta\mathbf{v}_{n-1}^{(r)})^T \delta\hat{\mathbf{v}}_n^{(r)} \right) \Delta s_n (\delta\hat{\mathbf{v}}_n^T \delta\hat{\mathbf{v}}_n)^{-1/2}. \quad (4.41)$$

Δs is the arc-length, defined in Crisfield's method [231] as the radius of the circle with a centre at the current equilibrium point. For the first iteration of the first load step, Δs is estimated by:

$$\Delta s = \delta\lambda_1^{(0)} \sqrt{\delta\hat{\mathbf{v}}_1^T \delta\hat{\mathbf{v}}_1}, \quad (4.42)$$

where $\delta\hat{\mathbf{v}}_1$ is calculated at an assumed solution \mathbf{v}_0 and $\delta\lambda_1^{(0)}$ is an assumed load increment, both values assigned by the user at the beginning. These values would change depending of the underlying problem to be solved. Usually for \mathbf{v}_0 , a known solution of an equilibrium point would be selected—the energy landscapes were considered to be a useful guide for this—while the assignment of a certain value for $\delta\lambda_1^{(0)}$ could occur after multiple trial and error runs. For subsequent load steps the arc-length can be adjusted by:

$$\Delta s_n = \Delta s_{n-1} \frac{I_d}{I_0}, \quad (4.43)$$

where I_d is the number of desired iterations, defined by the user, and I_0 the number of actual iterations performed in the previous step until convergence was achieved. This provides control over the number of iterations taken to converge in the subsequent load step, by automatically giving small arc-lengths in areas of severe nonlinearity. In our calculations we chose not to perform this adjustment and maintain a constant arc-length, as the initial arc-length defined was adequate to track the converged solutions within a reasonable number of iterations.

$\Delta\mathbf{v}_n^{(r)}$ is the correction to the solution calculated by:

$$\Delta\mathbf{v}_n^{(r)} = \Delta\mathbf{v}_n^{(r-1)} + \delta\mathbf{v}_n^{(r)}, \quad (4.44)$$

which for the first iteration of each load step becomes:

$$\Delta\mathbf{v}_n^{(1)} = \delta\mathbf{v}_n^{(1)}. \quad (4.45)$$

Finally, the total solution of the n th load step is given by:

$$\mathbf{v}_n = \mathbf{v}_{n-1} + \Delta \mathbf{v}_n^{(r)}, \quad (4.46)$$

$$\lambda_n = \lambda_n^{(r-1)} + \delta \lambda_n^{(r)}. \quad (4.47)$$

The above procedure is repeated until convergence is achieved, $\|\mathbf{R}\| < tol$, where tol is defined by the user.

For the calculations herein $tol = 10^{-8}$ has been selected.

The modified-Riks method by Crisfield [231], employed here, as well as other common path-following methods, allow us to follow arbitrary nonlinear equilibrium paths. However, these methods by themselves are unable to directly identify stability points—bifurcation or limit points—and switch to a different equilibrium path if secondary branches exist. The consideration of stability phenomena is deemed necessary for cases where the load-displacement curve does not increase monotonically and there are multiple possible displacements corresponding to one load level and the reverse. For this purpose, further algorithms are required [236–238].

Herein, additionally to the modified-Riks method, we employ an algorithm to detect bifurcations and limit points by investigating the eigenvalues of the system's tangential stiffness matrix. A perturbation based on the respective eigenvectors is then applied to the solution at the bifurcation points for the computation of the branching paths [237, 238]. The stability of an equilibrium branch is characterised by the eigenvalues, with negative eigenvalues indicating instability.

The use of the eigenvalues of the system's tangential stiffness matrix is a general and effective mean to describe the stability of a structure, independently of the method used for its structural analysis. For example, in a simple *von Mises* truss consisting of two identical members pin-jointed at the apex and base supports with a vertical load at the apex, one zero eigenvalue exists at the limit point where the snap-through takes place, while at least one of the eigenvalues is negative along the area of instability. Figure 4.5 shows the load-displacement curve of a von Mises truss with linear springs as its constituent elements and the corresponding areas of instability. It also shows the variation of the current eigenvalues for the equilibrium path. Stable and unstable equilibria have been also marked according to the corresponding strain energy contour in Figure 4.3b.

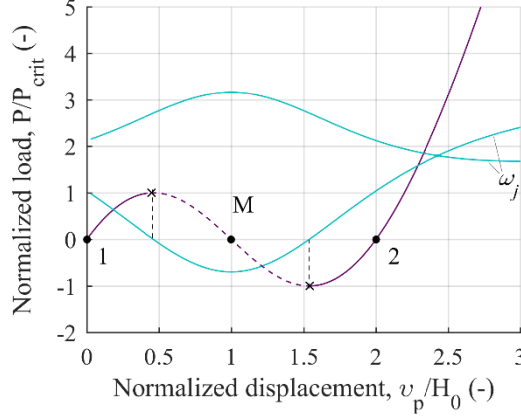


Figure 4.5: Load-displacement curve (purple) of the assembled *von Mises* truss of two identical linear spring elements under a vertical load P at the apex. Results are for initial truss angle $\alpha_{0,1} = 35^\circ$. Dashed line represents section of instability; points 1 and 2 are stable equilibrium points. Point M is an unstable equilibrium point. The load has been normalized with respect to the load value at the maximum peak (P_{crit}). The displacement has been normalized with respect to the initial height of the truss structure. The variation of the corresponding eigenvalues ω_j of the tangential stiffness matrix of the system are included (cyan lines). The eigenvalues have been normalised to a value 10^3 to fit the scale of the load-displacement curve.

Specifically, a stability point—either a bifurcation or a limit point—is defined as a point of singularity of the tangent stiffness matrix, thus it can be identified by the criteria below [237]:

$$\mathbf{K}_T(\mathbf{v})\boldsymbol{\phi} = 0, \quad (4.48)$$

$$\det \mathbf{K}_T(\mathbf{v}) = 0. \quad (4.49)$$

where $\boldsymbol{\phi}$ refers to an eigenvector of a specific eigenvalue problem. Hence, for each converged solution on the primary equilibrium path, obtained initially by employing the Riks-method to solve Eq. (4.19), the tangential stiffness matrix \mathbf{K}_T is calculated and the corresponding eigenvalues ω_j are evaluated. Next, the eigenvalues are inspected for a change in their sign between consecutive converged solution points to define positions of potential bifurcation or limit points. It is worth mentioning that the points on the primary equilibrium path, found as solutions using the arc-length method, are not the actual stability point but within sufficient accuracy close to the exact stability point. The exact calculation of the stability point is out of the scope of the present analysis. Applying the perturbation for the computation of branching paths at the converged solution of the primary equilibrium path that is close enough, within incremental calculation, to the actual stability point is deemed appropriate to obtain the secondary branch in case of a bifurcation point.

To distinguish between a bifurcation or a limit point the following criteria have been defined [238, 239]:

$$\text{limit points:} \quad \boldsymbol{\phi}^T \bar{\mathbf{P}}_{\text{ext}} \neq 0, \quad (4.50)$$

$$\text{bifurcation points:} \quad \boldsymbol{\phi}^T \bar{\mathbf{P}}_{\text{ext}} = 0. \quad (4.51)$$

Thus, at the detected point near the stability point the eigenvector is calculated and the above criteria are checked to define whether a bifurcation or a limit point exists at this stability position. Since we have not determined the exact stability point, in our calculations we used the following formula to define a bifurcation point:

$$\frac{\boldsymbol{\phi}^T \bar{\mathbf{P}}_{\text{ext}}}{\|\boldsymbol{\phi}\| \|\bar{\mathbf{P}}_{\text{ext}}\|} < 10^{-3}. \quad (4.52)$$

In case of a bifurcation point, the computation of the secondary branches is required. Similar to the computation of the primary equilibrium path, the modified-Riks method is employed, but in this case a perturbation to the solution at the bifurcation point is performed. A new initial displacement, $\mathbf{v}_{0,bf}$, is calculated as the starting displacement vector for the branching path given by [237]:

$$\mathbf{v}_{0,bf} = \mathbf{v} + \sum \xi_j \frac{\boldsymbol{\phi}_j}{\|\boldsymbol{\phi}_j\|}, \quad (4.53)$$

where \mathbf{v} is the displacement vector of the converged solution near the bifurcation point, $\boldsymbol{\phi}_j$ is the eigenvector corresponding to the ω_j eigenvalue that changes sign and ξ_j is a scaling factor, critical for successful computation of the branching path, defined by [237]:

$$\xi_j = \pm \frac{\|\mathbf{v}\|}{\tau_j}, \quad (4.54)$$

where τ_j is an imperfection factor with a value in the order of 100; in our calculations a value of 50 was selected.

The detection of limit and bifurcation points is performed in the secondary branch as well. The above procedure is followed for the computation of any other secondary branch that might exist. Combined, the path-following method and the stability analysis enable the load-displacement response of the structural assemblies to be characterised fully.

4.4 Summary

Current compliant mechanisms rely on flexible members, whose design is often limited by strength considerations. In this research, a new compliant mechanism is introduced that consists of nonlinear morphing elements. These elements: (i) are composed of composite strips in a double-helix architecture; (ii) exhibit nonlinear stiffness characteristics; and (iii) are able to undergo large axial deformations whilst maintaining structural integrity. These helical structures exhibit highly tailorable nonlinear stiffness characteristics, thus enabling the ensuing mechanism to feature a variety of structural responses.

To study the new mechanism—explore the potential behaviours and stability features it may develop—we focus on a simple structure, an assembly of two double-helices in a truss-like configuration. Two analysis methods are employed to explore the properties of the structural assemblies. Initially, we use strain energy landscapes to study the stability characteristics of the compliant mechanism qualitatively across its workspace and to identify equilibrium configurations. To investigate the response to specific loads, a path following method with bifurcation tracking is employed to capture the full nonlinear response. Combined, these methods provide full insight into the mechanical properties of the compliant mechanisms.

The following chapters present the rich design space of such mechanism; by tailoring the inherent properties of its elements—and subsequently its architecture—access to a wide design space is opened up. The next chapter presents results from the numerical analysis of the assemblies of double-helices with the simplest possible geometry, focusing on investigating the mechanical behaviour and stability characteristics, and their sensitivity to various design parameters. The reconfigurability of the mechanism is explored in a subsequent chapter, followed by the manufacture of a prototype and the experimental validation of the analytical results. Conclusions and final remarks are drawn in the last chapter of the thesis.

Chapter 5

Multistability in

Mechanisms of Nonlinear Morphing Elements

5.1 Introduction

Multistable mechanisms, *i.e.* mechanisms that are self-equilibrated in two or more stable configurations, continue to interest the research community, because they promise benefits for diverse applications, across a number of fields and length scales. For instance, multistability is investigated for use in devices such as switches, valves, precision positioning systems, reconfigurable structures, rehabilitation robotic devices, energy harvesters, and weight compensators [91, 94, 119, 122, 123, 136, 240, 241]. An attractive feature of multistable mechanisms is that they do not require any power input to hold stable configurations, which might help save energy during operation. This characteristic can be exploited, for instance, in deployable structures that, once actuated (sometimes even passively), can self-lock in either a stowed or extended configuration [118, 242]. In addition, since in general two stable equilibria will necessarily be separated by an unstable one, multistable devices present regions of negative stiffness over their workspace that can be used for statically balanced mechanisms [243, 244] or weight compensators [143].

It is noted that much of the literature on devices with multiple equilibria refers to bistable ones. Articles on multistability are scarcer. Oh and Kota [135] proposed the synthesis of a multistable compliant devices by combining bistable ones. In a similar manner, Han *et al.* [132] developed a quadristable mechanism, whilst tristability was achieved by Chen *et al.* [137] by employing orthogonally oriented compliant structures. The majority of these works are based on compliance, *i.e.* the ability to transfer motion, force or energy is achieved through elastic deformations of the underlying components, rather than the mobility

of joints [210]. While this may offer the possibility to achieve multistability [111], the complexities involved often result in high stresses being developed, thus posing strength limits to the potential design configurations and, consequently, the capabilities obtainable [137].

This work proposes the use of double-helix morphing composite structures as the flexible elements in a compliant truss-like mechanism (see Chapter 4). These helical DNA-like structures, as presented in Chapter 3, beyond variable geometry, exhibit tailorable nonlinear stiffness characteristics. This tailorability enables the ensuing mechanism to be tuned to feature a variety of responses, and a wide range of potential behaviours to be developed. The proposed truss-like mechanism may be used either on its own or as the unit cell in lattice structures [193, 214].

In this chapter, we reveal the richness of this new mechanism's design space and the range of attainable mechanical behaviours. In the following sections, the nonlinear behaviour and multistability of the mechanism is explored using both an energy approach and a path-following method to trace equilibrium branches in the force-displacement space. The results presented herein focus on the analysis of the simplest geometry for the mechanism, an assembly of two double-helices in a truss-like structure pin-jointed at the apex and base supports (see Chapter 4), for a variety of potential combinations of double-helices with lay-ups of the form $[\beta_2/0/\beta_2]$ and $[\beta_2/0/-\beta_2]$, where β is the fibre angle measured with respect to the local x -axis of the composite strip—as mentioned previously in Chapter 3—and on helix deformation limited to $\theta \in [0^\circ, 90^\circ]$. Section 5.2 introduces the results from initial analyses of these structural assemblies, while §5.3 and §5.4 focus on the effect of various design parameters on desirable features, such as multistability and constant stiffness. Finally, the chapter concludes with a summary and final remarks in §5.5.

5.2 Initial results

In the initial analyses the double-helices have the following geometric parameters: $L = 95$ mm, $R = 15$ mm, $R_i = 30$ mm, $W = 5$ mm. Two geometric configurations are considered: a shallow ($\alpha_{0,1} = 35^\circ$) and a steep ($\alpha_{0,1} = 70^\circ$) truss. Three composite lay-ups are chosen from Chapter 3 to represent the three types of curve in Figure 3.2 and explore the ensuing responses of the structural assemblies: a unidirectional (UD) lay-up ($[0_5]$); a symmetric lay-up ($[45_2/0/45_2]$); and an antisymmetric lay-up ($[45_2/0/-45_2]$). These truss and double-helix configurations are selected to illustrate representative obtainable properties.

The strain energy landscapes for different truss configurations are presented in Figure 5.1. The workspace is bounded by the maximum extension of the helices, and the initial configuration of the mechanism is indicated. The strain energy contours allow the mechanism's stability characteristics to be explored; valleys correspond to stable equilibria, whereas peaks and saddle points denote unstable equilibria. Stable and unstable internal equilibria are labelled with Arabic numbers (1–5) and Roman letters (A–H, J, K and M), respectively. Latin numerals (I–IV) are used for stable boundary equilibrium positions, where at least one of the two helices is fully extended.

For shallow trusses, the UD and symmetric lay-ups feature bistability, with stable states at the initial position and at a vertical displacement $2H_0$ (points 1 and 2 in Figure 5.1a, b). For double-helices of antisymmetric lay-up, the assembly displays only unstable interior equilibria (points G, H and M in Figure 5.1c), but four stable boundary equilibria can be observed (points I–IV in Figure 5.1c). For steep trusses, the structure can exhibit: i) bistability, for a $[0_5]$ lay-up (points 1 and 2 in Figure 5.1d); ii) quadrastability, when double-helices of a symmetric lay-up are combined (points 1–4 in Figure 5.1e); iii) pentastability, in case of an antisymmetric lay-up, with a single interior stable point, when the double-helices are collinear with a zero horizontal displacement (point 5 in Figure 5.1f), and an additional four boundary equilibria (points I–IV in Figure 5.1f).

The force-displacement response for a *vertical* load at the apex is presented in Figure 5.2. The corresponding positions of the apex are superimposed on the strain energy plots in Figure 5.1 (red markers). For most cases, a bifurcation of the equilibrium path is present, resulting in both horizontal and vertical displacements of the apex. The bifurcated branch intersects the primary path at two bifurcation points. Interestingly, the bifurcated branches enable the mechanism to deform to all the possible internal equilibrium configurations identified on the strain energy landscape just by applying a vertical load at the apex. For shallow trusses with a $[0_5]$ lay-up or an antisymmetric one, where no bifurcation of the equilibrium path occurs, all internal equilibrium configurations are also traversed. Areas of both stability and instability—marked with a solid and dashed line, respectively, in Figure 5.2—are present in most cases, with the stable regions found only on the primary equilibrium path with the exemption of steep trusses with a symmetric lay-up, where areas of stability are present in the bifurcated branch as well, and of shallow trusses with an antisymmetric lay-up, where the entire path is unstable.

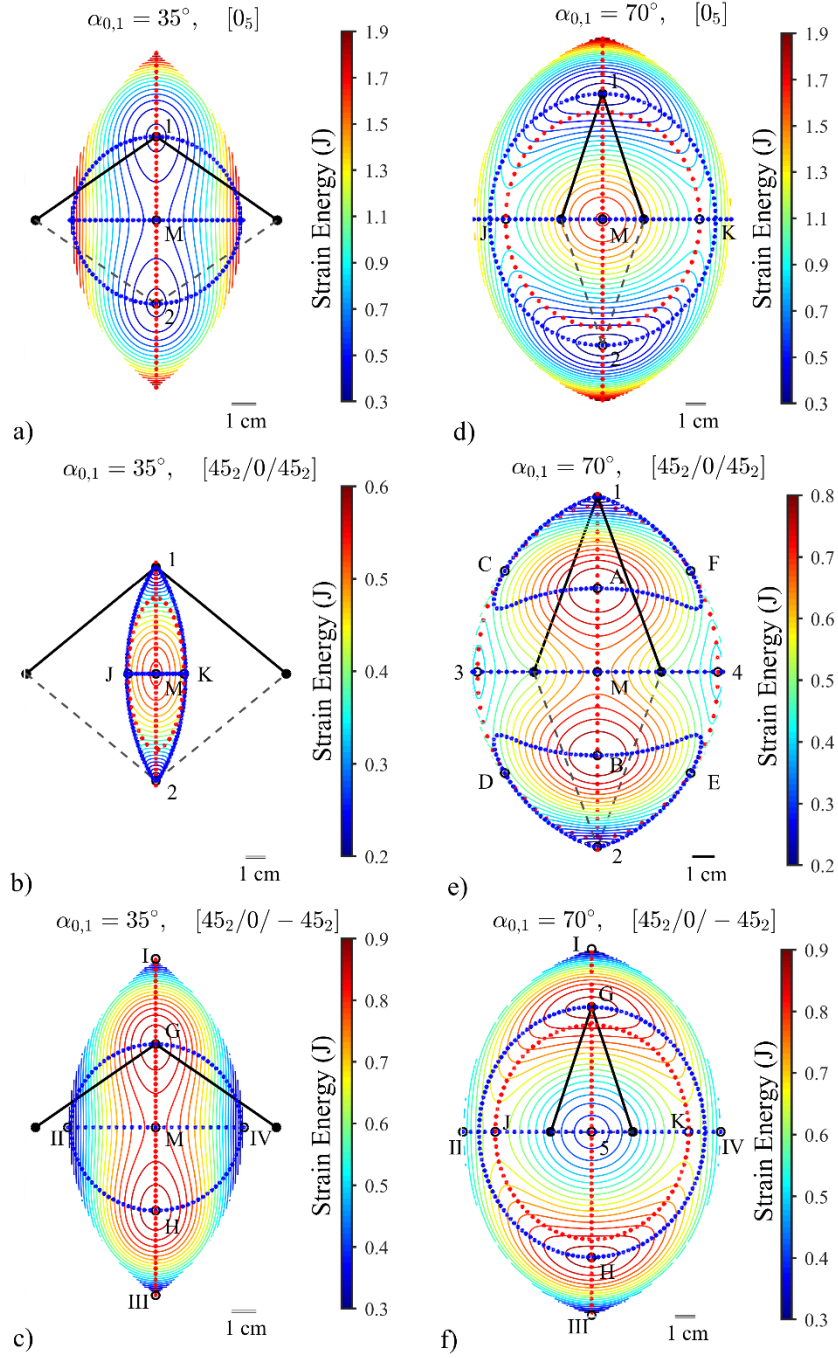


Figure 5.1: Strain energy landscapes for a compliant mechanism of identical double-helices assembled in a truss-like configuration. Results are for initial truss angles $\alpha_{0,1} = 35^\circ$ and $\alpha_{0,1} = 70^\circ$, with composite strips of $[0_5]$, $[45_2/0/45_2]$ and $[45_2/0/-45_2]$ lay-ups. The initial truss configurations are indicated with black lines. Points labelled 1–5 denote stable equilibria, while points A–H, J, K and M identify positions of unstable equilibrium; points I–IV denote stable boundary equilibria. The positions of the truss apex under an applied vertical load ($P_h = 0$) and/or horizontal load ($P_v = 0$) are superimposed on the landscapes: red points indicate the equilibrium paths of the apex under the application of a vertical load; blue points indicate the equilibrium paths of the apex under the application of a horizontal load.

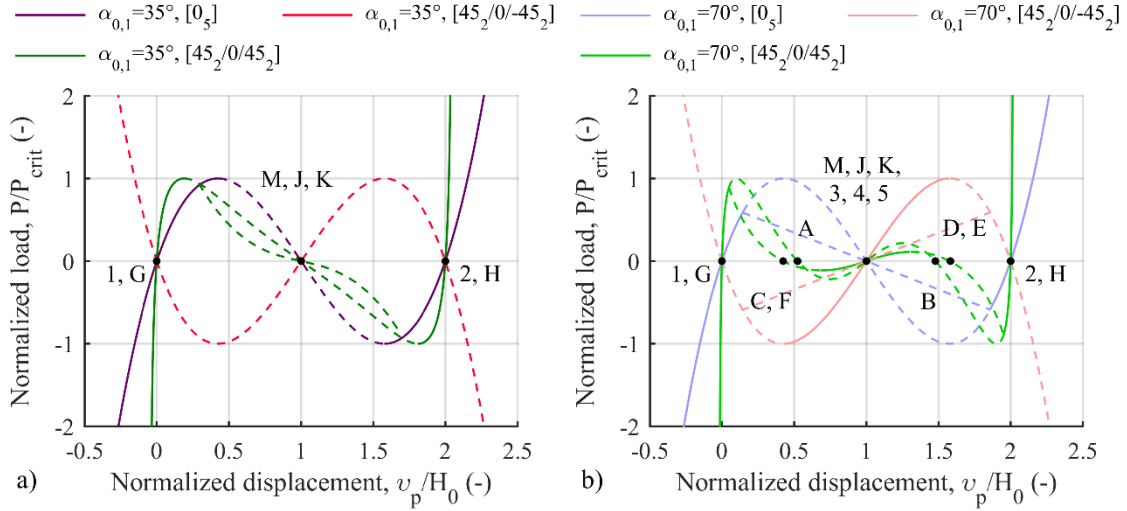


Figure 5.2: Load-displacement curves of the assembled structure of identical double-helices under the application of a vertical load at the apex. Results are for different initial truss angle a) $\alpha_{0,1} = 35^\circ$ and b) $\alpha_{0,1} = 70^\circ$ and of double-helices with varying lay-ups. Dashed line represents sections of instability; points 1–5 are stable equilibrium points. Points A–H, J, K and M are unstable equilibrium points. The load has been normalized with respect to the load value at the maximum peak (P_{crit}) in each case. The displacement has been normalized with respect to the initial height of the truss structure.

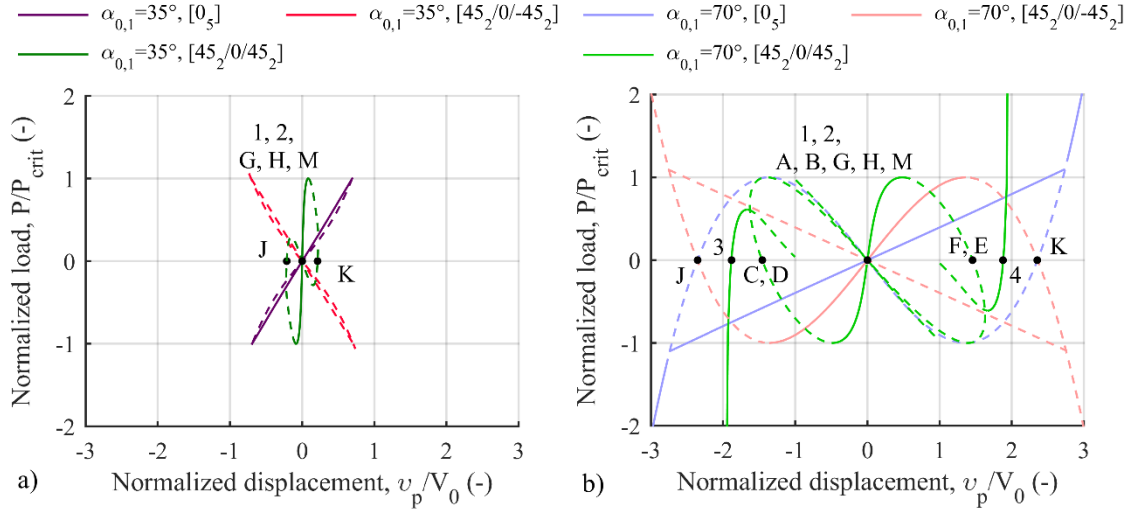


Figure 5.3: Load-displacement curves of the assembled structure of identical double-helices under the application of a horizontal load at the apex. Results are for different initial truss angle a) $\alpha_{0,1} = 35^\circ$ and b) $\alpha_{0,1} = 70^\circ$ and of double-helices with varying lay-ups. Dashed line represents sections of instability. Points 1 and 2 are stable equilibrium points; points A–H, J, K and M are unstable equilibrium points. The load has been normalized with respect to the load value at the maximum peak (P_{crit}) in each case. The displacement has been normalized with respect to the initial width of the truss structure.

The force-displacement response of the structure under a *horizontal* load at the apex is depicted in Figure 5.3. The corresponding positions of the apex are superimposed on the strain energy plots in Figure 5.1 (blue markers). A bifurcation of the equilibrium path—with the bifurcated branches intersecting the main path in two bifurcation points—occurs for all cases, except for double-helices of a symmetric lay-up assembled in a steep truss, where three disconnected equilibrium paths are observed, two of which are

mirrored with respect to the horizontal traversing the supports (Figure 5.1e). Similar to the case of a vertical applied load, all the internal equilibrium configurations can be traversed via the application of a horizontal load. Notable is the region of linear load-displacement response along the main equilibrium path despite the use of nonlinear elements. This response is accompanied by a circular displacement path of the apex, as illustrated in the respective strain energy plots (Figure 5.1a, c, d, f). This region is a stable area of constant stiffness for the $[0_5]$ lay-up, but is unstable for double-helices of antisymmetric lay-up (Figure 5.3). The use of double-helices with symmetric lay-up invokes non-linear behaviour, particularly for a steep truss. Additionally, for this configuration, a jump in the load-displacement curve of one of the disconnected equilibrium paths is noticed (Figure 5.3b). The mechanics of this jump is explained in §5.4. In all cases closed-loop deformation paths of the apex can be observed.

Figure 5.4 shows the response of the assembly of double-helices with symmetric lay-up in a shallow truss configuration under a *combined* loading ($P_h = P_v$). A more complex behaviour is observed with the load-displacement curve forming an “S-shaped” curve. Although no bifurcation of the equilibrium path occurs, the mechanism nonetheless traverses all five equilibrium points. The structure also maintains its bistability as the energy minimum exists independent of the loading conditions.

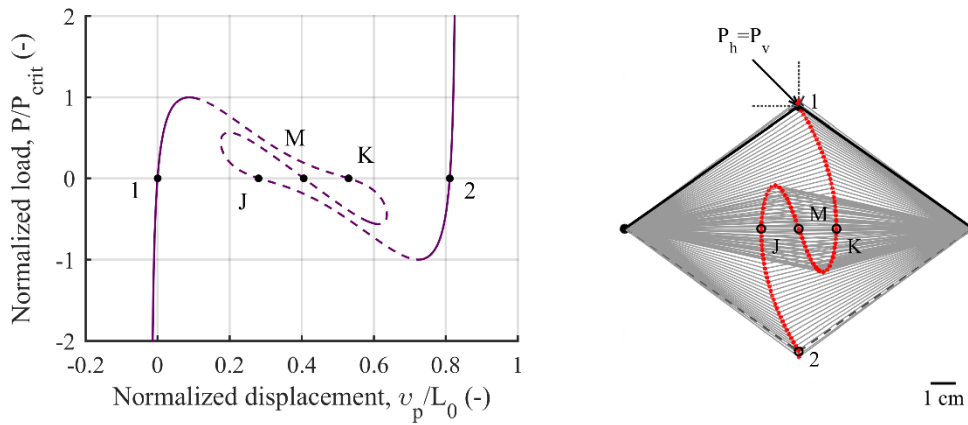


Figure 5.4: Load-displacement curve (left) and deformation (right) of the assembled structure (with initial angle $\alpha_{0,1} = 35^\circ$) of two identical double-helices (with a $[45_2/0/45_2]$ lay-up) under combined loading ($P_h = P_v$) at the apex. Points 1 and 2 are stable equilibrium points; points J, K and M are unstable equilibrium positions. Dashed lines (left) represents areas of instability. The load has been normalized with respect to the load value at the maximum peak (P_{crit}). The displacement, v_p , of the apex in the direction of the applied load has been normalized with respect to the initial length L_0 . Black lines (right) indicate the initial truss configuration.

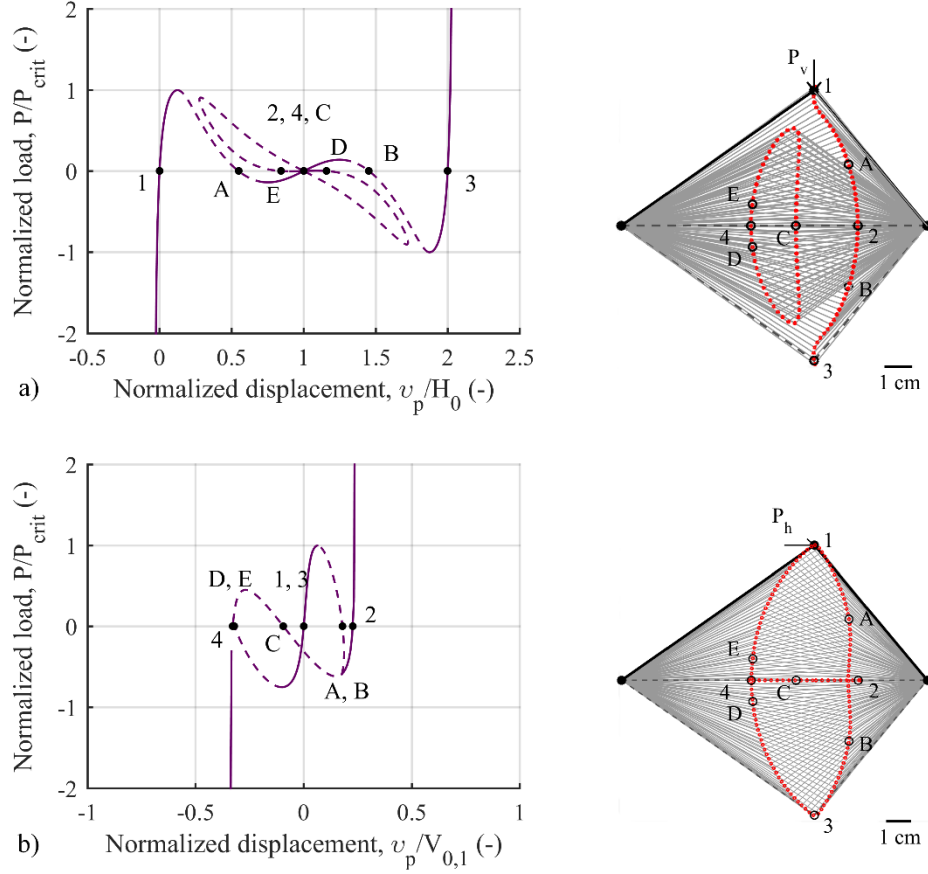


Figure 5.5: Load-displacement curves (left) and deformation (right) of the assembled structure of double-helices of different length under the application of a) a vertical load and b) a horizontal load at the apex. Points 1–4 are stable equilibrium points; points A–E are unstable equilibrium points. The truss has initial angle $\alpha_{0,1} = 35^\circ$ and double-helices of $[45_2/0/45_2]$ lay-up, and lengths $L_1 = 95$ mm, $L_2 = 71$ mm. Dashed lines (left) represent areas of instability. The load has been normalized with respect to the load value at the maximum peak (P_{crit}) for each case. The displacement has been normalized with respect to the initial height or width of the truss structure, respectively for vertical or horizontal loading. Black lines (right) indicate the initial truss configuration.

Combining double-helices of different properties further expands the ability to tailor the force-displacement response of the structural assemblies. Illustratively, Figure 5.5 shows the response of double-helices of identical symmetric lay-up $[45_2/0/45_2]$ but with different lengths L , combined in a shallow truss. It is noted that any symmetry present in previous cases in the assembled structure is lost. The assembled structure experiences quadristability. Under a vertical load, two disconnected equilibrium paths are identified, one of which forms a closed loop, while a horizontal load results in a bifurcation of the equilibrium path. In both loading conditions all possible equilibria, both stable and unstable, are accessed. Further investigation of asymmetric trusses is beyond the scope of this work, and we focus on cases of using truss members of the same properties.

In the following sections the sensitivity of salient behaviours identified above—specifically, multistability and constant stiffness—to changes in design parameters of the structure is further explored.

5.3 Multistability

Two double-helices with a symmetric $[45_2/0/45_2]$ lay-up assembled into a steep truss with initial angle $\alpha_{0,1} = 70^\circ$ exhibit four stable internal equilibrium configurations (see Figure 5.1e). Multistable mechanisms have found use in applications such as switches, positioners, and reconfigurable structures [137]. The characteristics of multistability of the trusses are therefore of particular interest. Here, we explore the effect of linear springs, initial truss geometry, and lay-up of the composite strips, on the reference configuration. For comparison purposes, the values in the load-displacement graphs (Figure 5.6–Figure 5.10) have been normalized with respect to a critical load P_{crit} —the maximum peak of the load-displacement curve—and the initial height H_0 of the truss structure.

Replacing the double-helices with linear springs results in the loss of quadristability; although a bifurcation of the equilibrium path is still present under an applied vertical load, no region of stability is identified on the bifurcated branch (see Figure 5.6). While points 3 and 4 (Figure 5.6a) are stable equilibrium positions for the case of double-helices, for linear springs these positions labelled as J and K become unstable. Points 3, 4, J and K refer to positions where the truss elements are collinear (Figure 5.6b). For both cases, linear springs and double-helices, the axial forces have opposite sign, thus the system self-equilibrates. For the case with linear springs (points J and K in Figure 5.6b) the equilibrium is unstable. Conversely, for the case with double-helices (points 3 and 4 in Figure 5.6b), the two helices also have axial stiffnesses of opposite sign: the helix displaying negative axial force has negative stiffness. As a consequence, the helices tend to deform in opposite directions, which ultimately stabilises the equilibrium state (Figure 5.6c).

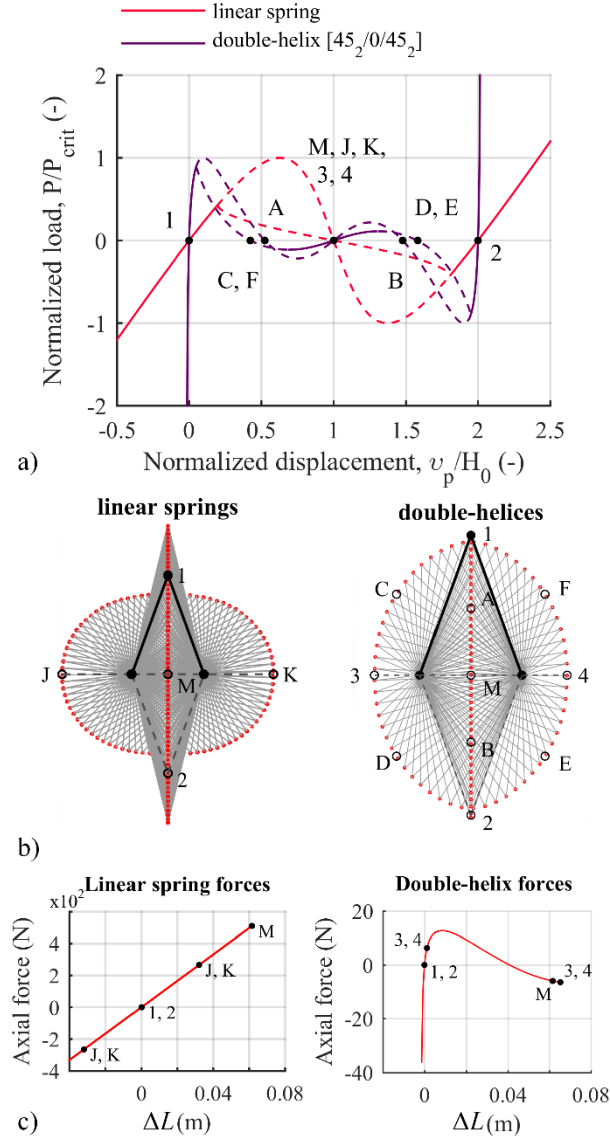


Figure 5.6: a) Load-displacement curve of a mechanism consisting of double-helices compared to one of linear springs under a vertical load at the apex. Initial truss angle $\alpha_{0,1} = 70^\circ$ is used for both assemblies. Points 1–4 are stable equilibrium points; points A–F, J, K and M are unstable equilibrium points. Dashed lines represent areas of instability. b) Deformation of the assembled structures. The initial truss configurations are indicated with black lines. c) Axial force with respect to displacement of a linear spring (left) and of a double-helix (right).

The initial geometry of the assembled structure significantly affects its multistable behaviour. A shallow truss ($\alpha_{0,1} = 35^\circ$) is bistable, while for higher initial truss angles, $\alpha_{0,1} = 45^\circ$ or $\alpha_{0,1} = 70^\circ$, the mechanism exhibits quadristability under the application of a vertical load (Figure 5.7a). This behaviour is closely linked to the characteristics of the double-helices themselves. In shallow trusses the two stable positions are the initial one and the one at a vertical displacement equal to $2H_0$ (points 1 and 2, respectively, in Figure 5.7a), while points M, J and K are unstable equilibria. Positions J and K on the bifurcation path, which occur when the double-helices are horizontal, are noticed in steeper trusses too, but as stable equilibria (points 3 and 4 in Figure 5.7a). In these stable equilibrium positions—where the helices are collinear—the

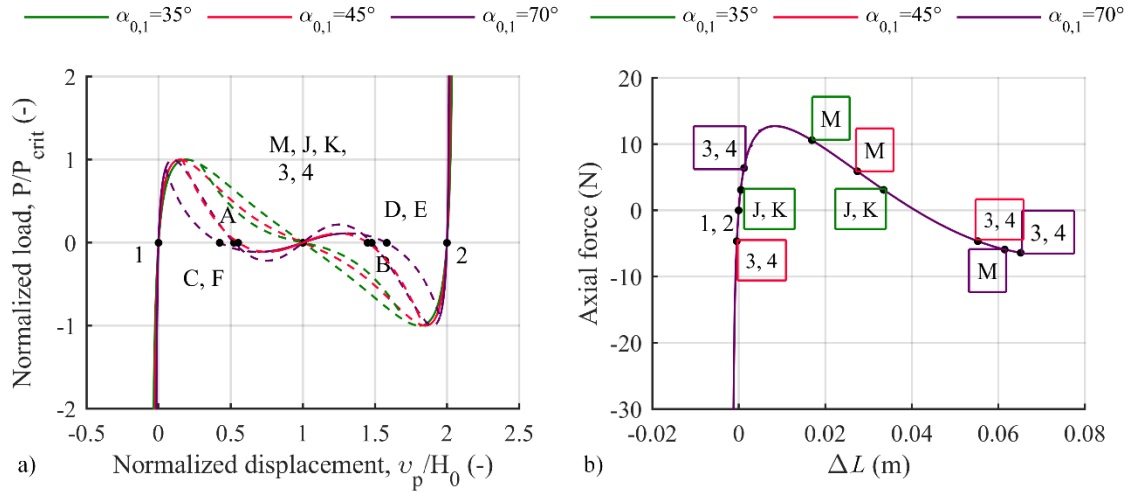


Figure 5.7: a) Load-displacement curves of a mechanism with different initial truss angles $\alpha_{0,1}$ consisting of double-helices of $[45_2/0/45_2]$ lay-up, under the application of a vertical load at the apex. Points 1–4 are stable equilibrium points. Points A–F, J, K and M are unstable equilibrium points. Dashed lines represent areas of instability. b) Axial forces of double-helices at selected equilibrium points for the different initial truss angles.

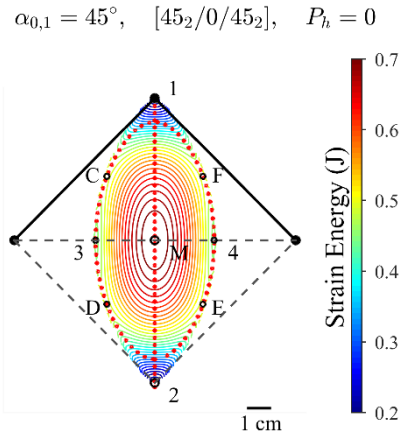


Figure 5.8: Strain energy landscape for a compliant mechanism of identical double-helices with a $[45_2/0/45_2]$ composite strip lay-up, $L = 95$ mm, $R = 15$ mm, $R_i = 30$ mm, $W = 5$ mm, assembled in a truss-like configuration with initial base angle $\alpha_{0,1} = 45^\circ$. Points 1–4 denote stable equilibrium positions, while points C–F and M indicate positions of unstable equilibrium. The positions of the truss apex under an applied vertical load ($P_h = 0$) are superimposed as red points. The initial truss configuration is indicated with black lines.

double-helices have axial stiffness of opposite sign and the axial forces have either opposite sign (points 3 and 4 for $\alpha_{0,1} = 70^\circ$ in Figure 5.7b) or are both negative (points 3 and 4 for $\alpha_{0,1} = 45^\circ$ in Figure 5.7b). In either case, due to the different truss geometry—for $\alpha_{0,1} = 45^\circ$ points 3 and 4 are located between the two base supports (Figure 5.8), while for $\alpha_{0,1} = 70^\circ$ outside—the helices pull against each other, thus stabilising the equilibrium.

The lay-up of the composite strips of the double-helix also significantly affects the load-displacement behaviour of the double-helix (see Figure 3.3). The reference structure consists of double-helices with a

symmetric $[45_2/0/45_2]$ lay-up. In Figure 5.9, we explore the behaviour of the mechanism with initial angle $\alpha_{0,1} = 70^\circ$ for varying ply angle β in symmetric lay-ups of the form $[\beta_2/0/\beta_2]$. For a ply angle $\beta = 0^\circ$ the assembly is bistable, with both the initial configuration and the configuration at vertical displacement $2H_0$ being stable (points 1 and 2 in Figure 5.9). Note that none of the equilibrium points encountered on the secondary path correspond to a stable state in this case. For a ply angle $\beta = 90^\circ$ the double-helix load-displacement curve is similar to that of an antisymmetric lay-up (Figure 3.3), thus the characteristics of the mechanism with $\beta = 90^\circ$ or an antisymmetric lay-up are the same, with the structure exhibiting one internal stable equilibrium when the double-helices are collinear (point 5 in the main path, Figure 5.9), plus four boundary equilibria (Figure 5.1f). For all other ply angles, $0^\circ < \beta < 90^\circ$, the assembly is quadristable. For the relevant deformation of the truss structures the reader is referred to Figure 5.1d-f.

Variations in the geometrical features of the double-helix result in minor differences in its load-displacement behaviour (see Chapter 3) and thus have a limited effect on the multistability of the mechanism. Relevant graphs of load-displacement for a steep truss ($\alpha_{0,1} = 70^\circ$) for different geometrical characteristics of the double-helices under an applied vertical load at the apex are gathered in Figure 5.10.

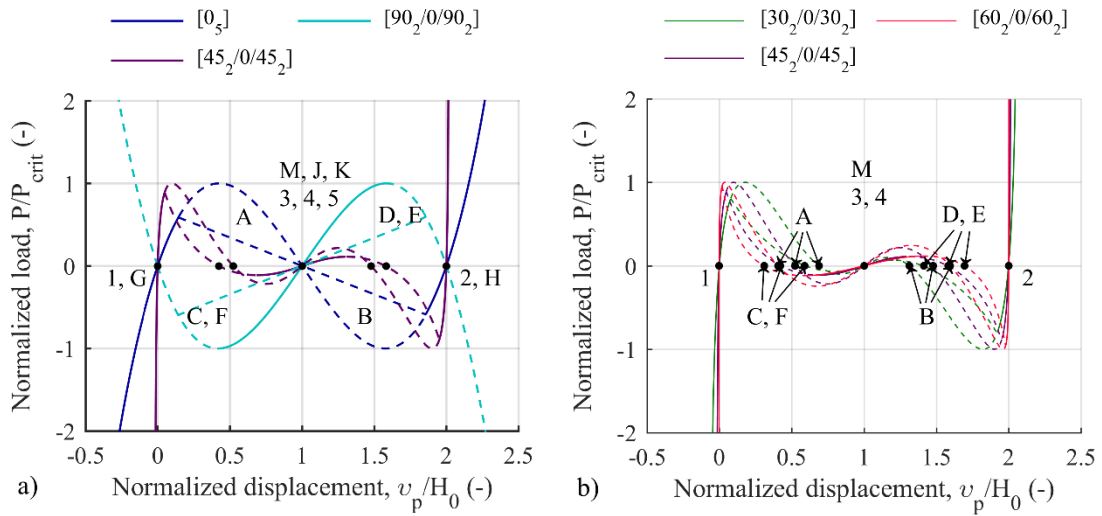


Figure 5.9: Load-displacement curves of the assembled structure into a steep truss with initial angle $\alpha_{0,1} = 70^\circ$ of identical double-helices for different symmetric lay-ups of the form $[\beta_2/0/\beta_2]$ for a) $\beta = 0^\circ, 45^\circ, 90^\circ$ and b) $\beta = 30^\circ, 45^\circ, 60^\circ$ under the application of a vertical load at the apex. Points 1, 2 and 5 are stable equilibrium points on the main paths; points 3 and 4 on the bifurcation paths. Points A, M, B, G and H are unstable equilibrium points on the main paths; points C–F, J and K on the bifurcation paths. Dashed lines represent areas of instability.

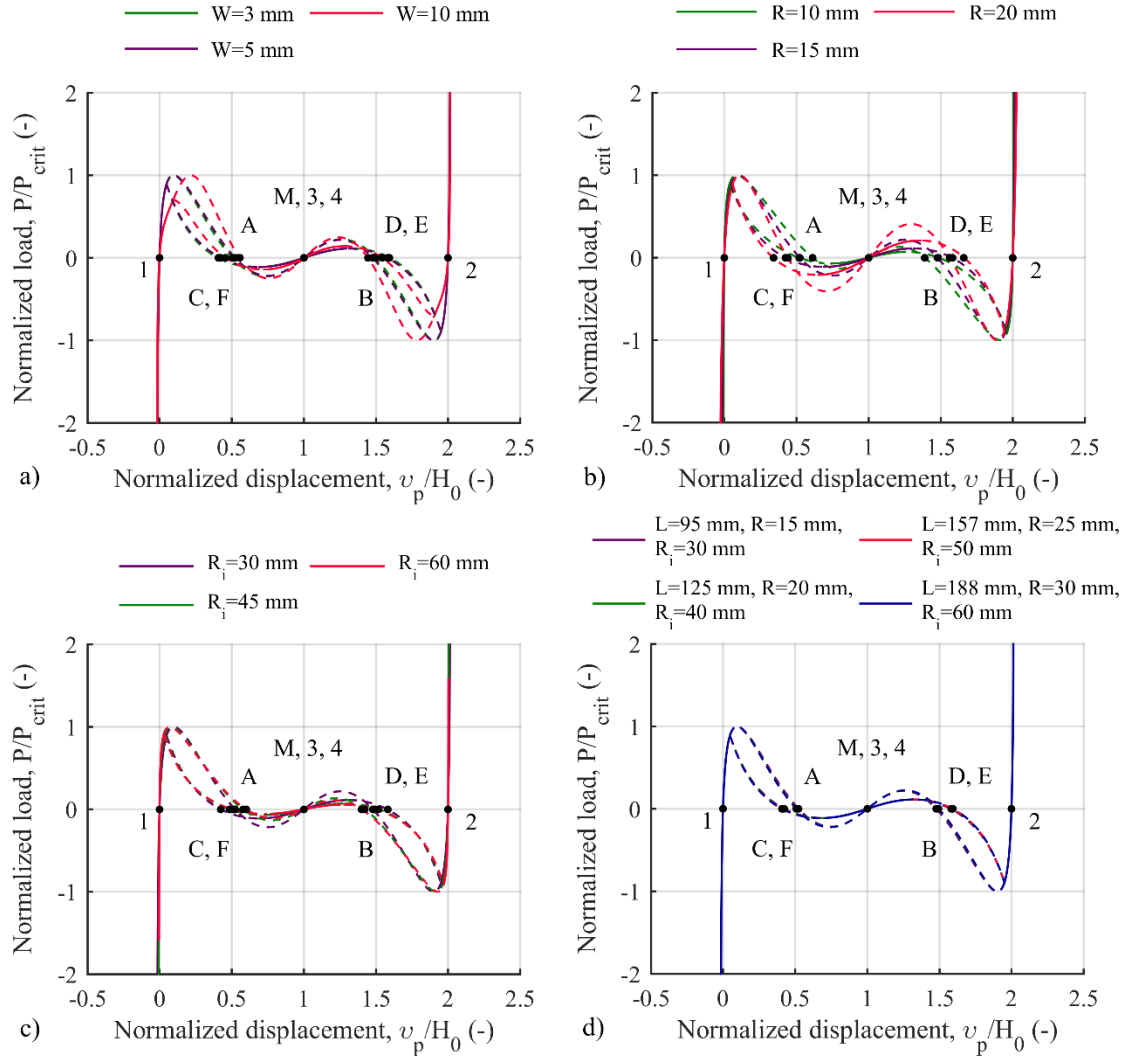


Figure 5.10: Load-displacement curves of the assembled structure into a steep truss with initial angle $\alpha_{0,1} = 70^\circ$ of identical double-helices under the application of a vertical load at the apex, with different a) widths W , lay-up $[45_2/0/45_2]$, $L = 95$ mm, $R = 15$ mm, $R_i = 30$ mm; b) radius R , lay-up $[45_2/0/45_2]$, $L = 95$ mm, $R_i = 30$ mm, $W = 5$ mm; c) initial curvatures of the strips R_i , lay-up $[45_2/0/45_2]$, $L = 95$ mm, $R = 15$ mm, $W = 5$ mm; d) dimensions L , R and R_i , keeping a constant ratio $R_i/R = 2$ and $L \approx 2\pi R$, lay-up $[45_2/0/45_2]$, $W = 5$ mm. Points 1 and 2 are stable equilibrium points on the main path; points 3 and 4 on the bifurcation path. Points A, M and B are unstable equilibrium points on the main path; points C–F on the bifurcation path. Dashed lines represent areas of instability.

Variations in the width W of the strips, the radius R and the initial curvature of the strips R_i result in different load-displacement curves for the double-helices (Figure 3.6). The mechanism remains quadristable, although the stiffness of the structure will vary. Changing the length L of the double-helix has no effect on the double-helix response (Figure 3.6a), so an investigation of this parameter on the response of the assembled structure is omitted. The ability of scaling up the structure is also explored. For this purpose, double-helices of different dimensions L , R , R_i but with constant ratios $R_i/R = 2$ and $L/R \approx 2\pi$ have been used. The load-displacement behaviour of such double-helices has been included in Figure 3.6e and the response of an assembled structure of these helices is presented in Figure 5.10d. The load-displacement

curves of the different mechanisms are identical, meaning that the structure can be scaled up or down while maintaining the quadristable behaviour.

5.4 Constant stiffness

Another interesting behaviour from the initial results is the development of a mechanism of constant stiffness while undergoing large deformations under a horizontal load at the apex. The mechanism with double-helices of $[0_5]$ lay-up ($L = 95$ mm, $R = 15$ mm, $R_i = 30$ mm and $W = 5$ mm) at an initial truss angle $\alpha_{0,1} = 70^\circ$, exhibits a stable main equilibrium path with constant stiffness, and is used as the reference mechanism for this feature. To investigate the reasons producing constant stiffness, Figure 5.11 presents a comparison to the case of a truss with linear springs instead of double-helices. In both cases bifurcation of the main equilibrium path is present. However, our focus here is on the behaviour of the main equilibrium path. The mechanism consisting of linear springs does not exhibit constant stiffness and its deformation follows an ellipsoidal path under the application of a horizontal load at the apex, while the reference mech-

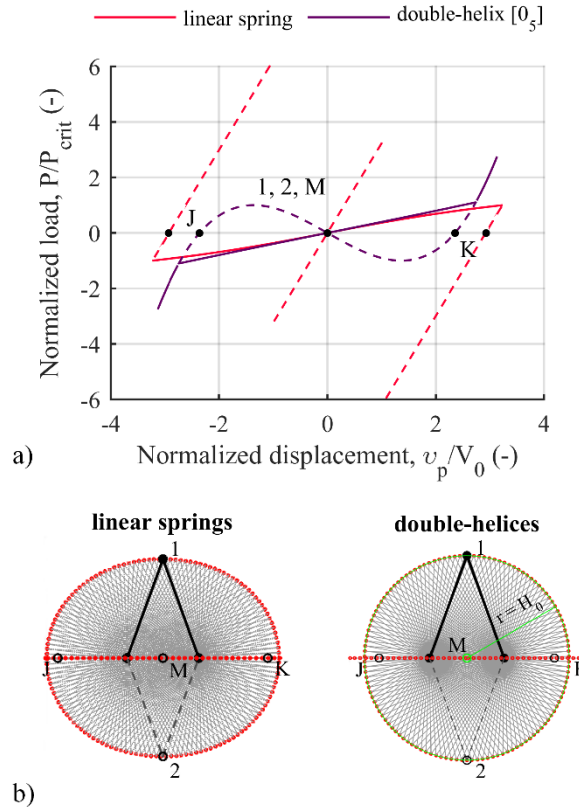


Figure 5.11: a) Load-displacement curve of a mechanism consisting of double-helices compared to one of linear springs under a horizontal load at the apex. Initial truss angle $\alpha_{0,1} = 70^\circ$ is used for both assemblies. Dashed lines represent areas of instability. b) Deformation of the assembled structures of linear springs (left) and of double-helices (right). The initial truss configurations are indicated with black lines. Points 1 and 2 are stable equilibrium positions; points J, K and M are unstable equilibrium positions.

anism of double-helices presents a linear load-displacement response (Figure 5.11a)—verified by the expression of the best fit curve ($y = 0.4001x$, $SE = 0.003$)—and a circular deformation path. The circular path has radius $r = H_0$ and is centred at the midpoint between the supports (Figure 5.11b).

Trusses of different initial geometry $\alpha_{0,1}$ all exhibit a linear load-displacement response corresponding to the main equilibrium path, while the bifurcated branch is nonlinear (Figure 5.12). A shallow truss presents a higher stiffness to a horizontal load at the apex. In all cases the main deformation path of the apex is circular (centred at the midpoint between the supports with radius equal to H_0), with a horizontal bifurcation path across the diameter when the apex is level with the supports (blue markers in Figure 5.1a, d).

Changes in the lay-up of the strips of the double-helix have a more significant impact on the behaviour of the compliant mechanism (Figure 5.13). Specifically, for $\beta = 0^\circ$ the mechanism exhibits a linear load-displacement response of the main equilibrium path and bifurcates to a path with a nonlinear response. The main path with constant stiffness is stable, compared to the bifurcated branch which is generally unstable. The mechanism exhibits a similar behaviour for a $[90_2/0/90_2]$ lay-up, but in this case the path with constant stiffness characteristics is unstable. For all other ply angles $0^\circ < \beta < 90^\circ$, a nonlinear load-displacement response is observed, and no bifurcation of the equilibrium path occurs. Instead, three independent equilibrium paths are identified—two mirrored closed-loop paths with identical load-displacement curves, and a horizontal path along the horizontal diameter, *i.e.* when the apex is level to the supports. Indicatively, the reader can refer to Figure 5.1e, which depicts the deformation of the mechanism with double-helices of a $[45_2/0/45_2]$ lay-up (blue markers). This horizontal equilibrium branch presents a jump in the corresponding load-displacement curve at the positions where the apex traverses the supports ($v_h = \pm V_0$). At these positions, the fully coiled helix turns around the support and switches direction, uncoiling out and away from the hinge point. In this scenario the helix reaction force also switches direction, which explains the sudden jump in the equilibrium manifold. It is noted that the double-helix in its fully coiled configuration is assumed to have zero length, thus the rotation of the helix around the support does not suggest a change in the horizontal displacement.

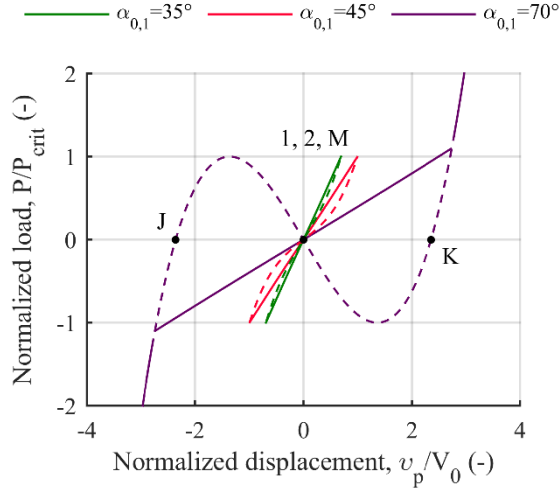


Figure 5.12: Load-displacement curves of a mechanism of different initial truss angles $\alpha_{0,1}$ consisting of double-helices of $[0_5]$ lay-up, under the application of a horizontal load at the apex. Points 1 and 2 are stable equilibrium points; points J, K and M are unstable equilibrium points. Dashed lines represent areas of instability.

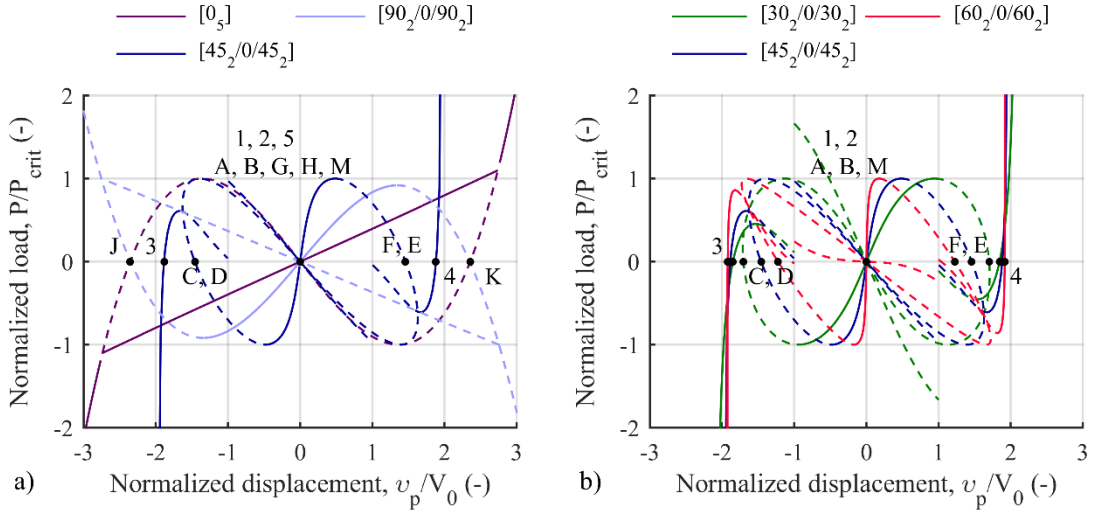


Figure 5.13: Load-displacement curves of the assembled structure into a steep truss with initial angle $\alpha_{0,1} = 70^\circ$ of identical double-helices for different symmetric lay-ups of the form $[\beta_2/0/\beta_2]$ for a) $\beta = 0^\circ, 45^\circ, 90^\circ$ and b) $\beta = 30^\circ, 45^\circ, 60^\circ$ under the application of a horizontal load at the apex. Points 1–5 are stable equilibrium points; points A, C, F–H, J, K and M are unstable equilibrium positions. Dashed lines represent areas of instability.

Less significant is the influence of the double-helix geometry on the behaviour of the assembled structure. The impact of varying the double-helix geometry on its response to a horizontal load applied at the apex is explored in Figure 5.14. Mechanisms of different dimensions L, R, R_i but with constant ratios $R_i/R = 2$ and $L/R \approx 2\pi$ present no influence in the response with the load-displacement curves matching each other, giving the ability of scaling the mechanism to the required dimensions for an application (Figure 5.14d). Varying the radius R or the initial curvature of the strips of the double-helices consisting the mechanism affect the mechanism's workspace. Although the load-displacement curves coincide for most of the

workspace, for small values of the radius R and/or higher values of the R_i there are limitations to the maximum horizontal displacement of the mechanism thus in these cases the load-displacement curve does not have a bifurcated branch, instead it consists of two independent load paths (Figure 5.14b, c). Changes in the width W of the strips of the double-helices has no significant influence on the response of the mechanism with the load-displacement curves being identical with a slight deviation being observed in the case of wider strips towards the maximum horizontal displacement (Figure 5.14a).

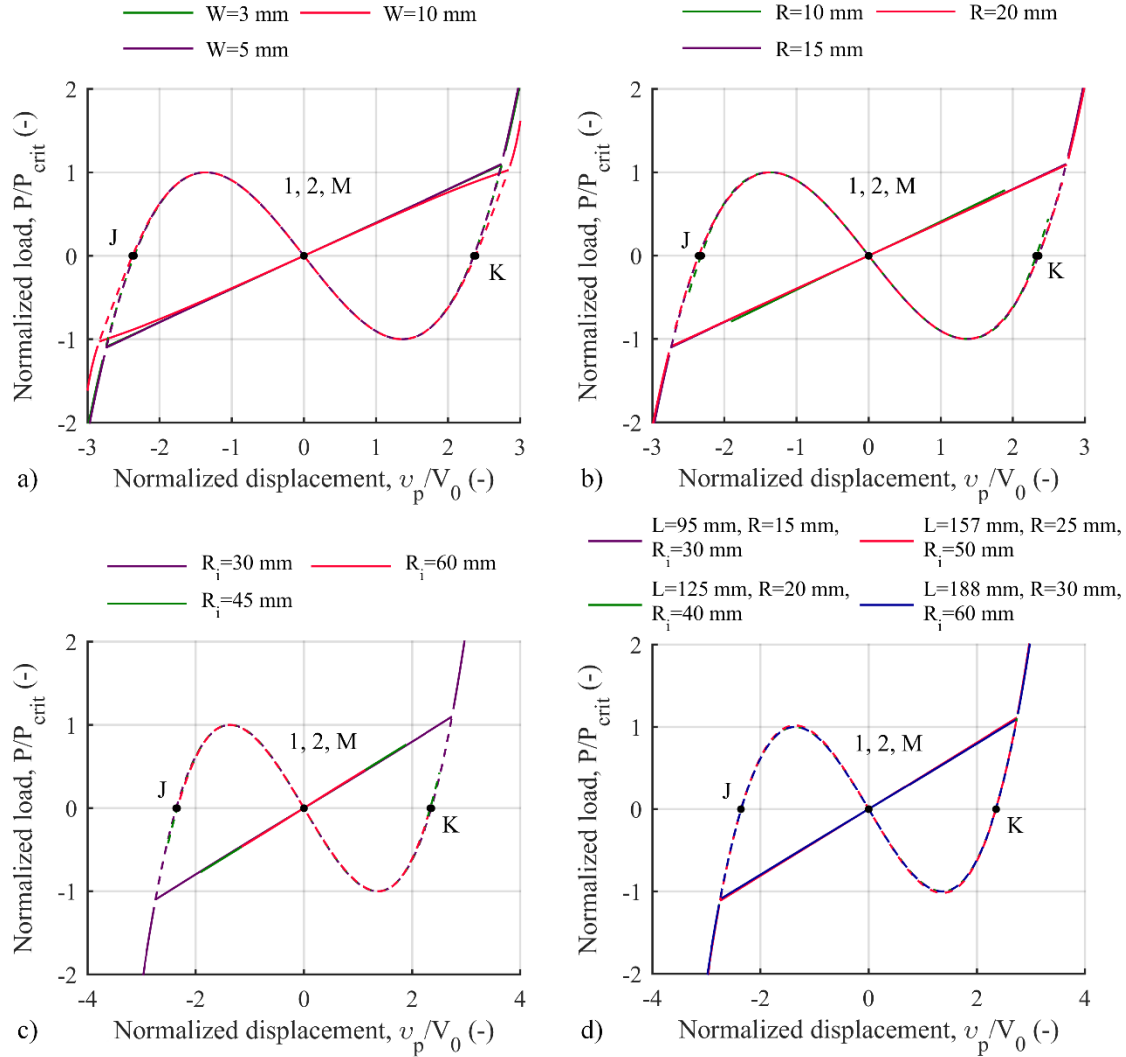


Figure 5.14: Load-displacement curves of the assembled structure into a steep truss with initial angle $\alpha_{0,1} = 70^\circ$ of identical double-helices under the application of a horizontal load at the apex with different d) widths W , lay-up $[0_5]$, $L = 95$ mm, $R = 15$ mm, $R_i = 30$ mm; b) radius R , lay-up $[0_5]$, $L = 95$ mm, $R_i = 30$ mm, $W = 5$ mm; c) initial curvatures of the strips R_i , lay-up $[0_5]$, $L = 95$ mm, $R = 15$ mm, $W = 5$ mm; d) dimensions L , R and R_i , keeping a constant ratio $R_i/R = 2$ and $L \approx 2\pi R$, lay-up $[0_5]$, $W = 5$ mm. Points 1 and 2 are stable equilibrium points; points J, K and M are unstable equilibrium points. Dashed lines represent areas of instability.

5.5 Summary

A new compliant mechanism consisting of morphing elements with tailorable nonlinear stiffness has been introduced in Chapter 4. In the current chapter, aiming to illustrate the rich design space of this new mechanism, we explore the ensuing nonlinear behaviour and multistability of the system—an assembly of two double-helices connected with pinned joints forming a truss-like structure. The proposed mechanism could be used either on its own or as a building block in a larger lattice structure. Its behaviour can be tailored by tuning global geometric parameters and/or the characteristics of the double-helices themselves.

The response of the mechanisms is analysed globally by inspecting its potential (strain) energy landscape; peaks and valleys corresponding to unstable and stable equilibria, respectively. The mechanism's multistability characteristics are investigated parametrically by varying the lay-up of the composite strips composing the double-helices, the geometrical features of the double-helices and the initial truss geometry. Quadristable behaviour is obtained for steep trusses and symmetric composite lay-ups of the form $[\beta_2/0/\beta_2]$, with $0^\circ < \beta < 90^\circ$. For $\beta = 0^\circ$ and $\beta = 90^\circ$, the mechanism becomes bistable and pentastable, respectively. Similarly, the mechanism transitions from being quadristable to being bistable for decreasing initial truss angles. Responses in load-displacement space are investigated by path-following equilibrium branches. Interestingly, via application of a vertical load, a path is found that connects all internal equilibria of the trusses: the equilibrium path bifurcates, with the bifurcated branch intersecting the main path in two points. Under the application of a horizontal load at the apex, the mechanism demonstrates a stable region of constant stiffness for $\beta = 0^\circ$, regardless of the initial truss angle, with the deformation path forming a circle. Again, bifurcations of the equilibrium path lead to connecting all internal equilibria. The type of structural behaviour is found to depend primarily on the lay-up of the strips of the double-helices and the initial geometry of the structural assembly. The geometrical characteristics of the double-helices have limited effect on the behaviour of the mechanism, thus making the concept scalable.

In this chapter we focused on the numerical analysis of the structural assemblies of double-helices with the simplest possible geometry and with helices limited to pitches θ in the range $[0^\circ, 90^\circ]$. A variety of behaviours were demonstrated that could be exploited to expand the design space of current compliant mechanisms. In the next chapter, this work is extended and the reconfigurability of the mechanism is explored taking advantage of the ability of the helical elements to deform to configurations with $\theta \in [0^\circ, -90^\circ]$, which leads to the development of different responses. Following up, Chapter 7 deals with

the manufacture and experimental testing of prototypes of the proposed mechanism and any challenges in this procedure, to conclude in the last chapter with some final remarks and future thoughts on this research.

Chapter 6

Reconfigurability in Mechanisms of Nonlinear Morphing Elements

6.1 Introduction

Over the past decades, the interest of researchers in reconfigurable mechanisms has increased [155]. Traditional mechanisms are disadvantageous in terms of flexibility and the ability to adapt to dynamic environments or changing operating requirements [154]. The capability of a mechanism to change its configuration, and to operate with different modes that can be exploited to serve multiple purposes, is what triggered the scientific interest in reconfigurable mechanisms [153]. Reconfigurability is attractive for numerous applications, such as antennas [156, 157], deployable structures [195, 245], robotics [163–165], adaptive building architecture [168], or even in carton packaging manipulation [153], where there is a need for change in structural configuration and behaviour for adaptation to different operating requirements.

As reconfiguration entails change in form, topology and configuration of the mechanism, various ways to achieve reconfigurability have been investigated [155]. Most of the approaches developed focus on achieving reconfigurability through changes of the joint motion range [175], limiting to a mechanism's mobility or degrees of freedom [170, 176], alterations in the geometry [158], changing orientation and number of links [172, 173] or a combination of the above [173]. Controlling the mobility and connectivity of revolute joints has been a common means to attain reconfiguration [158, 163, 170, 174, 177, 245]. Alternative ways to attain reconfiguration are based on the use of functional materials, such as shape memory alloys [189], architected materials [193], and/or the principles of origami [189, 193, 197, 198].

The compliant mechanism proposed in this work is able to change its behaviour and operate in different modes, whilst maintaining its connectivity and mobility. Reconfigurability in this mechanism is achieved through the exploitation of the inherently nonlinear elastic characteristics of the constitutive elements, not the joint characteristics. The mechanism, as presented in Chapter 4, consists of morphing composite structures of double-helix architecture assembled in a truss-like configuration. The helical elements' ability to change their twist direction combined with the diverse nonlinear stiffness characteristics enable the mechanism to be reconfigured, and a variety of potential behaviours to be developed.

The current chapter presents this novel, reconfigurable mechanism and the diverse mechanical responses induced from the different achievable configurations. In the following sections, the ensuing reconfigurability and stability characteristics of the mechanism are explored using both an energy approach and a path-following method to trace the mechanism's response in force-displacement space. The influence on the mechanism's behaviour of the double-helices' design parameters, and of the initial geometry of the truss itself, is also explored. First, in section 6.2, we investigate steep trusses by analysing the strain energy landscapes corresponding to all possible combinations of the helical deformation modes. We then study the trusses' response upon application of various load cases—a vertical, a horizontal or a combined load—at the end effector. Next, these results are compared to those for trusses with double-helices of different lay-ups (§6.3), as well as to those for shallower trusses (§6.4). Conclusions are drawn in the last section (§6.5).

6.2 Reconfigurability

The helical structure, used as the main component of this new mechanism, can deform from a straight to a completely coiled configuration defined by the helix angle $\theta \in [-90^\circ, 90^\circ]$ (see Chapter 3). Crucially, in the straight configuration ($\theta = 0^\circ$), the structure can be nudged into one of two connected, but distinct, deformation modes: one with $\theta \in [0^\circ, 90^\circ]$ or one with $\theta \in [0^\circ, -90^\circ]$ (Figure 6.1). The helical structure exhibits tailorable stiffness characteristics and strain energy profiles that can be customized by tuning various design parameters, such as the lay-up of the strips, pre-stress and geometry of the strips [25].

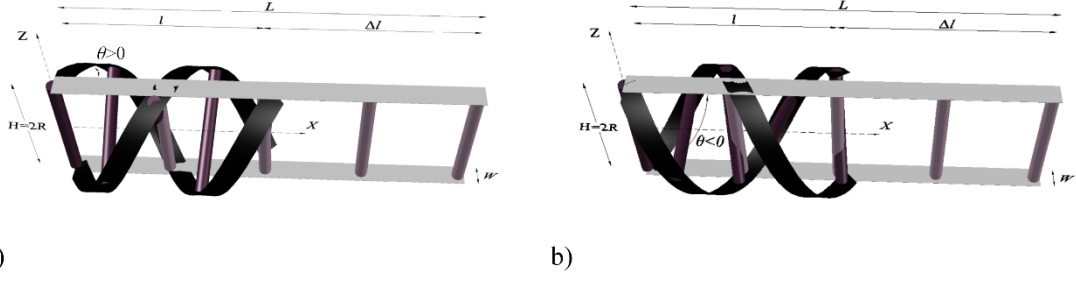


Figure 6.1: Straight (light grey) and twisted (dark) configurations of the double-helix composite structure with (a) $\theta \in [0^\circ, 90^\circ]$ and (b) $\theta \in [0^\circ, -90^\circ]$.

As presented in Chapter 3, the force-displacement response and thus the stiffness properties of double-helices with symmetric angle-ply lay-ups differ for pitch angles θ in $[0^\circ, 90^\circ]$ or $[0^\circ, -90^\circ]$ (Figure 3.2–Figure 3.3). This allows the mechanism to be reconfigured to exhibit different responses. The mechanism can be reconfigured by forcing it onto a state where one or both helices are fully extended and then nudging either one or both to switch twisting mode. Unlike common approaches, no change in the connectivity and/or pin joints of the mechanism is required; the reconfigurability is introduced solely by the nonlinear elastic components and their ability to switch twist direction once in their fully extended configuration. Thus, it is highlighted that the reconfiguration can take place only along the boundary of the workspace, where at least one helix is fully extended. There are two configurations that both helices are fully extended and thus they can be reconfigured at the same time. It is also noted that the reconfiguration positions do not necessarily correspond to equilibrium configurations.

Four different mechanism modes can be obtained combinatorically from the two helical modes. More specifically, the mechanism can be reconfigured into the following modes:

- **Mode I:** both helices twist with helix angle $\theta \in [0^\circ, 90^\circ]$;
- **Mode II:** both helices twist with helix angle $\theta \in [0^\circ, -90^\circ]$;
- **Mode III:** one helix deforms with $\theta \in [0^\circ, 90^\circ]$, and the second with $\theta \in [0^\circ, -90^\circ]$, and its reverse.

In the following, we consider a truss consisting of two identical helices, which can be reconfigured individually by changing their twist orientation. Since the difference in mechanical response in $\theta \in [0^\circ, 90^\circ]$ and $\theta \in [0^\circ, -90^\circ]$ provides the basis for the reconfigurability of the helix, only symmetric lay-ups of the form $[\beta_2/0/\beta_2]$, where $\beta \in [0^\circ, 90^\circ]$, are considered herein. The reconfigurability of the mechanism is explored by studying the behaviour and stability characteristics of the truss-like assembly.

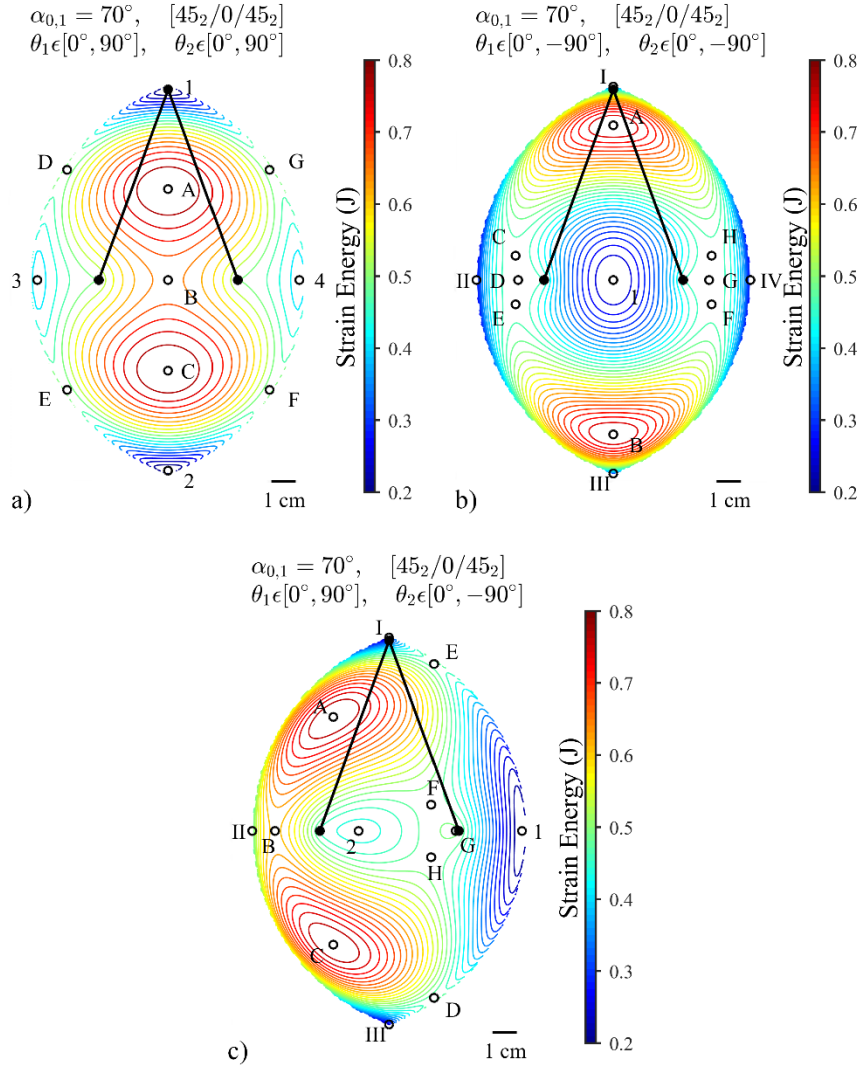


Figure 6.2: Strain energy landscapes for a compliant mechanism of double-helices of a $[45_2/0/45_2]$ composite strip lay-up, $L = 95$ mm, $R = 15$ mm, $R_i = 30$ mm, $W = 5$ mm assembled in a truss-like configuration with an initial angle $\alpha_{0,1} = 70^\circ$ for different reconfiguration modes. a) Mode I: $\theta_i \in [0^\circ, 90^\circ]$; b) Mode II: $\theta_i \in [0^\circ, -90^\circ]$; c) Mode III: $\theta_1 \in [0^\circ, 90^\circ]$, $\theta_2 \in [0^\circ, -90^\circ]$. Points labelled 1–4 denote stable equilibria, while points A–H identify positions of unstable equilibrium. Points I–IV denote stable boundary equilibria. Black lines represent the double-helices at the initial truss configuration.

Figure 6.2 depicts the strain energy landscapes for the three potential reconfiguration modes for mechanisms consisting of double-helices of a $[45_2/0/45_2]$ lay-up, arranged in a steep configuration with $\alpha_{0,1} = 70^\circ$. As evidenced by the different strain energy landscapes, once the mechanism is reconfigured to one of the different reconfiguration modes, its stability characteristics alter immediately. Stable and unstable equilibria, *i.e.* minima and maxima of the energy landscape, are marked, respectively, with Arabic numerals and Roman letters. Additionally, stable equilibria may be found on the boundary of the landscape; these points are marked with Roman numerals. For Mode I (Figure 6.2a), the mechanism displays quadristability; specifically, four interior minima. Conversely, Mode II (Figure 6.2b) features only one

interior minimum, plus four boundary equilibria. Mode III (Figure 6.2c) features ten extrema, of which two are minima, and three additional stable boundary equilibria.

The force-displacement response of the mechanism upon application of a *vertical* load at the end effector is presented in Figure 6.4. The corresponding solution manifolds are superimposed on the strain energy plots in Figure 6.3 (red markers). For Mode I, a bifurcation is present, intersecting at two points with the main path, resulting in sideways apex displacements. Two of the four stable states are located on the main (vertical) path, *i.e.* the initial configuration and the fully inverted state at a vertical displacement of $2H_0$

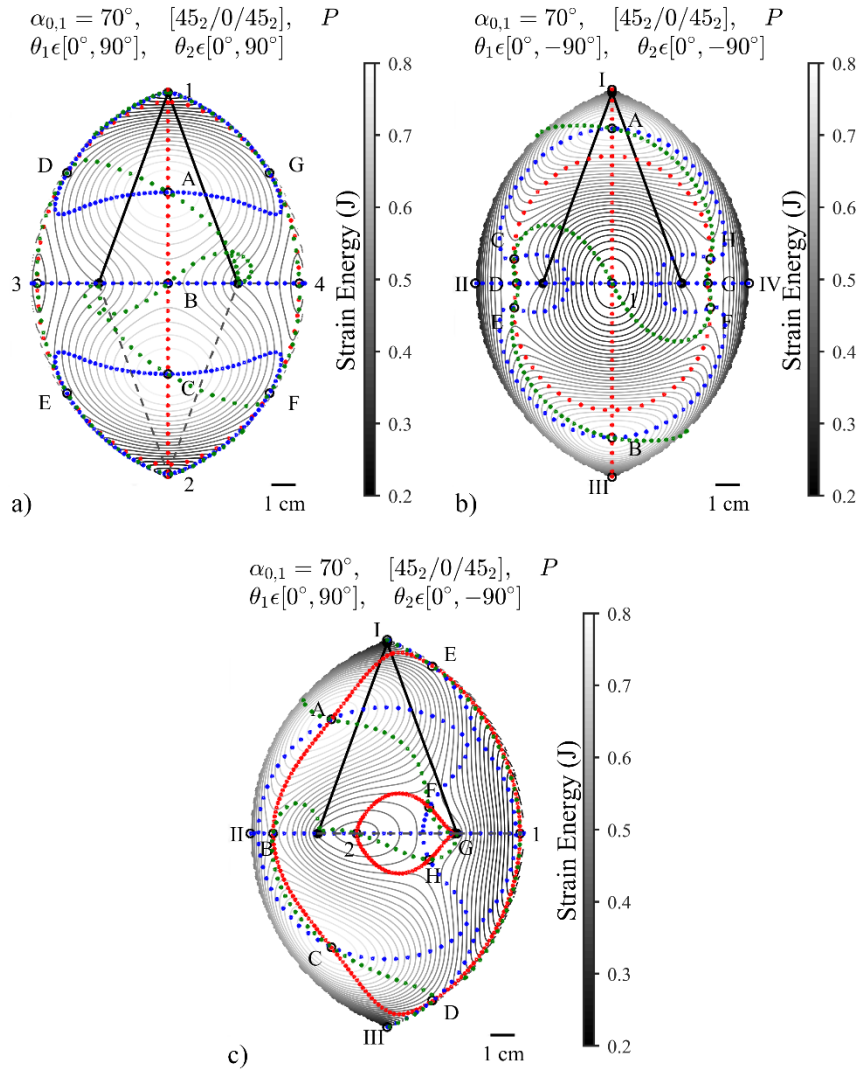


Figure 6.3: End effector positions upon application of a load P on the apex superimposed on the corresponding strain energy landscapes for different reconfiguration modes of the truss with an initial angle $\alpha_{0,1} = 70^\circ$ consisting of double helices of $[45_2/0/45_2]$ layup, $L = 95$ mm, $R = 15$ mm, $R_i = 30$ mm, $W = 5$ mm. a) Mode I; b) Mode II; c) Mode III. Red points indicate the equilibrium paths of the apex under the application of a vertical load ($P_h = 0$). Blue points indicate the equilibrium paths of the apex under the application of a horizontal load ($P_v = 0$). Green points indicate the equilibrium paths of the apex under the application of a combined load ($P_h = P_v$). Points 1–4 are stable equilibrium points. Points A–H are unstable equilibrium points. Points I–IV denote stable boundary equilibria.

(points 1 and 2, in Figure 6.4a). The other two equilibria are on the bifurcated branch on the horizontal, *i.e.* at a vertical displacement of H_0 (points 3 and 4 in Figure 6.4a). A bifurcation is present in Mode II as well, though the only stable interior configuration occurs when the double-helices are collinear with zero horizontal displacement of the apex (point 1 in Figure 6.4b). Along the bifurcated path two areas of nearly zero force can be observed for the motion range between points C, D, E and F, G, H (Figure 6.4b). In Mode III, no bifurcation occurs, however, the end effector experiences both horizontal and vertical displacement. Two independent closed loop equilibrium paths are identified with one stable equilibrium each. The stable states are encountered when the double-helices are collinear (points 1 and 2 in Figure 6.4c).

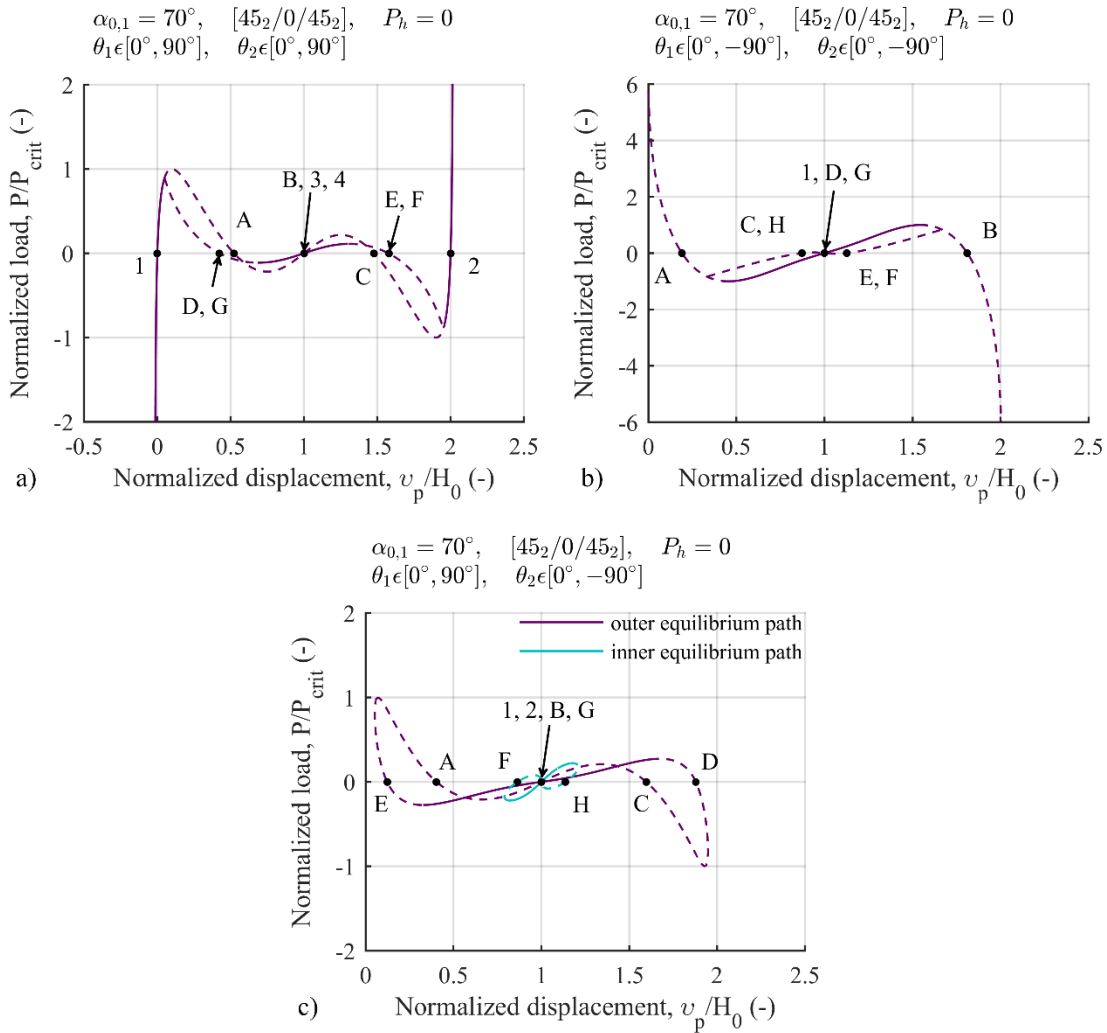


Figure 6.4: Load-displacement curves of the truss with an initial angle $\alpha_{0,1} = 70^\circ$ consisting of double helices of $[45_2/0/45_2]$ layup, $L = 95$ mm, $R = 15$ mm, $R_i = 30$ mm, $W = 5$ mm under the application of a vertical load at the apex ($P_h = 0$) for different reconfiguration modes: a) Mode I; b) Mode II; c) Mode III. Points 1–4 are stable equilibrium points. Points A–H are unstable equilibrium points. Dashed line represents the areas of instability. The load is normalized with respect to the load value at the maximum peak (P_{crit}) in each case.

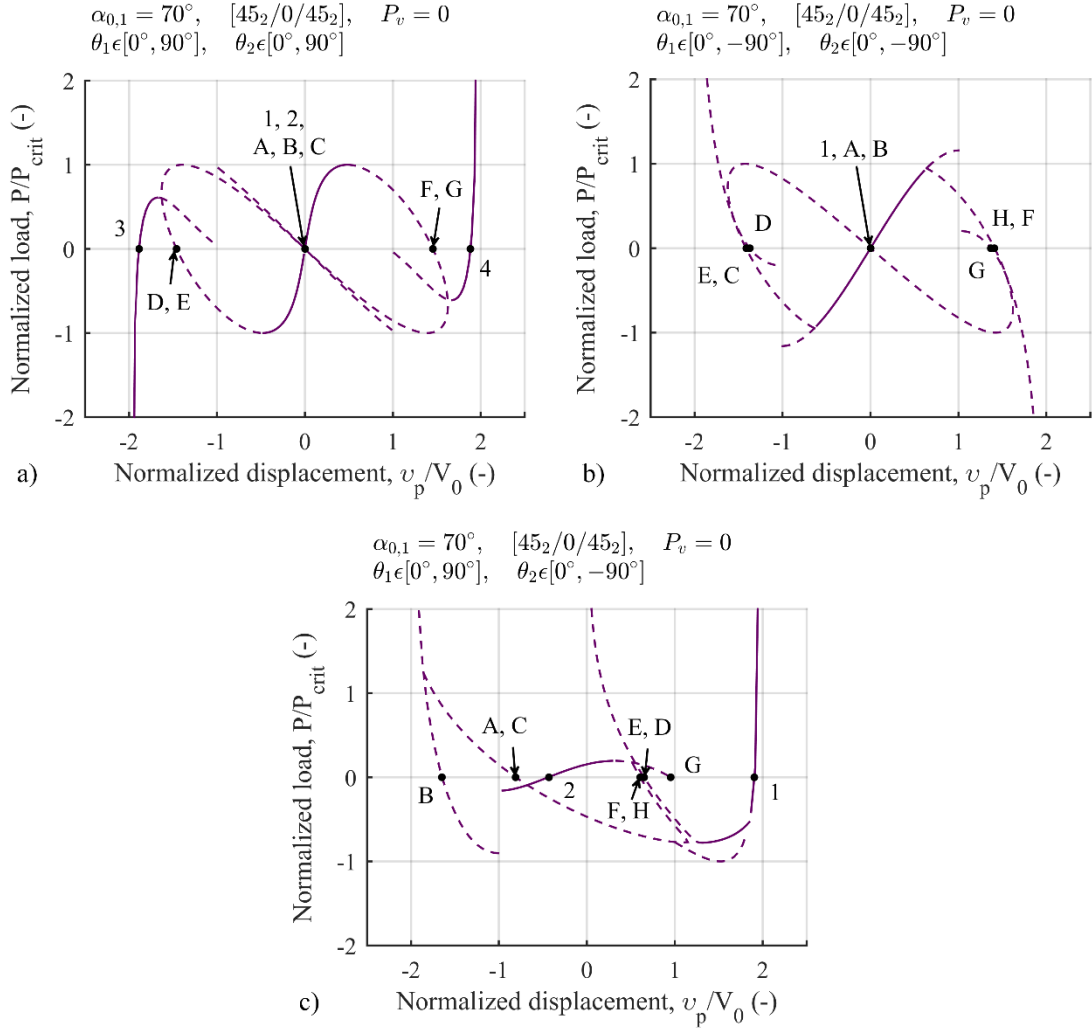


Figure 6.5: Load-displacement curves of the truss with an initial angle $\alpha_{0,1} = 70^\circ$ consisting of double helices of $[45_2/0/45_2]$ layup, $L = 95$ mm, $R = 15$ mm, $R_i = 30$ mm, $W = 5$ mm under the application of a horizontal load at the apex ($P_v = 0$) for different reconfiguration modes: a) Mode I; b) Mode II; c) Mode III. Points 1–4 are stable equilibrium points. Points A–H are unstable equilibrium points. Dashed line represents the areas of instability. The load is normalized with respect to the load value at the maximum peak (P_{crit}) in each case.

The equilibrium paths of the apex under a *horizontal* load at the end effector are also superimposed on the strain energy plots in Figure 6.3 (blue markers). The corresponding force-displacement response of the mechanism for the three reconfiguration modes is presented in Figure 6.5. For Mode I, three disconnected equilibrium paths are observed (blue markers in Figure 6.3a); two mirrored closed loop paths with identical load-displacement curves, and a horizontal path across the diameter when the apex is level with the supports. This latter path presents a jump in the corresponding load-displacement curve at a horizontal displacement of $\pm V_0$, positions where the apex traverses the supports, with the fully coiled helix turning around the support and switching direction, uncoiling out and away from the hinge point (Figure 6.5a). Therefore, the helix reaction force too switches direction, which explains the sudden jump in the

equilibrium manifold. For Mode II, a closed loop equilibrium path, entirely unstable, is identified intersecting twice with a horizontal bifurcation path across the diameter when the apex is level with the supports (blue markers in Figure 6.3b). As before, a jump in the load-displacement curve of the horizontal path is observed at a horizontal displacement of $\pm V_0$ (Figure 6.5b). In Mode III, bifurcation of the equilibrium paths occurs resulting in three connected equilibrium paths (blue markers in Figure 6.3c). A horizontal bifurcation path across the diameter when the apex is level with the supports is observed—as in Modes I and II—with a jump in its load-displacement curve at a horizontal displacement of $\pm V_0$. This path intersects at two points with the primary closed loop path that is unstable, and at one point with a third path characterized by areas of both stability and instability (Figure 6.5c). In all cases all possible equilibria, both stable and unstable are accessed.

Figure 6.6 shows the response of the mechanism under a *combined* load ($P_h = P_v$) at the apex. The corresponding positions of the apex are superimposed on the strain energy plots in Figure 6.3 (green markers). For both Mode I and Mode II, a single equilibrium path is identified, with no bifurcation, that traverses all possible equilibria, both stable and unstable. In Mode I, a jump is observed in the load-displacement curve at the positions the apex traverses the supports since the fully coiled helix, and thus its reaction force, turns around the support and switches direction uncoiling out and away from the hinge point (Figure 6.6a). In Mode II, two areas of nearly zero force can be observed for the motion range between points C, D, E and F, G, H (Figure 6.6b)—similar to the case of a vertical load. For Mode III, two independent equilibrium paths accessing all possible equilibria are observed, both exhibiting both stable and unstable areas (Figure 6.6c). A jump in the load-displacement curve of one of the paths is observed that corresponds to the locations that the apex traverses the supports. As explained above, the fully coiled helix switches direction, uncoiling out and away with its reaction force switching direction as well, justifying the sudden jump.

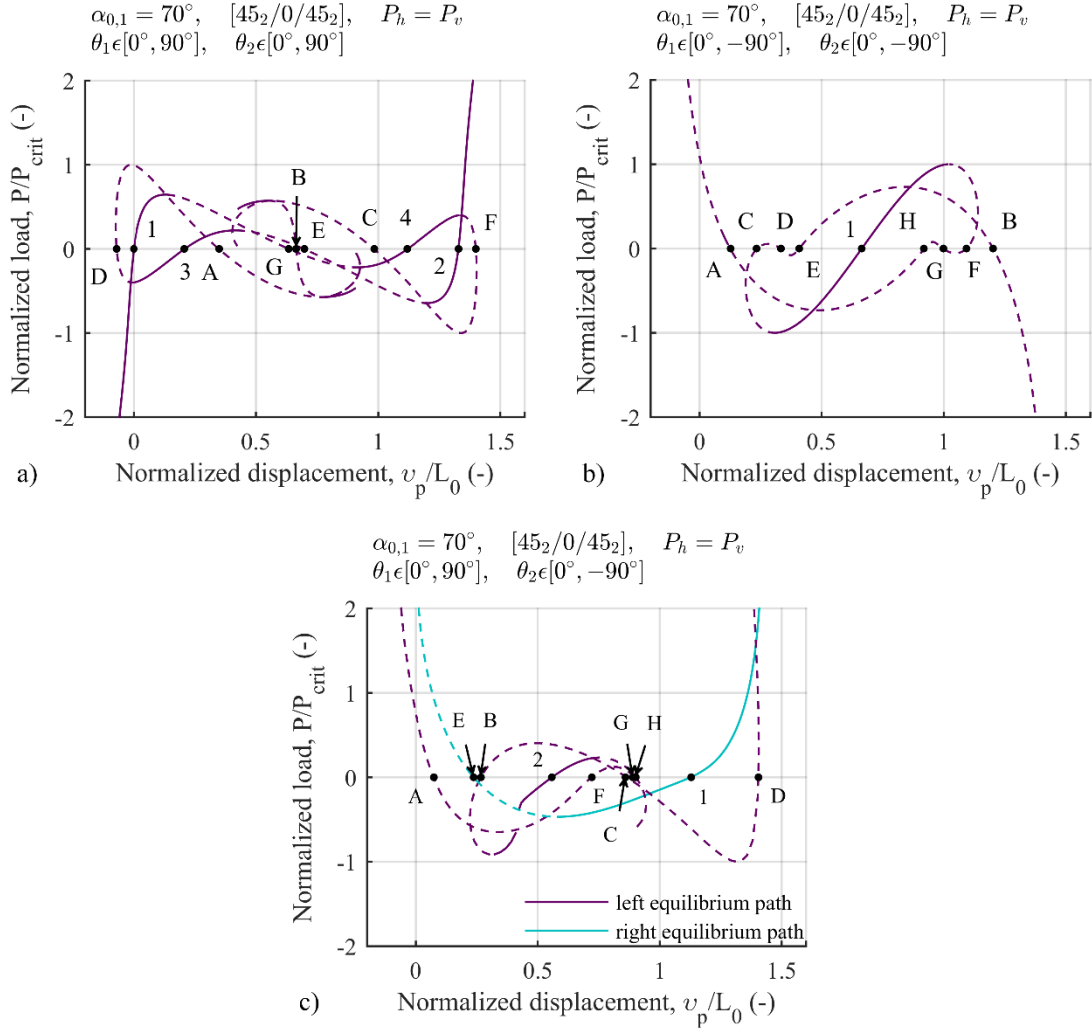


Figure 6.6: Load-displacement curves of the truss with an initial angle $\alpha_{0,1} = 70^\circ$ consisting of double helices of $[45_2/0/45_2]$ layup, $L = 95$ mm, $R = 15$ mm, $R_i = 30$ mm, $W = 5$ mm under the application of a combined load at the apex ($P_h = P_v$) for different reconfiguration modes: a) Mode I; b) Mode II; c) Mode III. Points 1–4 are stable equilibrium points. Points A–H are unstable equilibrium points. Dashed line represents the areas of instability. The load is normalized with respect to the load value at the maximum peak (P_{crit}) in each case.

6.3 Effect of composite lay-up

The composite lay-up affects the properties of the double-helices, namely their nonlinear axial stiffness, and thus the characteristics of the assembly. In this section, we investigate the effect of lay-up on the various reconfiguration modes.

6.3.1 Mode I

Figure 6.7 shows the energy landscapes for a truss identical to that of Figure 6.2a, with the strips' lay-up changed to $[30_2/0/30_2]$ and $[60_2/0/60_2]$. The landscapes show no qualitative differences, apart from overall rescaling, and changes in the absolute values and relative positions of the extrema. In conclusion, all

characteristic features, including quadristability, bifurcations and the connectivity between stable equilibria (Figure 6.8) under the various load cases, are preserved.

Figure 6.9 shows the load-displacement curves upon the application of a *vertical*, *horizontal* and *combined* load at the apex corresponding to the two laminate lay-ups. Similar to the $[45_2/0/45_2]$ strip lay-up, the load

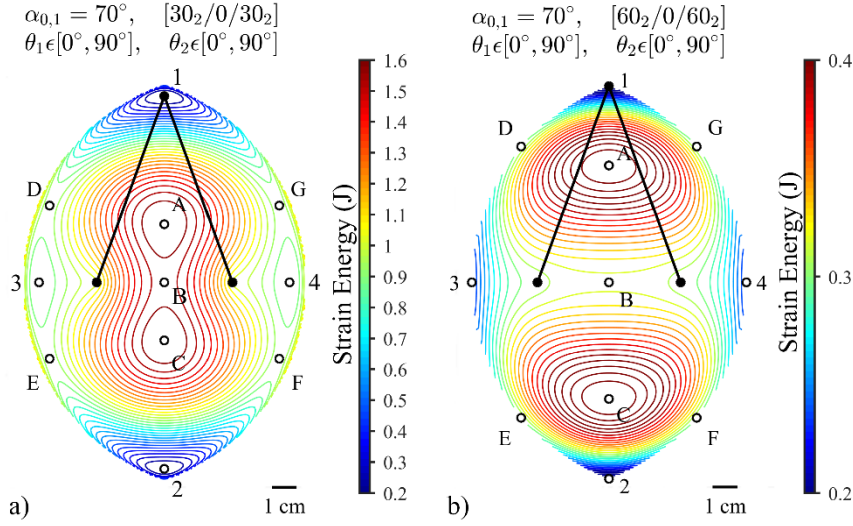


Figure 6.7: Strain energy landscapes for a compliant mechanism of double-helices of $L = 95$ mm, $R = 15$ mm, $R_i = 30$ mm, $W = 5$ mm assembled in a truss-like configuration with an initial angle $\alpha_{0,1} = 70^\circ$ for composite strips of $[\beta_2/0/\beta_2]$ lay-up for the reconfiguration Mode I. a) $[30_2/0/30_2]$; b) $[60_2/0/60_2]$. Points labelled 1–4 denote stable equilibria, while points A–G identify positions of unstable equilibrium. Black lines represent the double-helices at the initial truss configuration.

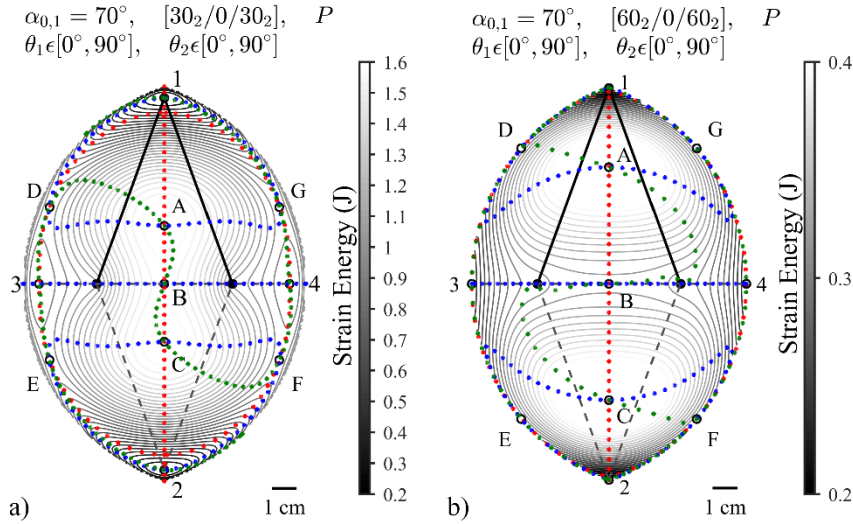


Figure 6.8: End effector positions upon application of a load P on the apex superimposed on the corresponding strain energy landscapes for reconfiguration Mode I of the truss with an initial angle $\alpha_{0,1} = 70^\circ$ consisting of double helices of $L = 95$ mm, $R = 15$ mm, $R_i = 30$ mm, $W = 5$ mm and lay-ups: a) $[30_2/0/30_2]$; b) $[60_2/0/60_2]$. Red points indicate the equilibrium paths of the apex under the application of a vertical load ($P_h = 0$). Blue points indicate the equilibrium paths of the apex under the application of a horizontal load ($P_v = 0$). Green points indicate the equilibrium paths of the apex under the application of a combined load ($P_h = P_v$). Points 1–4 are stable equilibrium points. Points A–G are unstable equilibrium points.

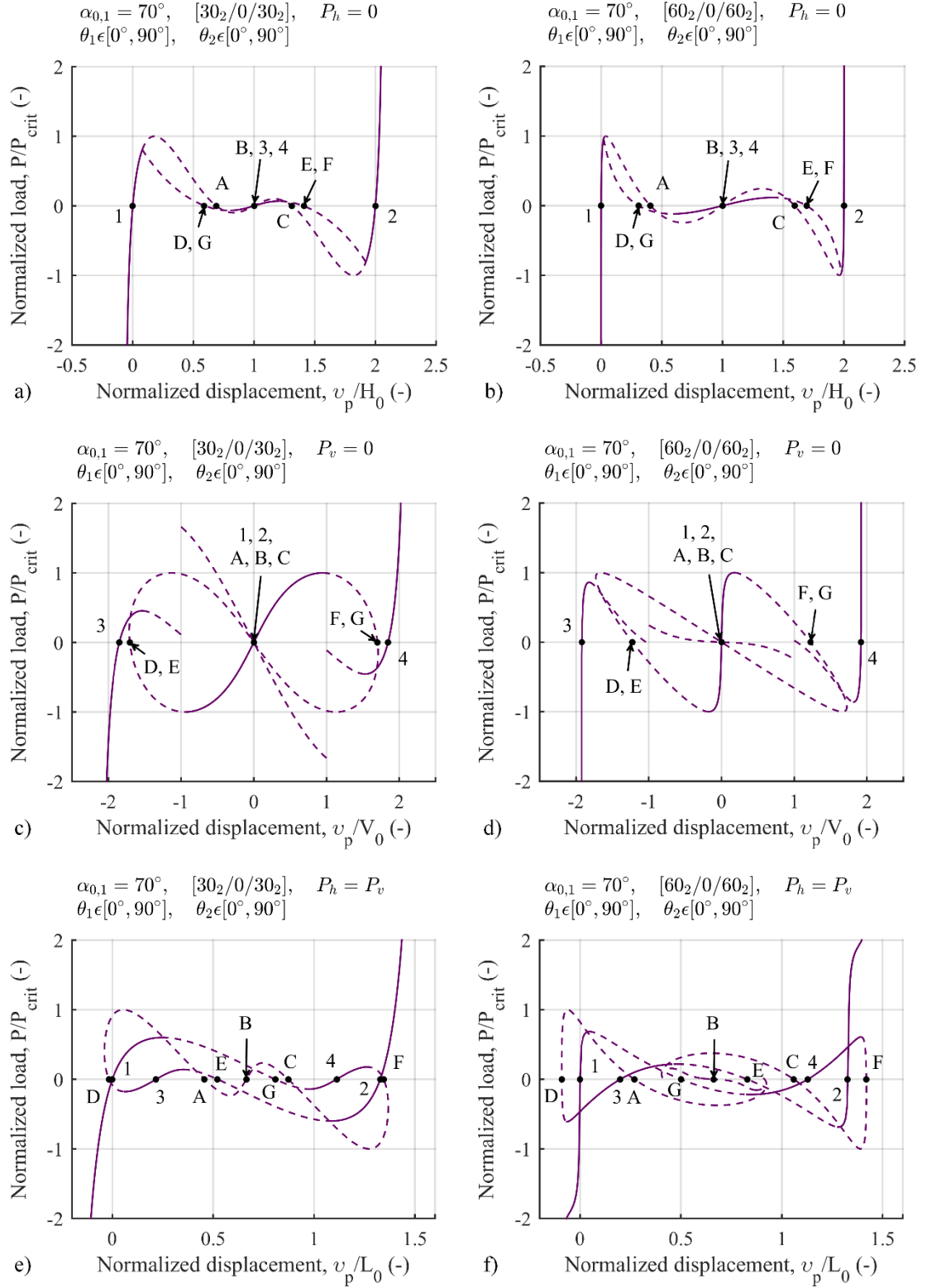


Figure 6.9: Load-displacement curves of the truss with an initial angle $\alpha_{0,1} = 70^\circ$ for different lay-ups, $[30_2/0/30_2]$ and $[60_2/0/60_2]$, for the reconfiguration Mode I under the application of a-b) a vertical ($P_h = 0$), c-d) a horizontal ($P_v = 0$) and e-f) a combined ($P_h = P_v$) load at the apex. Points 1–4 are stable equilibrium points. Points A–G are unstable equilibrium points. Dashed line represents the areas of instability. The load is normalized with respect to the load value at the maximum peak (P_{crit}) in each case.

path bifurcates to secondary branches upon a vertical load at the apex, while three independent equilibrium paths—a horizontal and two mirrored closed loop paths (blue markers in Figure 6.8)—are observed under a horizontal load and a single equilibrium path under a combined load. Yet in each loading condition all equilibrium positions are accessed. Each equilibrium path is characterized of the alteration between continuous areas of stability and instability, with the exception of the horizontal equilibrium path across the diameter with the supports in the case of a horizontal load at the apex where a jump in the load-displacement curve occurs at the positions of the supports ($v_h = \pm V_0$). As explained in the previous section (§6.2), this sudden jump is justified by the switch in the direction of the helix reaction force as the fully coiled helix is assumed to turn around the support.

6.3.2 Mode II

Figure 6.10 shows the energy landscapes for a truss identical to that of Figure 6.2b, with the strips' lay-up changed to $[30_2/0/30_2]$ and $[60_2/0/60_2]$, where the helices are now set for Mode II. For a $[30_2/0/30_2]$ lay-up the truss develops two interior stable equilibria (marked as points 1 and 2 in Figure 6.10a), positioned slightly above and below the centre of the landscape where the single minimum for the $[45_2/0/45_2]$ configuration is located. Again, apart from overall rescaling of the energy values and changes of the relative distance between extrema, all other features are maintained, leading to a total of eleven interior equilibrium configurations. Although shallower, the boundary equilibria too are maintained. As for the $[45_2/0/45_2]$ case, for $\beta = 60^\circ$ the mechanism exhibits a single stable equilibrium configuration, when the double-helices are collinear and the apex horizontal displacement is zero (point 1 in Figure 6.10b), as well as four boundary equilibria.

The mechanism's force-displacement responses upon application of a *vertical*, *horizontal* and *combined* load at the end effector are presented in Figure 6.12, with the corresponding apex position superimposed once more on the strain energy plots (red, blue and green markers, respectively, in Figure 6.11). For a *vertical* load, the bifurcations are preserved for both the $[30_2/0/30_2]$ and the $[60_2/0/60_2]$ lay-ups; still none of the equilibrium positions on the bifurcated branch is stable. For $\beta = 30^\circ$, areas of nearly zero force are present, both in the principal and bifurcated branch, for motion along the positions D, E and F, or 1, B and 2, or G, H and K (Figure 6.12a). For $\beta = 60^\circ$, the number of unstable equilibrium points along the bifurcated path reduced from six for the $[45_2/0/45_2]$ and $[30_2/0/30_2]$ lay-ups to two (Figure 6.12b). For a *horizontal* load, for $\beta = 60^\circ$ a closed loop equilibrium path is identified with a horizontal bifurcation path across the

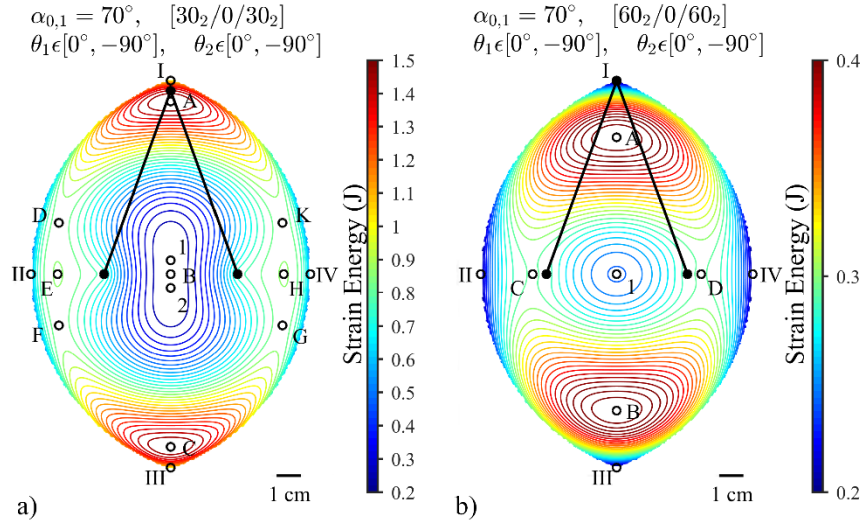


Figure 6.10: Strain energy landscapes for a compliant mechanism of double-helices of $L = 95$ mm, $R = 15$ mm, $R_i = 30$ mm, $W = 5$ mm assembled in a truss-like configuration with an initial angle $\alpha_{0,1} = 70^\circ$ for composite strips of $[\beta_2/0/\beta_2]$ lay-up for the reconfiguration Mode II. a) $[30_2/0/30_2]$; b) $[60_2/0/60_2]$. Points labelled 1 and 2 denote stable equilibria, while points A–H and K identify positions of unstable equilibrium. Points I–IV denote stable boundary equilibria. Black lines represent the double-helices at the initial truss configuration.

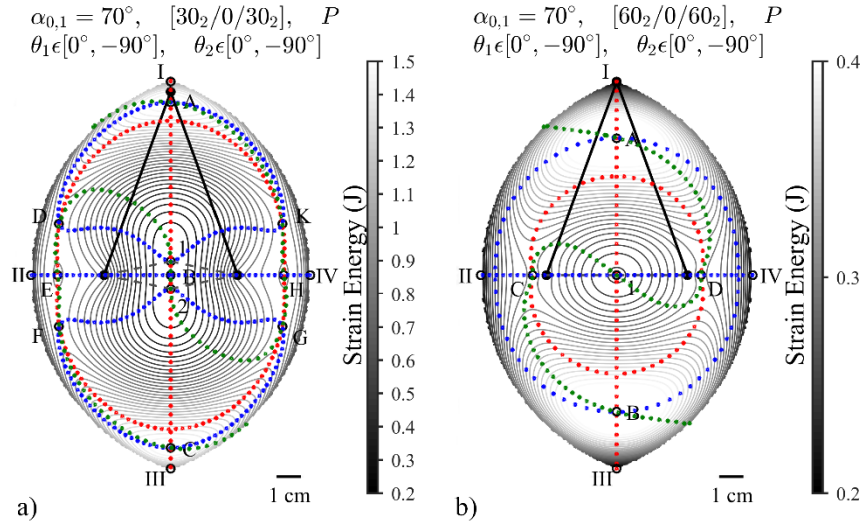


Figure 6.11: End effector positions upon application of a load P on the apex superimposed on the corresponding strain energy landscapes for reconfiguration Mode II of the truss with an initial angle $\alpha_{0,1} = 70^\circ$ consisting of double helices of $L = 95$ mm, $R = 15$ mm, $R_i = 30$ mm, $W = 5$ mm and lay-ups: a) $[30_2/0/30_2]$; b) $[60_2/0/60_2]$. Red points indicate the equilibrium paths of the apex under the application of a vertical load ($P_h = 0$). Blue points indicate the equilibrium paths of the apex under the application of a horizontal load ($P_v = 0$). Green points indicate the equilibrium paths of the apex under the application of a combined load ($P_h = P_v$). Points 1 and 2 are stable equilibrium points. Point A–H and K are unstable equilibrium points. Points I–IV denote stable boundary equilibria.

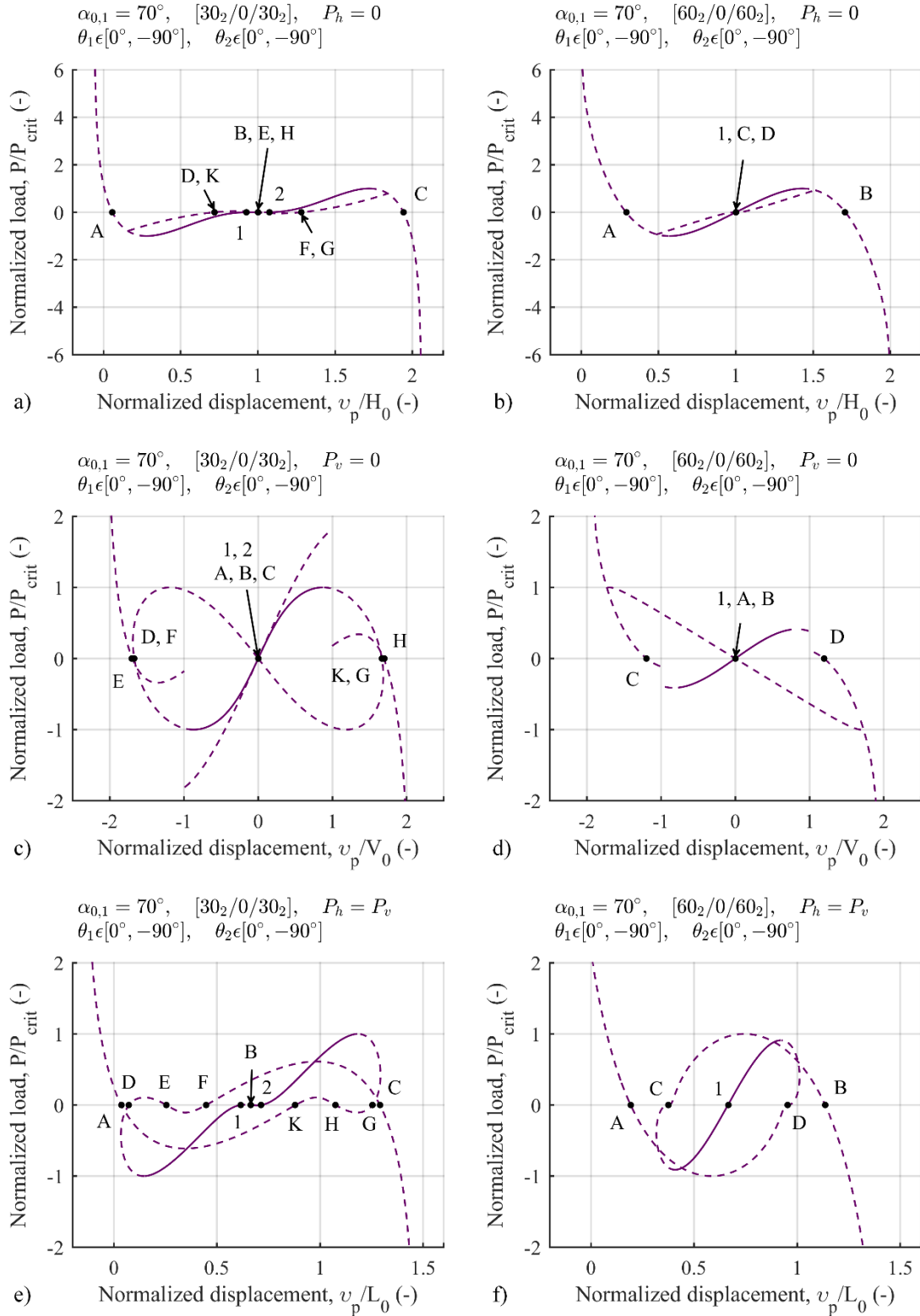


Figure 6.12: Load-displacement curves of the truss with an initial angle $\alpha_{0,1} = 70^\circ$ for different lay-ups, $[30_2/0/30_2]$ and $[60_2/0/60_2]$, for the reconfiguration Mode II under the application of a-b) a vertical ($P_h = 0$), c-d) a horizontal ($P_v = 0$) and e-f) a combined ($P_h = P_v$) load at the apex. Points 1 and 2 are stable equilibrium points. Points A–H and K are unstable equilibrium points. Dashed line represents the areas of instability. The load is normalized with respect to the load value at the maximum peak (P_{crit}) in each case.

diameter when the apex is level with the supports (blue markers in Figure 6.12d), similar to the $[45_2/0/45_2]$ case. Whereas for $\beta = 30^\circ$, three independent equilibrium paths are observed (blue markers in Figure 6.11a); two mirrored closed loop paths with identical load-displacement curves, and a horizontal path across the diameter traversing the supports. For both lay-ups, a jump in the load-displacement curve of the horizontal path is observed at a horizontal displacement of $\pm V_0$ (Figure 6.12c, d). For a *combined* load, a single equilibrium path, alternating between areas of stability and instability, is identified for both the $[30_2/0/30_2]$ and the $[60_2/0/60_2]$ lay-up that traverses all possible equilibria. Unlike the $[45_2/0/45_2]$ case, no area of nearly zero force can be observed for $\beta = 60^\circ$, while for $\beta = 30^\circ$ nearly zero force is required for the motion range between points 1, B and 2 (Figure 6.12e, f).

6.3.3 Mode III

The strain energy landscapes for Mode III are presented in Figure 6.13. For $\beta = 30^\circ$, a total of twelve interior equilibrium positions are identified, of which three are stable (marked as points 1–3 in Figure 6.13a), and two stable boundary equilibria (points I and II in Figure 6.13a). The mechanism is pentastable for a $[60_2/0/60_2]$ lay-up, with the two stable states when the two double-helices are collinear (points 1 and 2 in Figure 6.13b), plus three boundary equilibria (points I–III in Figure 6.13b). Figure 6.15a, b presents the load-displacement curves under a *vertical* load at the apex. The corresponding positions of the apex are superimposed on the strain energy plots with red markers in Figure 6.14. Similarly to the $[45_2/0/45_2]$ lay-up, for both ply angles, two independent closed loop equilibrium paths are found, with the apex experiencing both horizontal and vertical displacement, and with stable equilibrium positions present in both paths (points 1–3 in Figure 6.15a, b). Though only for $\beta = 30^\circ$, a nearly zero force area can be observed in the outer equilibrium path (motion range among points 1, E and 2 in Figure 6.15a).

Figure 6.15c, d shows the response of the mechanism under a *horizontal* load at the apex. The corresponding positions of the apex are superimposed too on the strain energy plots in Figure 6.14 (blue markers). As in the $[45_2/0/45_2]$ case, for $\beta = 30^\circ$ bifurcation of the equilibrium paths occurs resulting in three connected equilibrium paths—a horizontal bifurcation path across the diameter when the apex is level with the supports that intersects twice with a closed loop path and once with a third path—and all possible equilibria being accessed (blue markers in Figure 6.14a). For $\beta = 60^\circ$, three connected equilibrium paths

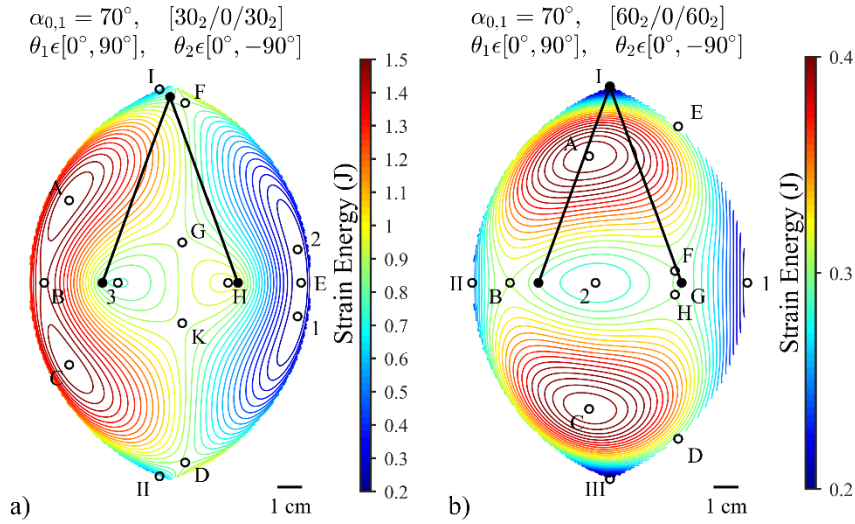


Figure 6.13: Strain energy landscapes for a compliant mechanism of double-helices of $L = 95$ mm, $R = 15$ mm, $R_i = 30$ mm, $W = 5$ mm assembled in a truss-like configuration with an initial angle $\alpha_{0,1} = 70^\circ$ for composite strips of $[\beta_2/0/\beta_2]$ lay-up for reconfiguration Mode III. a) $[30_2/0/30_2]$; b) $[60_2/0/60_2]$. Points labelled 1–3 denote stable equilibria, while points A–H and K identify positions of unstable equilibrium. Points I–III denote stable boundary equilibria. Black lines represent the double-helices at the initial truss configuration.

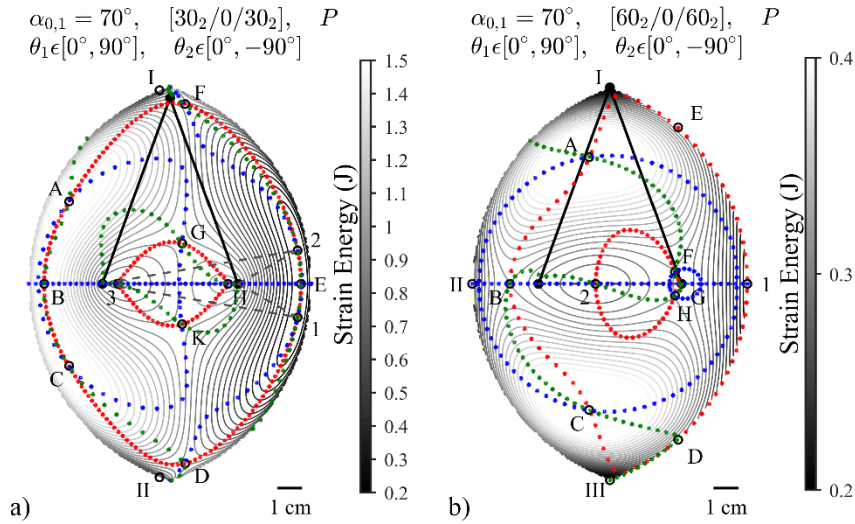


Figure 6.14: End effector positions upon application of a load P on the apex superimposed on the corresponding strain energy landscapes for reconfiguration Mode III of the truss with an initial angle $\alpha_{0,1} = 70^\circ$ consisting of double helices of $L = 95$ mm, $R = 15$ mm, $R_i = 30$ mm, $W = 5$ mm and lay-ups: a) $[30_2/0/30_2]$; b) $[60_2/0/60_2]$. Red points indicate the equilibrium paths of the apex under the application of a vertical load ($P_h = 0$). Blue points indicate the equilibrium paths of the apex under the application of a horizontal load ($P_v = 0$). Green points indicate the equilibrium paths of the apex under the application of a combined load ($P_h = P_v$). Points 1–3 are stable equilibrium points. Points A–H and K are unstable equilibrium points. Points I–IV denote stable boundary equilibria.

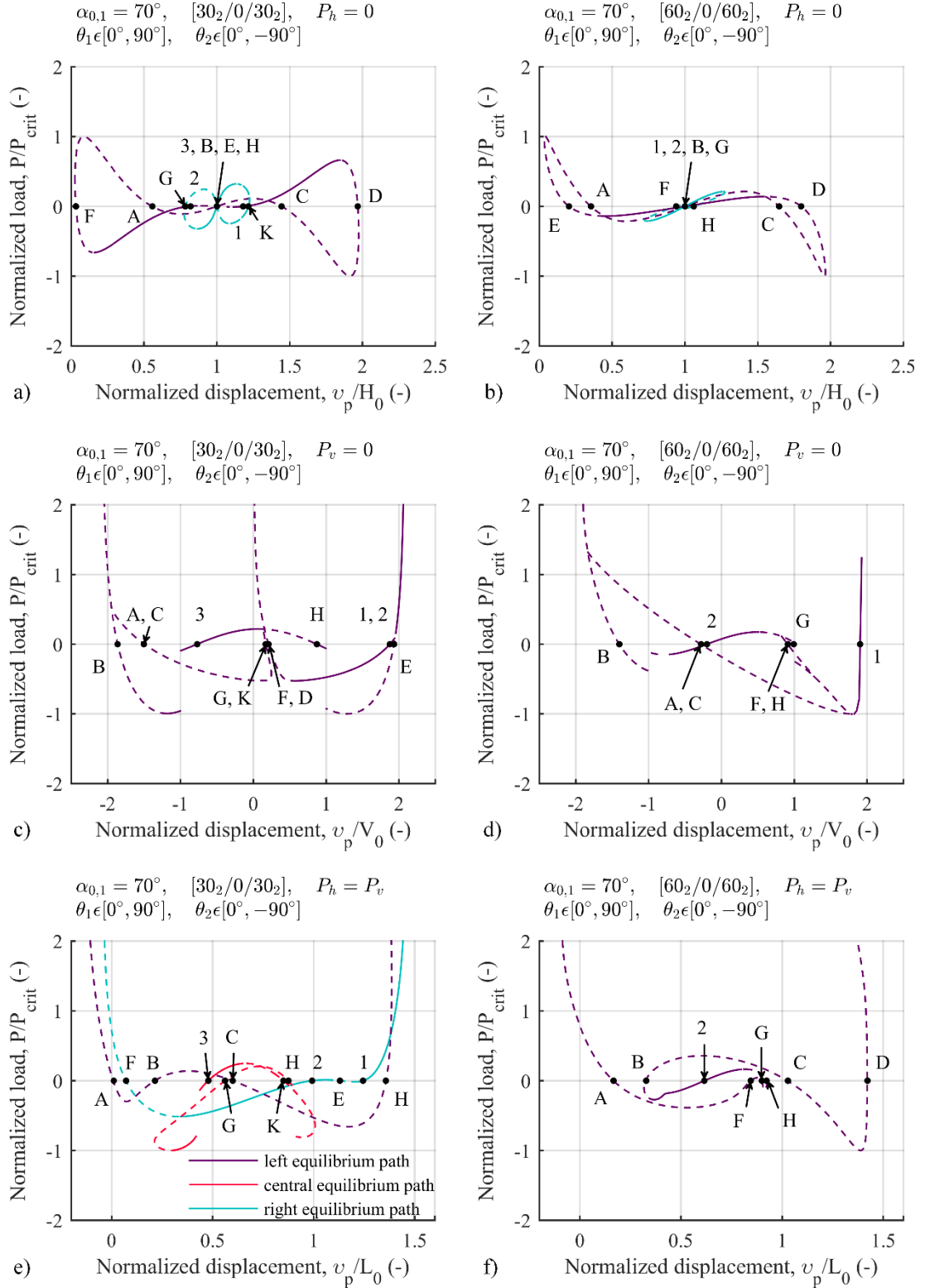


Figure 6.15: Load-displacement curves of the truss with an initial angle $\alpha_{0,1} = 70^\circ$ for different lay-ups, $[30_2/0/30_2]$ and $[60_2/0/60_2]$, for the reconfiguration Mode III under the application of a-b) a vertical ($P_h = 0$), c-d) a horizontal ($P_v = 0$) and e-f) a combined ($P_h = P_v$) load at the apex. Points 1–3 are stable equilibrium points. Points A–H and K are unstable equilibrium points. Dashed line represents the areas of instability. The load is normalized with respect to the load value at the maximum peak (P_{crit}) in each case.

are identified too—two closed loop equilibrium paths each intersecting at two points with the third horizontal equilibrium path along the diameter that traverses the supports—yet equilibrium positions D and E are left inaccessible (blue markers in Figure 6.14b). For both lay-ups, there is one entirely unstable closed loop equilibrium path, while the horizontal bifurcation path presents a jump in its load-displacement curve at a horizontal displacement of $\pm V_0$ (Figure 6.15c, d). This jump is explained by the switch in the direction and thus the reaction force of the fully coiled helix as it uncoils out and away from the hinge point.

The mechanism's force-displacement response upon application of a *combined* load at the end effector is presented in Figure 6.15e, f with the corresponding apex position superimposed once more on the strain energy plots in Figure 6.14 (green markers). For $\beta = 30^\circ$, three independent equilibrium paths are observed (Figure 6.15e), compared to the two identified earlier for $\beta = 45^\circ$ in Figure 6.6c. One of these equilibrium paths is completely unstable, while there is a closed loop one that exhibits a jump in its load-displacement curve that, as in previous cases, stems from the fact that the fully coiled helix is assumed to switching direction uncoiling out. For $\beta = 60^\circ$ a single path is observed (Figure 6.15f). Unlike for $\beta = 30^\circ$ and $\beta = 45^\circ$ where all possible equilibria are traversed, for a $[60_2/0/60_2]$ lay-up positions I and E are not accessed under a combined load at the apex (green markers in Figure 6.14).

6.4 Effect of initial truss geometry, $\alpha_{0,i}$

Finally, the effect of the initial truss geometry, $\alpha_{0,i}$, on the mechanism's behaviour and its reconfigurability is explored. Figure 6.16 presents the strain energy landscapes for a shallow truss configuration with $\alpha_{0,1} = 35^\circ$ and a $[45_2/0/45_2]$ strip lay-up for the three reconfiguration modes.

For a shallow truss with double-helices operating in Mode I, a total of five equilibrium positions are identified with only two being stable (marked as points 1 and 2 in Figure 6.16a), compared to the four stable configurations out of a total of eleven equilibria in a steep truss (marked as points 1–4 in Figure 6.2a). Mode II for a shallow truss shows three interior equilibrium positions, none of which are stable (Figure 6.16b), and four stable boundary equilibria (points I–IV). This contrasts with the steep truss, which has a single stable interior equilibrium position. Mode III shows four interior equilibria, of which one is stable (point 1 in Figure 6.16c), plus two stable boundary equilibria (points I and II).

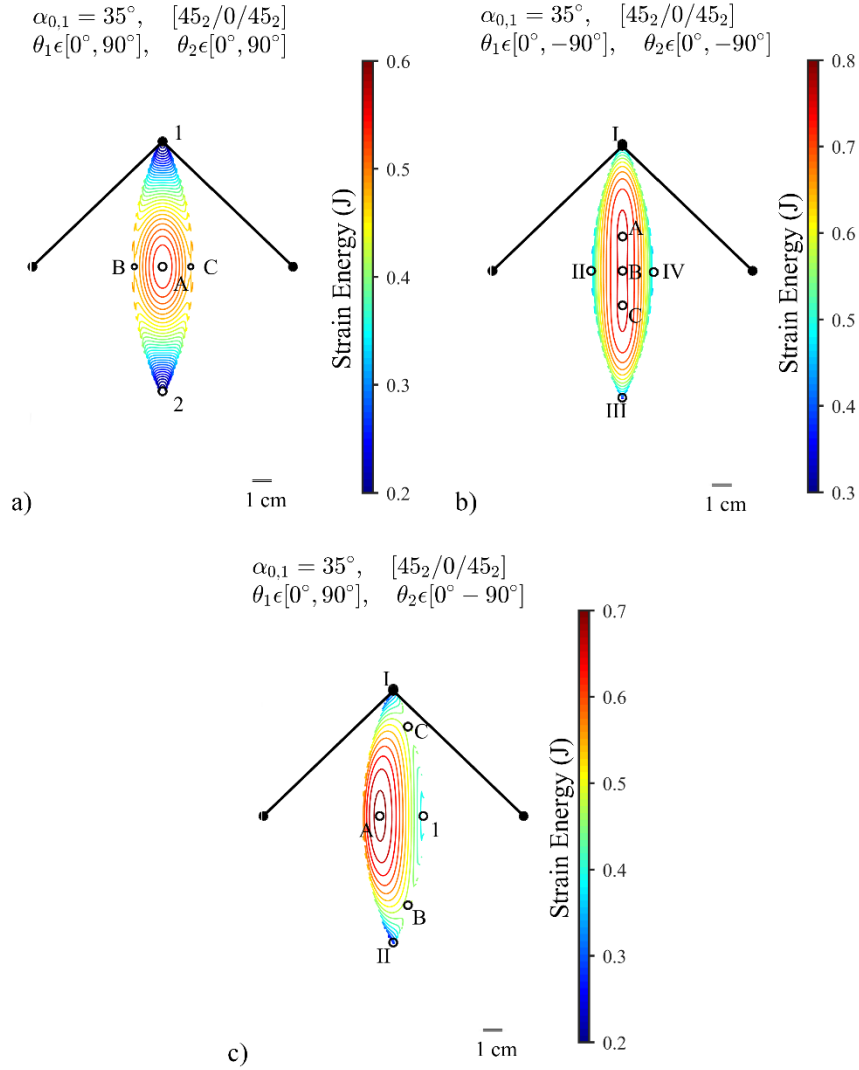


Figure 6.16: Strain energy landscapes for a compliant mechanism of double-helices of a $[45_2/0/45_2]$ composite strip lay-up, $L = 95$ mm, $R = 15$ mm, $R_t = 30$ mm, $W = 5$ mm assembled in a truss-like configuration with an initial angle $\alpha_{0,1} = 35^\circ$ for different reconfiguration modes. a) Mode I: $\theta_i \in [0^\circ, 90^\circ]$; b) Mode II: $\theta_i \in [0^\circ, -90^\circ]$; c) Mode III: $\theta_1 \in [0^\circ, 90^\circ]$, $\theta_2 \in [0^\circ, -90^\circ]$. Points labelled 1 and 2 denote stable equilibria, while points A–C identify positions of unstable equilibrium. Points I–III denote stable boundary equilibria. Black lines represent the double-helices at the initial truss configuration.

The load-displacement curves for the shallow truss under a *vertical*, *horizontal* and *combined* load at the end effector are presented in Figure 6.18–Figure 6.20. The apex positions are superimposed on the strain energy plots in Figure 6.17. Under a *vertical* load, for reconfiguration Mode I, for both the shallow and steep truss, a bifurcation of the equilibrium path occurs. However, the shallow truss only displays bistability, with stable states at the initial configuration and at a vertical displacement of $2H_0$ (points 1 and 2, in Figure 6.18a) and the bifurcated branch being entirely unstable (Figure 6.18a). For Mode II, the mech-

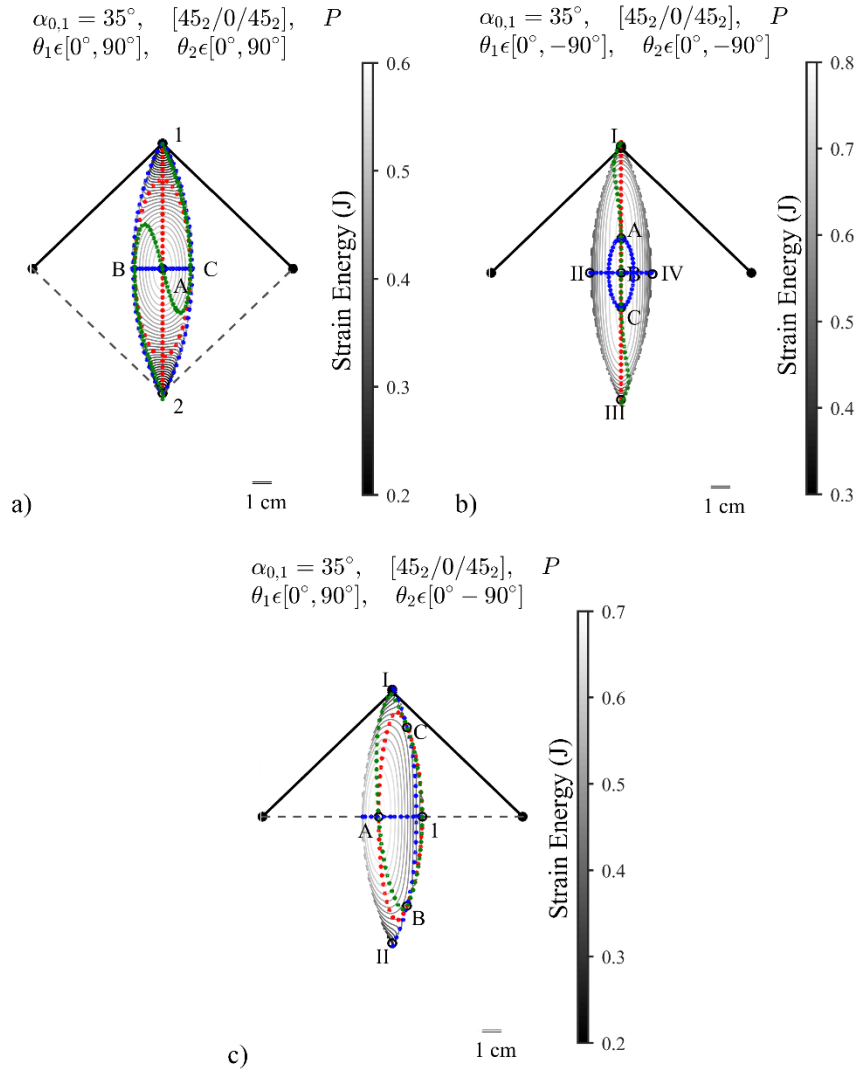


Figure 6.17: End effector positions upon application of a load P on the apex superimposed on the corresponding strain energy landscapes for different reconfiguration modes of the truss with an initial angle $\alpha_{0,1} = 35^\circ$ consisting of double helices of $[45_2/0/45_2]$ layup, $L = 95$ mm, $R = 15$ mm, $R_i = 30$ mm, $W = 5$ mm. a) Mode I; b) Mode II; c) Mode III. Red points indicate the equilibrium paths of the apex under the application of a vertical load ($P_h = 0$). Blue points indicate the equilibrium paths of the apex under the application of a horizontal load ($P_v = 0$). Green points indicate the equilibrium paths of the apex under the application of a combined load ($P_h = P_v$). Points 1 and 2 denote stable equilibria, while points A–C identify positions of unstable equilibrium. Points I–III denote stable boundary equilibria.

anism is unstable for a shallow truss. A statically balanced area with nearly zero force can be observed between points A, B and C (Figure 6.18b). In this mode, unlike in the steep truss, for the shallow truss no bifurcation occurs, with the apex experiencing only a vertical displacement under the applied load (red markers in Figure 6.17b). Mode III shows a closed loop load-displacement curve (Figure 6.18c). The compliant mechanism displays monostability with the single stable point encountered in one of the configurations where the helices are collinear (point 1 in Figure 6.17c). The mechanism experiences a single closed loop equilibrium path (red markers in Figure 6.17c), as opposed to the behaviour for a steep truss, where a second, disconnected equilibrium path is observed.

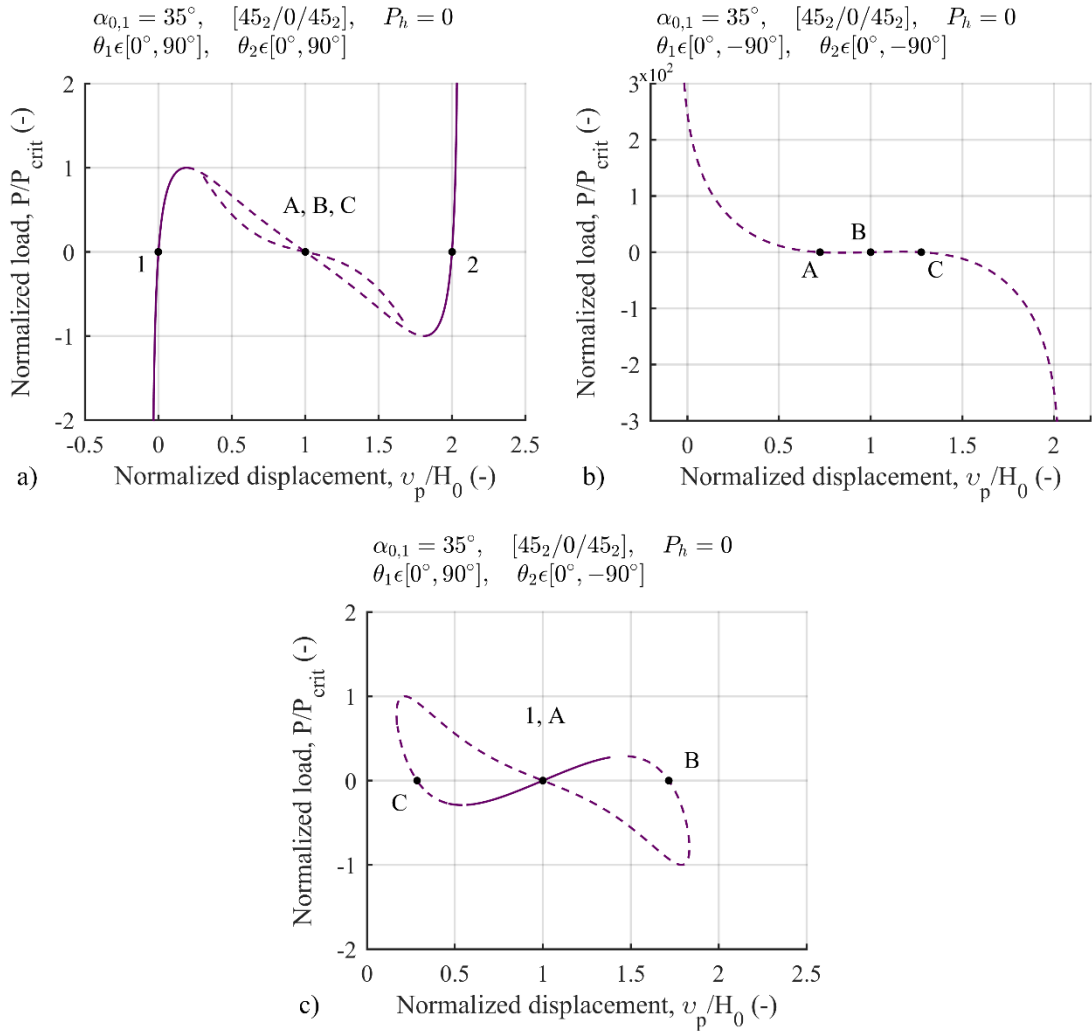


Figure 6.18: Load-displacement curves of the truss with an initial angle $\alpha_{0,1} = 35^\circ$ consisting of double helices of $[45_2/0/45_2]$ layup, $L = 95$ mm, $R = 15$ mm, $R_i = 30$ mm, $W = 5$ mm under the application of a vertical load at the apex ($P_h = 0$) for different reconfiguration modes: a) Mode I; b) Mode II; c) Mode III. Points 1 and 2 are stable equilibrium points. Points A–C are unstable equilibrium points. Dashed line represents the areas of instability. The load is normalized with respect to the load value at the maximum peak (P_{crit}) in each case.

Upon a *horizontal* load at the apex, for Mode I, for a shallow truss, the equilibrium path bifurcates. Unlike in a steep truss, where three disconnected equilibrium paths are identified (blue markers in Figure 6.3a), here two connected paths are observed (blue markers in Figure 6.17a); one closed loop and one horizontal across the diameter when the apex is level with the supports, yet due to the difference in geometry no jump in the load-displacement curve is observed for the shallow truss (Figure 6.19a). For Mode II, for both the shallow and steep truss, a closed loop equilibrium path is identified with a horizontal bifurcation path across the diameter when the apex is level with the supports (blue markers in Figure 6.17b). However, in

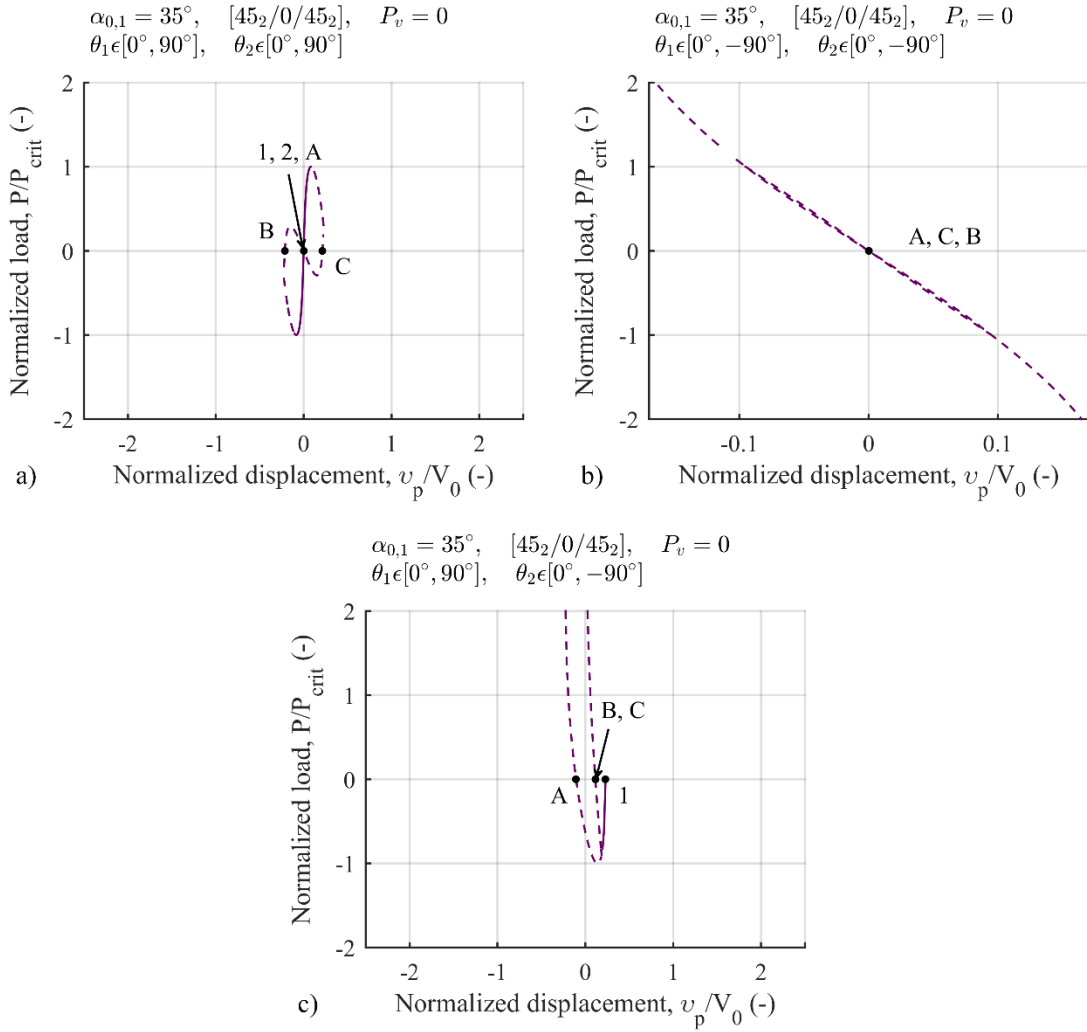


Figure 6.19: Load-displacement curves of the truss with an initial angle $\alpha_{0,1} = 35^\circ$ consisting of double helices of $[45_2/0/45_2]$ layup, $L = 95$ mm, $R = 15$ mm, $R_t = 30$ mm, $W = 5$ mm under the application of a horizontal load at the apex ($P_v = 0$) for different reconfiguration modes: a) Mode I; b) Mode II; c) Mode III. Points 1 and 2 are stable equilibrium points. Points A–C are unstable equilibrium points. Dashed line represents the areas of instability. The load is normalized with respect to the load value at the maximum peak (P_{crit}) in each case.

the shallow truss the load-displacement curve is a continuous one with a secondary branch and no jump since the apex at no position traverses the supports given the geometry of the truss (Figure 6.19b). In Mode III, bifurcation of the equilibrium path occurs resulting in two connected equilibrium paths (blue markers in Figure 6.17c), compared to the three in case of a steep truss. Additional to the main path—which is entirely unstable—a horizontal bifurcation path across the diameter when the helices are collinear is observed—as in a steep truss but with no jump in the load-displacement curve (Figure 6.19c). In all cases all possible equilibria, both stable and unstable are accessed.

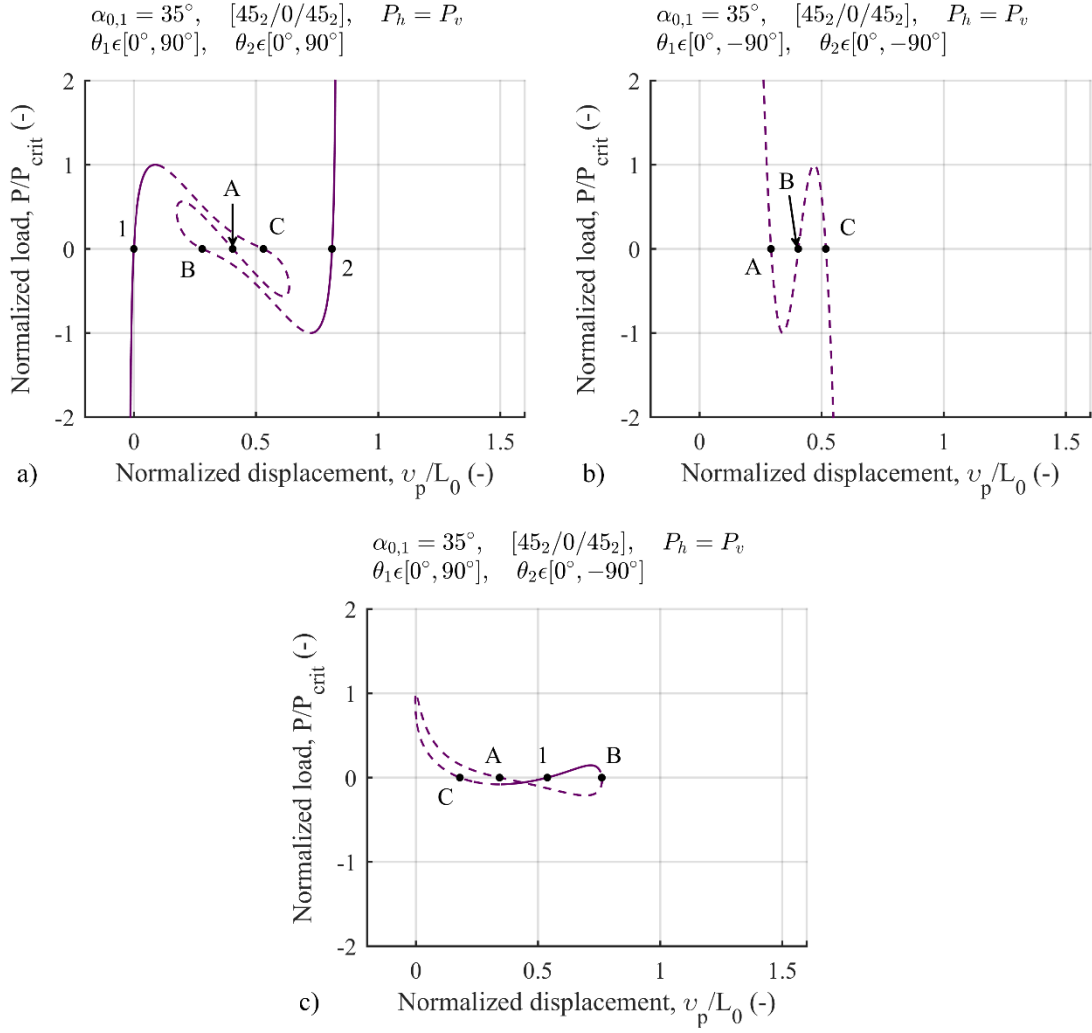


Figure 6.20: Load-displacement curves of the truss with an initial angle $\alpha_{0,1} = 35^\circ$ consisting of double helices of $[45_2/0/45_2]$ layup, $L = 95$ mm, $R = 15$ mm, $R_i = 30$ mm, $W = 5$ mm under the application of a combined load at the apex ($P_h = P_v$) for different reconfiguration modes: a) Mode I; b) Mode II; c) Mode III. Points 1 and 2 are stable equilibrium points. Points A–C are unstable equilibrium points. Dashed line represents the areas of instability. The load is normalized with respect to the load value at the maximum peak (P_{crit}) in each case.

For a *combined* load, for both Mode I and Mode II, similarly to the steep truss, a single equilibrium path is identified, with no bifurcation (green markers in Figure 6.17a, b). The corresponding load-displacement curves are continuous traversing all possible equilibria, characterized of both stable and unstable areas for Mode I (Figure 6.20a), but only unstable ones for Mode II (Figure 6.20b). For Mode III, for a shallow truss, a single closed loop equilibrium path is observed with a continuous load-displacement curve of both areas of stability and instability (Figure 6.20c), accessing all possible equilibria (green markers in Figure 6.17c), as opposed to the two independent equilibrium paths identified in a steep truss (Figure 6.6c).

6.5 Summary

The reconfigurability of the multistable mechanism consisting of morphing elements of a double-helix architecture arranged in a truss-like configuration is introduced in this chapter. The reconfigurability of the mechanism is based on the inherent ability of the double-helical elements to switch their twist direction when in the fully extended state, while the truss mechanism's connectivity and joint types are maintained. This constitutes a novel approach of attaining reconfigurability. As a result, a mechanism with two identical double-helical elements can achieve four different reconfiguration modes (Mode I, Mode II, Mode III and its reverse). The mechanism's multistability characteristics and its response in the force-displacement space are explored for the different reconfiguration modes.

Similarly to the previous chapter, two analysis methods have been employed to study the mechanism's characteristics in the different reconfiguration modes. Strain energy landscapes are used to identify stable and unstable equilibria, corresponding to valleys and peaks, respectively. A path-following method has been employed to trace equilibrium paths in force-displacement space for different cases of applied loads at the apex, *i.e.* a vertical ($P_h = 0$), a horizontal ($P_v = 0$) and a combined ($P_v = P_h$) load.

The various reconfiguration modes induce significant changes in the mechanical behaviour of the mechanism studied herein. For a steep truss ($\alpha_{0,1} = 70^\circ$) with a symmetric composite lay-up $[\beta_2/0/\beta_2]$, the mechanism is quadristable in Mode I, and the equilibrium paths access all equilibria either through bifurcation for a vertical load, or multiple independent paths for a horizontal load or a single path for a combined load. For Mode II, the response depends on the fibre angle, with $\beta = 30^\circ$ showing two internal stable equilibria, and one for $\beta = 45^\circ$ and $\beta = 60^\circ$, in addition to the four stable boundary equilibria. Again, bifurcations of the equilibrium path enable all internal equilibria to be traversed upon application of either a vertical or a horizontal load. In Mode III, the structure exhibits two internal stable equilibria for $\beta = 45^\circ$ and $\beta = 60^\circ$, but three for $\beta = 30^\circ$, and for a horizontal load at the apex, three connected equilibrium paths are identified. Upon application of a vertical load, however, two disconnected equilibrium paths are identified for all lay-ups, while under a combined load, the three independent equilibrium paths for $\beta = 30^\circ$, are reduced to two for $\beta = 45^\circ$, to a single for $\beta = 60^\circ$, thus leaving some equilibria isolated. Further to these results, the effect of the initial truss geometry on the mechanism's behaviour and its reconfigurability is explored. It is found that the geometry significantly affects the structural behaviour and characteristics of the truss assembly. For a shallow truss ($\alpha_{0,1} = 35^\circ$), the mechanism is bistable in Mode I, and tristable

in Mode III, while in Mode II none of the interior equilibrium positions identified are stable. The energy landscapes were found to be an effective means to convey the qualitative changes in mechanical behaviour between the reconfiguration modes.

The present chapter studied the reconfigurability of this assembly of double-helices and its mechanical response. The next chapter concentrates on the manufacturability of a prototype of the reconfigurable, multistable mechanism introduced in this work and the experimental validation of the results from the structural analysis of this mechanism. Subsequently, the thesis concludes in its final chapter with some final comments and suggestions for future work.

Chapter 7

Manufacture and Test of a Prototype Mechanism of Nonlinear Morphing Elements

7.1 Introduction

The manufacture of compliant and/or reconfigurable mechanisms can be challenging. Besides the potential development of high stresses in the mechanism's members during deformation when it comes to mechanisms with large deflections/displacements, the complex shapes and/or trajectories the mechanism is expected to achieve may result in structural impracticability of the mechanism for the selected dimensions and geometry, putting either further limitations in the design or requiring a different approach and/or the use of additional components for a practical feasible mechanism.

Specifically, in this chapter we focus on the manufacture of a prototype of the novel mechanism assembled of double-helices in a truss-like configuration introduced in the previous chapters and the experimental validation of the results from the analytical structural analysis. Our primary aim is to demonstrate the manufacturability of the proposed reconfigurable, multistable mechanism. Thus, the design presented herein attempts to demonstrate the ability to achieve the various reconfiguration modes, while the experimental testing focuses on a vertical load applied at the apex to validate the analytical model.

The rest of the chapter is structured as follows. Section 7.2 presents the design of the test rig required for the set-up and testing of the truss assembly. Section 7.3 includes a modification of the analytical model presented in Chapter 4 to account for changes in the truss geometry occurred from the design of the mechanism test rig. Section 7.4 presents the manufacture process, test set-up and results for a single double-

helix, whereas sections 7.5 and 7.6 focus on the experimental set-ups and test results of the assembly of double-helices in a truss-like configuration. The chapter concludes in section 7.7 with a summary.

7.2 Double-helix assembly mechanism test rig design

To demonstrate the manufacturability of the proposed reconfigurable mechanism and validate the results from the analytical model, a prototype was built. Figure 7.1 illustrates the design of the test rig for the assembly of the double-helices in a truss-like configuration, produced in the Autodesk Inventor 3D CAD software. Figure 7.2 presents the actual test rig. Detailed CAD drawings of the individual customized components and fixtures are included in the Appendix A.1.

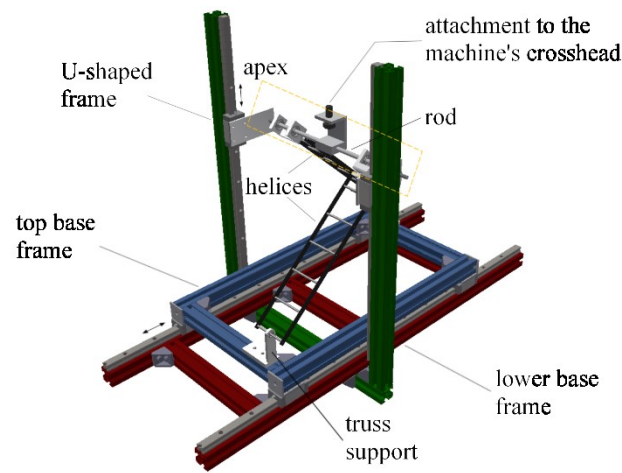


Figure 7.1: CAD design of the fixture for the assembly of the double-helices in a truss-like configuration. The two helices of the mechanism connect to a single rod along the apex of the truss. The apex is attached to a test machine to measure force and displacement, and is allowed to move vertically in a U-shaped frame (green profiles). The supports of the helices are attached to a base frame (blue profiles) that can move horizontally with respect to the fixed lower base frame (red profiles). This configuration effectively enables the lateral movement of the apex under a purely vertical applied load.

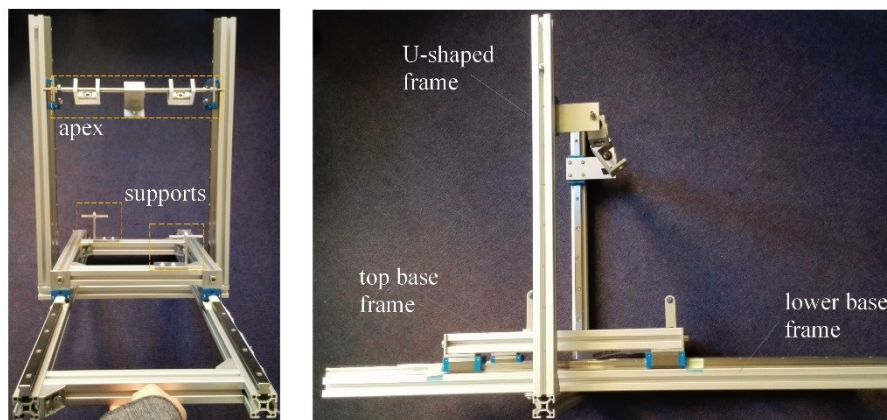


Figure 7.2: Test rig for the experimental testing of the mechanism of double-helices.

In the design of the prototype, several practical problems needed to be addressed, such as the attachment of the double-helices in a truss-like configuration allowing twist of the double-helices around the axis of the truss members upon application of a vertical load, the implementation of both a horizontal and a vertical movement of the apex, and the ability of the truss-like mechanism to deform to configurations where the truss members pass through the hinge point at the supports.

The strain energy landscapes derived from the structural analysis in the previous chapters present a symmetry around the horizontal that traverses the supports for all reconfiguration modes (see Figure 6.2). Therefore, being able to capture the deformations and mechanical responses of the upper half of the design space for the various reconfiguration modes is considered sufficient for the design of the test rig and the experimental testing. Additionally, for Mode I and II the strain energy landscapes are also symmetric with respect to a vertical axis passing through the apex in the initial truss configuration, thus for simplicity the experimental testing is performed in one of the quarters of the design space.

For the validation of the results from the analytical model, we focus on the mechanical response under the application of a vertical load at the apex. However, even upon applying a vertical load at the apex the mechanism is expected to undergo both a vertical and a horizontal displacement based on the structural analysis of the mechanism (see Figure 6.2). Therefore, one of the first challenges was to achieve sideways movement of the truss apex, given that the crosshead of the test machine is able to provide only a vertical movement and vertical load. Drawing upon the work of Radaelli and Herder [148] who used a platform of three orthogonally placed rollers underneath the base of a monolithic compliant mechanism to measure a vertical load while the horizontal movement is unconstrained, we designed our test rig so that the base of the actual truss structure is free to move horizontally, while the apex itself is restricted to move vertically. For this purpose, the design consists of a lower base frame that is fixed to the test machine and a top base frame, where the supports of the truss mechanism are attached, free to slide and move horizontally with respect to the lower frame (Figure 7.1). The result is a test arrangement which is statically equivalent to the system depicted in Figure 4.1. Both frames are assembled from aluminium profiles (Bosch Rexroth, 30 x 30 mm, 8 mm slot). Linear motion components, *i.e.* linear guideways with rails, are used to provide a rigid linear horizontal movement of the top base frame along the lower base frame.

For a steep truss, in the analytical model, we allow the mechanism to deform to configurations outside the area enclosed by the supports, effectively allowing the helices to pass through the supports. In practice,

achieving such configurations entails the helices to be connected in offset, parallel planes. However, having two helices connected opposed and in parallel planes creates a moment on the connecting rod. To account for the potential torsion that could be developed in such configuration, instead of using more helices in offset, parallel planes to create another couple force to equilibrium the first one, a vertical U-shaped frame (Figure 7.1) has been designed. This frame is connected to the rod forming the apex where the two helices are attached to and fixed to the static lower base frame. It allows vertical movement of the apex, while reacts the torque through the placement of linear guides, as we cannot rely on the load cell reacting the torque. This approach compromises for any space limitations—instead of using four helices—and benefits from minimising any additional torsion that may occur due to any minor dissimilarities between two helices from the manufacturing process. The downside is the increased friction due to the parallel linear guides. Aluminium profiles (Bosch Rexroth, 30 x 30 mm, 8 mm slot) are used to form the U-shaped frame. Linear guideways with rails are placed on the vertical members of this U-shaped frame to allow the vertical displacement of the apex. It is noted that indeed no torsion or deflection of the U-shaped frame was observed during the experiments.

For the ability of the double-helix to deform from an extended to a coiled configuration under an axial load, a fixture enabling twisting is required at one of the helix extremities. In our design we chose the upper end of the helices to allow the twist, at the apex of the truss structure. The fixture consisting the apex is made of a shaft—a rod attached at its ends to the U-shaped frame and at its middle to the load transducer of the test machine with a suitable designed fitting (see Appendix A.1)—and the fittings for the helices (see Appendix A.1). The end fitting of the helix is a U-shaped bracket with bearings press-fitted in each side (Figure 7.3). Ball bearings are used to allow: i) the rotation of the helix around the longitudinal axis of the shaft—the rod passes through the ball bearings on the two parallel edges of the U-shaped bracket, and ii) the twist of the helix around its longitudinal axis—the end spoke of the helix is attached to the remaining side of the bracket. A different design is required for the end spoke of the helix on this side to enable its attachment to the ball bearing of the end fitting (see Appendix A.1).

To ensure that the helix axis stays aligned with the end fitting as it deforms and avoid any out of plane deformation of the helix strips, a second spoke is located near the end spoke, bearing a pin to align the two spokes and keep the strips deforming along the longitudinal axis of the helix (Figure 7.3). The piston concept is adopted for this, with the pin fixed to the second spoke and free to slide in/out to the end spoke

enabling the helix to coil-uncoil while twisting maintaining the alignment. Special care was required in the refinement of the second spoke, with the side towards the end spoke flattened, and its location to avoid collision of the spokes early in the helix twist.

Finally, the other end of the helix is attached to an L-shaped bracket on the top base frame forming the supports of the truss structure of the assembly of the double-helices. This end fitting of the helix has a simpler design with only requirement to allow rotation of the helix around the support. This rotational degree is achieved with a ball bearing press-fitted between the end helix spoke and the end fitting (see Appendix A.1). The dimensions of the L-shaped bracket, specifically its vertical length, is selected such that it allows enough space, *i.e.* at least the radius of the helix, from the top base frame for when the helices become collinear once in the horizontal position.

It is worth noting that any friction in the ball bearings and/or other joints is neglected in the calculations.

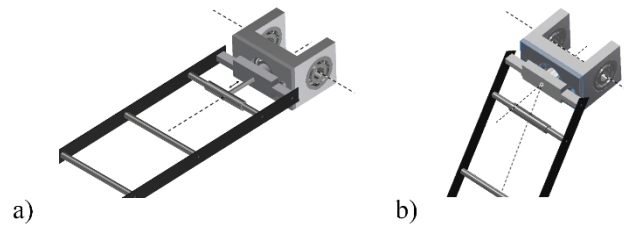


Figure 7.3: Double-helix configuration a) with a pin between the two end spokes to ensure deformation of the helix along the longitudinal X -axis of the helix; b) without a pin resulting in out of plane deformation.

7.3 Adapted analytical model

The design of the mechanism's test rig presented above, to address the challenges mentioned, resulted in introducing some features not included in the analytical model employed in the previous chapters. Our initial analytical model—presented in Chapter 4 and used to produce the results included in Chapter 5 and Chapter 6—assumes in the geometry of the truss-like mechanism that the truss members lengths consist entirely of the length of the double-helix and that the helix stroke deformation is its whole length. However, in the design developed above, additional length was required at either end of the helix to connect to the base support and apex. Furthermore, as pointed out during the manufacture and testing of the double-helix below, its deformation stroke is in practice limited by a stowed length from the strips and/or spokes touching in the fully coiled configuration (Figure 7.4).

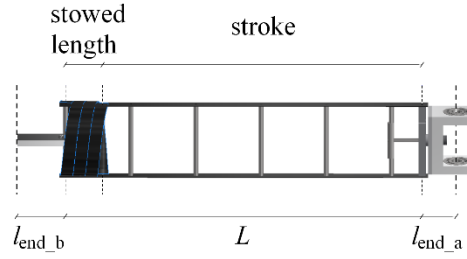


Figure 7.4: Schematic specifying the lengths for the constituent parts of the truss member in the mechanism.

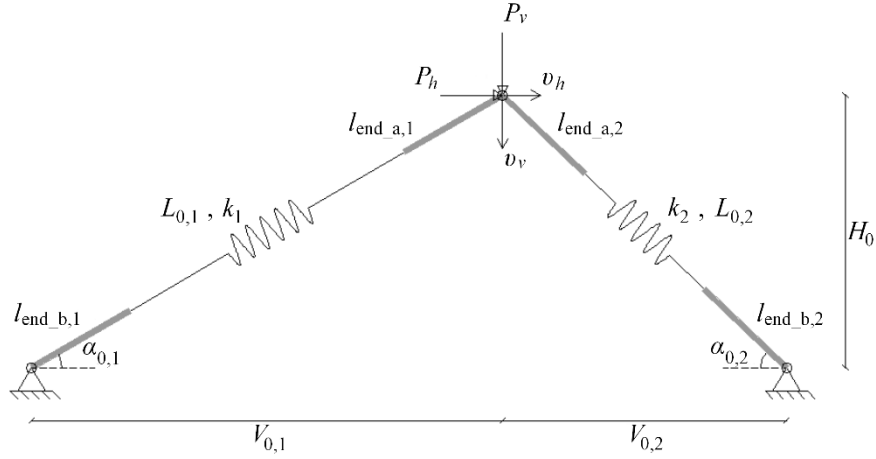


Figure 7.5: Schematic representation of the new geometry of the assembly of double-helices in a truss-like configuration. The initial configuration is determined by the equilibrium length $L_{0,i}$ of the double-helices, the lengths for the end fittings at the base support and apex, $l_{\text{end}_b,i}$ and $l_{\text{end}_a,i}$ respectively, and by the initial angle $\alpha_{0,i}$ of the truss configuration.

The end fitting lengths affect the truss geometry thus resulting in change of the kinematics of the mechanism, but it is easy to adopt in our initial model calculations. Figure 7.5 depicts the new truss geometry. In its initial configuration, the structure has height H_0 and a base angle $\alpha_{0,i}$ with respect to the horizontal; its members have length $l_{\text{bar},i}$ defined as:

$$l_{\text{bar},i} = l_{\text{end}_b,i} + L_{0,i} + l_{\text{end}_a,i}, \quad (7.1)$$

where $L_{0,i}$ corresponds to the length of the longest self-equilibrated configuration of the helix, $l_{\text{end}_b,i}$ is the length for the end fitting at the base support and $l_{\text{end}_a,i}$ is the length for the end fitting at the apex.

Equations 4.1–4.12 defining the geometrical relations need to be redefined to accommodate for the lengths of the end fittings by substituting $L_{0,i}$ to $l_{\text{bar},i}$. No other modifications are required in the model. The rest of the equations 4.13–4.54 are used as they are taking into consideration the new geometrical relations.

Unlike the end fitting lengths, the stowed length has no effect on the analytical calculations other than posing a limitation to the attainable deformed configurations in practice.

Strain energy landscapes are used to qualitatively detect any differences in the mechanical behaviour and stability characteristics between the two models. Figure 7.6 shows the strain energy landscapes of the mechanism assembled of double-helices in a truss-like configuration with initial truss angle $\alpha_{0,1} = 70^\circ$, and $l_{\text{end}_a,i} = 25$ mm and $l_{\text{end}_b,i} = 0$ mm—as derived from the test rig design—for the different reconfiguration modes. As in Figure 6.2, double-helices of a $[45_2/0/45_2]$ strip lay-up and with dimensions $L = 95$ mm, $R = 15$ mm, $R_i = 30$ mm and $W = 5$ mm are used. The strain energy landscapes, thus the design space, present gaps around the hinge points of the supports occurring from the length accounted for the end fittings. Changes in the relative distance between extrema are observed and features, including the stable equilibria and the connectivity between them, are affected.

For Mode I (Figure 7.6a) the mechanism develops five stable equilibria compared to the four in the previous results (Figure 6.2). The difference is detected in the position where the two helices are collinear with zero horizontal displacement of the apex (point 5 in Figure 7.6a). This configuration is now a stable equilibrium. This is due to the end fitting lengths considered in this model; on the one hand the energy landscape is now interrupted around the hinge points of the supports and the area around point 5 becomes a valley; on the other the helices deform more in that configuration than before resulting in both helices having negative axial forces and axial stiffnesses of a positive sign, thus the system self-equilibrates while the helices pull against each other, thus stabilizing the equilibrium (Figure 7.7). Additionally, a second bifurcation of the equilibrium path is detected, intersecting the primary equilibrium path in two positions (red markers in Figure 7.6a). This path is discontinuous owing to the gaps in the strain energy landscape from the end fitting lengths. Discontinuities are also present in the secondary equilibrium path for Mode II (red markers in Figure 7.6b) and in the inner equilibrium path for Mode III (red markers in Figure 7.6c). For Mode II the mechanism develops two interior stable equilibria (points 1 and 2 in Figure 7.6b), positioned slightly above and below the position where the single minimum for the results of the initial model is located. Similar is the two stable equilibria observed in the outer equilibrium path for Mode III (points 1 and 2 in Figure 7.6c), while no stable equilibrium is encountered in the inner path. For both Mode II and Mode III, the boundary equilibria are preserved.

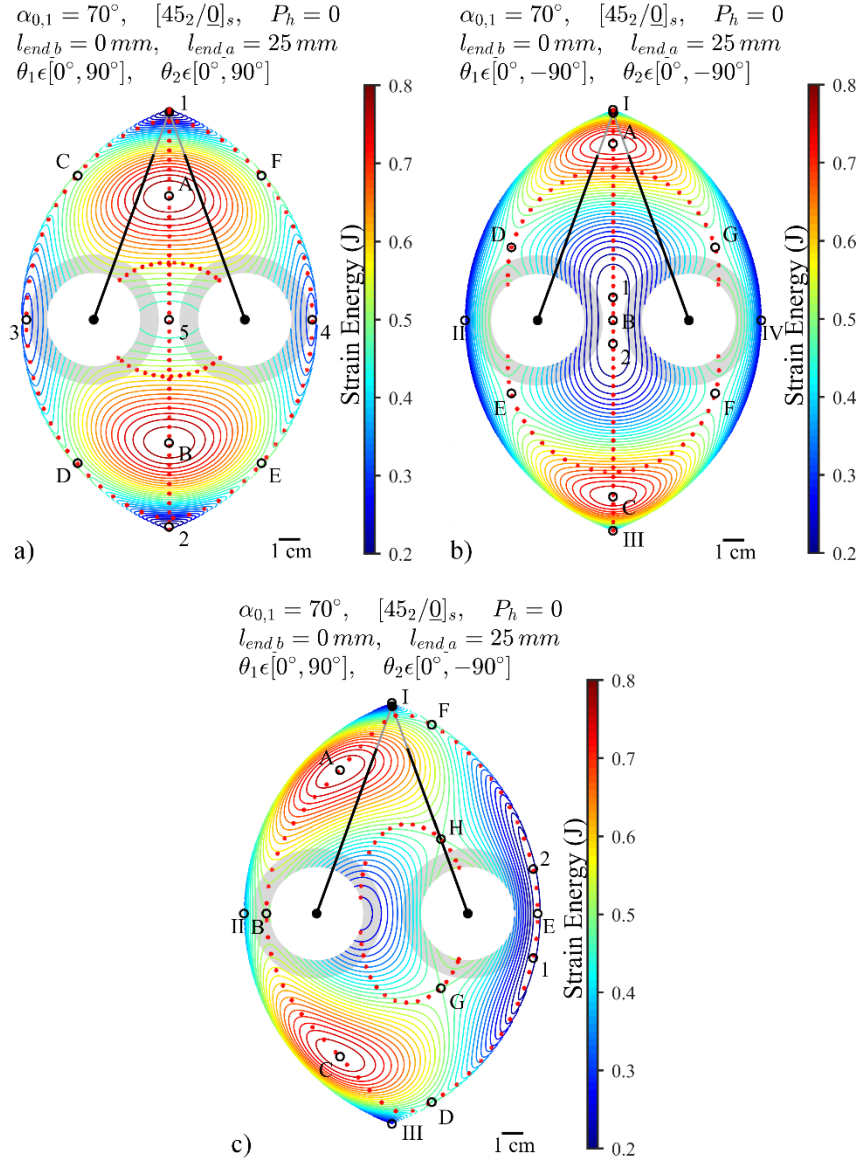


Figure 7.6: Strain energy landscapes for a compliant mechanism of double-helices of a $[45_2/0/45_2]$ composite strip lay-up, $L = 95 \text{ mm}$, $R = 15 \text{ mm}$, $R_i = 30 \text{ mm}$, $W = 5 \text{ mm}$ assembled in a truss-like configuration with an initial angle $\alpha_{0,1} = 70^\circ$, $l_{end,a,i} = 25 \text{ mm}$ and $l_{end,b,i} = 0 \text{ mm}$ for different reconfiguration modes. a) Mode I: $\theta_i \in [0^\circ, 90^\circ]$; b) Mode II: $\theta_i \in [0^\circ, -90^\circ]$; c) Mode III: $\theta_1 \in [0^\circ, 90^\circ]$, $\theta_2 \in [0^\circ, -90^\circ]$. Points labelled 1–5 denote stable equilibria, while points A–H identify positions of unstable equilibrium. Points I–IV denote stable boundary equilibria. Black lines represent the double-helices at the initial truss configuration. Red points indicate the equilibrium paths of the apex under the application of a vertical load ($P_h = 0$). Shaded ring areas represent the limitation from the stowed length of the helix.

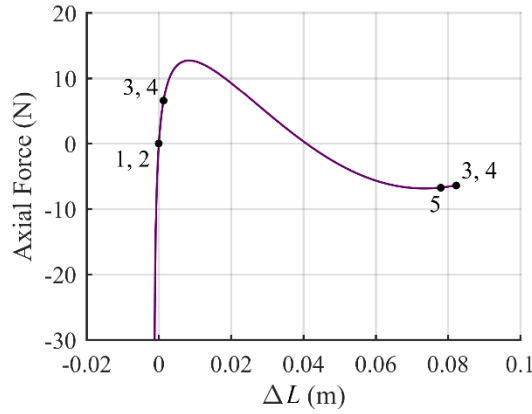


Figure 7.7: Axial forces of double-helices of a $[45_2/0/45_2]$ composite strip lay-up, $L = 95$ mm, $R = 15$ mm, $R_t = 30$ mm, $W = 5$ mm at selected equilibrium points of the mechanism for the reconfiguration Mode I.

A closer inspection of the strain energy landscapes taking into consideration the stowed length of the double-helices (shaded ring area in Figure 7.6) reveals equilibrium configurations, *i.e.* positions 3, 4 and 5 for Mode I (Figure 7.6a), 1, B and 2 for Mode II (Figure 7.6b), and E and B for Mode III (Figure 7.6c), close to the boundaries of the attainable design space that might create a practical difficulty in obtaining them or that cannot at all be achieved. Thus, changes to the dimensions of the double-helices are made to facilitate the manufacture and assembly of the double-helices, and to attain as many of the equilibria as possible during testing. Double-helices with dimensions $L = 300$ mm, $R = 30$ mm, $R_t = 60$ mm and $W = 10$ mm are employed for the manufacture and experimental testing of the mechanism. A width of 10 mm is selected to account for drilling holes on the composite strip for the attachment of the spokes, while the choice of a lengthy helix ($L = 300$ mm) is made to allow enough space for the mechanism to deform to equilibria where the helices are in tightly coiled configurations. Figure 7.8 shows the strain energy landscapes of the assembly of such double-helices with a $[45_2/0/45_2]$ lay-up in a truss-like configuration with initial angle $\alpha_{0,1} = 70^\circ$, $l_{\text{end_a},i} = 25$ mm and $l_{\text{end_b},i} = 0$ mm for the different reconfiguration modes. Conversely to the results above in Figure 7.6, these energy landscapes are similar to those of the initial model used for the analysis of the mechanism shown in Figure 6.2. Apart from the blank areas around the supports accounting for the end fitting lengths, and changes in the energy absolute values and relative positions of the extrema, all characteristic features, including stability, bifurcations and connectivity between stable equilibria are preserved for all reconfiguration modes.

Studying the effect of the end fitting lengths of the helix is out of the scope of this research. It is nonetheless clear that the end fitting length affects the mechanism behaviour and presumably some critical ratios of the end fitting lengths to the length of the helix exist defining the transition between the various behaviours.

As a final step before moving on to the manufacture and test of the mechanism, a stress evaluation of the double-helices is performed using the Classical Laminate Theory [246] as well as a finite element model analysis [25]. Both Tsai-Wu [247] and Tsai-Hill [248] criteria are employed to check the stresses. High stresses occur on the top layer in the composite strips as the helix deforms from an extended to a fully coiled configuration; thus a decrease of the helix twisting stiffness is required. Checking individually each of the longitudinal, transverse and in-plane shear stresses in this ply, high stress is encountered in the tensile transverse direction. By replacing this layer, as well as the bottom one to maintain the symmetry, to a layer with a fibre angle at 90° instead of 45° , the stress criteria are now fulfilled. Alternatively, the use of a material with similar properties but with higher strain capabilities could have been considered. However, the same material used for the earlier analytical results presented herein was preferred, the Hexcel IM7/8552 unidirectional carbon fibre prepreg (see Table 3.1), which is a representative aerospace engineering grade composite-laminate material system and to maintain consistency throughout the present work. The strain energy landscapes of the mechanism with double-helices of a $[90/45/0]_s$ are presented in Figure 7.9. No qualitative difference in the overall behaviour is observed other than an overall rescaling—compared to Figure 7.8—with all characteristic features maintained.

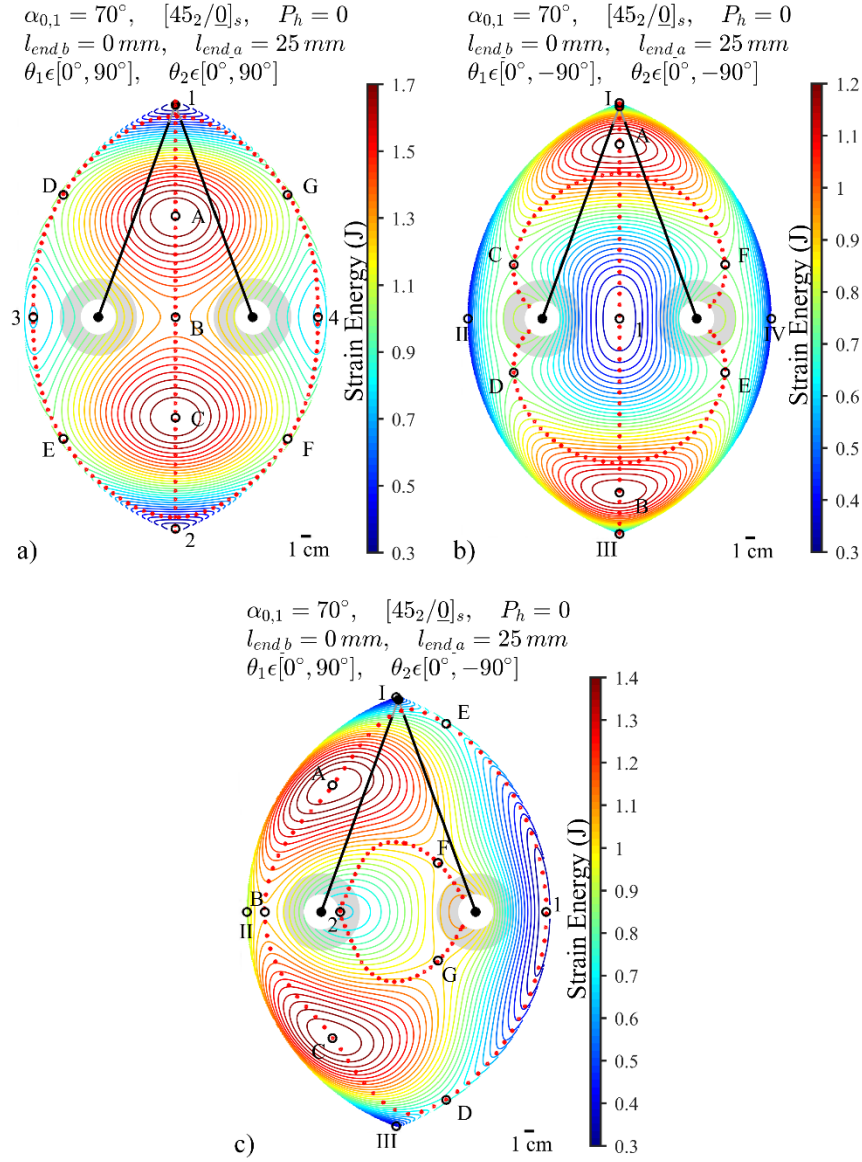


Figure 7.8: Strain energy landscapes for a compliant mechanism of double-helices of a $[45_2/0/45_2]$ composite strip lay-up, $L = 300\text{ mm}$, $R = 30\text{ mm}$, $R_i = 60\text{ mm}$, $W = 10\text{ mm}$ assembled in a truss-like configuration with an initial angle $\alpha_{0,1} = 70^\circ$, $l_{end\,a,i} = 25\text{ mm}$ and $l_{end\,b,i} = 0\text{ mm}$ for different reconfiguration modes. a) Mode I: $\theta_i \in [0^\circ, 90^\circ]$; b) Mode II: $\theta_i \in [0^\circ, -90^\circ]$; c) Mode III: $\theta_1 \in [0^\circ, 90^\circ]$, $\theta_2 \in [0^\circ, -90^\circ]$. Points labelled 1–5 denote stable equilibria, while points A–G identify positions of unstable equilibrium. Points I–IV denote stable boundary equilibria. Black lines represent the double-helices at the initial truss configuration. Red points indicate the equilibrium paths of the apex under the application of a vertical load ($P_h = 0$). Shaded ring areas represent the limitation from the stowed length of the helix.

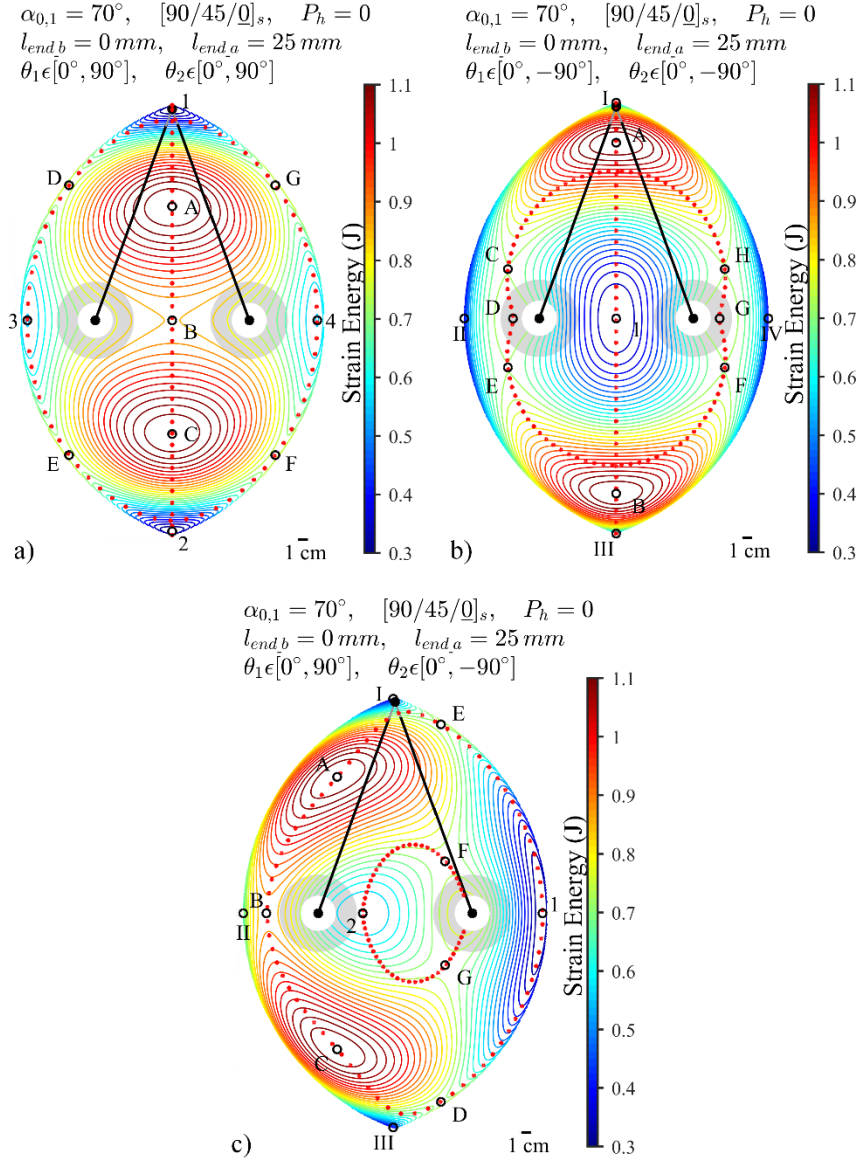


Figure 7.9: Strain energy landscapes for a compliant mechanism of double-helices of a $[90/45/0/45/90]$ composite strip lay-up, $L = 300\text{ mm}$, $R = 30\text{ mm}$, $R_i = 60\text{ mm}$, $W = 10\text{ mm}$ assembled in a truss-like configuration with an initial angle $\alpha_{0,1} = 70^\circ$, $l_{end\,a,i} = 25\text{ mm}$ and $l_{end\,b,i} = 0\text{ mm}$ for different reconfiguration modes. a) Mode I: $\theta_i \in [0^\circ, 90^\circ]$; b) Mode II: $\theta_i \in [0^\circ, -90^\circ]$; c) Mode III: $\theta_1 \in [0^\circ, 90^\circ]$, $\theta_2 \in [0^\circ, -90^\circ]$. Points labelled 1–5 denote stable equilibria, while points A–H identify positions of unstable equilibrium. Points I–IV denote stable boundary equilibria. Black lines represent the double-helices at the initial truss configuration. Red points indicate the equilibrium paths of the apex under the application of a vertical load ($P_h = 0$). Shaded ring areas represent the limitation from the stowed length of the helix.

7.4 Double-helix manufacture, experimental set-up and results

Prior to the assembly of the double-helices in the truss-like mechanism and the experimental testing for the validation of the analytical model and the results presented in the section above (§7.3), the constituent members of the mechanism, the double-helices, were examined separately. In this section the manufacture process of a double-helix prototype is presented and the experimental results of the individual helices upon an axial load at their extremity are discussed.

7.4.1 Double-helix manufacture

The manufactured double-helices are composed of composite strips of a $[90/45/0]_s$ lay-up and dimensions $L = 300 \text{ mm}$ by $W = 10 \text{ mm}$. A symmetric lay-up was chosen as representative to show the reconfigurability of the mechanism later on, while a 10 mm strip width was selected to allow for drilling the holes to accommodate the spokes. For the manufacture of the double-helices a similar process to the one described in [25] was followed. The composite strips consist of 5 plies of unidirectional Hexcel 8552/IM7 pre-impregnated carbon fibre reinforced plastic [208] with the 0° direction corresponding to the longitudinal x -axis of the strip (see Figure 3.1). Patches 10 x 10 mm of 90° unidirectional Hexcel 8552/IM7 were placed on top and bottom of the strip laminate as local reinforcement at the spoke's interface to avoid delamination issues (Figure 7.10a). The strips were initially laid-up flat and then placed on an aluminium cylindrical mould of radius $R_t = 60 \text{ mm}$ to cure (Figure 7.10a, b). A silicon sheet was placed on top of the release film to provide a nice surface finish to the strips, and a bag inside a bag was built to seal the laminate and apply vacuum bag to remove excess air and consolidate it (Figure 7.10c). An autoclave was used to cure the composite under a combination of pressure and heat [208].

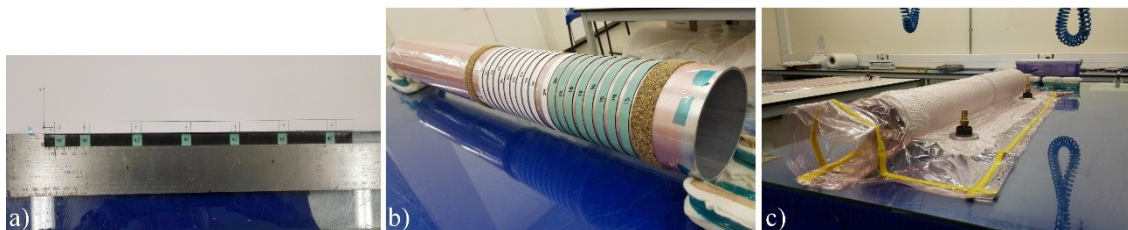


Figure 7.10: Manufacture stages of the helix strips: a) lay-up of the strips flat, including local reinforcement at the interface with the spokes; b) place of the strips on an aluminium cylindrical tool; c) vacuum bag of the laminate.

After curing, the composite strips were ground to remove excess resin from their perimeter, owing to resin flow during curing, using an EcoMet 250 Buehler grinder/polisher machine. Next, the holes to accommodate the spokes were drilled on the strips using a Herbert B High Speed Bench drilling machine with a suitable drill bit to ensure delamination was minimised. Moreover, a rig made of Perspex acrylic material was designed to facilitate the drilling by keeping the curved strip flat and securing the position of the hole (Appendix A.2). Seven holes with a 2 mm diameter were created in each strip; the first two at a 25 mm distance and the rest equally spaced. Stainless steel rods were used as the spokes to assemble the helices and keep the strips apart at a constant distance, machined at their ends to fit an M2 x 5 mm screw. Nylon washers were placed in-between the spokes, the strip and the screws to limit friction, while the spokes were loosely tightened to allow the strip to twist freely around the spokes' axes.

7.4.2 *Experimental set-up*

The double-helices are tested under the application of an axial load. One end of the helix is connected to the load transducer of the moving crosshead of a universal testing machine through a fixture that allows twist of the helix (see Appendix A.3). A ball bearing is placed where the end spoke of the helix is attached to the fixture to allow twist of the helix around its longitudinal axis. The other end of the helix is fixed; the end spoke of the helix is press-fitted to an L-shaped bracket that is fixed to the test machine, while bolts are used to constrain any movement of the spoke (see Appendix A.3). An AGS-X Series Shimadzu test machine with 1 kN load cell and a precision of the force measurement within $\pm 1\%$ of the indicated test force (at 1/500 to 1/1 load cell rating) was used to perform the test and a displacement-control loading was employed at a rate of 0.5 mm/sec. Both vertical load and displacement were recorded using the Trapezium X software of the Shimadzu machine. Figure 7.11 shows the experimental set-up at different stages during the testing.



Figure 7.11: Experimental set-up at different configurations: a) slightly twisted, b) twisted and c) coiled.

7.4.3 Results

The double-helices were tested for deformations with helix angles θ both in $[0^\circ, 90^\circ]$ and in $[0^\circ, -90^\circ]$, with $\theta = 0^\circ$ corresponding to the straight configuration. For each case two tests were performed: i) a compression test, starting from an extended configuration, the helix is deformed to reach a coiled configuration; and ii) a tensile test, starting from a coiled configuration, the helix is stretched until an extended configuration is reached. Figure 7.12a and b show the experimental results for double-helices deforming with helix angle $\theta \in [0^\circ, 90^\circ]$ for a compression and a tensile test, respectively. The results are compared with the results from the analytical model of the double-helix. The experimental results for helix deformations with $\theta \in [0^\circ, -90^\circ]$ for both compression and tensile tests are included in Figure 7.13a and b, respectively, and compared to the corresponding analytical results.

The experimental results of four double-helices are included in Figure 7.12–Figure 7.13. A notation, *i.e.* HS 4-5, is used to describe each manufactured helix (the sample number). There is a good agreement between the experimental results for the different helices, demonstrating repeatability of the manufactured prototypes. Any deviations in the absolute load values in the experimental set of curves for the same test can be explained by dissimilarities of the helices due to manufacturing imperfections, including: i) misalignment of the holes with respect to the centre-line of the strip, owing to the difficulty in drilling holes on a curved composite strip (Figure 7.14); ii) slight variations of the strip width between helices as

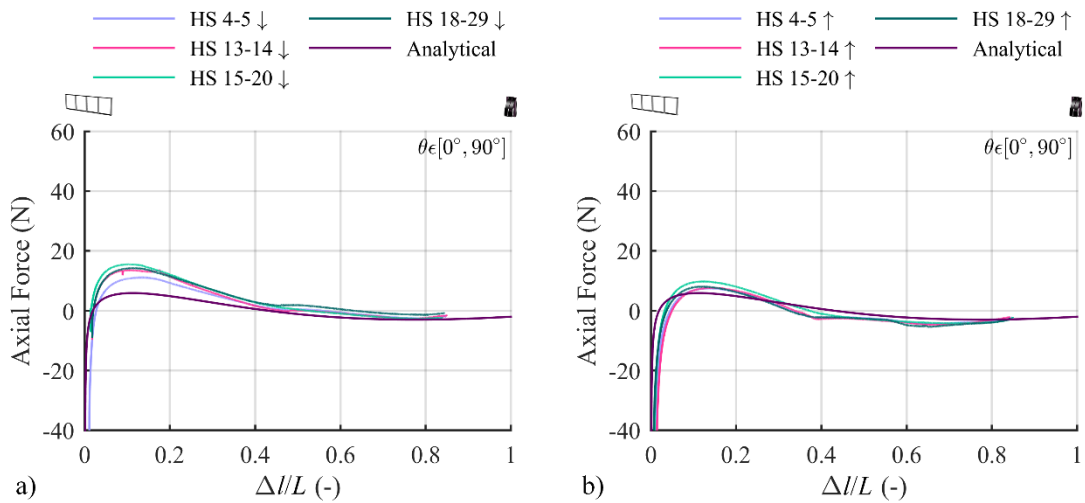


Figure 7.12: Load-displacement curves of double-helices for helix deformations with $\theta \in [0^\circ, 90^\circ]$ under a) a compression test and b) a tensile test. Results are for double-helices of a $[90/45/0/45/90]$ lay-up, with dimensions $L = 292$ mm, $R = 30$ mm, $R_t = 60$ mm, $W = 10$ mm. The displacement Δ is normalized to the length L of the strips, with $\Delta/L = 0$ representing the fully-extended and $\Delta/L = 1$ its fully coiled configuration.

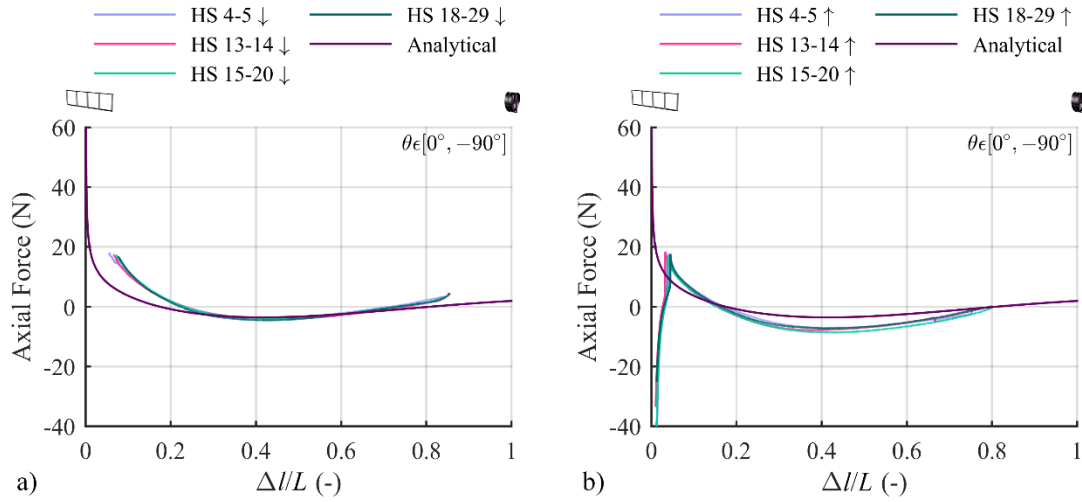


Figure 7.13: Load-displacement curves of double-helices for helix deformations with $\theta \in [0^\circ, -90^\circ]$ under a) a compression test and b) a tensile test. Results are for double-helices of a $[90/45/0/45/90]$ lay-up, with dimensions $L = 292$ mm, $R = 30$ mm, $R_i = 60$ mm, $W = 10$ mm. The displacement Δl is normalized to the length L of the strips, with $\Delta l/L = 0$ representing the fully-extended and $\Delta l/L = 1$ its fully coiled configuration.



Figure 7.14: Misalignment of the spokes with respect to the centre-line of the strip. Dashed line represents the axis that passes through the middle of the width of the strip along its length.

well as along the length of the strip of the helix itself from the grinding of the edges of the composites; and
iii) friction at the interface with the spokes.

Figure 7.12a and Figure 7.13a show the results from the compression test for helix deformations with $\theta \in [0^\circ, 90^\circ]$ and $\theta \in [0^\circ, -90^\circ]$, respectively. An initial twist was applied at the start of the experiment to nudge the helix to a configuration with either $\theta \in [0^\circ, 90^\circ]$ or $\theta \in [0^\circ, -90^\circ]$, hence the delayed start of the experimental curves for the compression test. Starting from a slightly twisted configuration, the helix was then compressed to reach a coiled configuration. The test was stopped once the strips of the helix started colliding, and thus the experimental curves stop at a displacement $\Delta l/L \approx 0.85$, close to the helix stowed length. Similarly, for the tensile test (Figure 7.12b and Figure 7.13b), the experiment for helix deformations with $\theta \in [0^\circ, 90^\circ]$ started from a coiled configuration where the helix strips collided. For $\theta \in [0^\circ, -90^\circ]$ the tests started at the stable coiled configuration (see Chapter 3). The helix was stretched until it reached the straight configuration ($\Delta l/L = 0$), however, the helix operating in $\theta \in [0^\circ, -90^\circ]$, would snap to a

configuration with $\theta \in [0^\circ, 90^\circ]$ as it approached the straight state, thus the sudden jump of the experimental curves in Figure 7.13b at $\Delta l/L \approx 0.04$.

A difference between the experimental results obtained by a compression and a tensile test is observed (Figure 7.12 and Figure 7.13). Overall higher load values are observed for a compression test, notably at the early stage of the test where the helix starts to twist and coil from an extended configuration (Figure 7.12a and Figure 7.13a). This difference suggests a difficulty in the deformation of the helix at this section and the need of a higher axial force to achieve the coiling of the helix. This can be attributed to the friction developed at the joint of the helix with the fixture, *i.e.* the bearing, since through an applied vertical load we try to provoke a twist at the helix for it to coil, as well as the shear buckling of the helix noticed at this early stage during testing (Figure 7.15a). The use of elongated helices made them susceptible to buckling and additional imperfections, such as the nonuniform deformation of the helix noticed during the test, with the pitch varying across the helix length (Figure 7.15b). The nonuniform coiling was not observed in previous work by Lachenal *et al.* [25, 26] and is presumably dependent on the length-to-radius ratio of the helices. All these are thought to have caused the overall differences observed in the load values between a compression and a tensile test.

Figure 7.12 and Figure 7.13 include also the corresponding results from the analytical model of the double-helix. The actual lengths of the double-helices, from centre to centre of the end spokes, were measured at $L = 292$ mm after curing and grinding of the strips, thus the results herein were compared to the analytical results of a helix with dimensions $L = 292$ mm, $R = 30$ mm, $R_i = 60$ mm and $W = 10$ mm. These dimensions are also used for the results from the structural analysis of the mechanism assembled of double-helices further below for a more accurate comparison to the experimental results.

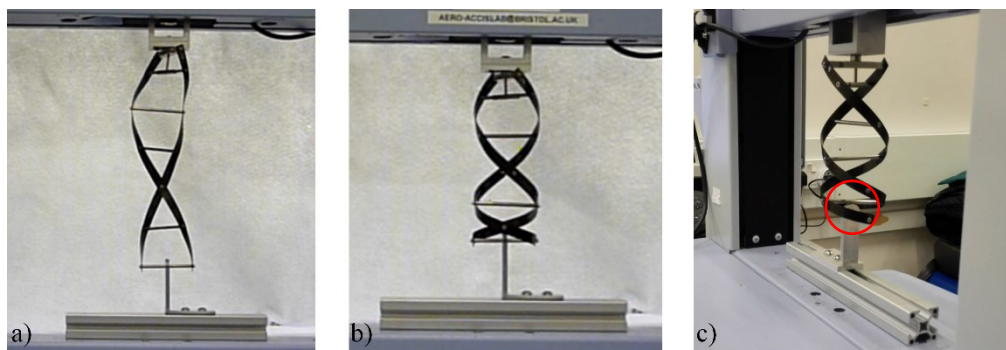


Figure 7.15: a) Shear buckling of the helix; b) nonuniform deformation of the helix; c) contact between adjacent spokes.

The analytical curves are in good qualitative agreement with the experimental data (Figure 7.12 and Figure 7.13). Large quantitative differences are noticed between the experimental curves from a compression test and the analytical predictions for helix configurations slightly twisted ($\Delta/L < 0.25$) that can be explained by the friction in the bearing and/or the localised buckling of the helix as explained above. For the rest of the helix configurations and the experimental results from a tensile test a close agreement is observed with the analytical model. The small differences between these curves can be attributed to variations between the model and the helix prototypes. Friction at the interface with the spokes and localised effect of the holes in the strips have not been taken into consideration in the analytical model. The local reinforcement placed at the regions of the holes to limit delamination, thus locally constraining the transverse curvature, was not modelled. Most significant nonetheless is the unexpected nonuniform deformation of the helix with the pitch varying across the helix length. This behaviour breaches a fundamental assumption for the analytical model of the helices. It is presumably dependent on the length-to-radius ratio of the helices as herein we used more elongated helices compared to the previous work by Lachenal *et al.* [25, 26], where, despite the mismatch of the experimental data and the analytical model predictions, such behaviour was not reported. In addition to this, the nonuniform deformation resulted in the spokes of the helices touching during coiling/uncoiling (Figure 7.15c) and the presence of slight kinks in the load-displacement curves.

7.5 Initial experimental set-up and results for assembly of double-helices

A truss prototype of the mechanism assembled of double-helices was manufactured and tested under application of a vertical load at the apex. This section presents initial test results to validate the analytical model and assess the feasibility of the proposed mechanism.

7.5.1 Initial experimental set-up

Figure 7.16 shows the set-up for the test of the assembly of double-helices in a truss-like configuration. In this initial set-up linear guides with ball bearing carriages were used to achieve the motion of the top base frame relative to the lower base frame to allow sideways movement of the truss structure, and thus the apex. This enabled measurement of equilibrium paths where both horizontal and vertical displacement of the apex occur, *i.e.* the bifurcation paths for Mode I and II or the equilibrium paths in Mode III (see red markers in Figure 7.9). The details of the test rig design have been discussed in previous section (§7.2).

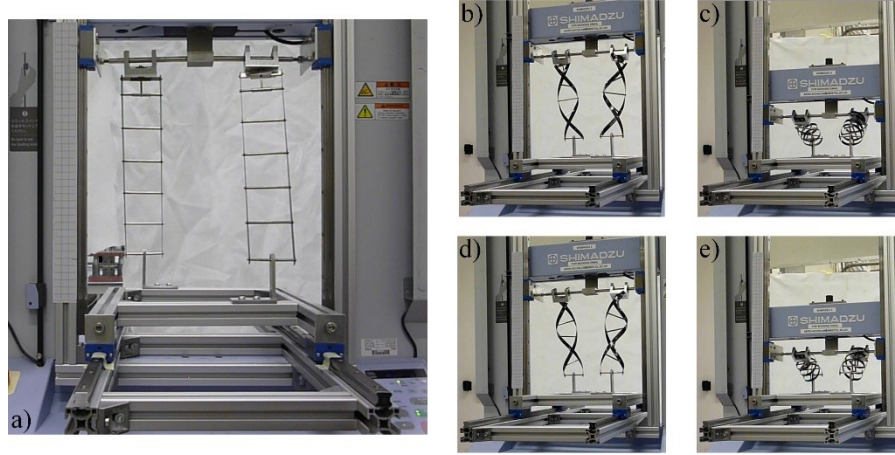


Figure 7.16: Experimental set-up of the truss assembly of double helices in different configurations during testing: a) configuration with both helices fully-extended; b-c) configurations along the main equilibrium path between points 1 and B for Mode I with both helices twisted equally; d-e) configurations along the main equilibrium path between points 1 and A for Mode II with both helices twisted equally.

An AGS-X Series Shimadzu test machine with 1 kN load cell and a precision of the force measurement within $\pm 1\%$ of the indicated test force (at 1/500 to 1/1 load cell rating) was used to perform the test and apply a vertical load on the fixture, using a displacement-control loading at a rate of 0.5 mm/sec. Both vertical load and displacement were recorded using the Trapezium X software of the Shimadzu machine. To capture the horizontal displacement of the top base frame, and thus of the truss apex, an Imetrum Video Gauge camera system, with 17 fps frame rate and a 1392 x 1040 pixel camera with a 25 mm focal length lens, was used, set to track the horizontal displacement of a point close to the base support of the truss.

7.5.2 Results

First, the response of the prototype of the mechanism of the double-helices assembled in a steep truss ($\alpha_{0,1} = 70^\circ$), with both helices twisting with $\theta \in [0^\circ, 90^\circ]$ (reconfiguration Mode I) was investigated. Both a compression and a tensile test were performed, applying a vertical load at the apex of the assembled structure starting from different configurations. For the compression test, the helices were set close to the initial truss configuration with a truss angle $\alpha_{0,1} = 70^\circ$ (point 1 in the energy landscape in Figure 7.9a), then compressed by applying a downwards displacement at the apex. The test stopped slightly after the helices become collinear. For the tensile test, starting from a configuration with the helices set collinear (*i.e.* point B in the energy landscape in Figure 7.9a) the apex was stretched upwards until both helices reach an extended configuration. The tests were also performed without the helices attached on the rig to measure the friction force due to the vertical linear guides placed on the U-shaped frame, which was then subtracted

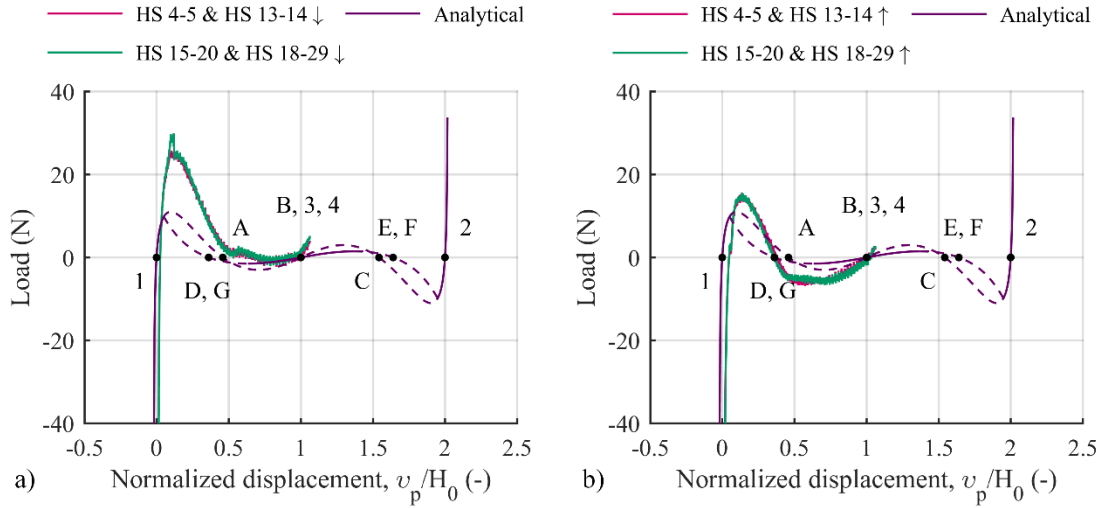


Figure 7.17: Load-displacement curves under the application of a vertical load at the apex of the truss of double-helices for reconfiguration Mode I, $\theta \in [0^\circ, 90^\circ]$, for a) a compression test and b) a tensile test. Dashed lines represent areas of instability for the analytical data. Results are for initial truss angle $\alpha_{0,1} = 70^\circ$ and double-helices of a [90/45/0/45/90] lay-up, with dimensions $L = 292$ mm, $R = 30$ mm, $R_i = 60$ mm, $W = 10$ mm. Points 1–4 are stable equilibrium points. Points A–G are unstable equilibrium points. The displacement has been normalized with respect to the initial height of the truss structure.

from the force reading obtained for the assembly of the double-helices. Figure 7.17 depicts the load-displacement curves from the experimental tests and the structural analysis of the mechanism. Large differences in the load values are observed between the analytical model and the experimental data from the compression test at the early stages of the experiment, when the helices are at slightly twisted configurations (Figure 7.17a). This discrepancy, noticed in the results from the compression test of a single helix too, is thought to be caused by the friction at the joint of the helix with the fixture at the truss apex, *i.e.* the bearing, trying to force a twist on the helices by an applied axial load, and/or by the occurrence of localised buckling in the helix which has not been observed before (Figure 7.18a, b). This localised buckling is primarily attributed to the use of such elongated helices, while it indicates also that the distance between the spokes and any misalignment in their position can affect the deformation of the strips. Other than this, a good correlation between the analytical model and the experimental data exists. Differences can be attributed to friction both between the spokes and the helical strips and at all other joints in the fixture, any imperfections during manufacturing of the helices and/or the presence of a nonuniform deformation of the helix, *i.e.* its pitch varying across the helix length (Figure 7.18c, d); all which were unaccounted for in the model. As a result of the nonuniform deformation of the helices, the spokes would touch during coiling/uncoiling (Figure 7.18e, f), introducing additional loads in the static equilibrium of the system, thus the kinks in the load-displacement curves for $u_p/H_0 > 0.4$. The experiment was repeated

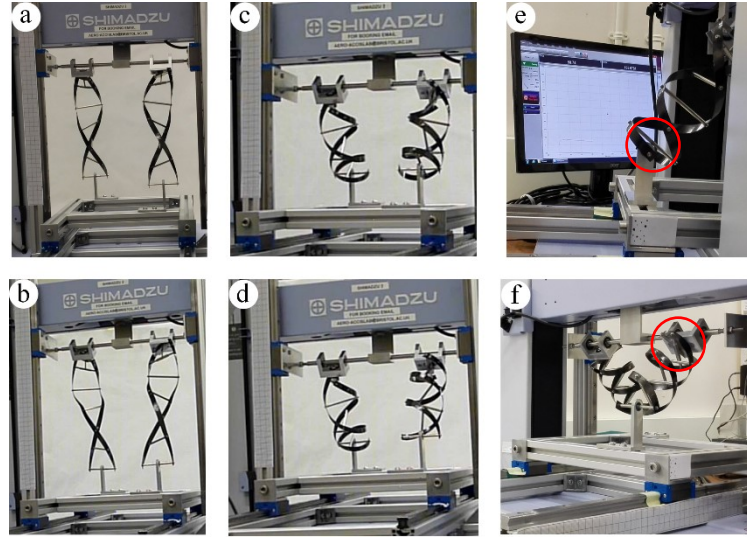


Figure 7.18: a-b) Localised buckling of the helix strips; c-d) nonuniform deformation of the helix along its length; e-f) contact between adjacent spokes during coiling/uncoiling.

for different sets of double-helices and a similar response was obtained. The sudden jump in one of the load-displacement curves for a compression test at $u_p/H_0 \approx 0.1$ (Figure 7.17a) occurred from a misfit of the pin between the two end spokes resulting in a wobbly end fitting and an out of plane deformation of the helix at that point.

Next, to demonstrate the reconfigurability of the proposed mechanism, the truss prototype of the double-helices was tested for reconfiguration Mode II, with both helices twisting with $\theta \in [0^\circ, -90^\circ]$. Figure 7.19 shows the load-displacement curve for the analytical model and the experimental results for a compression (Figure 7.19a) and a tensile test (Figure 7.19b). For the compression test, starting from a position with both helices at an extended configuration and a truss angle $\alpha_{0,1} = 70^\circ$, the truss apex was then compressed until the helices become collinear. An initial twist was applied at the start of the experiment to nudge the helices to a configuration with $\theta \in [0^\circ, -90^\circ]$, hence the delayed start of the experimental curves (Figure 7.19a). The experimental results are in good agreement with the predictions from the analytical model. Slightly higher absolute load values observed at configurations where both helices are slightly twisted are presumably the result of friction at the end fitting's bearing from provoking a twist under an axial load while restricting the helices tendency to buckle or deform out of plane. For a tensile test, starting from a position where the helices are collinear (*i.e.* point 1 in the energy landscape in Figure 7.9b), the truss apex is pulled upwards to approach a configuration with both helices extended. As the helices uncoiled to reach their straight configurations, they would snap to configurations with $\theta \in [0^\circ, 90^\circ]$, hence the sudden jump in the load-displacement curve at $u_p/H_0 \approx 0$. Again, a good correlation between the analytical model and

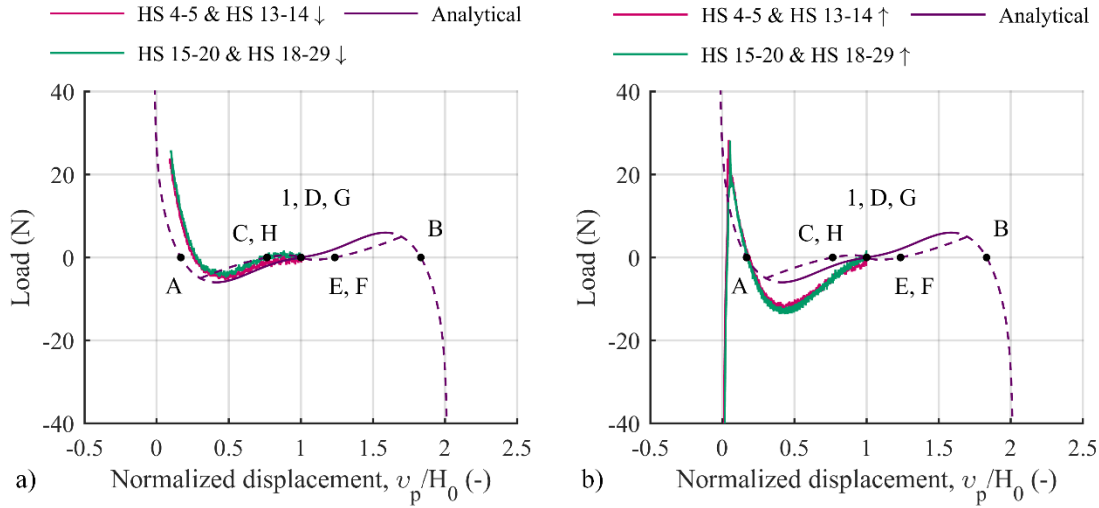


Figure 7.19: Load-displacement curves under the application of a vertical load at the apex of the truss of double-helices for reconfiguration Mode II, $\theta \in [0^\circ, -90^\circ]$, for a) a compression test and b) a tensile test. Dashed lines represent areas of instability for the analytical data. Results are for initial truss angle $\alpha_{0,1} = 70^\circ$ and double-helices of a [90/45/0/45/90] lay-up, with dimensions $L = 292$ mm, $R = 30$ mm, $R_i = 60$ mm, $W = 10$ mm. Point 1 denote a stable equilibrium. Points A–H are unstable equilibrium points. The displacement has been normalized with respect to the initial height of the truss structure.

experimental data exists. The differences can be traced back to the individual helix behaviour for the same test and features that were not modelled, including the spokes effect, the local reinforcement at the holes, friction at the joints in the fixture, and/or were not expected, *i.e.* the nonuniform deformation of the helices that resulted in spokes colliding during testing, as already mentioned.

In this set of experiments, we were unable to obtain the bifurcation paths of the reconfiguration Mode I and II or the equilibrium paths for the mechanism operating in the reconfiguration Mode III. The friction of the linear guides exceeded the horizontal force that the mechanism could provide, especially since only a vertical load is applied at the apex; this meant that the truss would not move laterally. In an attempt to overcome this problem, the set-up design was modified, as presented in the section below.

7.6 Modified experimental set-up and results for assembly of double-helices

The inability to achieve and trace the deformations of the apex on the bifurcation paths for the reconfiguration Mode I and Mode II or the equilibrium paths for Mode III, led to a revaluation of the set-up design. The main problem was identified in the inability of the structure to slide on the linear guides and allow sideways movement of the truss structure. Thus, the linear guides were replaced by lower-friction rollers that ran on the existing aluminium frame. The modified experimental set-up and the corresponding test results are presented below.

7.6.1 Modified experimental set-up

Figure 7.20 shows the modified set-up for the test of the assembly of double-helices. In this set-up, the linear guides with ball bearing carriages used in the initial experimental set-up were replaced by rollers. The rollers were attached to the top base frame, that consists the base of the truss mechanism, and slid in the slot of the aluminium profiles of the lower base frame, that is fixed to the machine. The slot of the aluminium profiles was used as the guide for the rollers and kept them aligned. No other changes were made to the experimental set-up and the same experimental procedure was followed.

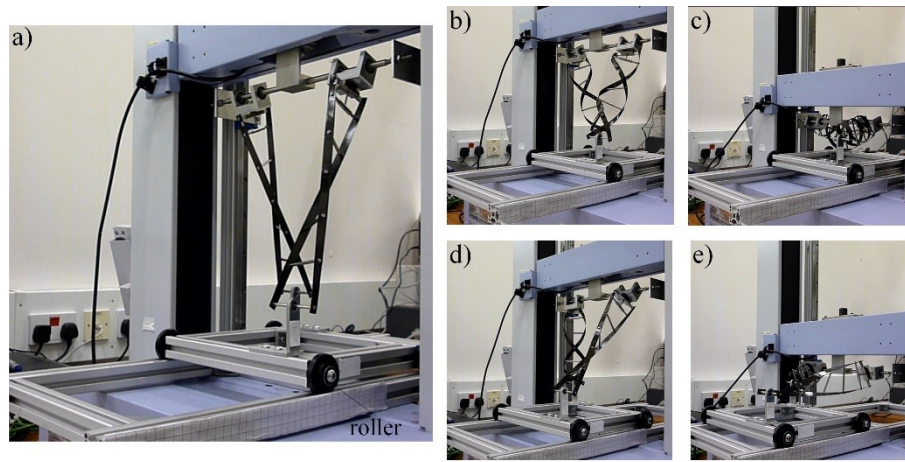


Figure 7.20: a) Modified experimental set-up, comprising rollers, of the truss assembly of double-helices. b-e) Different configurations of a prototype during testing: b) a configuration along the main equilibrium path between points 1 and A for Mode I with both helices twisted equally; c) a configuration close to point B for Mode I, with the helices collinear and twisted equally; d) a configuration on the bifurcation path between points 1 and D for Mode I, with the helices twisted to different extent; e) a configuration close to point 3 for Mode I, with the helices collinear but one in a slightly twisted and the other in a coiled configuration.

7.6.2 Results

The use of the rollers allowed the structure to move horizontally, thus we were able to achieve configurations of the truss mechanism on the bifurcation paths for both reconfiguration Mode I and Mode II, additionally to their primary vertical equilibrium paths. It also enabled to perform the test with the mechanism reconfigured to Mode III. The experimental results of the mechanism for all reconfiguration modes are presented in Figure 7.21–Figure 7.23 and compared to the corresponding analytical results.

Figure 7.21 shows the load-displacement curves obtained from the experimental testing of the prototype and the analytical model for the reconfiguration Mode I, where both helices are deforming to helix angles $\theta \in [0^\circ, 90^\circ]$. The strain energy landscape is included with the positions of the apex superimposed both as predicted from the model (red markers in Figure 7.21, right) and as obtained from the displacement record-

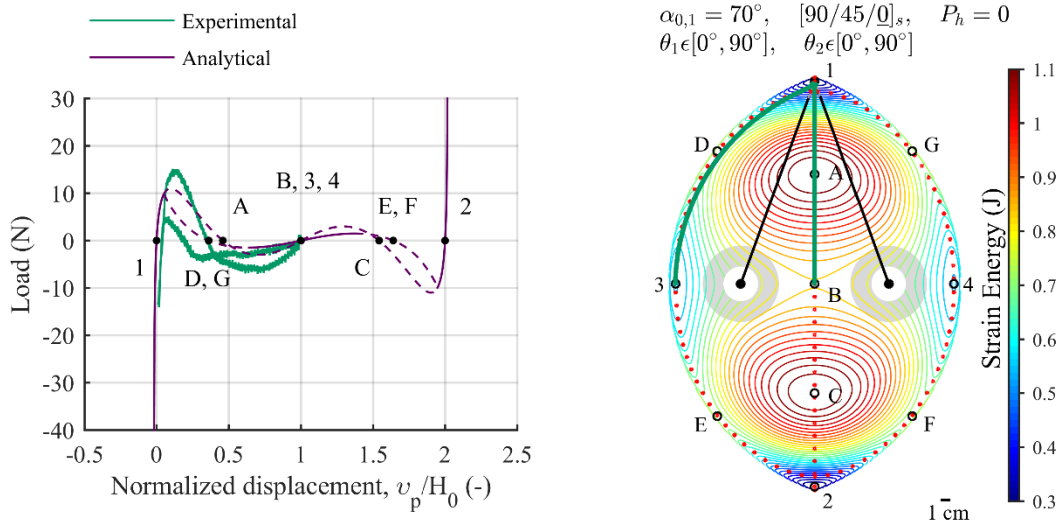


Figure 7.21: Load-displacement curves (left) under the application of a vertical load at the apex of the truss of double-helices for reconfiguration Mode I. Dashed lines represent areas of instability for the analytical data. The truss has initial angle $\alpha_{0,1} = 70^\circ$ and double-helices of $[90/45/0/45/90]$ lay-up, with dimensions $L = 292$ mm, $R = 30$ mm, $R_i = 60$ mm, $W = 10$ mm. The positions of the truss apex under an applied vertical load ($P_h = 0$) at the end effector are superimposed on the corresponding strain energy landscape (right); red markers are used for the analytical and green markers for the experimental data. Black lines represent the double-helices at the initial truss configuration. Points 1–4 are stable equilibrium points. Points A–G are unstable equilibrium points. Shaded ring areas represent the limitation from the stowed length of the helix.

ings during testing (green markers in Figure 7.21, right). A tensile test was carried out on the prototype; starting from positions on the equilibrium paths with the helices collinear, the apex is moved upwards. To obtain the primary equilibrium path, the test started from the position where the helices are collinear and experience the same deformation, point B in Figure 7.21. To attain configurations on the bifurcation path, the position with one helix at an extended and one at a twisted configuration, yet being collinear, was selected as the starting position for the test (point 3 in Figure 7.21). In both cases, the test stopped once the rollers started losing contact with the lower base frame and the truss base was lifted. This outcome was not considered in the design of the test set-up, posing an unforeseen limitation to achieve certain configurations; nonetheless, the mechanism's model could be validated. The experimental data are in good qualitative agreement with the predictions of the analytical model. Some differences in the actual values are observed that can be attributed to a variety of reasons as mentioned above, including: i) friction, which is unaccounted for in the model, both between the spokes and the composite helical strips and at all other joints in the fixture; ii) nonuniform deformation of the helix noticed during the test, with the pitch varying across the helix length; iii) the spokes of the helices touching during coiling/uncoiling as a result of the nonuniform helix deformation, evidenced by slight kinks in the load-displacement curves; iv) any imperfections during manufacturing of the helices.

The results for the mechanism operating in reconfiguration Mode II, with both helices twisting with helix angles $\theta \in [0^\circ, -90^\circ]$, are presented in Figure 7.22. The load-displacement curves as well as the strain energy landscape with the corresponding equilibrium paths of the apex for both the experimental and the analytical data are included. Like in Mode I, a tensile test was carried out, starting from different positions of the helices for the main equilibrium path and for its bifurcated branch, and applying a displacement-control loading on the fixture, pulling the apex upwards. The test was terminated once the helices snapped to configurations with $\theta \in [0^\circ, 90^\circ]$, forcing the rollers to detach from the lower base frame, as evidenced by the sudden jump in the load-displacement curve at $u_p/H_0 \approx 0$ (Figure 7.22, left). For configurations on the primary equilibrium path, with zero horizontal displacement (vertical paths on the strain energy landscape in Figure 7.22, right), the test was initiated at a position with the helices collinear and with the same deformation (point 1 in Figure 7.22). A good correlation between the experimental data and the analytical predictions exists. Small differences can be attributed to differences between the model and the prototype that were unaccounted for, *i.e.* friction at the joints, effect of the spokes, nonuniform deformation of the helices resulting also in contact of adjacent spokes during testing, manufacture imperfections. The relatively higher values in the “belly” of the curve can be traced back to the behaviour of the individual helices, with the manufactured ones being stiffer at this mode of $\theta \in [0^\circ, -90^\circ]$. To attain the bifurcation

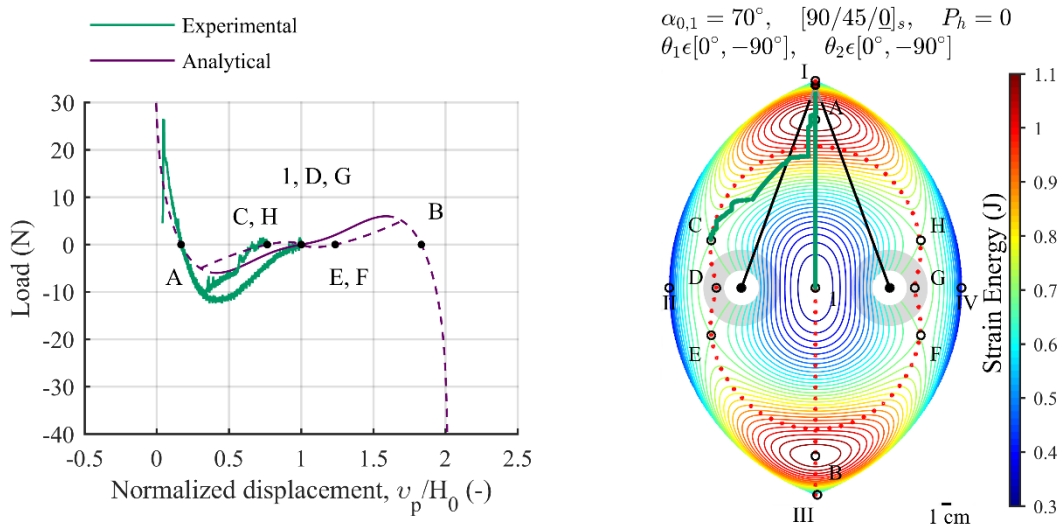


Figure 7.22: Load-displacement curves (left) under the application of a vertical load at the apex of the truss of double-helices for reconfiguration Mode II. Dashed lines represent areas of instability for the analytical data. The truss has initial angle $\alpha_{0,1} = 70^\circ$ and double-helices of $[90/45/0/45/90]$ lay-up, with dimensions $L = 292$ mm, $R = 30$ mm, $R_f = 60$ mm, $W = 10$ mm. The positions of the truss apex under an applied vertical load ($P_h = 0$) at the end effector are superimposed on the corresponding strain energy landscape (right); red markers are used for the analytical and green markers for the experimental data. Black lines represent the double-helices at the initial truss configuration. Point 1 denote a stable equilibrium. Points A–H are unstable equilibrium points. Points I–IV denote stable boundary equilibria. Shaded ring areas represent the limitation from the stowed length of the helix.

path, an equilibrium configuration on it is selected as the starting point for the test (point C in Figure 7.22). Unlike in Mode I, the position with the helices being collinear, one at an extended and the other at a twisted configuration (point D in Figure 7.22), was infeasible due to limitation for the helices' stowed length (shaded ring regions in Figure 7.22). Small sudden jumps observed in the load-displacement curve of the bifurcation path occurred from the rollers losing contact with the fixed, lower base frame and the truss base being lifted momentarily at these points, then manually put back and nudged to a position close to the desired path to continue the test. These positions can be traced as jumps in the corresponding path of the positions of the apex too (green markers in Figure 7.22, right) and help explain the mismatch of the apex positions path between the experimental and analytical data.

Finally, the truss prototype was tested under a vertical load with the helices operating in Mode III. In this reconfiguration mode one helix deforms with $\theta \in [0^\circ, 90^\circ]$ and the second with $\theta \in [0^\circ, -90^\circ]$. As above, a tensile test was performed. Starting from positions on the equilibrium paths where the helices are collinear (points 1 and 2 in Figure 7.23), a displacement-control loading was applied to move the apex upwards. The experimental results are displayed in Figure 7.23 and compared to the analytical ones. Both the load-displacement curves and the strain energy landscape with the apex positions both from the analytical and

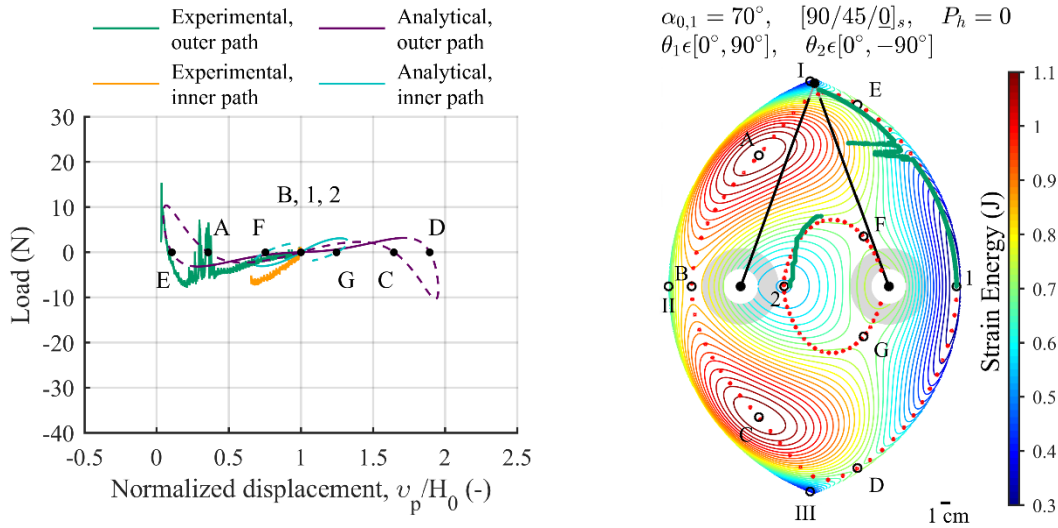


Figure 7.23: Load-displacement curves (left) under the application of a vertical load at the apex of the truss of double-helices for reconfiguration Mode III. Dashed lines represent areas of instability for the analytical data. The truss has initial angle $\alpha_{0,1} = 70^\circ$ and double-helices of $[90/45/0/45/90]$ lay-up, with dimensions $L = 292$ mm, $R = 30$ mm, $R_i = 60$ mm, $W = 10$ mm. The positions of the truss apex under an applied vertical load ($P_h = 0$) at the end effector are superimposed on the corresponding strain energy landscape (right); red markers are used for the analytical and green markers for the experimental data. Black lines represent the double-helices at the initial truss configuration. Points 1 and 2 are stable equilibrium points. Points A–G are unstable equilibrium points. Points I–III denote stable boundary equilibria. Shaded ring areas represent the limitation from the stowed length of the helix.

the experimental data superimposed are shown. Overall, there is a good correlation between the experimental data and the predictions from the analytical model. Differences in the actual values can be attributed to features that were not modelled, as described previously. Sudden jumps in the load-displacement curve of the outer equilibrium path occur at the positions that the rollers detached from the fixed, lower base frame; the truss base was lifted, then manually placed back and nudged to settle in a position and continue the test, evidenced by jumps in the apex positions path as well (green markers in Figure 7.23, right). The sudden jump observed in the load-displacement curve at $u_p/H_0 \approx 0$ (Figure 7.23, left), where both helices are slightly twisted, was caused by the helix with $\theta \in [0^\circ, -90^\circ]$ snapping to a configuration with $\theta \in [0^\circ, 90^\circ]$; that was the termination point for this test. This reason, the snap of the helix with $\theta \in [0^\circ, -90^\circ]$ once in a slightly twisted configuration to a configuration with $\theta \in [0^\circ, 90^\circ]$, was also the obstacle in attaining configurations of the rest of the outer equilibrium path, in the region of the equilibrium points A and B where the helix with $\theta \in [0^\circ, -90^\circ]$ operates close to slightly twisted configurations (see Figure 7.23). While that was the issue for the outer equilibrium path, a difficulty in obtaining the inner path was caused by the helices' stowed length restraints (shaded ring regions in Figure 7.23). Therefore, an attempt to obtain the path in the region of point F (see Figure 7.23) was not made, given the limited area of feasible configurations. Even the position at point 2 (see Figure 7.23), a configuration very close to the boundary of the helix coiled deformation owing to its stowed length, was difficult to achieve and perform the test, requiring occasionally a gentle touch to assure the desired path was followed, explaining a slight divergence in the apex positions between the model predictions and the experimental data (Figure 7.23, right).

7.7 Summary

The present chapter focuses on the development of a prototype of the proposed mechanism to validate the analytical model and assess the feasibility of the concept. A test rig is designed, and a truss prototype is manufactured and tested under application of a vertical load at the apex. Several challenges are recognized in the design process, including the attachment of the double-helices in a truss-like configuration, and the implementation of both a horizontal and a vertical movement of the apex. To address the latter, the base of the truss mechanism is designed to have unconstrained horizontal movement by sliding along a lower frame fixed to the test machine; the result is a test arrangement statically equivalent to the system of the analytical model.

Variations in the geometry of the mechanism are induced by the design of the attachments of the helices in a truss configuration in the mechanism prototype. A change in the truss geometry affects the kinematics of the mechanism, and thus an amendment of the analytical model used in the previous chapters was required. The analytical results are updated to take into consideration the length required for the end fittings of the helices as occurred from the design, plus any stress limitations during the deformation of the helices and compared to the previous model. The modified model shows slight differences in the mechanical characteristics and response of the mechanism, with the helix length-to-end fittings length ratio becoming a key parameter.

First, individual double-helices are manufactured and tested under an axial load at their extremity. Then, the helices are assembled in the truss mechanism and tested under a vertical load at the apex in the different reconfiguration modes. The experimental results are in good qualitative agreement with the predictions of the analytical model. Some differences in the actual values are observed that can be attributed to a variety of reasons, including: i) friction, which is unaccounted for in the model, both between the spokes and the composite helical strips and at all other joints in the fixture; ii) localised effect of the holes and iii) local reinforcements placed around the holes to limit delamination, that were also not modelled; iv) shear buckling of the helix and v) nonuniform deformation of the helix noticed during the test, with the pitch varying across the helix length, which were not observed in previous work by Lachenal *et al.* [25] and are presumably dependent on the length-to-radius ratio of the helix; vi) contact of adjacent spokes of the helices during coiling/uncoiling as a result of the nonuniform helix deformation, evidenced by slight kinks in the load-displacement curves; vii) any imperfections during manufacturing of the helices.

These preliminary tests of the mechanism prototype include results for configurations exclusively on the primary equilibrium path for the reconfiguration Mode I and Mode II. The friction in the linear guides used to achieve the horizontal movement of the truss base of the mechanism was prohibitive of obtaining configurations of the mechanism in the reconfiguration Mode III and on the bifurcation path for the reconfiguration Mode I and Mode II, where the mechanism experiences both a horizontal and a vertical displacement of the apex. Thus, the linear guides are replaced by rollers and the test of the prototype is repeated. Within a broad aspect, the experimental results obtained and the analytical model showed a good correlation in the trend of the load-displacement curve. The manufacture of such helices and their assembly in a truss structure has been proven challenging, but the potential mechanical responses make it

worthwhile. The existing analytical model is inherently limited, thus the nonuniform coiling/uncoiling along the length of the helix was unanticipated. This behaviour and challenges in the set-up, *i.e.* the detachment of the truss base from the fixed lower frame, are not something that would have obviously appeared during the modelling, and only when considering practical prototypes.

This chapter consisted the experimental section of this work. The next chapter concludes the thesis with a summary of the outcomes of the overall work presented in previous chapters, and some thoughts for future research.

Chapter 8

Conclusions and Future Work

8.1 Conclusions

The main objective of this work has been to explore the design space of structural assemblies of nonlinear elements and reveal the variety of attainable mechanical responses. A novel compliant mechanism has been introduced consisting of composite morphing elements of a double-helix architecture assembled in a simple truss configuration. These helical composite structures are able to undergo large axial deformations while maintaining their structural integrity. Existing compliant mechanisms often rely on flexible members and their elastic deformations for their operation and to achieve multistability, however, their range of motion is restricted by strength limitations. The compliant mechanism presented in this work uses the morphing elements as the flexible members, enabling higher effective strains to be achieved and thus the expansion of the range of motion currently available.

The helical structure used can deform from an extended to a completely coiled configuration, resembling the behaviour of springs, but with nonlinear stiffness. The double-helix exhibits tailorable nonlinear stiffness characteristics and strain energy profiles, including bistability, that can be customized by tuning various design parameters, including the composite lay-up and the geometry of the helix strips. Therefore, the helical elements' variable geometry and customizable nonlinear stiffness characteristics enable the mechanism to be tailored, and a wide range of behaviours to be developed.

In addition, the helical structure features two connected, but distinct, deformation modes; from the straight configuration the structure can be nudged to deform to helix angles of opposite chirality. For a symmetric

lay-up, a difference in the stiffness characteristics and the mechanical response of the helix is noted between the two deformation modes. This ability of the helix to change the helical pitch and the resulting stiffness profile enables the reconfigurability of the mechanism. The mechanism can be reconfigured to operate in different modes through the exploitation of the inherent nonlinear elastic characteristics of the helix, whilst maintaining its connectivity and mobility.

To demonstrate the richness of the design space the effect of various design parameters on the stability characteristics and the mechanical response of the mechanism has been investigated. Two methods have been employed for the analysis of the mechanism. Strain energy landscapes have been used to study the multistability of the mechanism and have been shown an effective way to trace the qualitative changes in the behaviour between mechanisms with different characteristics. For the analysis of the mechanism in the force-displacement space, given the nonlinearity of the system, the modified-Riks method has been implemented and potential load paths between stable configurations have been obtained.

The proposed compliant mechanism can exhibit up to five stable configurations. The mechanism's multistability has been investigated by varying the composite lay-up of the helix strips, the geometrical features of the double-helices and the initial truss geometry of the mechanism. For steep trusses, the mechanism exhibits: i) bistability, for a $[0_5]$ lay-up; ii) quadrastability, for a $[\beta_2/0/\beta_2]$ symmetric lay-up with $0^\circ < \beta < 90^\circ$; iii) pentastability with one internal stable equilibrium and four stable boundary equilibria, for a $[\beta_2/0/\beta_2]$ symmetric lay-up with $\beta = 90^\circ$ and/or a $[\beta_2/0/-\beta_2]$ antisymmetric lay-up. The mechanism with helices of a $[\beta_2/0/\beta_2]$ symmetric lay-up with $0^\circ < \beta < 90^\circ$ transitions from being quadrastable to being bistable for decreasing initial truss angles. No internal equilibrium is encountered for a mechanism with helices of a $[\beta_2/0/\beta_2]$ symmetric lay-up with $\beta = 90^\circ$ and/or a $[\beta_2/0/-\beta_2]$ antisymmetric lay-up assembled in a shallow truss, yet the four boundary equilibria are maintained. The geometrical features of the double-helices were found to have a limited effect on the mechanism's behaviour.

The application of a vertical or a horizontal load at the apex of the truss mechanism has revealed equilibrium paths that connect all its internal equilibria. Regardless of the initial truss angle, under the application of a vertical load the equilibrium path bifurcates enabling all equilibria to be accessed. Under the application of a horizontal load, bifurcations are present too, except for a mechanism with helices of a $[\beta_2/0/\beta_2]$ symmetric lay-up with $0^\circ < \beta < 90^\circ$, where three disconnected equilibrium paths are found. Furthermore, it has been shown that a mechanism of constant stiffness can be developed while undergoing

large deformations, with the mechanism with helices of a $[0_s]$ strip lay-up demonstrating a stable region of constant stiffness upon a horizontal load at the apex with a circular deformation path.

This multistable mechanism exhibits four reconfiguration modes (Mode I, Mode II, Mode III and its reverse), thanks to the double-helix ability to switch its twist direction once in a fully extended state and the different mechanical response obtained for symmetric lay-ups of the form $[\beta_2/0/\beta_2]$, with $0^\circ < \beta < 90^\circ$. The reconfigurability of the mechanism has been explored and the effect of the fibre angle β in the symmetric lay-up of the helix strips and the initial truss geometry of the mechanism has been investigated. For a steep truss, regardless of the fibre angle, the mechanism exhibits quadristability in Mode I, where both helices are twisted clockwise, whereas the response in Mode II, where both helices are twisted anticlockwise, and Mode III, where one helix is twisted clockwise the other anticlockwise, depends on the fibre angle. The mechanism shows two internal stable equilibria for $\beta = 30^\circ$ and one for $\beta = 45^\circ$ and $\beta = 60^\circ$, plus four boundary equilibria in Mode II. In Mode III, the mechanism transitions from three stable interior equilibria and two stable boundary equilibria for $\beta = 30^\circ$ to two stable interior equilibria and three boundary equilibria for $\beta = 45^\circ$ and $\beta = 60^\circ$. For a shallow truss, the mechanism is bistable in Mode I, tristable in Mode III with one stable internal equilibrium, and quadristable in Mode II, yet none of the interior equilibrium positions identified are stable.

The mechanism's response in the force-displacement space upon a vertical, horizontal and a combined load at the apex has been explored for the different reconfiguration modes. It was found that the load paths obtained for a vertical, horizontal and a combined load in Mode I and Mode II access all internal equilibria through either bifurcation, multiple independent paths or even a single path. In Mode III, two disconnected equilibrium paths are identified for all lay-ups under the application of a vertical load enabling all internal equilibria to be traversed, however, upon a horizontal load at the apex, despite the three connected equilibrium paths, some equilibria are left isolated for $\beta = 60^\circ$. Likewise, equilibria remain inaccessible for $\beta = 60^\circ$ upon a combined load where the three independent equilibrium paths obtained for $\beta = 30^\circ$, are reduced to two for $\beta = 45^\circ$, to a single for $\beta = 60^\circ$.

Finally, a prototype of the truss mechanism was manufactured and tested under a vertical load at the apex to assess its feasibility and validate the analytical model of the proposed mechanism. The design of the truss prototype has been proven challenging with several practical difficulties to be addressed. The deformation of the truss mechanism in its design space under a vertical load entails both a horizontal and

a vertical displacement of the mechanism's end effector. The universal test machine used for the testing allows only vertical displacement of its crosshead and thus of the truss apex attached to it. The implementation of the horizontal displacement of the truss apex has been achieved by enabling the horizontal movement of the truss base. This approach involved a design of the prototype with a truss base frame free to slide on a lower frame fixed onto the test machine. Moreover, to assemble the helices into a truss-like configuration, a customized design of the helices end fittings has been implemented. This feature has resulted in a variation of the analytical model. The updated results have shown that the end fitting length-to-the helix length ratio is a key parameter of the mechanical behaviour of the mechanism, however, no major differences have been recorded on the stability characteristics of the mechanism.

Individual double-helix prototypes were manufactured and tested under the application of an axial load at their extremity, followed by the experimental testing of the truss prototype upon a vertical load at the apex in the different reconfiguration modes. The use of linear guides to achieve the horizontal movement of the truss base was shown to be inadequate for our system, restricting the experimental results to equilibrium paths with only vertical displacement of the apex and zero horizontal. Improvements were made and the linear guides were replaced with rollers that successfully enabled configurations with both horizontal and vertical displacement of the apex to be attained. The testing of the truss prototype was challenging. A nonuniform deformation of the helix, experiencing different helix angle along its length, was noticed that has not been recorded before in the literature, questioning the effect of the helix radius-to-length ratio on the helix behaviour. This in turn resulted in adjacent spokes of the helix touching during coiling/uncoiling. The helix stowed length added limitations to the attainable configurations of the mechanism. Nonetheless, the experimental data obtained are in good qualitative agreement with the analytical predictions of the model proving the feasibility of the proposed mechanism. Differences in the actual values have been observed, attributed primarily to features that were not modelled and issues on the practical implementation encountered during testing. The experimental results have demonstrated that a detailed design and high precision in manufacturing is required, especially when nonlinear behaviours are involved since the slightest change might have a significant impact on the result.

In this work, we developed a morphing structural element into a novel reconfigurable mechanism. Stepping on the customizable nonlinear stiffness characteristics of this morphing element, the interaction of multiple such components in a mechanism configuration was studied and the variety of mechanical responses were

explored analytically, followed by an experimental implementation. The overall outcome of this study has been proven constructive, allowing, of course, room for improvements and further research both in the analytical section as well as in the design of the mechanism prototype. A novel rich design space has been introduced, which can be promising for exploitation in future applications such as in robotics, prosthetics or deployable structures.

8.2 Future work

This research has introduced a novel compliant, reconfigurable mechanism consisting of morphing composite structures of a double-helix architecture. The variety of attainable mechanical responses of a mechanism assembled of two double-helices in the simplest truss geometry has been demonstrated and a prototype was manufactured to assess the feasibility of this concept. However, acknowledging the limitations considered for the analysis of this mechanism along with several challenges identified during manufacturing and testing of the prototype, this work can set the foundations for future studies. Below potential paths for further exploration are presented.

This research has studied the multistability and reconfigurability of the proposed mechanism by showing energy landscapes and load-displacement curves. The effect of various parameters on these has been explored by assigning different values to the various design parameters. Our aim was to demonstrate the different behaviours that can be achieved, however, a more thorough analysis and a parametric study of the design space of the mechanism could be valuable to the scientific community.

A variety of different attainable responses was shown for the mechanism of double-helices. Our results focused on symmetric assemblies of the helices in a truss-like configuration using identical helices. Even though we briefly presented results of the effect on the multistability and the mechanical response of a mechanism with helices of different lengths in Chapter 5, it would be of interest to investigate further the design space of non-symmetric truss configurations.

As an outcome of the design of the prototype, in Chapter 7 an amendment to the analytical model was implemented to account for the length of the end fittings of the helices. It was observed that this yields an impact on the characteristics of the mechanism, varying the multistability between mechanisms with helices of different length. A more thorough investigation of the effect of the end fitting length to the mechanism's behaviour would be appropriate, recognising there is a correlation between the helix length

and the end fittings length, and identifying the critical limits of their ratio for the transition between different behaviours.

Among other observations from the testing of the truss prototype, was the nonuniform deformation of the helix, with the helix angle varying along the helix length during its coiling/uncoiling. As there was no precedent of this behaviour in the literature, it was considered presumably dependent on the radius-to-length ratio of the helix and possibly the presence of some end effects occurring from the use of long strips. Such effects were not taken into consideration in the model assumptions, therefore, they could be explored and addressed either by developing the model to accommodate for this or by defining limitations to the dimensions of the helices for the model.

The analysis performed in this study referred to the simplest truss geometry for the assemblies of double-helices, it being essentially a two-element truss pin-jointed at the apex and base supports. Eventually, it would be of interest to extend this analysis to a more complicated synthesis and design of the initial configurations for the mechanism. Indicatively, variations of this truss geometry accounting for different boundary conditions could be a first step towards more complex layouts. For example, replacing one of the supports with a roller support (Figure 8.1a) would add another degree of freedom and a new set of behaviours of possible interest. Subsequently, this configuration could accommodate an additional double-helix between the two base supports resulting in an arrangement with three helices (Figure 8.1b).

Having in mind potential applications that such a mechanism may be of use, *i.e.* in deployable structures, for dynamic applications, as energy harvester or vibration isolator, it would be of interest not only study the various configurations for a 2D truss assemblies but extend the work to the design and analysis of 3D space assemblies. For example, a configuration of these helical elements assembled in a pyramid (Figure 8.2) could be a natural extension of the current mechanism into the 3D space.

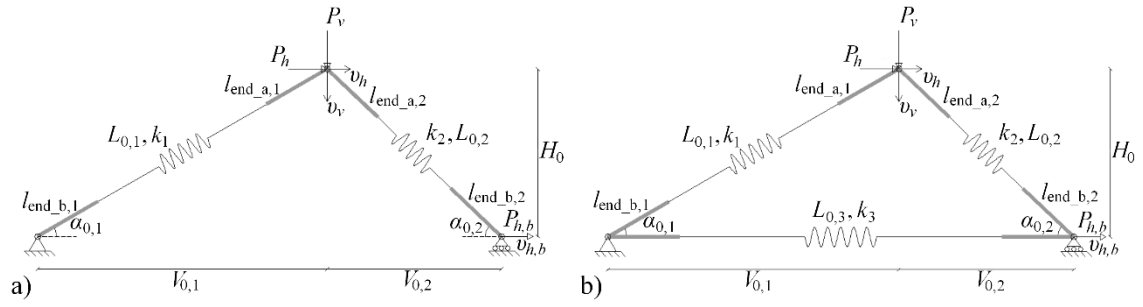


Figure 8.1: Schematic representation of potential different initial configurations for the truss-like mechanism of double-helices: a) two-element truss with one support (right) a roller; b) three-element truss with one support (right) a roller.

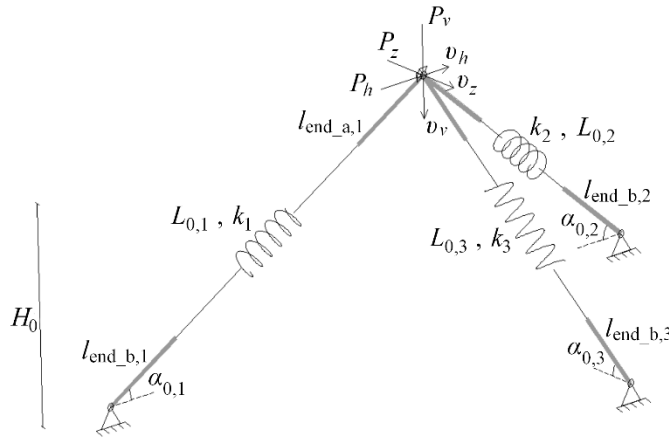


Figure 8.2: Schematic representation of potential initial configuration for a mechanism assembled of double-helices in a pyramid configuration in the 3D space.

A good qualitative agreement has been shown between the experimental data and the predictions of the analytical model. However, the experimental testing of the prototype revealed a number of issues, from assembly challenges to structural impracticalities, that should be addressed in future work. A refinement of the prototype design and the development and test of further prototypes will be required for a full experimental characterization of the mechanism, both qualitatively and quantitatively, and for a practical, application targeted implementation.

The actuation of the proposed mechanism of double-helices is currently based on mechanical means and the direct application of a load or displacement at the end effector of the truss assembly. Given the different alternatives of actuating a structure being developed in the literature, it would be of interest to consider and explore alternative ways to trigger this mechanism, particularly as a certain type of actuation might be of a benefit for specific applications.

In this study we have shown the potentials of an assembly of nonlinear elements with certain geometrical and stiffness characteristics in a truss-like mechanism. Essentially, any element with a similar mechanical response could be used to achieve such behaviours. Thus, it would be of interest to replace the double-helices to other structures of a similar geometry and variable stiffness, *i.e.* the cylindrical composite lattice structure introduced in [73] or a double-helix with variable radius, and examine their response, particularly as it may reveal a vast of new behaviours or address some of the impracticalities found in the current design.

References

- [1] T. Yan, M. Cempini, C. M. Oddo, and N. Vitiello, "Review of assistive strategies in powered lower-limb orthoses and exoskeletons," *Rob. Auton. Syst.*, vol. 64, pp. 120–136, Feb. 2015.
- [2] A. J. Veale and S. Q. Xie, "Towards compliant and wearable robotic orthoses: A review of current and emerging actuator technologies," *Med. Eng. Phys.*, vol. 38, no. 4, pp. 317–325, Apr. 2016.
- [3] K. A. Shorter, J. Xia, E. T. Hsiao-Weeksler, W. K. Durfee, and G. F. Kogler, "Technologies for Powered Ankle-Foot Orthotic Systems: Possibilities and Challenges," *IEEE/ASME Trans. Mechatronics*, vol. 18, no. 1, pp. 337–347, Feb. 2013.
- [4] H. Vallery, J. Veneman, E. van Asseldonk, R. Ekkelenkamp, M. Buss, and H. van Der Kooij, "Compliant actuation of rehabilitation robots," *IEEE Robot. Autom. Mag.*, vol. 15, no. 3, pp. 60–69, Sep. 2008.
- [5] B. Brackx *et al.*, "Design of a modular add-on compliant actuator to convert an orthosis into an assistive exoskeleton," in *5th IEEE RAS/EMBS International Conference on Biomedical Robotics and Biomechatronics*, 2014, pp. 485–490.
- [6] R. Ham, T. Sugar, B. Vanderborght, K. Hollander, and D. Lefeber, "Compliant actuator designs," *IEEE Robot. Autom. Mag.*, vol. 16, no. 3, pp. 81–94, Sep. 2009.
- [7] T. Bacek *et al.*, "Conceptual design of a novel variable stiffness actuator for use in lower limb exoskeletons," in *2015 IEEE International Conference on Rehabilitation Robotics (ICORR)*, 2015, vol. 2015-Septe, pp. 583–588.
- [8] S. Pfeifer, A. Pagel, R. Riener, and H. Vallery, "Actuator With Angle-Dependent Elasticity for Biomimetic Transfemoral Prostheses," *IEEE/ASME Trans. Mechatronics*, vol. 20, no. 3, pp. 1384–1394, Jun. 2015.
- [9] S. Wolf *et al.*, "Variable Stiffness Actuators: Review on Design and Components," *IEEE/ASME Trans. Mechatronics*, vol. 21, no. 5, pp. 2418–2430, Oct. 2016.
- [10] C. E. English and D. Russell, "Mechanics and stiffness limitations of a variable stiffness actuator for use in prosthetic limbs," *Mech. Mach. Theory*, vol. 34, no. 1, pp. 7–25, Jan. 1999.
- [11] R. W. Horst and R. R. Marcus, "FlexCVA: A Continuously Variable Actuator for Active Orthotics," in *2006 International Conference of the IEEE Engineering in Medicine and Biology Society*, 2006, pp. 2425–2428.
- [12] L. Masia *et al.*, "CARAPACE: A novel composite advanced robotic actuator powering assistive compliant exoskeleton preliminary design," in *2013 IEEE 13th International Conference on Rehabilitation Robotics (ICORR)*, 2013, pp. 1–8.
- [13] B. Vanderborght *et al.*, "Variable impedance actuators: A review," *Rob. Auton. Syst.*, vol. 61, no. 12, pp. 1601–1614, Dec. 2013.
- [14] M. Weckx *et al.*, "Prototype design of a novel modular two-degree-of-freedom variable stiffness actuator," in *2014 IEEE-RAS International Conference on Humanoid Robots*, 2014, vol. 2015-Febru, pp. 33–38.
- [15] Z. G. Haoyog Yu, Sunan Huang, Gong Chen, Yongping Pan, "Human – Robot Interaction Control of Human – Robot Interaction Control of Rehabilitation Robots With Series Elastic Actuators," *Ieee Trans. Robot. Vol. 31, No. 5*, vol. 31, no. October, pp. 1089–1100, 2015.
- [16] M. Dzahir and S. Yamamoto, "Recent Trends in Lower-Limb Robotic Rehabilitation Orthosis: Control Scheme and Strategy for Pneumatic Muscle Actuated Gait Trainers," *Robotics*, vol. 3, no. 2, pp. 120–148, Apr. 2014.
- [17] G. A. Pratt and M. M. Williamson, "Series elastic actuators," in *Proceedings 1995 IEEE/RSJ*

International Conference on Intelligent Robots and Systems. Human Robot Interaction and Cooperative Robots, vol. 1, pp. 399–406.

- [18] T. G. Sugar, “A novel selective compliant actuator,” *Mechatronics*, vol. 12, no. 9–10, pp. 1157–1171, Nov. 2002.
- [19] J. F. Veneman, R. Ekkelenkamp, R. Kruidhof, F. C. T. van der Helm, and H. van der Kooij, “A Series Elastic- and Bowden-Cable-Based Actuation System for Use as Torque Actuator in Exoskeleton-Type Robots,” *Int. J. Rob. Res.*, vol. 25, no. 3, pp. 261–281, Mar. 2006.
- [20] E. J. Rouse, L. M. Mooney, E. C. Martinez-Villalpando, and H. M. Herr, “Clutchable series-elastic actuator: Design of a robotic knee prosthesis for minimum energy consumption,” in *2013 IEEE 13th International Conference on Rehabilitation Robotics (ICORR)*, 2013, pp. 1–6.
- [21] J. Pratt, B. Krupp, and C. Morse, “Series elastic actuators for high fidelity force control,” *Ind. Robot An Int. J.*, vol. 29, no. 3, pp. 234–241, Jun. 2002.
- [22] D. Accoto, G. Carpino, F. Sergi, N. L. Tagliamonte, L. Zollo, and E. Guglielmelli, “Design and Characterization of a Novel High-Power Series Elastic Actuator for a Lower Limb Robotic Orthosis,” *Int. J. Adv. Robot. Syst.*, vol. 10, no. 10, p. 359, Oct. 2013.
- [23] L. Cappello, X. Lachenal, A. Pirrera, F. Mattioni, P. M. Weaver, and L. Masia, “Design, characterization and stability test of a multistable composite compliant actuator for exoskeletons,” in *5th IEEE RAS/EMBS International Conference on Biomedical Robotics and Biomechatronics*, 2014, pp. 1051–1056.
- [24] Haoyong Yu *et al.*, “A novel compact compliant actuator design for rehabilitation robots,” in *2013 IEEE 13th International Conference on Rehabilitation Robotics (ICORR)*, 2013, pp. 1–6.
- [25] X. Lachenal, P. M. Weaver, and S. Daynes, “Multi-stable composite twisting structure for morphing applications,” *Proc. R. Soc. A Math. Phys. Eng. Sci.*, vol. 468, no. 2141, pp. 1230–1251, May 2012.
- [26] X. Lachenal, P. M. Weaver, and S. Daynes, “Influence of transverse curvature on the stability of pre-stressed helical structures,” *Int. J. Solids Struct.*, vol. 51, no. 13, pp. 2479–2490, 2014.
- [27] L. Cappello, A. Pirrera, P. Weaver, and L. Masia, “A series elastic composite actuator for soft arm exosuits,” *IEEE Int. Conf. Rehabil. Robot.*, vol. 2015, pp. 61–66, Sep 2015.
- [28] A. D. Norman, M. R. Golabchi, K. A. Seffen, and S. D. Guest, “Multistable Textured Shell Structures,” *Adv. Sci. Technol.*, vol. 54, pp. 168–173, Sep. 2008.
- [29] F. Dai, H. Li, and S. Du, “A multi-stable lattice structure and its snap-through behavior among multiple states,” *Compos. Struct.*, vol. 97, pp. 56–63, Mar. 2013.
- [30] J. C. Hawks, M. B. Colton, and L. L. Howell, “A Variable-Stiffness Straight-Line Compliant Mechanism,” in *Volume 5A: 39th Mechanisms and Robotics Conference*, 2015, p. V05AT08A011.
- [31] G. A. Naselli, L. Rimassa, M. Zoppi, and R. Molino, “A variable stiffness joint with superelastic material,” *Meccanica*, vol. 52, no. 4–5, pp. 781–793, Mar. 2017.
- [32] A. Mekaouche, F. Chapelle, and X. Balandraud, “A compliant mechanism with variable stiffness achieved by rotary actuators and shape-memory alloy,” *Meccanica*, vol. 53, no. 10, pp. 2555–2571, Aug. 2018.
- [33] T. J. Roberts and E. Azizi, “Flexible mechanisms: the diverse roles of biological springs in vertebrate movement,” *J. Exp. Biol.*, vol. 214, no. 3, pp. 353–361, Feb. 2011.
- [34] N. Konow, E. Azizi, and T. J. Roberts, “Muscle power attenuation by tendon during energy dissipation,” *Proc. R. Soc. B Biol. Sci.*, vol. 279, no. 1731, pp. 1108–1113, Mar. 2012.
- [35] N. Konow and T. J. Roberts, “The series elastic shock absorber: tendon elasticity modulates energy dissipation by muscle during burst deceleration,” *Proc. R. Soc. B Biol. Sci.*, vol. 282, no. 1804, pp. 20142800–20142800, Feb. 2015.

References

- [36] A. M. Grabowski and H. M. Herr, "Leg exoskeleton reduces the metabolic cost of human hopping," *J. Appl. Physiol.*, vol. 107, no. 3, pp. 670–678, Sep. 2009.
- [37] D. J. Farris, B. D. Robertson, and G. S. Sawicki, "Elastic ankle exoskeletons reduce soleus muscle force but not work in human hopping," *J. Appl. Physiol.*, vol. 115, no. 5, pp. 579–585, Sep. 2013.
- [38] J. Zhang, C. C. Cheah, and S. H. Collins, "Experimental comparison of torque control methods on an ankle exoskeleton during human walking," in *2015 IEEE International Conference on Robotics and Automation (ICRA)*, 2015, pp. 5584–5589.
- [39] S. H. Collins, M. B. Wiggin, and G. S. Sawicki, "Reducing the energy cost of human walking using an unpowered exoskeleton," *Nature*, vol. 522, no. 7555, pp. 212–215, Jun. 2015.
- [40] G. Kovacs, L. Düring, S. Michel, and G. Terrasi, "Stacked dielectric elastomer actuator for tensile force transmission," *Sensors Actuators A Phys.*, vol. 155, no. 2, pp. 299–307, Oct. 2009.
- [41] Q. Yang, J. Fan, and G. Li, "Artificial muscles made of chiral two-way shape memory polymer fibers," *Appl. Phys. Lett.*, vol. 109, no. 18, p. 183701, Oct. 2016.
- [42] D. Yang *et al.*, "Buckling Pneumatic Linear Actuators Inspired by Muscle," *Adv. Mater. Technol.*, vol. 1, no. 3, p. 1600055, 2016.
- [43] D. A. Winter, *Biomechanics and Motor Control of Human Movement*. Hoboken, NJ, USA: John Wiley & Sons, Inc., 2009.
- [44] E. M. Arnold, S. R. Ward, R. L. Lieber, and S. L. Delp, "A Model of the Lower Limb for Analysis of Human Movement," *Ann. Biomed. Eng.*, vol. 38, no. 2, pp. 269–279, Feb. 2010.
- [45] T. McGeer, "Passive Dynamic Walking," *Int. J. Rob. Res.*, vol. 9, no. 2, pp. 62–82, Apr. 1990.
- [46] N. Berme, E. Oggero, and G. Pagnacco, "Modeling and Simulation of Human Locomotion," in *Human and Machine Locomotion*, Vienna: Springer Vienna, 1997, pp. 87–105.
- [47] S. Onyshko and D. A. Winter, "A mathematical model for the dynamics of human locomotion," *J. Biomech.*, vol. 13, no. 4, pp. 361–368, Jan. 1980.
- [48] M. Sartori, L. Gizzi, D. G. Lloyd, and D. Farina, "A musculoskeletal model of human locomotion driven by a low dimensional set of impulsive excitation primitives," *Front. Comput. Neurosci.*, vol. 7, p. 79, Jun. 2013.
- [49] R. M. Alexander, "Simple Models of Human Locomotion," *J. Theor. Med.*, vol. 1, no. 2, pp. 129–135, 1997.
- [50] A. D. Kuo, "Energetics of Actively Powered Locomotion Using the Simplest Walking Model," *J. Biomech. Eng.*, vol. 124, no. 1, p. 113, Sep. 2001.
- [51] J. M. Donelan, R. Kram, and A. D. Kuo, "Mechanical work for step-to-step transitions is a major determinant of the metabolic cost of human walking," *J. Exp. Biol.*, vol. 205, pp. 3717–27, Dec. 2002.
- [52] T. Kim and S. Jo, "Simulation of human locomotion using a musculoskeletal model," in *2008 International Conference on Control, Automation and Systems*, 2008, pp. 1761–1764.
- [53] S. Siegler, R. Seliktar, and W. Hyman, "Simulation of human gait with the aid of a simple mechanical model," *J. Biomech.*, vol. 15, no. 6, pp. 415–425, Jan. 1982.
- [54] F. Lacquaniti *et al.*, "Human Locomotion in Hypogravity: From Basic Research to Clinical Applications," *Front. Physiol.*, vol. 8, p. 893, Nov. 2017.
- [55] W. Lacarbonara, *Nonlinear Structural Mechanics: Theory, Dynamical Phenomena and Modeling*. New York: Springer US, 2013.
- [56] P. M. Reis, "A Perspective on the Revival of Structural (In)Stability With Novel Opportunities for

- Function: From Buckliphobia to Buckliphilia,” *J. Appl. Mech.*, vol. 82, no. 11, p. 111001, Sep. 2015.
- [57] T. Butlin, J. Woodhouse, and A. R. Champneys, “The landscape of nonlinear structural dynamics: an introduction,” *Philos. Trans. R. Soc. A Math. Phys. Eng. Sci.*, vol. 373, no. 2051, p. 20140400, Sep. 2015.
- [58] N. Hu and R. Burgueño, “Buckling-induced smart applications: recent advances and trends,” *Smart Mater. Struct.*, vol. 24, no. 6, p. 063001, Jun. 2015.
- [59] B. Li, Y.-P. Cao, X.-Q. Feng, and H. Gao, “Mechanics of morphological instabilities and surface wrinkling in soft materials: a review,” *Soft Matter*, vol. 8, no. 21, p. 5728, May 2012.
- [60] A. Lazarus, J. T. Miller, and P. M. Reis, “Continuation of equilibria and stability of slender elastic rods using an asymptotic numerical method,” *J. Mech. Phys. Solids*, vol. 61, no. 8, pp. 1712–1736, Aug. 2013.
- [61] R. M. J. Groh, D. Avitabile, and A. Pirrera, “Generalised path-following for well-behaved nonlinear structures,” *Comput. Methods Appl. Mech. Eng.*, vol. 331, pp. 394–426, Apr. 2018.
- [62] R. Burgueño, N. Hu, A. Heeringa, and N. Lajnef, “Tailoring the elastic postbuckling response of thin-walled cylindrical composite shells under axial compression,” *Thin-Walled Struct.*, vol. 84, pp. 14–25, Nov. 2014.
- [63] X. Ning and S. Pellegrino, “Imperfection-insensitive axially loaded thin cylindrical shells,” *Int. J. Solids Struct.*, vol. 62, pp. 39–51, Jun. 2015.
- [64] C. G. Diaconu, P. M. Weaver, and F. Mattioni, “Concepts for morphing airfoil sections using bi-stable laminated composite structures,” *Thin-Walled Struct.*, vol. 46, no. 6, pp. 689–701, Jun. 2008.
- [65] A. Pirrera, D. Avitabile, and P. M. Weaver, “Bistable plates for morphing structures: A refined analytical approach with high-order polynomials,” *Int. J. Solids Struct.*, vol. 47, no. 25–26, pp. 3412–3425, Dec. 2010.
- [66] S. Daynes, P. M. Weaver, and J. A. Trevarthen, “A Morphing Composite Air Inlet with Multiple Stable Shapes,” *J. Intell. Mater. Syst. Struct.*, vol. 22, no. 9, pp. 961–973, Jun. 2011.
- [67] K. A. Seffen and S. D. Guest, “Prestressed Morphing Bistable and Neutrally Stable Shells,” *J. Appl. Mech.*, vol. 78, no. 1, p. 011002, 2011.
- [68] A. F. Arrieta, D. J. Wagg, and S. A. Neild, “Dynamic Snap-through for Morphing of Bi-stable Composite Plates,” *J. Intell. Mater. Syst. Struct.*, vol. 22, no. 2, pp. 103–112, Jan. 2011.
- [69] A. Brinkmeyer, M. Santer, A. Pirrera, and P. M. Weaver, “Pseudo-bistable self-actuated domes for morphing applications,” *Int. J. Solids Struct.*, vol. 49, no. 9, pp. 1077–1087, May 2012.
- [70] F. Dai, H. Li, and S. Du, “Design and analysis of a tri-stable structure based on bi-stable laminates,” *Compos. Part A Appl. Sci. Manuf.*, vol. 43, no. 9, pp. 1497–1504, Sep. 2012.
- [71] I. K. Kuder, A. F. Arrieta, W. E. Raither, and P. Ermanni, “Variable stiffness material and structural concepts for morphing applications,” *Prog. Aerosp. Sci.*, vol. 63, pp. 33–55, Nov. 2013.
- [72] B. H. Coburn, A. Pirrera, P. M. Weaver, and S. Vidoli, “Tristability of an orthotropic doubly curved shell,” *Compos. Struct.*, vol. 96, pp. 446–454, Feb. 2013.
- [73] A. Pirrera, X. Lachenal, S. Daynes, P. M. Weaver, and I. V. Chenchiah, “Multi-stable cylindrical lattices,” *J. Mech. Phys. Solids*, vol. 61, no. 11, pp. 2087–2107, Nov. 2013.
- [74] X. Lachenal, S. Daynes, and P. M. Weaver, “A non-linear stiffness composite twisting I-beam,” *J. Intell. Mater. Syst. Struct.*, vol. 25, no. 6, pp. 744–754, Apr. 2014.
- [75] E. Eckstein, A. Pirrera, and P. M. Weaver, “Multi-mode morphing using initially curved composite plates,” *Compos. Struct.*, vol. 109, no. 1, pp. 240–245, Mar. 2014.

References

- [76] A. F. Arrieta, I. K. Kuder, T. Waeber, and P. Ermanni, "Variable stiffness characteristics of embeddable multi-stable composites," *Compos. Sci. Technol.*, vol. 97, pp. 12–18, Jun. 2014.
- [77] S. A. Emam and D. J. Inman, "A Review on Bistable Composite Laminates for Morphing and Energy Harvesting," *Appl. Mech. Rev.*, vol. 67, no. 6, p. 060803, Dec. 2015.
- [78] F. Chen, L. Liu, X. Lan, Q. Li, J. Leng, and Y. Liu, "The study on the morphing composite propeller for marine vehicle. Part I: Design and numerical analysis," *Compos. Struct.*, vol. 168, pp. 746–757, May 2017.
- [79] K. Bertoldi, P. M. Reis, S. Willshaw, and T. Mullin, "Negative Poisson's Ratio Behavior Induced by an Elastic Instability," *Adv. Mater.*, vol. 22, no. 3, pp. 361–366, Jan. 2010.
- [80] J. T. B. Overvelde, S. Shan, and K. Bertoldi, "Compaction Through Buckling in 2D Periodic, Soft and Porous Structures: Effect of Pore Shape," *Adv. Mater.*, vol. 24, no. 17, pp. 2337–2342, May 2012.
- [81] J. Shim, C. Perdigou, E. R. Chen, K. Bertoldi, and P. M. Reis, "Buckling-induced encapsulation of structured elastic shells under pressure," *Proc. Natl. Acad. Sci.*, vol. 109, no. 16, pp. 5978–5983, Apr. 2012.
- [82] S. Babae, J. Shim, J. C. Weaver, E. R. Chen, N. Patel, and K. Bertoldi, "3D Soft Metamaterials with Negative Poisson's Ratio," *Adv. Mater.*, vol. 25, no. 36, pp. 5044–5049, Sep. 2013.
- [83] J. Shim *et al.*, "Harnessing instabilities for design of soft reconfigurable auxetic/chiral materials," *Soft Matter*, vol. 9, no. 34, p. 8198, 2013.
- [84] B. Florijn, C. Coullais, and M. van Hecke, "Programmable Mechanical Metamaterials," *Phys. Rev. Lett.*, vol. 113, no. 17, p. 175503, Oct. 2014.
- [85] A. Rafsanjani, A. Akbarzadeh, and D. Pasini, "Snapping Mechanical Metamaterials under Tension," *Adv. Mater.*, vol. 27, no. 39, pp. 5931–5935, Oct. 2015.
- [86] S. Shan *et al.*, "Multistable Architected Materials for Trapping Elastic Strain Energy," *Adv. Mater.*, vol. 27, no. 29, pp. 4296–4301, Aug. 2015.
- [87] D. Yang *et al.*, "Buckling of Elastomeric Beams Enables Actuation of Soft Machines," *Adv. Mater.*, vol. 27, no. 41, pp. 6323–6327, Nov. 2015.
- [88] Y. Gerson, S. Krylov, B. Ilic, and D. Schreiber, "Design considerations of a large-displacement multistable micro actuator with serially connected bistable elements," *Finite Elem. Anal. Des.*, vol. 49, no. 1, pp. 58–69, Feb. 2012.
- [89] E. G. Loukaides, S. K. Smoukov, and K. a. Seffen, "Magnetic actuation and transition shapes of a bistable spherical cap," *Int. J. Smart Nano Mater.*, vol. 5, no. 4, pp. 270–282, Oct. 2014.
- [90] D. K. Agrawal, J. Woodhouse, and A. A. Seshia, "Modeling nonlinearities in MEMS oscillators," *IEEE Trans. Ultrason. Ferroelectr. Freq. Control*, vol. 60, no. 8, pp. 1646–1659, Aug. 2013.
- [91] S. P. Pellegrini, N. Tolou, M. Schenk, and J. L. Herder, "Bistable vibration energy harvesters: A review," *J. Intell. Mater. Syst. Struct.*, vol. 24, no. 11, pp. 1303–1312, Jul. 2013.
- [92] R. L. Harne and K. W. Wang, "A review of the recent research on vibration energy harvesting via bistable systems," *Smart Mater. Struct.*, vol. 22, no. 2, p. 023001, Feb. 2013.
- [93] C. Winkelmann, S. S. Kim, and V. La Saponara, "Design and development of hybrid composite bistable structures for energy absorption under quasi-static tensile loading," *Compos. Struct.*, vol. 93, no. 1, pp. 171–178, Dec. 2010.
- [94] A. D. Shaw, S. A. Neild, D. J. Wagg, P. M. Weaver, and A. Carrella, "A nonlinear spring mechanism incorporating a bistable composite plate for vibration isolation," *J. Sound Vib.*, vol. 332, no. 24, pp. 6265–6275, Nov. 2013.

- [95] X. Lachenal, S. Daynes, and P. M. Weaver, "A zero torsional stiffness twist morphing blade as a wind turbine load alleviation device," *Smart Mater. Struct.*, vol. 22, no. 6, p. 065016, Jun. 2013.
- [96] F. Dai, H. Li, and S. Du, "A multi-stable wavy skin based on bi-stable laminates," *Compos. Part A Appl. Sci. Manuf.*, vol. 45, pp. 102–108, Feb. 2013.
- [97] A. F. Arrieta, I. K. Kuder, M. Rist, T. Waeber, and P. Ermanni, "Passive load alleviation aerofoil concept with variable stiffness multi-stable composites," *Compos. Struct.*, vol. 116, no. 1, pp. 235–242, Sep. 2014.
- [98] A. D. Norman, K. A. Seffen, and S. D. Guest, "Morphing of curved corrugated shells," *Int. J. Solids Struct.*, vol. 46, no. 7–8, pp. 1624–1633, Apr. 2009.
- [99] J. M. Fernandez, M. Schenk, G. Prassinis, V. J. Lappas, and S. O. Erb, "Deployment Mechanisms of a Gossamer Satellite Deorbiter," in *15th European Space Mechanisms and Tribology Symposium*, 2013, no. 718, p. 15.
- [100] M. Schenk, A. D. Viquerat, K. A. Seffen, and S. D. Guest, "Review of Inflatable Booms for Deployable Space Structures: Packing and Rigidization," *J. Spacecr. Rockets*, vol. 51, no. 3, pp. 762–778, May 2014.
- [101] J. Shim, P. Wang, and K. Bertoldi, "Harnessing instability-induced pattern transformation to design tunable phononic crystals," *Int. J. Solids Struct.*, vol. 58, pp. 52–61, Apr. 2015.
- [102] M. W. Hyer, "Some Observations on the Cured Shape of Thin Unsymmetric Laminates," *J. Compos. Mater.*, vol. 15, no. 2, pp. 175–194, Mar. 1981.
- [103] M. W. Hyer, "The Room-Temperature Shapes of Four-Layer Unsymmetric Cross-Ply Laminates," *J. Compos. Mater.*, vol. 16, no. 4, pp. 318–340, Jul. 1982.
- [104] D. A. Galletly and S. D. Guest, "Bistable composite slit tubes. I. A beam model," *Int. J. Solids Struct.*, vol. 41, no. 16–17, pp. 4517–4533, Aug. 2004.
- [105] E. Kebabze, S. . Guest, and S. Pellegrino, "Bistable prestressed shell structures," *Int. J. Solids Struct.*, vol. 41, no. 11–12, pp. 2801–2820, Jun. 2004.
- [106] K. D. Potter and P. M. Weaver, "A concept for the generation of out-of-plane distortion from tailored FRP laminates," *Compos. Part A Appl. Sci. Manuf.*, vol. 35, no. 12, pp. 1353–1361, Dec. 2004.
- [107] S. Daynes, K. D. Potter, and P. M. Weaver, "Bistable prestressed buckled laminates," *Compos. Sci. Technol.*, vol. 68, no. 15–16, pp. 3431–3437, Dec. 2008.
- [108] S. . Guest and S. Pellegrino, "Analytical models for bistable cylindrical shells," *Proc. R. Soc. A Math. Phys. Eng. Sci.*, vol. 462, no. 2067, pp. 839–854, Mar. 2006.
- [109] Z. Zhang, H. Wu, X. He, H. Wu, Y. Bao, and G. Chai, "The bistable behaviors of carbon-fiber/epoxy anti-symmetric composite shells," *Compos. Part B Eng.*, vol. 47, pp. 190–199, Apr. 2013.
- [110] G. Knott and A. Viquerat, "Helical bistable composite slit tubes," *Compos. Struct.*, vol. 207, no. September 2018, pp. 711–726, Jan. 2019.
- [111] L. L. Howell, *Compliant Mechanisms*. John Wiley & Sons, Inc., 2001.
- [112] N. Lobontiu, *Compliant Mechanisms : Design of Flexure Hinges*. CRC Press, 2003.
- [113] A. E. Albanesi, V. D. Fachinotti, and M. A. Pucheta, "A review on design methods for compliant mechanisms," *Mecánica Comput.*, vol. XXIX, no. 3, pp. 59–72, 2010.
- [114] L. L. Howell, S. P. Magleby, and B. M. (Brian M. Olsen, *Handbook of Compliant Mechanisms*. Wiley, John & Sons Ltd, 2013.
- [115] C. V. Jutte and S. Kota, "Design of Nonlinear Springs for Prescribed Load-Displacement

References

- Functions,” *J. Mech. Des.*, vol. 130, no. 8, p. 081403, 2008.
- [116] R. M. Fowler, L. L. Howell, and S. P. Magleby, “Compliant space mechanisms: a new frontier for compliant mechanisms,” *Mech. Sci.*, vol. 2, no. 2, pp. 205–215, Oct. 2011.
 - [117] G. Hao, J. Yu, and H. Li, “A brief review on nonlinear modeling methods and applications of compliant mechanisms,” *Front. Mech. Eng.*, vol. 11, no. 2, pp. 119–128, Jun. 2016.
 - [118] S. A. Zirbel, K. A. Tolman, B. P. Trease, and L. L. Howell, “Bistable Mechanisms for Space Applications,” *PLoS One*, vol. 11, no. 12, p. e0168218, Dec. 2016.
 - [119] Y. H. Hu, K. H. Lin, S. C. Chang, and M. Chang, “Design of a Compliant Micromechanism for Optical-Fiber Alignment,” *Key Eng. Mater.*, vol. 381–382, pp. 141–144, Jun. 2008.
 - [120] K. Chandrasekaran and A. Thondiyath, “Design of a Two Degree-of-Freedom Compliant Tool Tip for a Handheld Powered Surgical Tool,” *J. Med. Device.*, vol. 11, no. 1, p. 014502, Dec. 2016.
 - [121] Y. Liu, Y. Zhang, and Q. Xu, “Design and Control of a Novel Compliant Constant-Force Gripper Based on Buckled Fixed-Guided Beams,” *IEEE/ASME Trans. Mechatronics*, vol. 22, no. 1, pp. 476–486, Feb. 2017.
 - [122] E. Sung, A. H. Slocum, R. Ma, J. F. Bean, and M. L. Culpepper, “Design of an Ankle Rehabilitation Device Using Compliant Mechanisms,” *J. Med. Device.*, vol. 5, no. 1, p. 011001, Mar. 2011.
 - [123] D. L. Wilcox and L. L. Howell, “Fully compliant tensural bistable micromechanisms (FTBM),” *J. Microelectromechanical Syst.*, vol. 14, no. 6, pp. 1223–1235, Dec. 2005.
 - [124] M. Verotti, A. Dochshanov, and N. P. Belfiore, “Compliance Synthesis of CSFH MEMS-Based Microgrippers,” *J. Mech. Des.*, vol. 139, no. 2, p. 022301, Nov. 2016.
 - [125] D. C. Freeman, “Nonlinear Springs with Applications to Flow Regulation Valves and Mechanisms,” Massachusetts Institute of Technology, 2008.
 - [126] S. L. Weeke, N. Tolou, G. Semon, and J. L. Herder, “A Monolithic Force-Balanced Oscillator,” *J. Mech. Robot.*, vol. 9, no. 2, p. 021004, Mar. 2017.
 - [127] G. Hao and X. Kong, “A structure design method for compliant parallel manipulators with actuation isolation,” *Mech. Sci.*, vol. 7, no. 2, pp. 247–253, Nov. 2016.
 - [128] B. P. Trease, Y.-M. Moon, and S. Kota, “Design of Large-Displacement Compliant Joints,” *J. Mech. Des.*, vol. 127, no. 4, p. 788, 2005.
 - [129] M. Verotti, R. Crescenzi, M. Balucani, and N. P. Belfiore, “MEMS-Based Conjugate Surfaces Flexure Hinge,” *J. Mech. Des.*, vol. 137, no. 1, p. 012301, Jan. 2015.
 - [130] U. Hanke, M. Zichner, A. Tudorache, N. Modler, and M. Ashir, “Design of monolithic compliant mechanisms with beam elements of distributed stiffness,” *Materwiss. Werksttech.*, vol. 47, no. 11, pp. 1132–1139, Nov. 2016.
 - [131] M. Ohsaki and S. Nishiwaki, “Shape design of pin-jointed multistable compliant mechanisms using snapthrough behavior,” *Struct. Multidiscip. Optim.*, vol. 30, no. 4, pp. 327–334, Oct. 2005.
 - [132] J. S. Han, C. Müller, U. Wallrabe, and J. G. Korvink, “Design, Simulation, and Fabrication of a Quadstable Monolithic Mechanism With X- and Y-Directional Bistable Curved Beams,” *J. Mech. Des.*, vol. 129, no. 11, p. 1198, 2007.
 - [133] H.-J. Su and J. M. McCarthy, “Synthesis of Bistable Compliant Four-Bar Mechanisms Using Polynomial Homotopy,” *J. Mech. Des.*, vol. 129, no. 10, p. 1094, 2007.
 - [134] Y. Oh, “Synthesis of Multistable Equilibrium Compliant Mechanisms,” University of Michigan, 2008.
 - [135] Y. S. Oh and S. Kota, “Synthesis of Multistable Equilibrium Compliant Mechanisms Using

- Combinations of Bistable Mechanisms,” *J. Mech. Des.*, vol. 131, no. 2, p. 021002, 2009.
- [136] G. Chen, Y. Gou, and L. Yang, “Research on Multistable Compliant Mechanisms: The State of the Art,” in *9th International Conference on Frontiers of Design and Manufacturing*, 2010.
 - [137] G. Chen, Q. T. Aten, S. Zirbel, B. D. Jensen, and L. L. Howell, “A Tristable Mechanism Configuration Employing Orthogonal Compliant Mechanisms,” *J. Mech. Robot.*, vol. 2, no. 1, p. 014501, 2010.
 - [138] H.-T. Pham and D.-A. Wang, “A quadristable compliant mechanism with a bistable structure embedded in a surrounding beam structure,” *Sensors Actuators A Phys.*, vol. 167, no. 2, pp. 438–448, Jun. 2011.
 - [139] G. Chen, D. L. Wilcox, and L. L. Howell, “Fully compliant double tensural tristable micromechanisms (DTTM),” *J. Micromechanics Microengineering*, vol. 19, no. 2, p. 025011, Feb. 2009.
 - [140] J. L. Herder, “Energy-free Systems. Theory, conception and design of statically balanced spring mechanisms,” Delft University of Technology, 2001.
 - [141] K. Hoetmer, G. Woo, C. Kim, and J. Herder, “Negative Stiffness Building Blocks for Statically Balanced Compliant Mechanisms: Design and Testing,” *J. Mech. Robot.*, vol. 2, no. 4, p. 041007, 2010.
 - [142] F. M. Morsch and J. L. Herder, “Design of a Generic Zero Stiffness Compliant Joint,” in *Volume 2: 34th Annual Mechanisms and Robotics Conference, Parts A and B*, 2010, pp. 427–435.
 - [143] G. Chen and S. Zhang, “Fully-compliant statically-balanced mechanisms without prestressing assembly: concepts and case studies,” *Mech. Sci.*, vol. 2, no. 2, pp. 169–174, Aug. 2011.
 - [144] H.-T. Pham and D.-A. Wang, “A constant-force bistable mechanism for force regulation and overload protection,” *Mech. Mach. Theory*, vol. 46, no. 7, pp. 899–909, Jul. 2011.
 - [145] Y.-H. Chen and C.-C. Lan, “An Adjustable Constant-Force Mechanism for Adaptive End-Effector Operations,” *J. Mech. Des.*, vol. 134, no. 3, p. 031005, 2012.
 - [146] J. Human, F. Morsch, K. Hoetmer, and J. L. Herder, “Experimental Assessment of Stiffness Reduction by Static Balancing in a Cross-Flexural Joint and a Compliant Gripper,” in *2nd IFToMM Asian Conference on Mechanism and Machine Science*, 2012.
 - [147] L. Berntsen, D. H. Gosenshuis, and J. L. Herder, “Design of a Compliant Monolithic Internally Statically Balanced Four-Bar Mechanism,” in *Volume 5A: 38th Mechanisms and Robotics Conference*, 2014, p. V05AT08A040.
 - [148] G. Radaelli and J. L. Herder, “A monolithic compliant large-range gravity balancer,” *Mech. Mach. Theory*, vol. 102, pp. 55–67, Aug. 2016.
 - [149] S. R. Deepak, A. N. Hansoge, and G. K. Ananthasuresh, “Application of Rigid-Body-Linkage Static Balancing Techniques to Reduce Actuation Effort in Compliant Mechanisms,” *J. Mech. Robot.*, vol. 8, no. 2, p. 021005, Nov. 2015.
 - [150] K. A. Tolman, E. G. Merriam, and L. L. Howell, “Compliant constant-force linear-motion mechanism,” *Mech. Mach. Theory*, vol. 106, pp. 68–79, Dec. 2016.
 - [151] P. Wang and Q. Xu, “Design and modeling of constant-force mechanisms: A survey,” *Mech. Mach. Theory*, vol. 119, pp. 1–21, Jan. 2018.
 - [152] M. Schenk and S. D. Guest, “On zero stiffness,” *Proc. Inst. Mech. Eng. Part C J. Mech. Eng. Sci.*, vol. 228, no. 10, pp. 1701–1714, Jul. 2014.
 - [153] C.-H. Kuo, J. S. Dai, and H.-S. Yan, “Reconfiguration principles and strategies for reconfigurable mechanisms,” in *2009 ASME/IFTToMM International Conference on Reconfigurable Mechanisms and Robots*, 2009, pp. 1–7.

References

- [154] M. F. Aïmedee, “Synthesis and Control of Reconfigurable mechanisms,” Université Blaise Pascal - Clermont Ferrand II, 2015.
- [155] F. Aïmedee, G. Gogu, J. S. Dai, C. Bouzgarrou, and N. Bouton, “Systematization of morphing in reconfigurable mechanisms,” *Mech. Mach. Theory*, vol. 96, pp. 215–224, Feb. 2016.
- [156] L.-Y. Ji, Y. J. Guo, P.-Y. Qin, S.-X. Gong, and R. Mittra, “A Reconfigurable Partially Reflective Surface (PRS) Antenna for Beam Steering,” *IEEE Trans. Antennas Propag.*, vol. 63, no. 6, pp. 2387–2395, Jun. 2015.
- [157] Y. J. Guo, P.-Y. Qin, S.-L. Chen, W. Lin, and R. W. Ziolkowski, “Advances in Reconfigurable Antenna Systems Facilitated by Innovative Technologies,” *IEEE Access*, vol. 6, no. c, pp. 5780–5794, 2018.
- [158] J. S. Dai and J. R. Jones, “Kinematics and mobility analysis of carton folds in packing manipulation based on the mechanism equivalent,” *Proc. Inst. Mech. Eng. Part C J. Mech. Eng. Sci.*, vol. 216, no. 10, pp. 959–970, Oct. 2002.
- [159] J. S. Dai and J. R. Jones, “Mobility in Metamorphic Mechanisms of Foldable/Erectable Kinds,” *J. Mech. Des.*, vol. 121, no. 3, p. 375, 1999.
- [160] R. Li, Y. Yao, and X. Kong, “A class of reconfigurable deployable platonic mechanisms,” *Mech. Mach. Theory*, vol. 105, pp. 409–427, Nov. 2016.
- [161] R. Li, Y. Yao, and X. Ding, “A family of reconfigurable deployable polyhedral mechanisms based on semiregular and Johnson polyhedra,” *Mech. Mach. Theory*, vol. 126, pp. 344–358, Aug. 2018.
- [162] B. P. DeFigueiredo, K. A. Tolman, E. Crampton, N. A. Pehrson, S. P. Magleby, and L. L. Howell, “Origami-Based Design of Conceal-and-Reveal Systems,” in *Volume 5B: 42nd Mechanisms and Robotics Conference*, 2018, p. V05BT07A055.
- [163] W. Wang, H. Zhang, G. Zong, and J. Zhang, “Design and Realization of a Novel Reconfigurable Robot with Serial and Parallel Mechanisms,” in *2006 IEEE International Conference on Robotics and Biomimetics*, 2006, pp. 697–702.
- [164] G. Wei, J. S. Dai, S. Wang, and H. Luo, “Kinematic Analysis and Prototype of a Metamorphic Anthropomorphic Hand with a Reconfigurable Palm,” *Int. J. Humanoid Robot.*, vol. 08, no. 03, pp. 459–479, Sep. 2011.
- [165] H. Heidari, M. J. Pouria, S. Sharifi, and M. Karami, “Design and fabrication of robotic gripper for grasping in minimizing contact force,” *Adv. Sp. Res.*, vol. 61, no. 5, pp. 1359–1370, Mar. 2018.
- [166] G. Hao, H. Li, A. Nayak, and S. Caro, “Design of a Compliant Gripper With Multimode Jaws,” *J. Mech. Robot.*, vol. 10, no. 3, p. 031005, Mar. 2018.
- [167] F. Gioia, D. Dureisseix, R. Motro, and B. Maurin, “Design and Analysis of a Foldable/Unfoldable Corrugated Architectural Curved Envelop,” *J. Mech. Des.*, vol. 134, no. 3, p. 031003, 2012.
- [168] M. Matheou, M. C. Phocas, E. G. Christoforou, and A. Müller, “On the kinetics of reconfigurable hybrid structures,” *J. Build. Eng.*, vol. 17, no. October 2017, pp. 32–42, May 2018.
- [169] K. Wohlhart, “Kinematotropic Linkages,” in *Recent Advances in Robot Kinematics*, Dordrecht: Springer Netherlands, 1996, pp. 359–368.
- [170] C. Galletti and P. Fanghella, “Single-loop kinematotropic mechanisms,” *Mech. Mach. Theory*, vol. 36, no. 6, pp. 743–761, Jun. 2001.
- [171] C.-C. Lee and J. M. Hervé, “Discontinuously Movable Seven-Link Mechanisms Via Group-Algebraic Approach,” *Proc. Inst. Mech. Eng. Part C J. Mech. Eng. Sci.*, vol. 219, no. 6, pp. 577–587, Jun. 2005.
- [172] M. Leonesio, G. Bianchi, and P. Manara, “A general approach for Self-locking Analysis in Closed Kinematic Chains,” in *12th World Congress in Mechanism and Machine Theory*, 2007, pp. 141–

147.

- [173] L. Zhang and J. S. Dai, "Reconfiguration of Spatial Metamorphic Mechanisms," *J. Mech. Robot.*, vol. 1, no. 1, p. 011012, 2009.
- [174] D. Gan, J. S. Dai, and Q. Liao, "Mobility Change in Two Types of Metamorphic Parallel Mechanisms," *J. Mech. Robot.*, vol. 1, no. 4, p. 041007, 2009.
- [175] W. X. Zhang, X. L. Ding, and J. S. Dai, "Morphological synthesis of metamorphic mechanisms based on constraint variation," *Proc. Inst. Mech. Eng. Part C J. Mech. Eng. Sci.*, vol. 225, no. 12, pp. 2997–3010, Dec. 2011.
- [176] N. Plitea, D. Lese, D. Pislă, and C. Vaida, "Structural design and kinematics of a new parallel reconfigurable robot," *Robot. Comput. Integr. Manuf.*, vol. 29, no. 1, pp. 219–235, Feb. 2013.
- [177] S. Li and J. S. Dai, "Structure Synthesis of Single-Driven Metamorphic Mechanisms Based on the Augmented Assur Groups," *J. Mech. Robot.*, vol. 4, no. 3, p. 031004, 2012.
- [178] P. C. López-Custodio, J. M. Rico, J. J. Cervantes-Sánchez, and G. I. Pérez-Soto, "Reconfigurable Mechanisms From the Intersection of Surfaces," *J. Mech. Robot.*, vol. 8, no. 2, p. 021029, Mar. 2016.
- [179] L. Nurahmi, S. Caro, P. Wenger, J. Schadlbauer, and M. Husty, "Reconfiguration analysis of a 4-RUU parallel manipulator," *Mech. Mach. Theory*, vol. 96, pp. 269–289, Feb. 2016.
- [180] R. Li, Y. Yao, and X. Kong, "Reconfigurable deployable polyhedral mechanism based on extended parallelogram mechanism," *Mech. Mach. Theory*, vol. 116, pp. 467–480, Oct. 2017.
- [181] R. Jovichikj, A. Yasir, and G. Kiper, "Reconfigurable Deployable Umbrella Canopies," in *2018 International Conference on Reconfigurable Mechanisms and Robots (ReMAR)*, 2018, vol. 1, no. d, pp. 1–6.
- [182] K. Miura, H. Furuya, and K. Suzuki, "Variable geometry truss and its application to deployable truss and space crane arm," *Acta Astronaut.*, vol. 12, no. 7–8, pp. 599–607, Jul. 1985.
- [183] M. Badescu and C. Mavroidis, "New Performance Indices and Workspace Analysis of Reconfigurable Hyper-Redundant Robotic Arms," *Int. J. Rob. Res.*, vol. 23, no. 6, pp. 643–659, Jun. 2004.
- [184] Y. Zhao, S. Hu, and Y. Yang, "Inverse kinematics for the variable geometry truss manipulator via a Lagrangian dual method," *Int. J. Adv. Robot. Syst.*, vol. 13, no. 6, p. 172988141666677, Dec. 2016.
- [185] A. D. Finistauri and F. J. Xi, "Type Synthesis and Kinematics of a Modular Variable Geometry Truss Mechanism for Aircraft Wing Morphing," in *2009 ASME/IFTOMM International Conference on Reconfigurable Mechanisms and Robots*, 2009, pp. 478–485.
- [186] M. Schenk, S. D. Guest, and J. L. Herder, "Zero stiffness tensegrity structures," *Int. J. Solids Struct.*, vol. 44, no. 20, pp. 6569–6583, Oct. 2007.
- [187] M. Schenk, J. L. Herder, and S. D. Guest, "Design of a Statically Balanced Tensegrity Mechanism," in *Volume 2: 30th Annual Mechanisms and Robotics Conference, Parts A and B*, 2006, vol. 2006, pp. 501–511.
- [188] V. Böhm, S. Sumi, T. Kaufhold, and K. Zimmermann, "Compliant multistable tensegrity structures," *Mech. Mach. Theory*, vol. 115, pp. 130–148, Sep. 2017.
- [189] E. A. Peraza Hernandez, D. J. Hartl, R. J. Malak, E. Akleman, O. Gonen, and H.-W. Kung, "Design Tools for Patterned Self-Folding Reconfigurable Structures Based on Programmable Active Laminates," *J. Mech. Robot.*, vol. 8, no. 3, p. 031015, Mar. 2016.
- [190] Y. Liu, B. Shaw, M. D. Dickey, and J. Genzer, "Sequential self-folding of polymer sheets," *Sci. Adv.*, vol. 3, no. 3, p. e1602417, Mar. 2017.

References

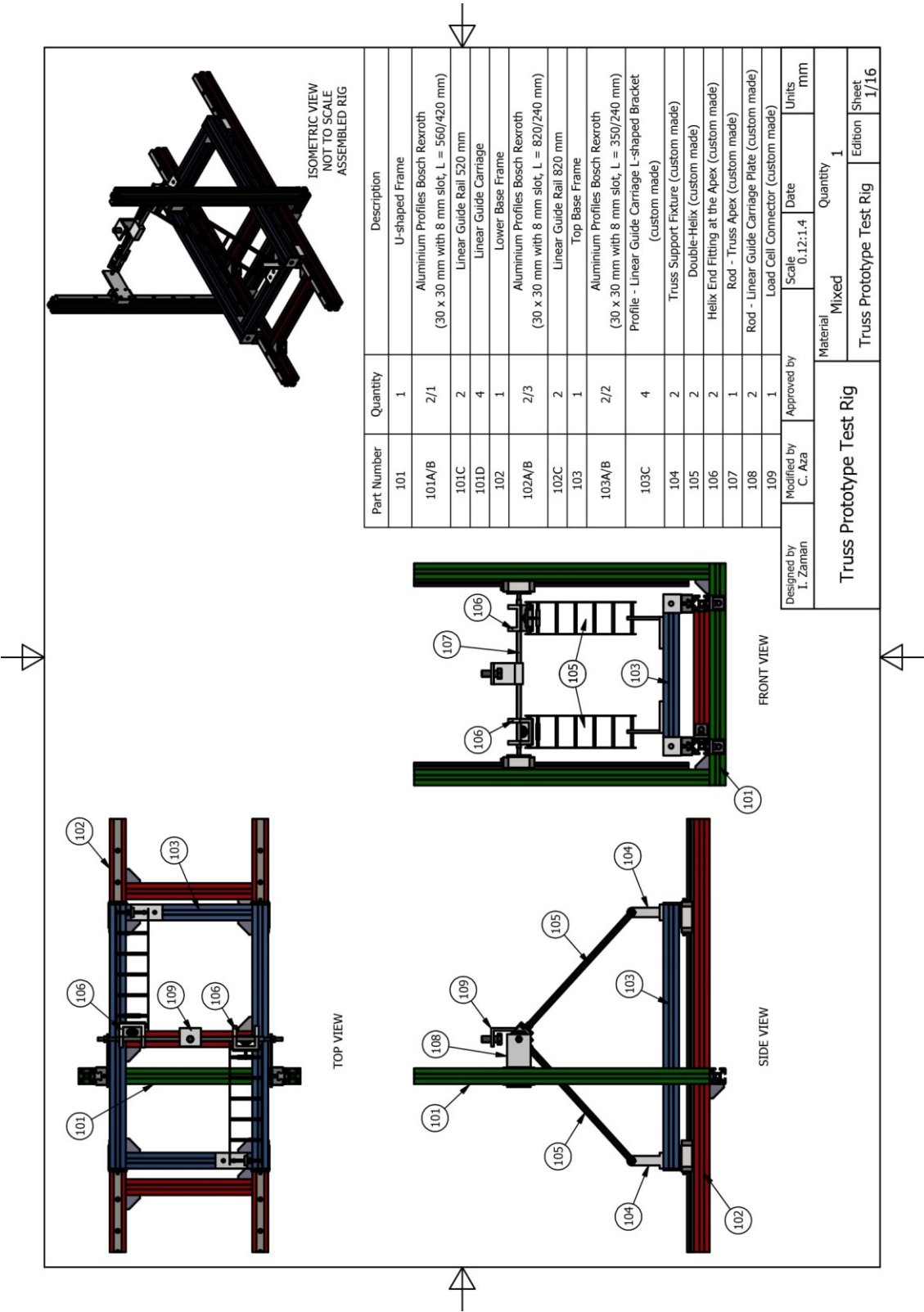
- [191] G. Oliveri, D. H. Werner, and A. Massa, “Reconfigurable Electromagnetics Through Metamaterials—A Review,” *Proc. IEEE*, vol. 103, no. 7, pp. 1034–1056, Jul. 2015.
- [192] J. T. B. Overvelde, J. C. Weaver, C. Hoberman, and K. Bertoldi, “Rational design of reconfigurable prismatic architected materials,” *Nature*, vol. 541, no. 7637, pp. 347–352, Jan. 2017.
- [193] B. Haghpanah, L. Salari-Sharif, P. Pourrajab, J. Hopkins, and L. Valdevit, “Multistable Shape-Reconfigurable Architected Materials,” *Adv. Mater.*, vol. 28, no. 36, pp. 7915–7920, Sep. 2016.
- [194] H. Fu *et al.*, “Morphable 3D mesostructures and microelectronic devices by multistable buckling mechanics,” *Nat. Mater.*, vol. 17, no. 3, pp. 268–276, Mar. 2018.
- [195] K. Miura, “Method of Packaging and Deployment of Large Membranes in Space,” *Inst. Sp. Astronaut. Sci.*, vol. 618, pp. 1–9, 1985.
- [196] E. T. Filipov, T. Tachi, and G. H. Paulino, “Origami tubes assembled into stiff, yet reconfigurable structures and metamaterials,” *Proc. Natl. Acad. Sci.*, vol. 112, no. 40, pp. 12321–12326, Oct. 2015.
- [197] L. Valdevit, K. Bertoldi, J. Guest, and C. Spadaccini, “Architected materials: Synthesis, characterization, modeling, and optimal design - Introduction,” *J. Mater. Res.*, vol. 33, no. 3, pp. 241–246, Feb. 2018.
- [198] N. A. Pehrson, S. P. Magleby, and L. L. Howell, “An Origami-based Thickness-Accommodating Bistable Mechanism in Monolithic Thick-sheet Materials,” in *2018 International Conference on Reconfigurable Mechanisms and Robots (ReMAR)*, 2018, pp. 1–7.
- [199] J. T. Miller *et al.*, “Buckling-induced lock-up of a slender rod injected into a horizontal cylinder,” *Int. J. Solids Struct.*, vol. 72, pp. 153–164, 2015.
- [200] J. M. Gordo, C. G. Soares, and D. Faulkner, “Approximate Assessment of the Ultimate Longitudinal Strength of the Hull Girder,” *J. Sh. Res.*, vol. 40, no. 1, pp. 60–69, 1996.
- [201] D. Y. Jeong, R. Bruzek, and A. Tajaddini, “Engineering Studies on Joint Bar Integrity: Part I — Field Surveys and Observed Failure Modes,” in *2014 Joint Rail Conference*, 2014, p. V001T01A001.
- [202] X. Lachenal, “Concepts for morphing composite structures using non-linear stiffness tailoring,” University of Bristol, 2013.
- [203] L. Giomi and L. Mahadevan, “Multistability of free spontaneously curved anisotropic strips,” *Proc. R. Soc. A Math. Phys. Eng. Sci.*, vol. 468, no. 2138, pp. 511–530, Feb. 2012.
- [204] L. P. Kollár and G. S. Springer, *Mechanics of Composite Structures*. Cambridge: Cambridge University Press, 2003.
- [205] R. M. Jones, *Mechanics of Composite Materials*, 2nd ed. Taylor & Francis, Inc., 1999.
- [206] C. Aza, “Design Optimization of Multistable Composite Compliant Actuator for Wearable Robotic Devices,” Bristol, UK, 2015.
- [207] C. Aza, A. Pirrera, and M. Schenk, “Reconfigurable Trusses of Nonlinear Morphing Elements,” in *Volume 5B: 42nd Mechanisms and Robotics Conference*, 2018, p. V05BT07A004.
- [208] Hexcel, “HexPly® 8552 Product Data Sheet.” pp. 1–6, 2016.
- [209] S. Ishida, H. Uchida, H. Shimosaka, and I. Hagiwara, “Design Concepts and Prototypes of Vibration Isolators Using Bi-Stable Foldable Structures,” in *Volume 5B: 39th Mechanisms and Robotics Conference*, 2015, p. V05BT08A030.
- [210] C. J. Kim, S. Kota, and Y.-M. Moon, “An Instant Center Approach Toward the Conceptual Design of Compliant Mechanisms,” *J. Mech. Des.*, vol. 128, no. 3, p. 542, 2006.
- [211] B. Rivlin and D. Elata, “Design of nonlinear springs for attaining a linear response in gap-closing

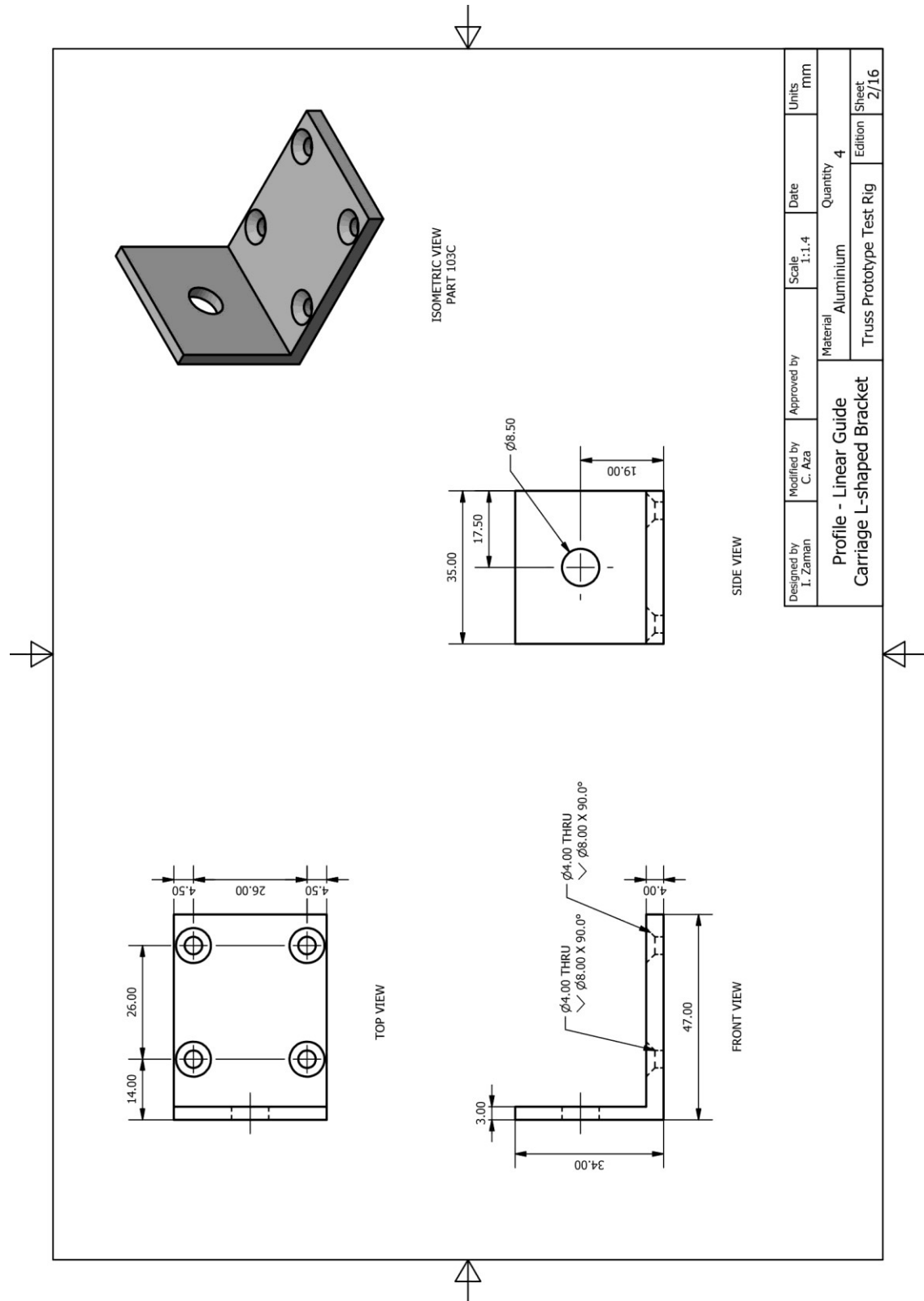
- electrostatic actuators,” *Int. J. Solids Struct.*, vol. 49, no. 26, pp. 3816–3822, Dec. 2012.
- [212] R. R. Torrealba and S. B. Udelman, “Design of cam shape for maximum stiffness variability on a novel compliant actuator using differential evolution,” *Mech. Mach. Theory*, vol. 95, pp. 114–124, Jan. 2016.
- [213] N. A. Fleck, V. S. Deshpande, and M. F. Ashby, “Micro-architected materials: past, present and future,” *Proc. R. Soc. A Math. Phys. Eng. Sci.*, vol. 466, no. 2121, pp. 2495–2516, Sep. 2010.
- [214] A. Vigliotti and D. Pasini, “Stiffness and strength of tridimensional periodic lattices,” *Comput. Methods Appl. Mech. Eng.*, vol. 229–232, pp. 27–43, Jul. 2012.
- [215] T. Chen, J. Mueller, and K. Shea, “Integrated Design and Simulation of Tunable, Multi-State Structures Fabricated Monolithically with Multi-Material 3D Printing,” *Sci. Rep.*, vol. 7, no. 1, p. 45671, May 2017.
- [216] R. V. Mises, “Über die Stabilitätsprobleme der Elastizitätstheorie,” *ZAMM - Zeitschrift für Angew. Math. und Mech.*, vol. 3, no. 6, pp. 406–422, Jan. 1923.
- [217] R. V. Mises and J. Ratzersdorfer, “Die Knicksicherheit von Fachwerken,” *ZAMM - Zeitschrift für Angew. Math. und Mech.*, vol. 5, no. 3, pp. 218–235, Jan. 1925.
- [218] C. Aza, A. Pirrera, and M. Schenk, “Multistable Trusses of Nonlinear Morphing Elements,” in *2018 International Conference on Reconfigurable Mechanisms and Robots (ReMAR)*, 2018, pp. 1–6.
- [219] G. Radaelli, J. A. Gallego, and J. L. Herder, “An Energy Approach to Static Balancing of Systems With Torsion Stiffness,” *J. Mech. Des.*, vol. 133, no. 9, p. 091006, 2011.
- [220] G. Radaelli and J. L. Herder, “A potential energy field (PEF) approach to the design of a compliant self-guiding statically-balanced straight-line mechanism,” *Mech. Mach. Theory*, vol. 114, pp. 141–155, Aug. 2017.
- [221] Z. Kala and M. Kalina, “Static equilibrium states of von Mises trusses,” *Int. J. Mech.*, vol. 10, pp. 294–298, 2016.
- [222] Y. G. Panovko and I. I. Gubanov, *Stability and Oscillation of Elastic Systems: Modern concepts, paradoxes and errors*, 2nd ed. National Aeronautics and Space Administration, 1973.
- [223] L. Kwasniewski, “Complete equilibrium paths for Mises trusses,” *Int. J. Non. Linear. Mech.*, vol. 44, no. 1, pp. 19–26, Jan. 2009.
- [224] Z. P. Bazant and L. Cedolin, *Stability of Structures: Elastic, Inelastic, Fracture, and Damage Theories*. World Scientific Publishing Co. Pte. Ltd., 2010.
- [225] V. Galishnikova, P. Dunaiski, and P. Jan Pahl, *Geometrically Nonlinear Analysis of Plane Trusses and Frames*. Sun Media, 2009.
- [226] M. Kalina, “Stability Problems of Pyramidal von Mises Planar Trusses with Geometrical Imperfection,” *Int. J. Theor. Appl. Mech.*, vol. 1, pp. 118–123, 2016.
- [227] P. X. Bellini, “The concept of snap-buckling illustrated by a simple model,” *Int. J. Non. Linear. Mech.*, vol. 7, no. 6, pp. 643–650, Dec. 1972.
- [228] M. Psotný and J. Ravinger, “Von Misses Truss with Imperfection,” *Slovak J. Civ. Eng.*, pp. 1–7, 2003.
- [229] D. A. Pecknold, J. Ghaboussi, and T. J. Healey, “Snap-Through and Bifurcation in a Simple Structure,” *J. Eng. Mech.*, vol. 111, no. 7, pp. 909–922, Jul. 1985.
- [230] S. S. Ligarò and P. S. Valvo, “Large displacement analysis of elastic pyramidal trusses,” *Int. J. Solids Struct.*, vol. 43, no. 16, pp. 4867–4887, Aug. 2006.
- [231] M. A. Crisfield, “A fast incremental/iterative solution procedure that handles ‘snap-through,’”

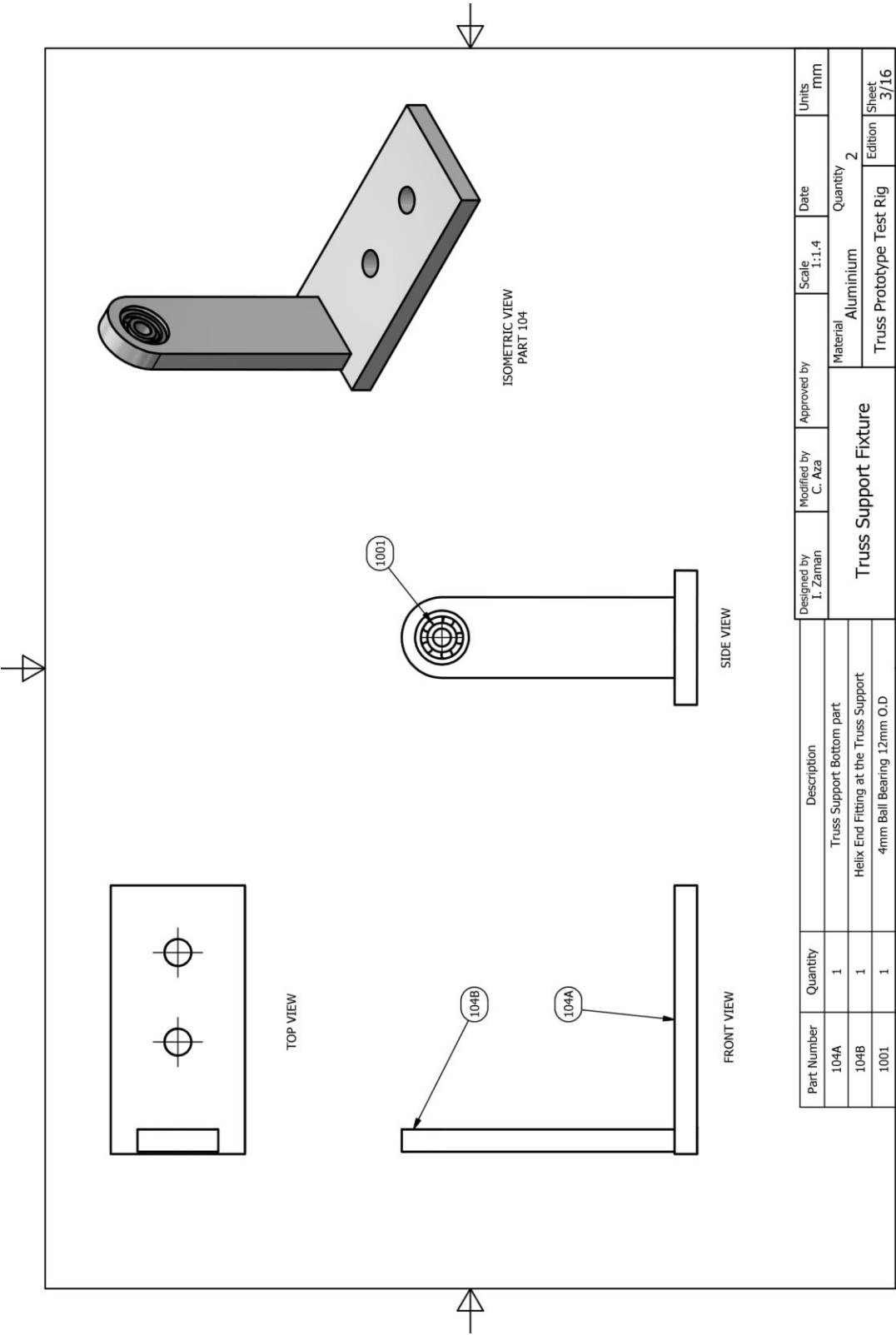
References

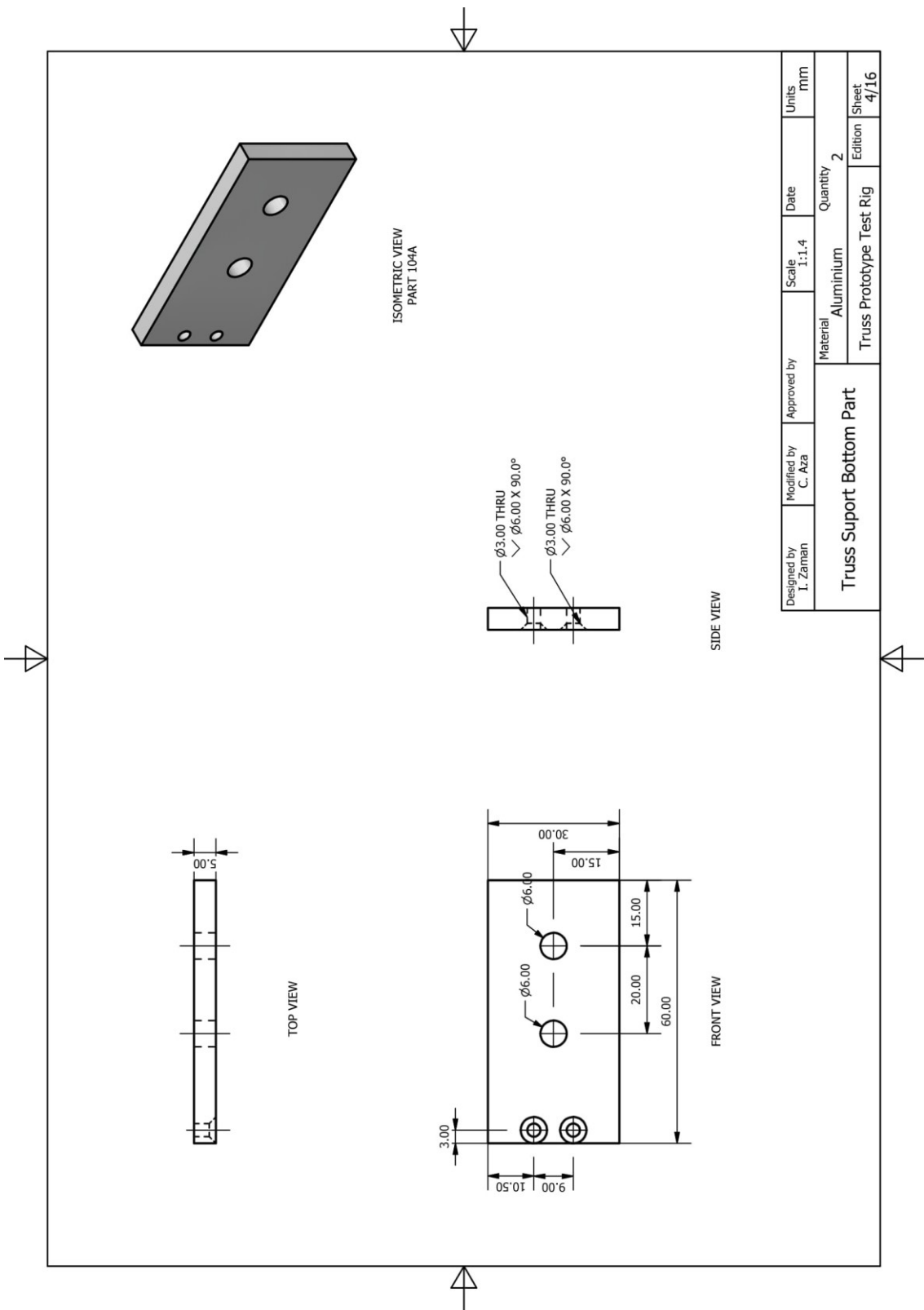
- Comput. Struct.*, vol. 13, no. 1–3, pp. 55–62, Jun. 1981.
- [232] E. Carrera, “A study on arc-length-type methods and their operation failures illustrated by a simple model,” *Comput. Struct.*, vol. 50, no. 2, pp. 217–229, Jan. 1994.
- [233] M. Fafard and B. Massicotte, “Geometrical interpretation of the arc-length method,” *Comput. Struct.*, vol. 46, no. 4, pp. 603–615, Feb. 1993.
- [234] N. Vassios, “Nonlinear Analysis of Structures The Arc Length Method: Formulation, Implementation and Applications,” Harvard University, 2015.
- [235] J. N. Reddy, *An Introduction to Nonlinear Finite Element Analysis*, 2nd ed. Oxford University Press, 2015.
- [236] P. Wriggers, W. Wagner, and C. Miehe, “A quadratically convergent procedure for the calculation of stability points in finite element analysis,” *Comput. Methods Appl. Mech. Eng.*, vol. 70, no. 3, pp. 329–347, Oct. 1988.
- [237] W. Wagner and P. Wriggers, “A simple method for the calculation of postcritical branches,” *Eng. Comput.*, vol. 5, no. 2, pp. 103–109, Feb. 1988.
- [238] P. Wriggers and J. C. Simo, “A general procedure for the direct computation of turning and bifurcation points,” *Int. J. Numer. Methods Eng.*, vol. 30, no. 1, pp. 155–176, 1990.
- [239] A. Jepson and A. Spence, “Folds in Solutions of Two Parameter Systems and Their Calculation. Part I,” *SIAM J. Numer. Anal.*, vol. 22, no. 2, pp. 347–368, Apr. 1985.
- [240] G. Chen, S. Zhang, and G. Li, “Multistable Behaviors of Compliant Sarrus Mechanisms,” *J. Mech. Robot.*, vol. 5, no. 2, p. 021005, Mar. 2013.
- [241] T. G. Nelson, R. J. Lang, N. A. Pehrson, S. P. Magleby, and L. L. Howell, “Facilitating Deployable Mechanisms and Structures Via Developable Lamina Emergent Arrays,” *J. Mech. Robot.*, vol. 8, no. 3, p. 031006, Mar. 2016.
- [242] A. Norman, S. Guest, and K. Seffen, “Novel Multistable Corrugated Structures,” in *48th AIAA/ASME/ASCE/AHS/ASC Structures, Structural Dynamics, and Materials Conference*, 2007.
- [243] N. Tolou, V. A. Henneken, and J. L. Herder, “Statically Balanced Compliant Micro Mechanisms (SB-MEMS): Concepts and Simulation,” in *Volume 2: 34th Annual Mechanisms and Robotics Conference, Parts A and B*, 2010, pp. 447–454.
- [244] K. Hoetmer, J. L. Herder, and C. J. Kim, “A Building Block Approach for the Design of Statically Balanced Compliant Mechanisms,” in *Volume 7: 33rd Mechanisms and Robotics Conference, Parts A and B*, 2009, pp. 313–323.
- [245] J.-S. Zhao, Z.-F. Yan, and F.-L. Chu, “A Reconfigurable Linkage and Its Applications in Lift Mechanism,” in *Advances in Reconfigurable Mechanisms and Robots I*, London: Springer London, 2012, pp. 815–829.
- [246] G. H. Staab, “Laminate Analysis,” in *Laminar Composites*, 2nd ed., Butterworth-Heinemann, 2015, pp. 189–284.
- [247] S. W. Tsai and E. M. Wu, “A General Theory of Strength for Anisotropic Materials,” *J. Compos. Mater.*, vol. 5, no. 1, pp. 58–80, Jan. 1971.
- [248] G. H. Staab, “Lamina Failure Theories,” in *Laminar Composites*, 1st ed., Butterworth-Heinemann, 1999, pp. 142–188.

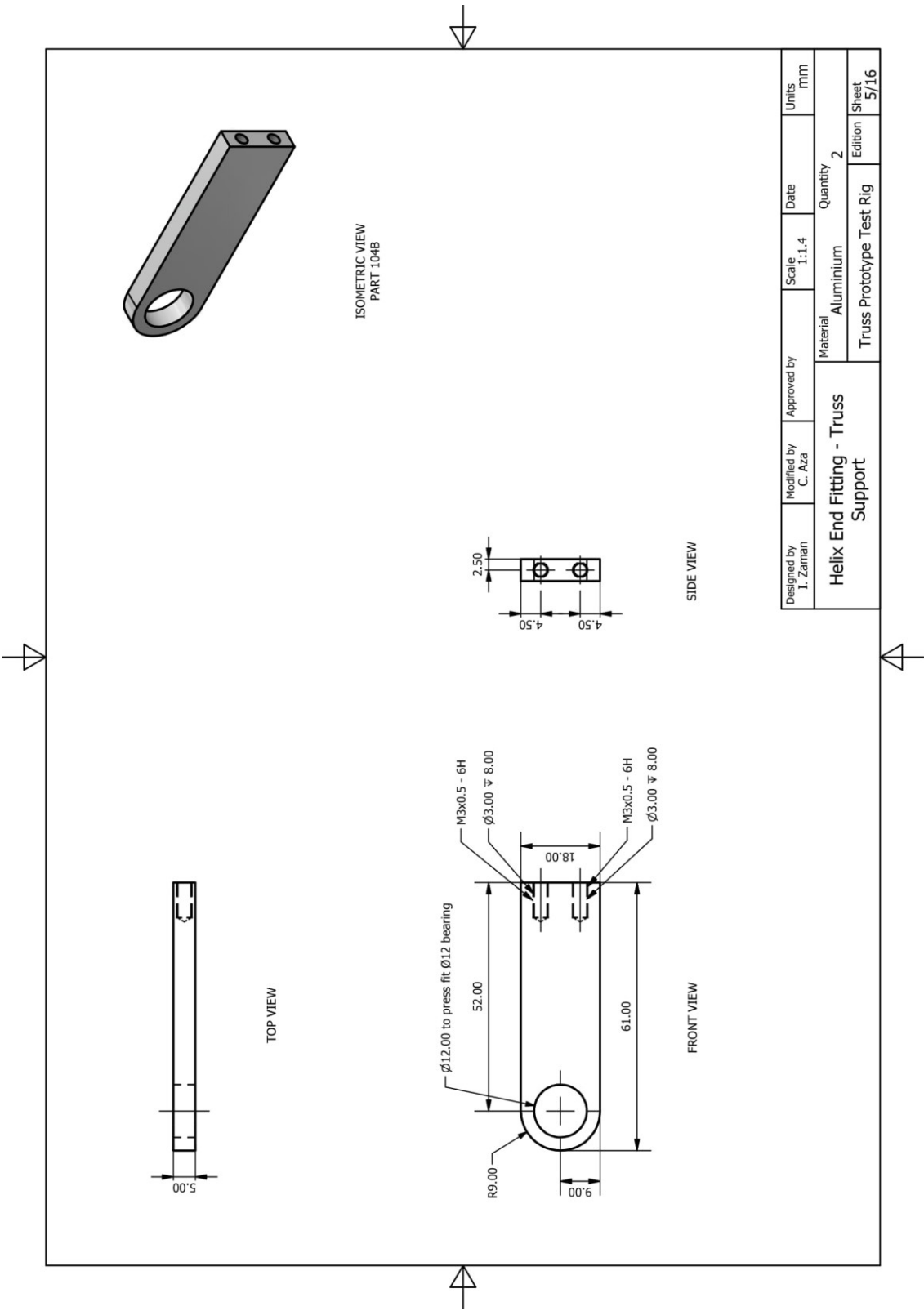
Appendix A.1 – Truss Prototype Test Rig

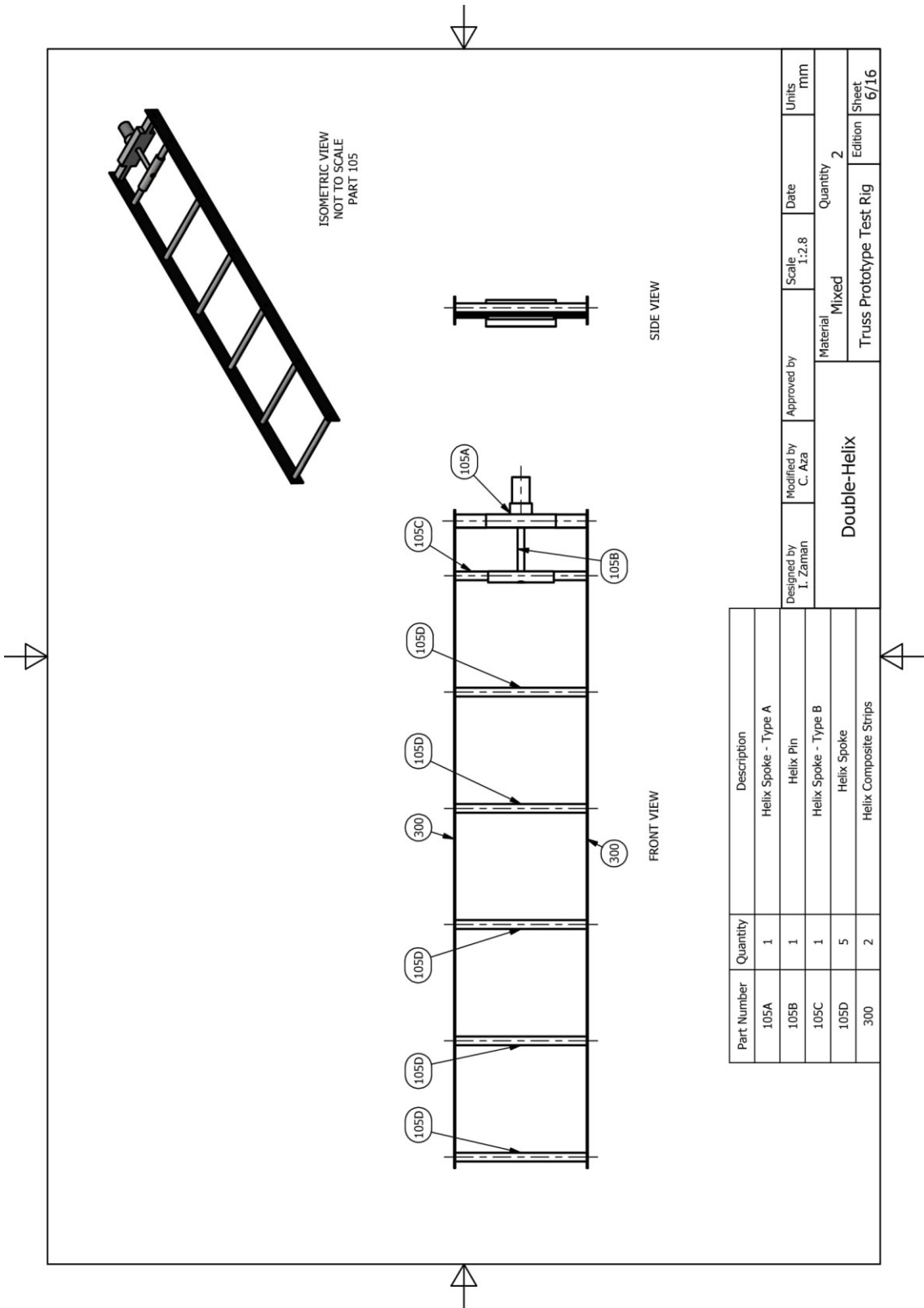


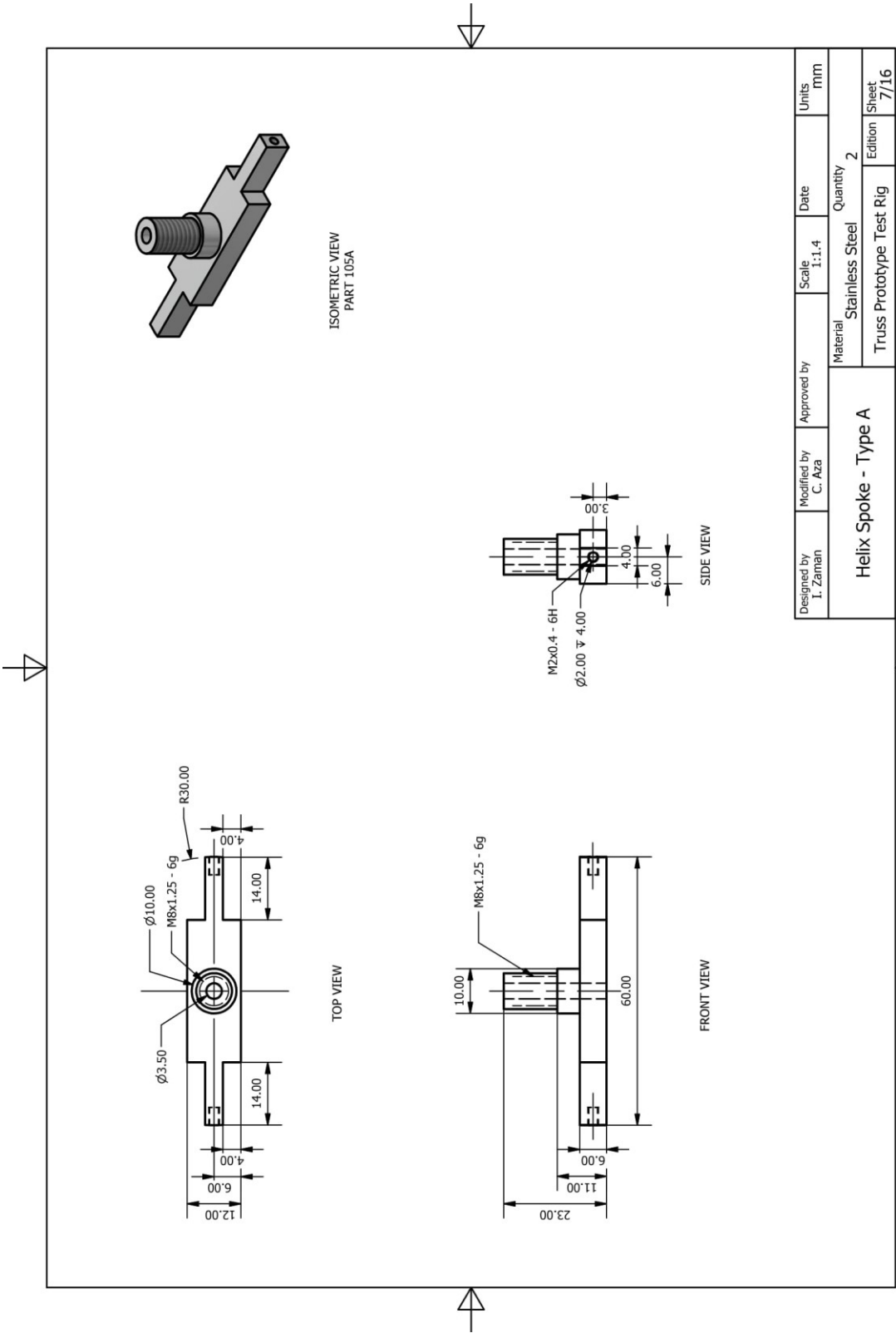


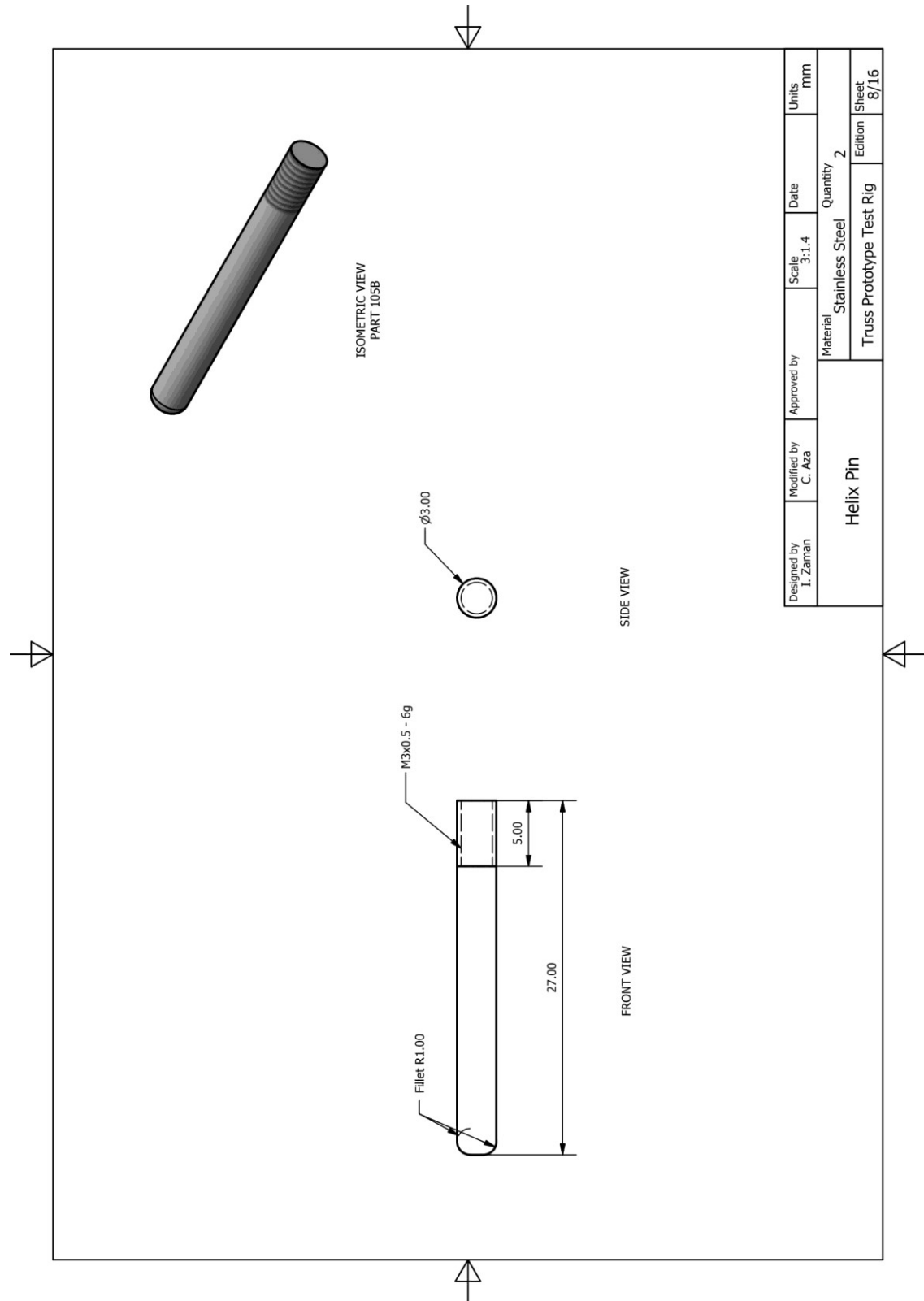


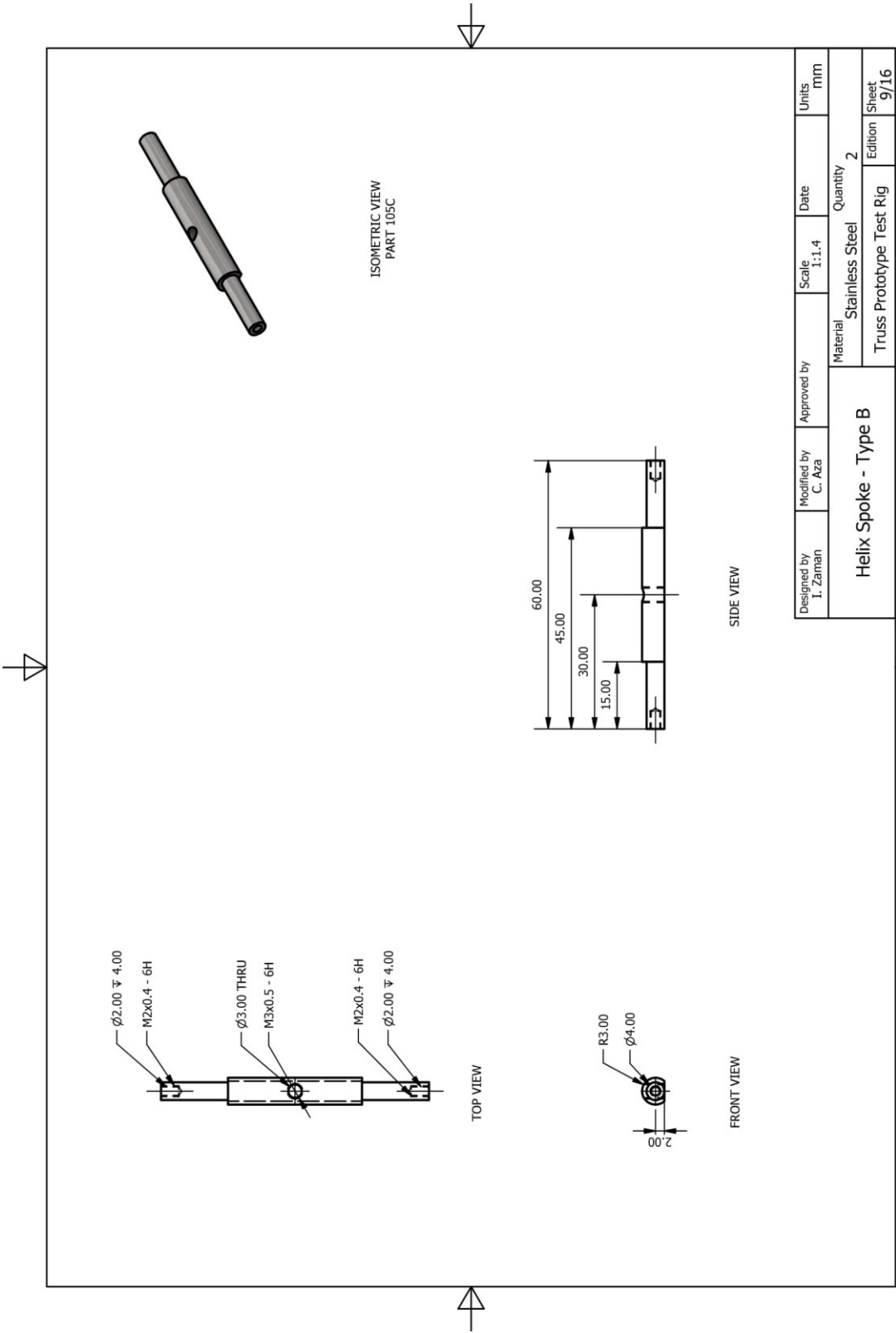


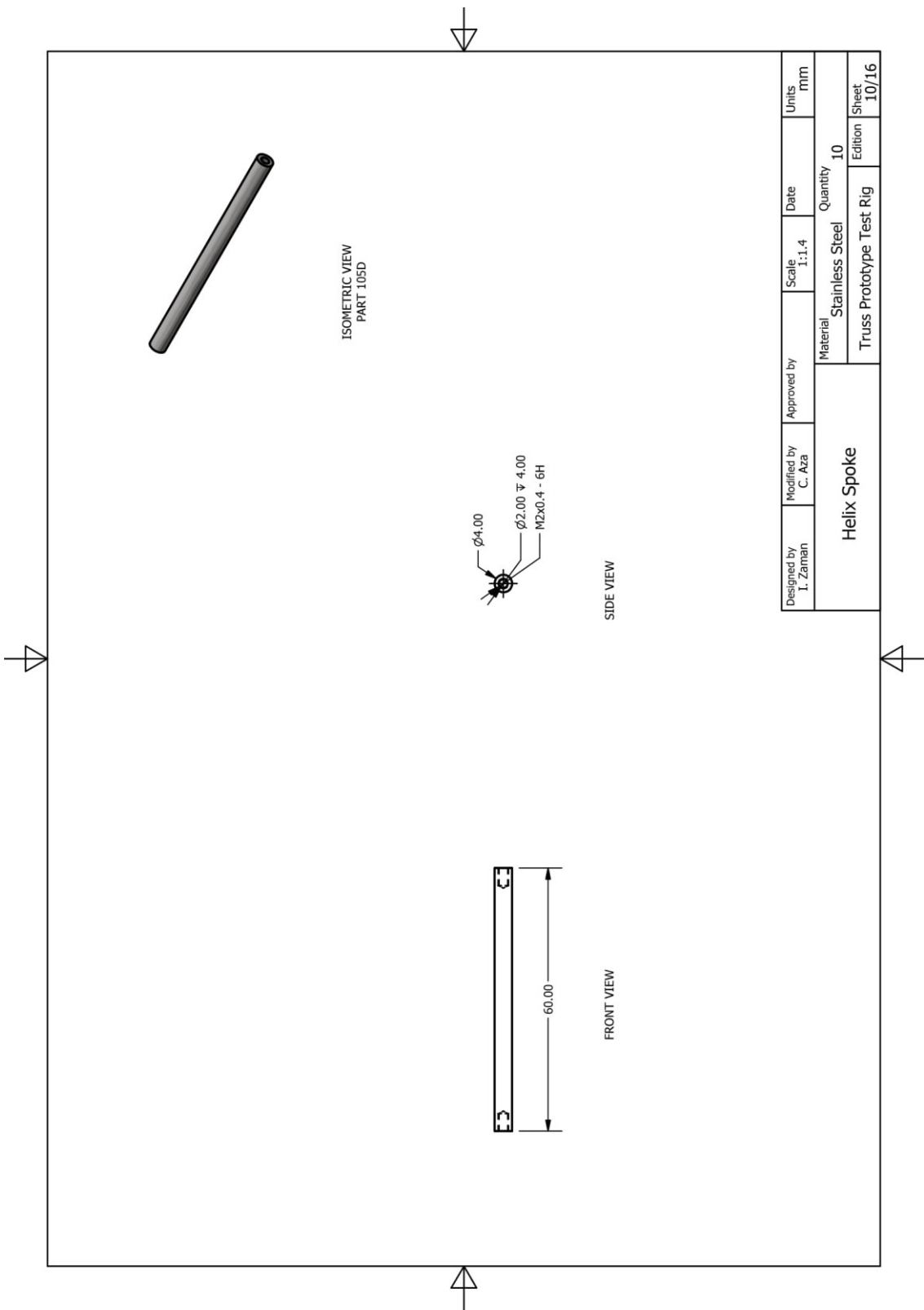


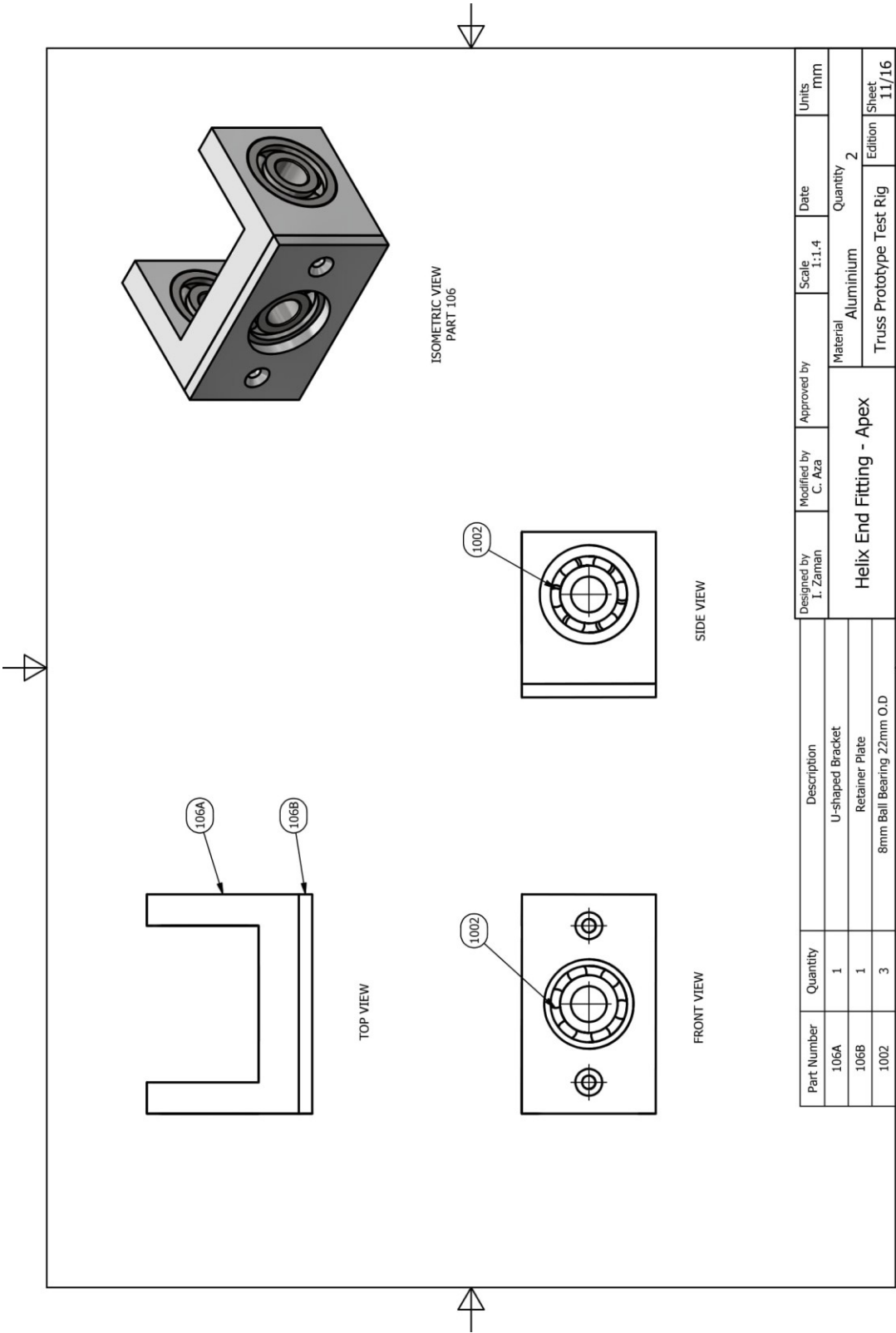


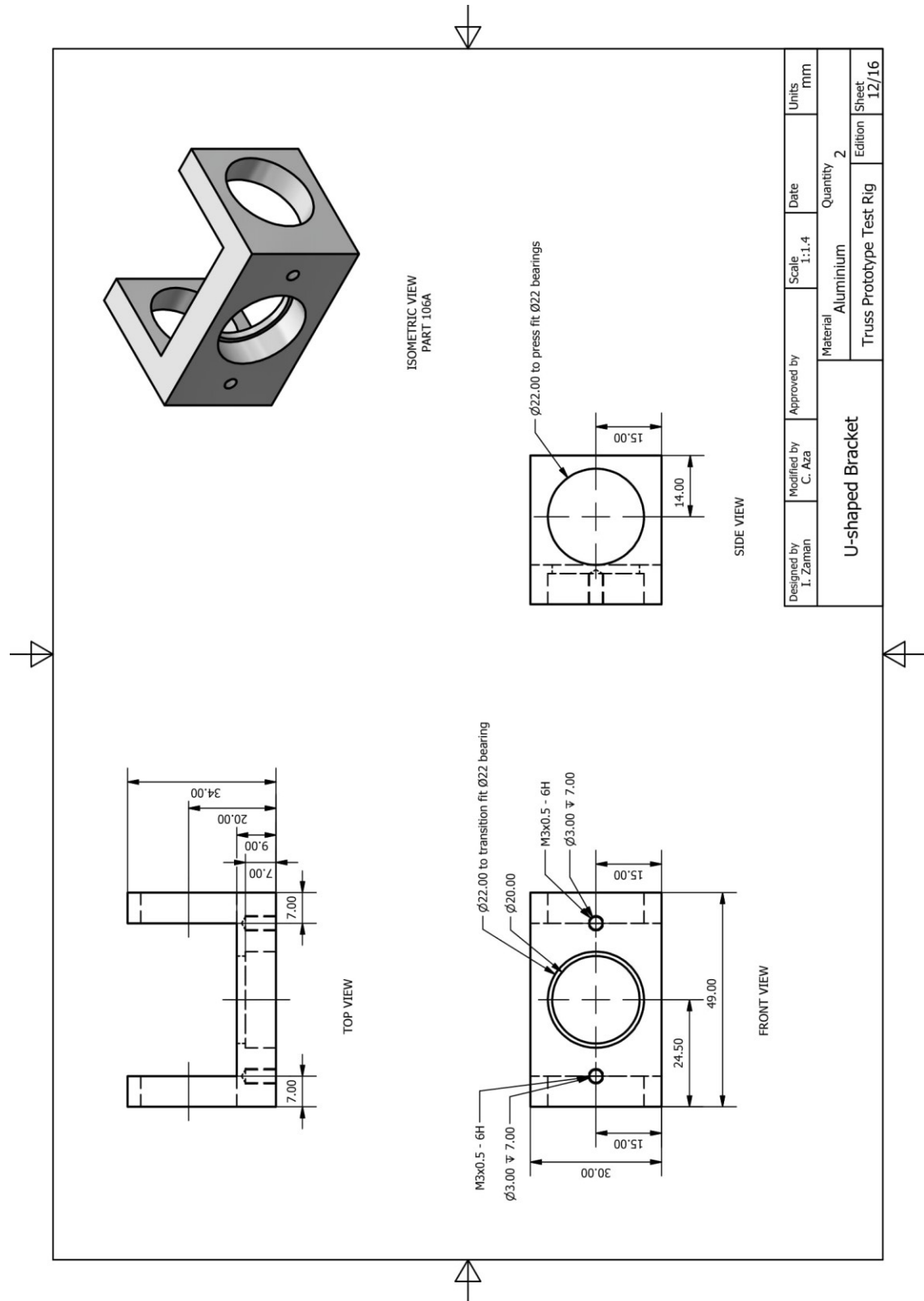


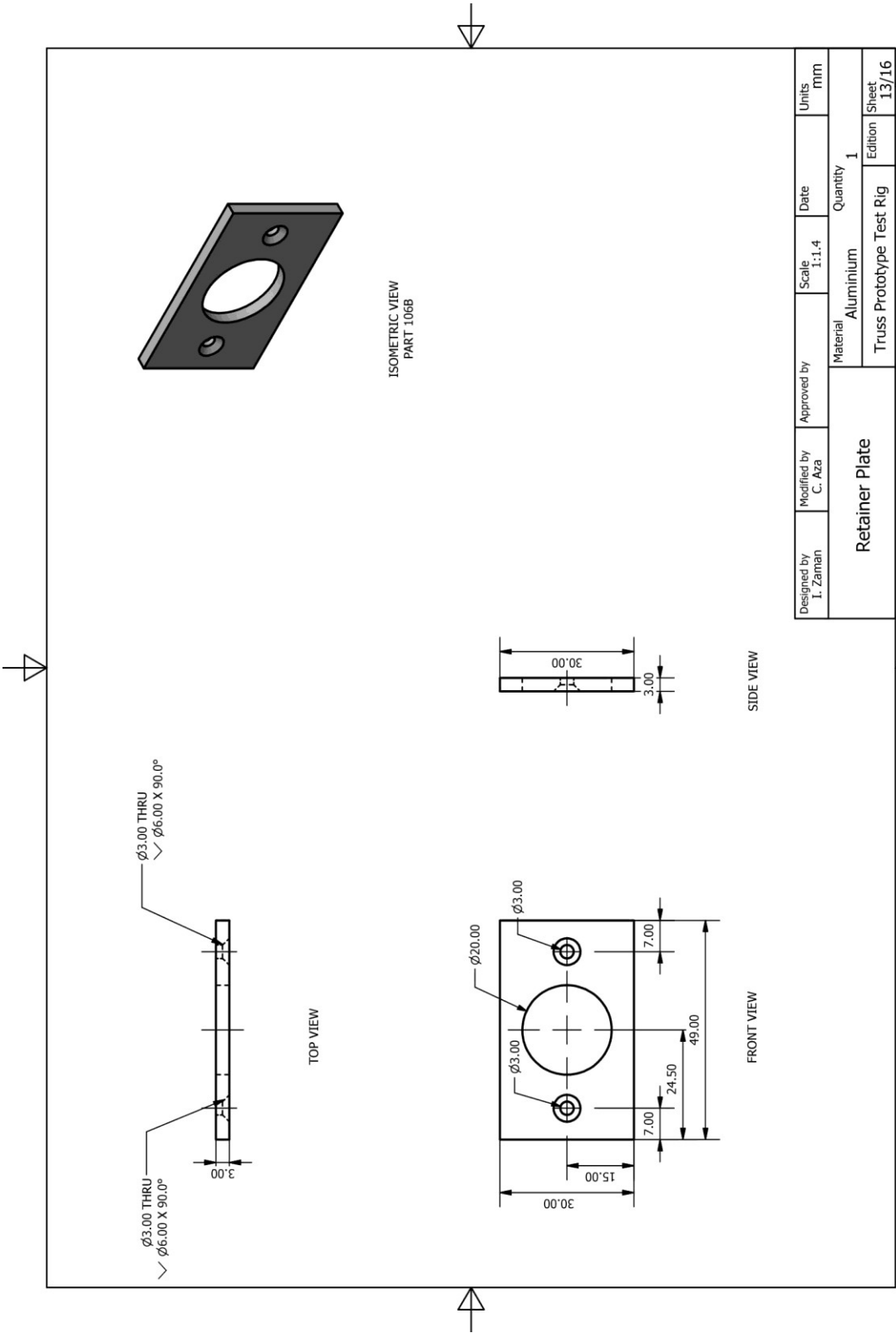


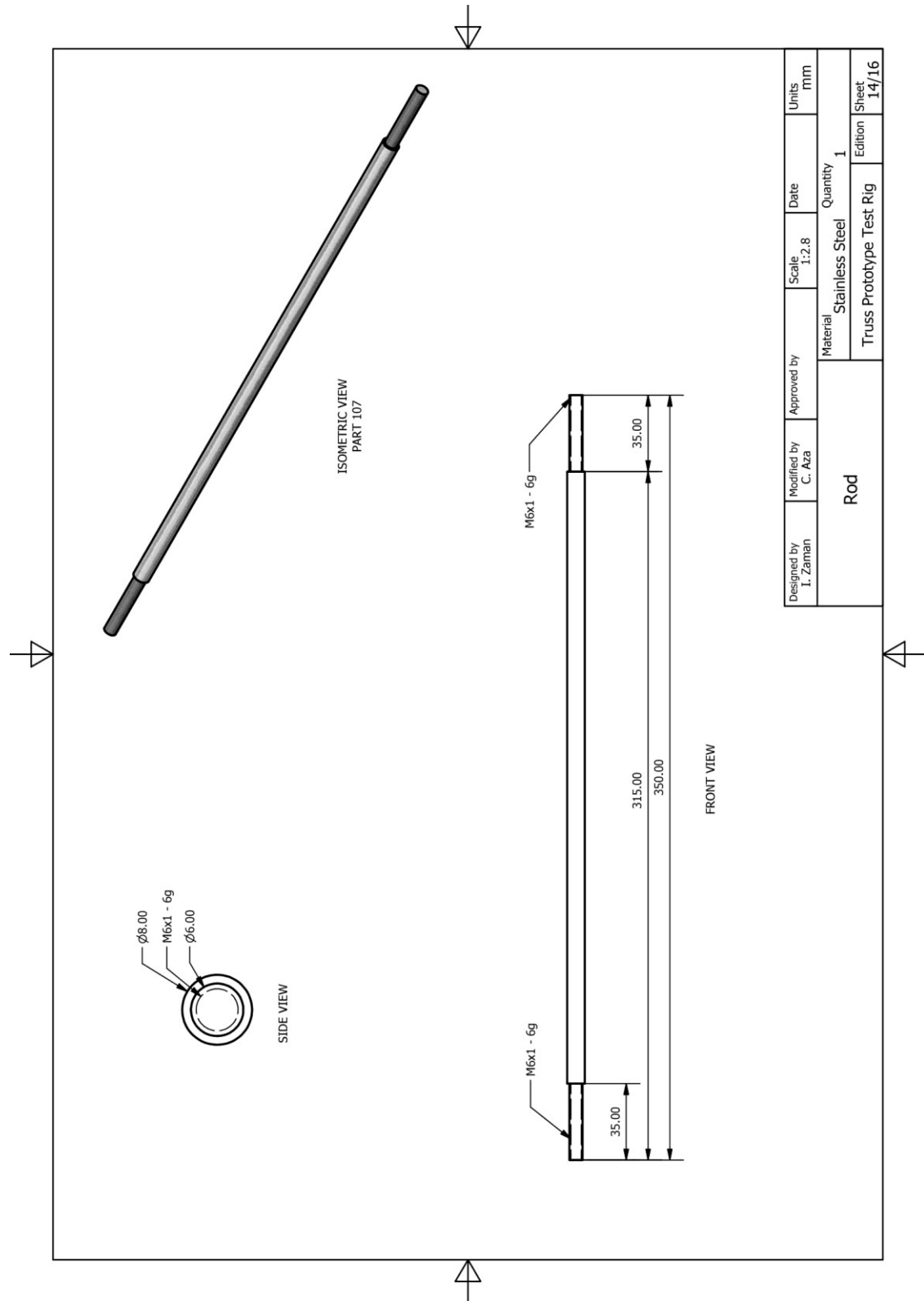


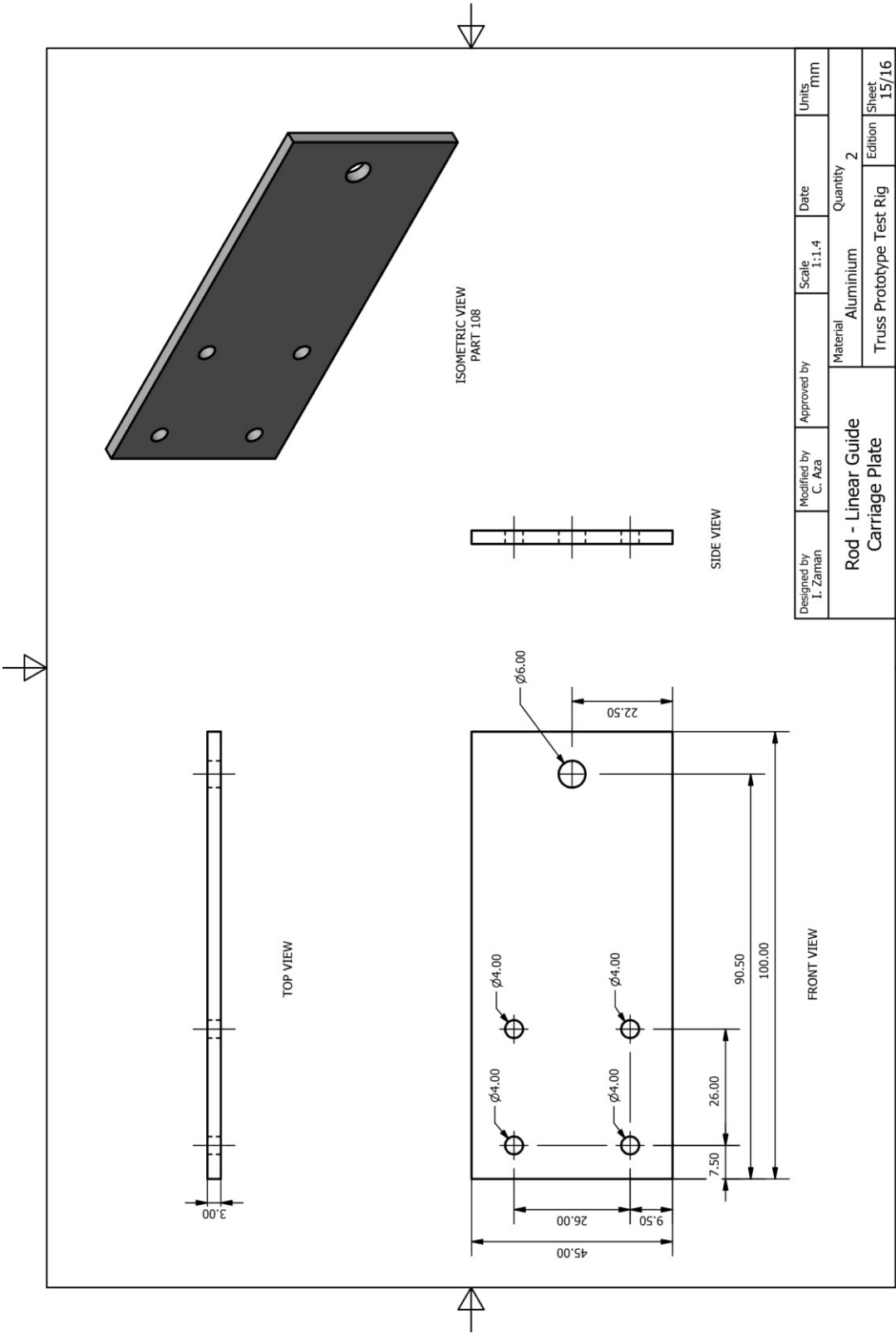


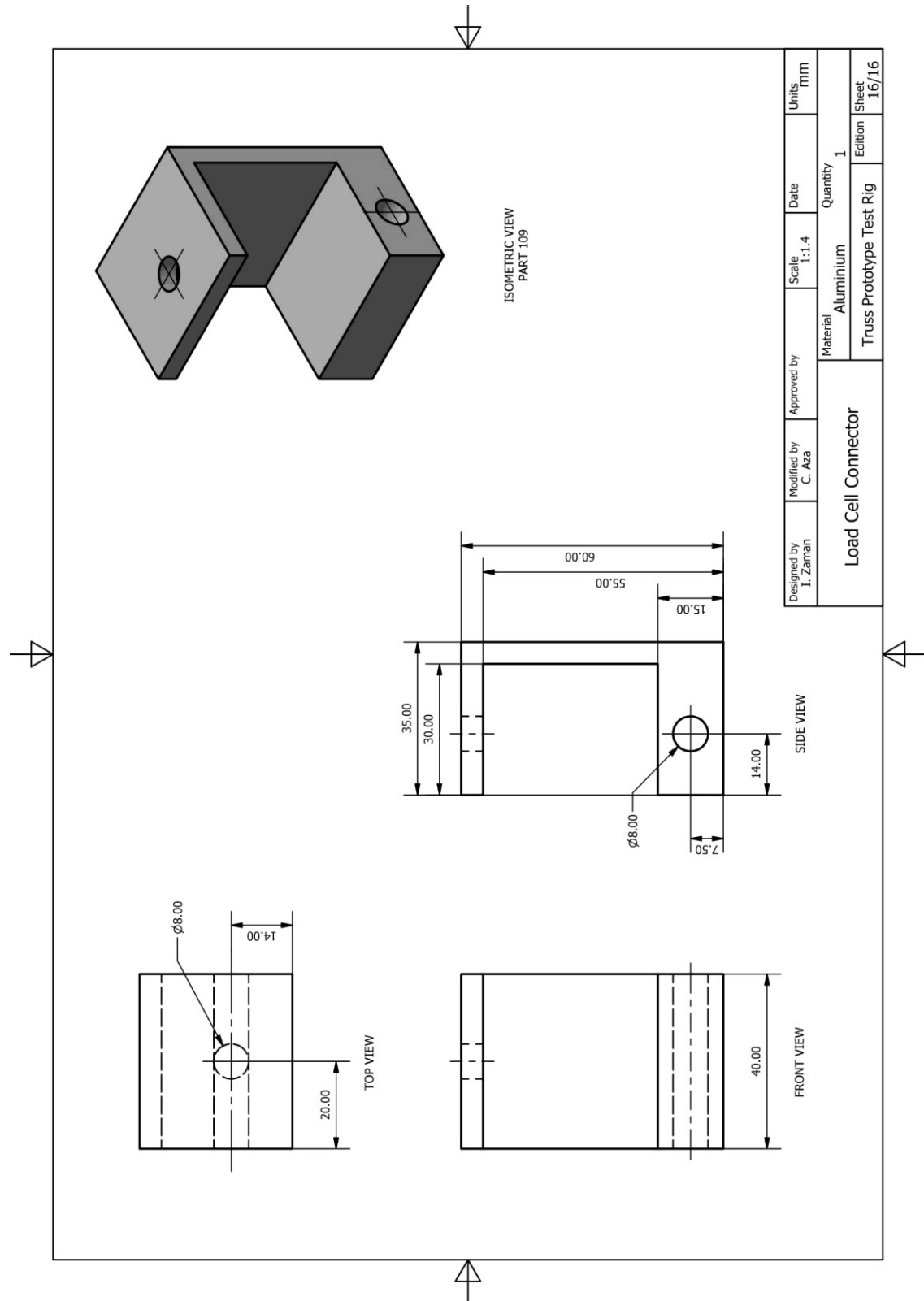




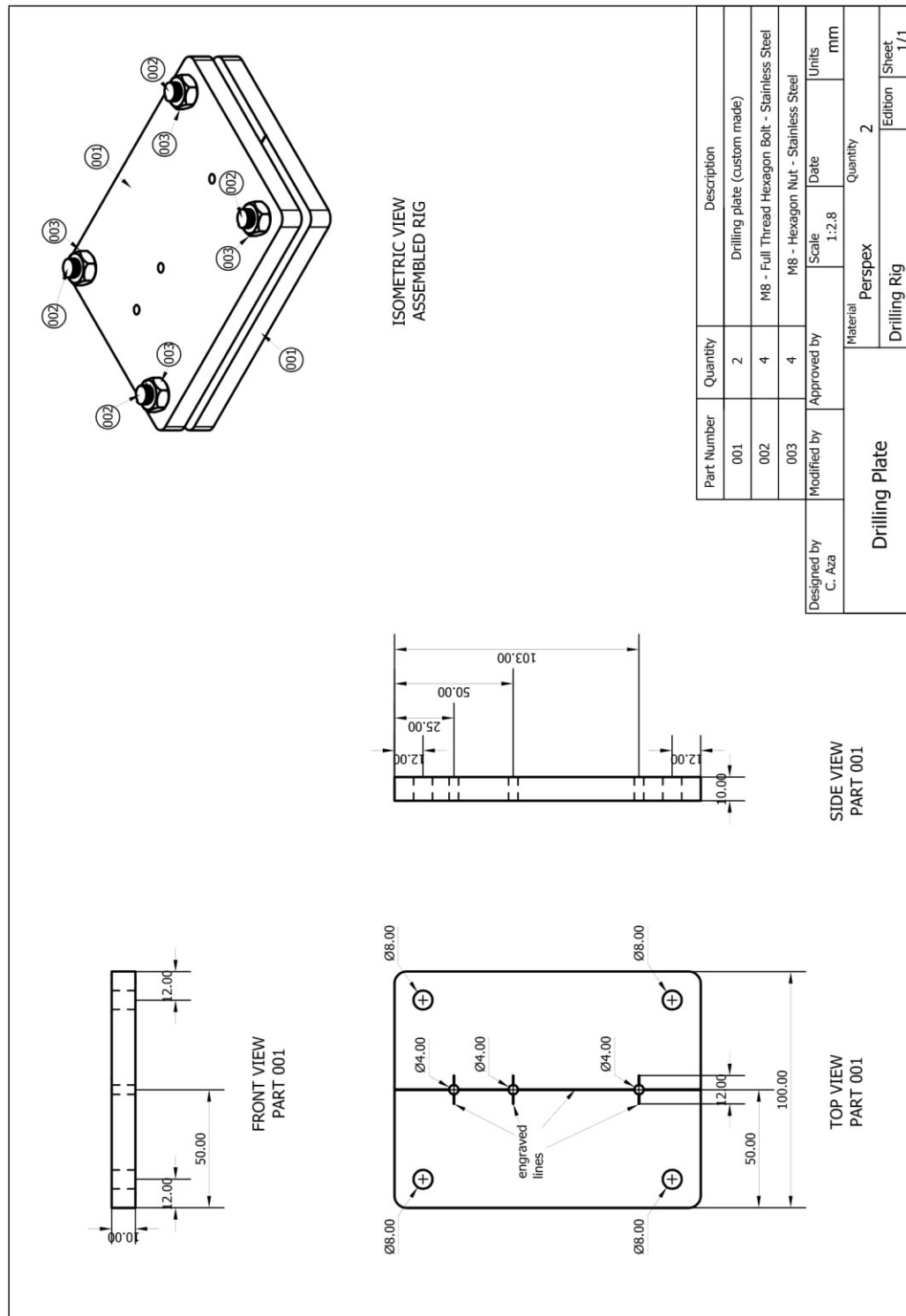








Appendix A.2 – Supplementary Rig for Drilling



Appendix A.3 – Helix Test Rig

